HYDROTHERMAL TOPOCHEMICAL CONVERSION OF $Bi_4Ti_3O_{12}$ NANOPLATELETS FOR FORMATION OF FUNCTIONAL HETEROSTRUCTURAL PEROVSKITE TITANATES

Alja Čontala

Doctoral Dissertation
Jožef Stefan International Postgraduate School
Ljubljana, Slovenia

Supervisor: Dr. Marjeta Maček Kržmanc, Jožef Stefan Institute, Ljubljana, Slovenia

Evaluation Board:
Prof. Darko Makovec, Chair, Jožef Stefan Institute, Ljubljana, Slovenia
Prof. Petar Djinović, Member, National Institute of Chemistry, Ljubljana, Slovenia
Prof. Vincenzo Buscaglia, Member, National Research Council - Institute of Condensed Matter Chemistry and Technologies for Energy, Genova, Italy

MEDNARODNA PODIPLOMSKA ŠOLA JOŽEFA STEFANA
JOŽEF STEFAN INTERNATIONAL POSTGRADUATE SCHOOL

Alja Čontala

HYDROTHERMAL TOPOCHEMICAL CONVERSION OF $Bi_4Ti_3O_{12}$ NANOPLATELETS FOR FORMATION OF FUNCTIONAL HETEROSTRUCTURAL PEROVSKITE TITANATES

Doctoral Dissertation

HIDROTERMALNA TOPOKEMIJSKA PRETVORBA $Bi_4Ti_3O_{12}$ NANOPLOŠČIC ZA PRIPRAVO NOVIH FUNKCIONALNIH HETEROSTRUKTURIRANIH PEROVSKITNIH TITANATOV

Doktorska disertacija

Supervisor: Dr. Marjeta Maček Kržmanc, Jožef Stefan Institute, Ljubljana, Slovenia

Ljubljana, Slovenia, December 2023

“If you don’t see a clear path for what you want, sometimes you have to make it for yourself” (Mindy Kaling)

To Dino and Eva…

… as a reminder and encouragement.

Acknowledgments

Doctoral studies bring their own challenges, not only cognitive ones, but also communicative, organizational, and personal. Everyone steps on this journey with their own knowledge, values, goals, and personal luggage. Doctoral studies and research work at the Advanced Materials Department at the Jožef Stefan Institute was a special experience. JSI, as the largest research institute in Slovenia, boasts a huge amount of state-of-the-art equipment and a veritable treasure trove of knowledge. For me, working in such an environment was therefore a privilege, but at the same time also a huge responsibility. Moreover, working in a research environment is demanding and requires a great deal of self-control and clear purpose. Scientific work requires a lot of creativity, which is difficult to achieve with a busy schedule or a low energy capacity. Therefore, it is so important to take breaks and fill up your battery. As learned from the kids, boredom is the best catalyst for fruitful ideas. Sometimes it is good to step back or look at the problem from a different perspective. It is not necessary to do and figure out everything by yourself. It is okay to ask for help, to be seen, heard and felt. The last year was a big change for me. I made some noise and waves, but also learned from my mistakes. I found new paths and met new people. I cannot see where and how my journey will go. But I see my next step and it is enough.

Challenging paths are easier to overcome by having someone to rely on. Here, I would like to thank all who contributed with your own piece of the puzzle to my doctoral research work within and beyond this dissertation.

Foremost, I would like to thank my supervisor, Dr. Marjeta Maček Kržmanc, for giving me the opportunity for research work and doctoral study at the Advanced Materials Department at the Jožef Stefan Institute and the Jožef Stefan International Postgraduate School. Not every supervisor takes as much time and care for a student as you did. Thank you for every carefully read and reviewed abstract, presentation, article, and of course, this thesis. Thank you for sharing your views and approaches to research work and life with me. All the challenges brought me to the top of that one hill, from which I have a beautiful and wider view today.

I would also like to thank Prof. Danilo Suvorov for welcoming me to the department and for your advice and help during the first year of my doctoral study. Thanks also to Assoc. Prof. Matjaž Spreitzer for all the bits of advice and support in finishing my doctoral study.

I am also thankful to the evaluation board, Prof. Darko Makovec, Assist. Prof. Petar Djinović and Prof. Vincenzo Buscaglia for reading and evaluating my thesis and for all valuable suggestions to improve the dissertation, as well as for the ideas for further research.

I would like to thank the Slovenian Research Agency (ARRS, from May 11, 2023, the agency operates as the Slovenian Research and Innovation Agency (ARIS), project PR-07596) and the M-Era.net projects (3184 HarvEnPiez and 6081 SunToChem) for the financial support during my doctoral education and work.

Thanks to Assoc. Prof. Nina Daneu for all the fruitful debates, advice, and suggestions. Thanks for all the ARM analyses that clarified many ambiguities and gave a new perspective on reactions and prepared materials.

Thanks to Dr. Khaja Mohaideen Kamal and Assoc. Prof. Dr. Blaž Likozar for the measurements of photocatalytic hydrogen evolution, help with the interpretation of the results and discussions.

Thanks to Suraj Gupta, Ph.D. for your help with the photocatalytic hydrogen evolution, and all the conversations about science and life, and advice on my next steps. Thanks to Assoc. Prof. Srečo D. Škapin for introducing me to the world of XRD, and especially, thank you for all the small chats with a great value. Thanks to Dr. Špela Kunej for the help with the particle's self-assembly, photocatalytic measurements, UV/VIS measurements, and determination of band gap energies. Thanks to Damjan Vengust for helping me with Raman spectroscopy and for all the joyful moments. Thanks to Silvo Zupančič for performing BET measurements. Thanks to Blaž Jaklič for the XPS measurements. I am grateful to Medeja Gec for the sample preparation for cross-sectional STEM analyses. I would also like to thank Prof. Anton Meden for high-temperature and high-resolution XRD measurements and calculations of the unit cell parameters.

Thank you, Dr. Jitka Hreščak, for bringing the world of scanning electron microscopy closer to me, for widening my perspective of what my further journey could be, and for all the encouragement.

Every joy is a double joy, and every worry is half a worry when shared with friends. Lea Gazvoda, Dr. Uroš Hribar, Nina Kuzmić, Petruša Borštnar, Dr. Sonja Jovanović, Dr. Urška Trstenjak and Dr. Tjaša Parkelj Potočnik, I am grateful for having you onboard, and for being heard and understood. Thanks for all the laughs, pieces of advice, and conversations. Thank you for offering your shoulder when needed. Thank you also for all the professional and technical help.

Thanks to Vesna Butinar, the IPS secretariat, and the JSI colleagues in the FRS for the help with the documentation and all the formalities.

Thanks also to all other K9 colleagues. Each of you contributed a piece of the mosaic to my story.

Thanks also to my friends, neighbors, and family members who stood by me, encouraged me, and filled me with courage and energy. Thank you for believing in me even when I did not.

A special thanks goes to my Blanka, who has been by my side since high school. Moving, falling in love, giving birth to our children, new jobs and other major events did not drive us apart, but only brought us closer. I am grateful for having you by my side.

Bojan, thank you for your love, for your support, and for your patience. Thanks for the different perspectives and for going with me through all the challenges that are pushing me into the unknown, allowing me to learn and grow further.

Dino and Eva, I am beyond grateful for having you. Sometimes, you are my mirror picture, but at the same time, you can picture me what life can be without limits and expectations. Thanks for being my greatest teacher and know that I am trying my best. I love you.

I am excited for a new chapter in my life.

Abstract

In the view of designing new nanostructured materials and tailoring their functional properties, understanding the nucleation and crystal growth mechanisms is becoming increasingly important.

Nowadays, one of the most addressed scientific and social problems are those facing energy shortage and global warming. People started to realize the value and importance of a clean and healthy environment. To become independent from fossil fuels and to achieve the EU goal related to zero emissions of CO_2 by 2050, intensive efforts are going on in searching for alternative energy sources. One of the sustainable approaches is to use abundant free energy from the environment (sun, wind, waste vibrations, etc.) to produce renewable fuels through various catalytic or electrochemical processes.

An enormous number of studies have been done on the topic of photocatalytic and photoelectrochemical hydrogen evolution from water splitting in the past years. Still, the hydrogen fuel is not in everyday use yet. Mainly due to the low efficiency of photocatalytic reactions and insufficient solar energy utilization. The main challenges are related to photon absorption, photoinduced charge carrier separation, and their transport to the surface, where redox reactions take place.

Size, shape, and type of exposed facets can significantly affect a material's electrical, optical, and photocatalytic properties. Compared to large 3D particles, 2D structures with appropriate low thicknesses are more advantageous for lowering photoinduced charge carriers' recombination. Additionally, the formation of heterostructures is known to be beneficial for the improvement of photocatalytic performance in many aspects, such as enhancing charge carrier separation, widening of utilized spectral range, and increasing stability. The photocatalysts in my thesis were designed including the above-mentioned considerations.

In my research, I focused on the preparation of H_2-evolution photocatalysts based on heterostructural $SrTiO_3/Bi_4Ti_3O_{12}$ nanoplatelets and I studied the mechanism for their formation. The $SrTiO_3$ and $Bi_4Ti_3O_{12}$ were selected based on similar structural elements that allow epitaxial growth and enable the formation of the heterostructure or pseudomorphic transformation. Additionally, $Bi_4Ti_3O_{12}$ spontaneously grows in a two-dimensional shape, which is not typical for $SrTiO_3$. Both materials also have favorable relative positions of the conduction and valence bands for the formation of hydrogen and oxygen, respectively.

My studies were performed in several steps. In the first step, the process of $Bi_4Ti_3O_{12}$ template preparation was optimized. In the second step, $Bi_4Ti_3O_{12}$ platelets were used as a template for the topochemical conversion into different $SrTiO_3/Bi_4Ti_3O_{12}$ heterostructures and pure $SrTiO_3$. An in-depth study of the transformation mechanism was performed through atomic scale analysis of the platelets at different transformation stages and Rietveld structural refinements of the $SrTiO_3$ and $Bi_4Ti_3O_{12}$ phases. Based on the latter we examined the misfits in relevant orientation relationships and at actual temperatures.

A combination of various techniques (X-ray diffraction, electron microscopy, X-ray photoelectron spectroscopy) enabled me to perform very thorough research on how to steer the topochemical conversion by balancing the lattice mismatch, template quality, and supersaturation as well as how to tailor the functional properties of the product platelets by varying experimental conditions. Moreover, the principles inferred from the study of the $Bi_4Ti_3O_{12}$-to-$SrTiO_3$ conversion were translated for the transformation from $Bi_4Ti_3O_{12}$ to $BaTiO_3$ and $CaTiO_3$. Finally, the photocatalytic hydrogen evolution of prepared heterostructural $SrTiO_3/Bi_4Ti_3O_{12}$ and $SrTiO_3$ platelets was evaluated.

This comprehensive investigation of the topochemical conversion mechanism from $Bi_4Ti_3O_{12}$ to $SrTiO_3$ with the intermediate formation of 2D epitaxial heterostructures not only contributes to a refined understanding of this system but also paves the way for the engineering of other new intricate epitaxial heterostructures in the future. Furthermore, insights gleaned from this dissertation offer a fertile ground for the development of advanced functional materials, characterized by heightened stability, efficiency, and eco-friendliness. These materials hold promise in diverse catalytic realms, spanning hydrogen evolution, CO_2 reduction as well as pollutant decompositions, among others.

Povzetek

Z vidika načrtovanja novih nanostrukturnih materialov in prilagajanja njihovih funkcionalnih lastnosti postaja razumevanje mehanizmov nukleacije in rasti kristalov vse bolj pomembno.

Izzivi, povezani s pomanjkanjem energije in globalnega segrevanja, so eni od najbolj obravnavanih znanstvenih in družbenih problemov dandanes. Ljudje se vedno bolj zavedamo vrednosti in pomena čistega in zdravega okolja. Za vzpostavitev neodvisnosti od fosilnih goriv in za doseganje ciljev EU glede ničelnih emisij CO_2 do leta 2050 potekajo intenzivna prizadevanja v iskanju alternativnih virov energije. Eden od trajnostnih pristopov je uporaba proste energije iz okolja (sonce, veter, odpadne vibracije) za proizvodnjo obnovljivih goriv s katalitskimi ali elektrokemijskimi procesi.

V preteklih letih je bilo opravljenih ogromno raziskav na temo fotokatalitskega in fotoelektrokemijskega nastanka vodika s cepitvijo vode. Kljub temu zelen vodik kot gorivo še ni v vsakodnevni uporabi. Predvsem zaradi nizke učinkovitosti fotokatalitskih reakcij in nezadostnega izkoristka sončne energije. Glavni izzivi so povezani z absorpcijo fotonov, nezadostno ločitvijo fotoinduciranih nosilcev naboja in njihovim neučinkovitim transportom na površino, kjer potekajo redoks reakcije.

Velikost, oblika in vrsta izpostavljenih ploskev lahko pomembno vplivajo na električne, optične in fotokatalitske lastnosti materiala. V primerjavi z velikimi 3D delci so 2D strukture z ustrezno nizko debelino ugodnejše za zmanjšanje rekombinacije nosilcev naboja. Poleg tega je znano, da je tvorba heterostruktur koristna za izboljšanje fotokatalitske učinkovitosti v številnih vidikih, kot je izboljšana ločitev nosilcev naboja, razširitev uporabljenega spektralnega območja in povečanje stabilnosti. Fotokatalizatorji v moji doktorski disertaciji so bili zasnovani z upoštevanjem zgoraj omenjenih ugotovitev.

V doktorski nalogi sem se osredotočila na pripravo in proučevanje mehanizma nastanka heterostrukturiranih ploščic $SrTiO_3/Bi_4Ti_3O_{12}$, ki bi lahko služile kot fotokatalizatorji za proizvodnjo vodika kot vira energije. Materiali so bili izbrani na podlagi podobnih strukturnih elementov, ki omogočajo epitaksialno rast in nastanek heterostrukture. Oba materiala imata tudi ugoden relativni položaj valenčnega in prevodnega pasu za tvorbo vodika in kisika.

Študija je obsegala več korakov. V prvem koraku sem optimizirala postopek priprave $Bi_4Ti_3O_{12}$ ploščic. V drugem koraku sem uporabila te $Bi_4Ti_3O_{12}$ ploščice kot templat (matrico) za pretvorbo v različne heterostrukture $SrTiO_3/Bi_4Ti_3O_{12}$ in čisti $SrTiO_3$. Za razumevanje mehanizma sem določila orientacijsko razmerje in ujemanje struktur, pregledala delno pretvorjene delce $SrTiO_3/Bi_4Ti_3O_{12}$ in preučevala reakcijski mehanizem z razvojem morfologije pri različnih stopnjah prenasičenja. Raziskovala sem medsebojni vpliv kakovosti templata in prenasičenosti. Rentgenska difrakcija in elektronska mikroskopija sta mi pomagali razumeti te procese. Poleg tega so bili ugotovljeni principi uporabljeni tudi za pretvorbo $Bi_4Ti_3O_{12}$ v $BaTiO_3$ in $CaTiO_3$. Na koncu je bilo ovrednoteno fotokatalitsko razvijanje vodika pripravljenih heterostrukturiranih ploščic $SrTiO_3/Bi_4Ti_3O_{12}$ in $SrTiO_3$.

Ta obsežna raziskava mehanizma topokemijske pretvorbe iz $Bi_4Ti_3O_{12}$ v $SrTiO_3$ z vmesnim nastankom 2D epitaksialnih heterostruktur ne prispeva le k izpopolnjenemu razumevanju tega specifičnega sistema, ampak tudi utira pot za načrtovanje drugih novih zapletenih epitaksialnih heterostruktur v prihodnosti. Poleg tega so spoznanja, pridobljena iz te disertacije, pomembna za razvoj drugih naprednih funkcionalnih materialov, za katere je značilna večja stabilnost, učinkovitost in prijaznost do okolja. Možnost uporabe teh materialov je na različnih katalitskih področjih, od razvoja vodika, redukcije CO_2 in razgradnje onesnaževal.

Contents

List of Figures

List of Tables

Abbreviations

ARM	. . .	atomic resolved microscope
BET	. . .	Brunauer–Emmett–Teller surface area measurements
BIT	. . .	bismuth titanate, $Bi_4Ti_3O_{12}$
BSE	. . .	backscattered electrons
BT, BTO	. . .	barium titanate, $BaTiO_3$
CB	. . .	conduction band
CT, CTO	. . .	calcium titanate, $CaTiO_3$
CVD	. . .	Chemical vapor deposition
DSC	. . .	differential scanning calorimetry
DRS	. . .	diffuse reflectance spectroscopy
EDXS	. . .	electron diffraction x-ray spectroscopy
E_{CB}	. . .	conduction band energy
E_F	. . .	Fermi level energy
E_g	. . .	band gap energy
E_{VB}	. . .	valence band energy
FE-SEM	. . .	field emission scanning electron microscopy
FEG	. . .	field emission gun
FT-IR	. . .	Fourier transform infrared spectroscopy
HAADF	. . .	high angular annual dark field
HER	. . .	hydrogen evolution reaction
HR	. . .	high resolution
K-M	. . .	Kubelka-Munk
MBE	. . .	Molecular beam epitaxy
NW	. . .	nanowires
PA	. . .	photocatalytic activity
PECS	. . .	precision etching coating system
PL	. . .	photoluminescence
PLD	. . .	Pulsed laser deposition
RhB	. . .	rhodamine B
SE	. . .	secondary electrons
SEM	. . .	scanning electron microscopy
SPR	. . .	surface plasmon resonance
ST, STO	. . .	strontium titanate, $SrTiO_3$
STEM	. . .	scanning transmission electron microscopy
STH	. . .	solar to hydrogen
TC	. . .	topochemical conversion
TCE	. . .	thermal expansion coefficient
TEM	. . .	transmission electron microscopy
UV/VIS	. . .	ultraviolet/visible light spectroscopy
VB	. . .	valence band
XPS	. . .	x-ray photoelectron spectroscopy
XRD	. . .	x-ray diffraction

Symbols

α	. . .	interfacial free energy
α	. . .	intrinsic absorption coefficient of the material
$\alpha(A)$	. . .	activity of A
a_f	. . .	lattice spacing of a film
a_s	. . .	lattice spacing of a substrate
A	. . .	Arrhenius coefficient
c	. . .	concentration
λ	. . .	wavelength
g_n	. . .	activation nucleation energy barrier
K	. . .	K-M absorption coefficient
K_S	. . .	solubility product
χ	. . .	Mullikan's electron negativity
r	. . .	atomic radius
R	. . .	ratio of reflectance of the sample and the standard
s	. . .	scattering coefficient of the material
S	. . .	K-M scattering coefficient
S	. . .	supersaturation
T	. . .	temperature
t	. . .	time
t	. . .	tolerance factor
x_0	. . .	average spacing between misfit dislocations

Chapter 1

Introduction

This dissertation is focused on functional perovskite titanates, including $ATiO_3$ (A=Sr, Ba, Ca) and $ATiO_3/Bi_4Ti_3O_{12}$ heterostructures. Particularly, I investigated the reaction mechanisms for the preparation of perovskite particles (structures/nanostructures) with predefined controlled morphologies. The emphasis is on innovative synthesis approaches based on knowledge of the structure of materials and a thorough understanding of the nucleation-crystallization theory. In the beginning, some basics about the main studied materials, perovskites, are presented. Aurivillius phase layered perovskite-like $Bi_4Ti_3O_{12}$ and $SrTiO_3$, the main materials of this dissertation, are described in greater detail. The main emphasis is on their synthesis routes and approaches for morphology control, while their properties are briefly described. The most prominent studies describing topochemical transformations are presented. The second part presents the basics of crystal nucleation and growth. The third part of the introduction is dedicated to the presentation of photocatalytic hydrogen production.

1.1 Perovskites and Perovskite Titanates

Perovskite is the name originally given to the oxide mineral calcium titanate, $CaTiO_3$, which was discovered in the Ural Mountains of Russia by Gustav Rose in 1839. The mineral was named after a Russian mineralogist Lev Aleksevich Perovski (1792-1856). Later, the whole family of materials with the same crystal structure as $CaTiO_3$ was named perovskites. The perovskite (ABX_3) group of materials is very broad, and it is not limited only to oxide perovskites (ABO_3), but for example, also includes halide perovskites (e.g., $CsPbI_3$). The perovskite family has been studied because of their diverse properties and wide-range application potential. Significant attention was gained in recent years, especially in the field of photovoltaics (solar cells) due to their exceptional optical and electronic properties. Perovskite solar cells have the potential to be highly efficient along with their low cost and easy manufacturing making them a promising alternative to traditional silicon-based solar cells. Apart from solar cells, perovskite materials have applications in other areas such as light-emitting diodes (LEDs), lasers, sensors, catalysis, and fuel cells [1]–[3].

The perovskite compound with a general formula ABX_3 consists of two types of cations (A and B) and anion (X), which is, in the case of perovskite oxides, oxygen (Figure 1). The cations can differ in their valence states. The combinations of divalent A and tetravalent B ions give a very broad group of important functional materials predominantly based on $ATiO_3$ and $AZrO_3$ (A=Pb, Ca, Sr, Ba). Important functional materials are also perovskites, where A and B are both trivalent cations (e.g., $LaGaO_3$) or a combination of A^{1+} and B^{5+} (e.g., $KNbO_3$). The focus of this thesis is on ABO_3 perovskites with Ti^{4+} on the B-site. Those materials are called perovskite titanates. An ideal unit cell is sketched in Figure 1. A-site atom (green), B-site atom (blue), and oxygen (red) occupy the corner site, body-centered site, and face-centered site, respectively. So, in perovskite titanates, the Ti^{4+} cation is corner-sharing bonded to six O^{2-} anions, forming an octahedral TiO_6 unit. However, many perovskites display distortions from the ideal structure, which manifest themselves as rotation or tilting of the BO_6 octahedra, distortion of the BO_6 octahedra, and distortion of the A and B cation polyhedra. The displacement of the B-site atom generates an electric dipole moment and hence, generates spontaneous polarization [1], [4].

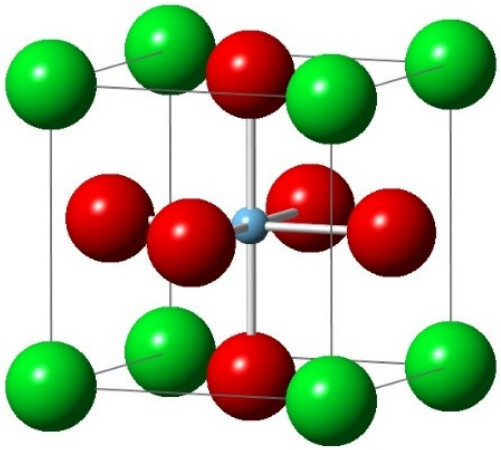

Figure 1: Atomic structure of ABO_3-type perovskite unit cell. The sizes of the spheres represent the atomic radii of ions in $SrTiO_3$.

In an ideal case, the sizes of the cations, bond lengths, and angles are perfectly balanced, as shown in Figure 1. This is the case of $SrTiO_3$. In other perovskite titanates, the distortions take place due to the difference in the size of the cations on the A and B sites and importantly influence the properties of the materials. The distortion occurs to minimize the strain caused by the size mismatch between the cations. As a result, crystal structures became tetragonal, orthorhombic, rhombohedral, or other, depending on the degree and nature of the distortion. It is important to note that the crystal structure of a perovskite titanate significantly influences its physical and chemical properties [1], [4].

The link between the difference in cation size and the possibility for the formation of the perovskite structure represents Goldschmidt's tolerance factor, *t*, which is defined by Equation 1, where r_A, r_B, and r_O are the radii of the ions on the A, B, and C sites, respectively. Distortions can be controlled and predicted, therefore, specific properties of designed perovskites can be envisaged, which saves time and cost. In the process of designing the materials with perovskite structure, the ionic radii and charges must be considered.

$$t = \frac{r_A + r_O}{\sqrt{2}(r_B + r_O)} \tag{1}$$

According to Eq. (1), the tolerance factor is smaller than 1 when the ionic radius of the A-site cation is slightly smaller. Because of the smaller cation on the A-site, the octahedral unit $[BO_6]$ tilts forward and fills up the additional available space. Such distortion results in the change of cubic unit cell to the orthorhombic structure. [4] On the contrary, the tolerance factor is greater than 1 when either the A-site cation is too large, or the B-site cation is too small. This group can result in a hexagonal or tetragonal structure. $BaTiO_3$ is one of the most known examples of tetragonal perovskites. It is a ferroelectric material due to dipole momentum arising from the Ti^{4+} ion displacement in the octahedral sites. The TiO_6 octahedra are slightly distorted due to the different lengths of Ti-O bonds.

Crystal structure affects the morphology of perovskite titanates in the sense that the arrangement of atoms within the crystal lattice influences the shape, size, and surface characteristics of the resulting particles or structures. Perovskite titanates usually adopt cubic (e.g., $SrTiO_3$) or tetragonal (e.g., $BaTiO_3$) and orthorhombic (e.g., $CaTiO_3$) crystal structure. Also, the most usual morphologies of perovskite titanates appeared to be cubes and cuboids. This happens because crystal structures with a higher degree of symmetry (cubic) lead to more isotropic growth and result in the formation of particles with more regular shapes (cubes, spheres, cuboids). On the contrary, crystal structures with a lower degree of symmetry (tetragonal, orthorhombic) may lead to anisotropic growth and result in anisotropic morphologies, such as platelets or even needles. However, these are not the shapes in which $ATiO_3$ (A = Sr, Ba) perovskite particles spontaneously grow.

Table 1: The link between the tolerance factor and crystal structure with the examples. Ionic radii data was found in [5].

Tolerance Factor	Structure	Example	Ionic radius A-site cation	Ionic radius B-site cation
>1.0	hexagonal tetragonal	$BaNiO_3$ $BaTiO_3$	1.61 Å 1.61 Å	0.48 Å 0.605 Å
0.9-1.0	cubic	$SrTiO_3$	1.44 Å	0.605 Å
0.71-0.9	orthorhombic	$CaTiO_3$	1.34 Å	0.605 Å

Achieving desired morphology is one of the challenges in perovskite titanate synthesis. Most commonly, perovskite titanates crystallize in cubic or spherical morphologies. However, for some applications and achieving enhanced properties, sometimes other morphologies would be beneficial. Therefore, different approaches are commonly employed for morphology control including the control or precursor composition, reaction conditions, method selection, use of solvent and/or additives, template-assisted synthesis, and post-synthesis processing.

The precursor composition (e.g. nominal ratio of A-site and B-site cations) as well as the choice of solvent or additives can be used to manipulate the nucleation and crystal growth processes, helping to achieve different particle morphologies. Additionally, the selection of the solvent and/or additive with different polarities and boiling point affect the solubility and crystallization behavior and therefore lead to variations in product particle morphology. Similarly, the choice of synthesis method and reaction conditions can influence final particle morphology by influencing the kinetics of nucleation and crystal growth. Template-assisted methods (e.g. template grain growth, topochemical conversion) are using templates to guide the growth of perovskite titanate particles and control their morphology. Final morphologies obtained through these methods are most commonly nanowires, nanoplatelets, hierarchical structures with multi-level organization, and porous structures. The porous structures are interesting because of the presence of interconnected pores or voids within the material, providing a large surface area, which can be a great advantage for catalysis, energy storage, or sensor applications. The last group of methods used for morphology control are post-synthesis processing methods, including annealing, calcination, and etching. Here, particle rearrangement, phase transformations, or removal of certain components usually occur, leading to morphological changes [2].

Perovskite titanates can be synthesized using various methods, including solid-state reaction, molten salt synthesis (MSS), sol-gel processing, hydro- and solvothermal reactions, pulsed laser deposition (PLD), chemical vapor deposition (CVD), and others. The choice of synthesis method depends on the desired composition, crystallinity, morphology, properties, and targeted application. The selection of the synthesis approach is also based on simplicity, low costs, and reproducibility along with environmental and health impact [2].

As a variety of elements in the periodic table can possess positions at A and B unit cell sites, an enormous number of compounds with structural similarity, but a variety of properties can be achieved. This makes perovskite titanates suitable for a wide range of applications [6]–[15]. The main reasons for perovskite titanates being widely researched materials are: (i) versatile functionalities – ferroelectricity, ferromagnetism, piezoelectricity, and high dielectric constants make them attractive for applications in electronics, energy storage, sensors, and catalysis, (ii) tunable properties – the properties can be easily modified and tuned by doping or substituting elements within the crystal structure, thus obtaining application-specific requirements and improving the properties, (iii) multifunctionality – perovskite titanates often exhibit multiple functional properties simultaneously, opening up possibilities for improving the performance and novel applications, (iv) high dielectric constant is a benefit for materials used in capacitors and energy storage devices, and (v) sustainability and low costs – help to promote using those materials in large-scale applications. [1], [2]

In the past decade, perovskite titanates were recognized as promising materials for the development of novel electronic devices, data storage systems, and energy-efficient technologies that could revolutionize various fields. Perovskite titanates are also of great interest to researchers due to their fundamental scientific importance. Their structure, properties, and behavior are studied to get a deeper understanding of material science, solid-state physics, and the interplay between phenomena at the atomic and electronic levels.

Despite the perovskite titanates possessing numerous attractive properties and potential applications, they also have certain limitations, such as: (i) long-term stability and durability – the exposure to high temperatures, humidity, or to reactive gases can lead to degradation to structural changes over time, affecting their long-term performance and reliability, (ii) processing challenges – complex synthesis and processing procedures can be challenging to achieve high reproducibility; large scale production can also be hindered if desired composition, purity,

crystallinity of materials are required, (iii) high-temperature processing – certain perovskite titanates require high-temperature processing methods, which consume a lot of energy and consequently produce high costs; such materials are consequently less or non-appropriate for large-scale applications, (iv) toxicity and environmental concerns – some perovskite titanates show excellent properties and offer great application potential, but contain elements that are harmful to people or environment (e.g. Pb and $PbTiO_3$), (v) limited scalability – many perovskite titanates show promising results in lab-scale research, however, the scale-up process remains a challenge due to many reasons, e.g. maintaining consistent properties, performance, cost-effectiveness, (vi) efficiency – several perovskite titanates are low-cost, safe and non-toxic, easy to prepare, but suffer from too low efficiency, which would lead to (near) impossible scale-up and general use [1], [2].

1.1.1 $SrTiO_3$

Strontium titanate ($SrTiO_3$, STO) is a typical representative of the perovskite structural family. Above 105 K, it exhibits a cubic perovskite structure with a *Pm3m* space group and a lattice constant of 0.3905 nm. In the crystal structure, Ti^{4+} ions occupy centrosymmetric positions within $[TiO_6]^{8-}$ octahedra, while Sr^{2+} ions reside in twelve-coordinate interstices [16].

$SrTiO_3$ has a high temperature of melting, T_c = 2080 °C, which makes it useful in high-temperature applications [17]. The tetragonal structure of $SrTiO_3$ formed by cooling of cubic modification below 105 K does not display ferroelectricity. Therefore, $SrTiO_3$ is a part of quantum paraelectric or incipient ferroelectric materials. $SrTiO_3$ is known for its high dielectric constants, which makes it suitable for applications in capacitors, varistors, and other electronic devices where high dielectric materials are required. It is one of the most interesting multifunctional oxides because its properties can be easily modified and tailored by changing the oxygen stoichiometry, doping with foreign elements, and applying elastic stresses in the case of films [18], [19]. Commonly, in the fabrication of thin films by physical methods (e.g. PLD), $SrTiO_3$ is used as a substrate for epitaxial growth due to its lattice-matching properties, excellent crystal quality, flexibility in doping, and surface termination control [20]. Strontium titanate also exhibits good catalytic and photocatalytic properties [16], [21], [22], to some extent similar to that of TiO_2. Especially, $SrTiO_3$ is widely investigated for water-splitting processes [23]–[27] and solar cells [7], [28], [29]. In comparison to TiO_2, $SrTiO_3$ has about 200 mV more negative conduction band and it shows good thermal and chemical stability. It is also a non-toxic, non-volatile, and relatively cheap material. However, as a photocatalyst or photo electrocatalyst, the main drawback of $SrTiO_3$ is a wide band gap (3.2 eV indirect or 3.7 eV direct band gap) and consequently, its activity is limited mostly to UV light. However, the band gap as well as catalytic activity can vary for $SrTiO_3$ depending on the preparation method, not only on the surface area, particle size, crystal phase, morphology, etc. [17]. More about the possibilities and roles of $SrTiO_3$ in photocatalytic hydrogen evolution will be presented in 1.3.

It was long believed that the simplest process to prepare perovskite titanates, including $SrTiO_3$, is solid-state synthesis. This method produces single-phase materials. Unfortunately, this method requires high temperatures (commonly above 1000 °C) and consequently high costs. Additionally, the reaction products are highly aggregated large particles with a small surface area, which is not beneficial for catalytic application. In the last 50 years, a vast number of studies employing various synthesis methods, including molten salt and hydrothermal synthesis, sol−gel method, co-precipitation, and microemulsion have been developed to fabricate $SrTiO_3$ (nano)crystals [17], [30]–[32]. The $SrTiO_3$ compound has been obtained in different shapes, such as spheres [33], dendrites [34], stars [35], fibers [36], and cubes [31], [37].

Under thermodynamically controlled conditions, when no anisotropic template or special structure directing agents are used, $SrTiO_3$ usually crystallizes with a cubic crystal structure and in cube-like shapes, whereby the (100) facets are usually the dominant exposed facets. This arises from the fact that the (100) facet in $SrTiO_3$ is flat and characterized by a minimal number of unsaturated bonds and consequently exhibits the lowest energy and the slowest growth rate. The other two low-index facets in $SrTiO_3$ are stepped (110) and kinked (111) facets, both with a higher number of unsaturated bonds and higher growth rates, increasing from (110) to (111) facets. Depending on the reaction conditions (media, concentrations (supersaturation), impurities), which can retard the growth rates of otherwise faster-growing facets (e.g. low index (110) and (111) facets or even high index facets (023) [38], [39], $SrTiO_3$ crystallites can in addition to prevailing (100) facets to some extent expose also another type of facets. For example, slower growth of stepped (110) facets can be explained by the bunching of monoatomic steps, which can occur due to local fluctuations in supersaturation or impurities [40], [41]. Namely, the steps with higher height require a greater flux of ions for the growth and therefore advance at lower rate than

monoatomic steps. As a result of the slower growing rate, such stepped (110) surfaces remain visible in the final crystallites [41]. Retarding the growth of low-index (110) and (111) facets can lead to various cube-like shapes of $SrTiO_3$ with different ratios of (100), (110), and (111) exposed facets [41]. Moreover, the selective adhesion of surfactants on the specific crystal facet can also lower the facet's surface energy and hence its growth rate, resulting in the formation of well-defined $SrTiO_3$ crystallites, exposing other facets in addition to (100) [41], [42]. By this mechanism, versatile $SrTiO_3$ crystallites with the shape of cubes, truncated cubes, and dodecahedra form under hydrothermal or solvothermal and molten salt conditions [38], [39], [41]–[47]. In general, none of these $SrTiO_3$ crystallites possess very anisotropic morphology. For the preparation of $SrTiO_3$ in more anisotropic shapes (2D (nano)platelets), the topochemical conversions of platelet templates were reported. This was intensively studied for the transformation of Aurivillius phase platelets (i.e. $Bi_4Ti_3O_{12}$ [46] and $SrBi_4Ti_4O_{15}$ [45]) and (001) TiO_2 [30], [48] mesocrystalline platelets into $SrTiO_3$ platelets under molten salts and alkaline hydrothermal conditions, respectively. We have developed an alternative low-temperature hydrothermal topochemical transformation approach for the preparation of $SrTiO_3$ (nano)platelets from the $Bi_4Ti_3O_{12}$ nanoplatelets. We have also performed in-depth mechanistic study of the process and identified the key parameters for steering the morphological development and transformation pathway, which can lead to very versatile functional properties of the platelets.

1.1.1.1 $SrTiO_3$ by hydrothermal synthesis

Considering that $SrTiO_3$ and its formation under hydrothermal conditions are the main topics of the present dissertation, the general principles of the hydrothermal synthesis method are explained first, followed by a short summary of the literature examples of $SrTiO_3$ formation under hydrothermal conditions.

Hydrothermal synthesis was developed as one of the low-temperature alternatives to solid-state and molten-salt syntheses. The term *hydrothermal* was originally introduced by geologist Roderick Murchison to describe the action of water at elevated temperature and pressure in the earth's crust and the formation of various minerals and stones. Crystal growth by hydrothermal method experienced its development in the years 1930–1940. In the next decades, many single-crystal and polycrystalline materials were obtained, e.g. complex oxides, carbonates, silicates and phosphates [49].

Hydrothermal synthesis is a heterogeneous reaction in the presence of an aqueous solution under high pressure and at elevated temperatures [49]. There are still no officially determined limit values for the reaction temperature and pressure. The pressure is determined by the concentration of the reactants, reaction temperature, and filling capacity. Most commonly temperatures between 150 °C and 250 °C and pressures between 10 bar and 300 kbar are used. However, lower temperatures (around 100 °C) can also be applied. In this case, the term *mild hydrothermal conditions* is sometimes used.

Hydrothermal technique has undergone a major development in different fields of science and industry, originating from a variety of different types of reactions: synthesis of new phases, stabilization of new complexes, preparation of finely divided materials and microcrystallites with well-defined size and morphology for specific applications, leaching ores in metal extraction and decomposition, alteration, corrosion, etching [49]. From the end of the 20th century, the hydrothermal technique was used for various purposes, including the decomposition of hazardous chemical substances, and organic and pharmaceutical wastes removing caffeine and other food-related compounds selectively, etc. [50]–[54].

The main *disadvantage* of the hydrothermal technique was the *"black box"* nature of the apparatus. Due to the closed steel vessel operating at high temperature and high pressure, it was impossible to observe the crystallization and processes inside the autoclave. Nowadays, researchers can use special *hydrothermal autoclaves for visual examination*. The main goals in the hydrothermal technique are better understanding crystallization and crystal growth, reaction mechanism, kinetics, and thermodynamics, and pushing reaction conditions further to lower temperatures and pressure. *In-situ* hydrothermal techniques are attracting more and more attention [49].

Process kinetics and properties of prepared materials are influenced by the initial pH of the solution, reaction time and temperature, and the pressure inside the autoclave. Under hydrothermal conditions, the solubility of many oxides in salt solution is much higher than in pure water; such salts are called mineralizers. When used in small concentrations, mineralizer plays the role of a catalyst. The most used mineralizers are hydroxides NaOH and KOH. However, the difficulties related to controlling the reaction and the morphology of the target material were commonly reported [49]. In comparison to some other methods such as chemical precipitation,

solid-state reaction, sol-gel method, etc., the hydrothermal method has many advantages such as better control over the shape and size, narrower size distribution, lower reaction temperature, high crystallinity and high purity, lower costs in comparison to solid state or molten salt synthesis.

Typically, the formation of $SrTiO_3$ under alkaline hydrothermal conditions from precursors like TiO_2, $TiCl_4$, or $Ti(OC_4H_9)_4$ for titanium and $Sr(OH)_2$, $SrCl_2{\cdot}xH_2O$, $Sr(Ac)_2$ or $Sr(NO_3)_2$ for strontium precursor follows the dissolution-precipitation mechanism. The main reaction steps are the following: during the mixing of reagents (Sr- and Ti-precursor, NaOH solution), $Sr(OH)_2$ precipitates. At higher temperatures (>100 °C), dissolution of $Sr(OH)_2$ and titanium precursor lead to dissolved $(Sr^{2+})_{aq}$ and $Ti(OH)_6^{2-}$ species. The formation of the latter is expected according to the "charge-pH diagram" for the formation of "aqua", "oxo" and hydroxo" species of transition metal ions depending on the pH [55]. When the product of concentrations of $(Sr^{2+})_{aq}$ and $Ti(OH)_6^{2-}$ exceed the solubility product, $SrTiO_3$ starts to nucleate and precipitate. Nucleation can be homogeneous but since some solid (nano)particles are always present, heterogeneous nucleation is more common. After $SrTiO_3$ precipitation, the processes of $SrTiO_3$ dissolution and precipitation continue. Smaller $SrTiO_3$ particles dissolve, followed by $SrTiO_3$ deposition on larger $SrTiO_3$ particles, which consequently further increase their size through the so-called Ostwald ripening process. Consequently, larger particles with more uniform size distribution are obtained after prolonged reaction times.

Mechanical stirring is also an important parameter, because stirring during the hydrothermal reaction can increase the collision of particles. It affects the concentration gradients as well as molecular dynamics and kinetics.

The nucleation energy barrier (see Eq. (14) page 78) is specially lowered on the solid particles or substrates with similar structural characteristics to that of $SrTiO_3$. In this case, $SrTiO_3$ nucleates and grows on these substrates, which then also dictates its crystal orientation. In the case of titanate structures (particles), these can simultaneously serve as the substrate (template) and through dissolution as the source of $Ti(OH)_6^{2-}$. A continuation of the process can result in pseudomorphic replacement of the initial template by $SrTiO_3$. This means that $SrTiO_3$ preserves the shape of the substrate (template). These are the characteristics of hydrothermal topochemical transformation. This process can be exploited for the preparation of $SrTiO_3$ (nano)structures with controlled anisotropic morphologies. In the literature, this kind of process is described in detail for the formation of elongated mesocrystalline $SrTiO_3$ nanostructures from anatase nanowires, while in my doctoral thesis, I study the formation of $SrTiO_3$ and heterostructural $SrTiO_3/Bi_4Ti_3O_{12}$ platelets from $Bi_4Ti_3O_{12}$ template platelets.

1.1.2 $Bi_4Ti_3O_{12}$

In the scope of my doctoral thesis research, the $Bi_4Ti_3O_{12}$ (BIT) nanoplatelets were the starting 2D precursor and I have studied the conditions and mechanisms for their transformation into $ATiO_3$ (nano)structures with maintained anisotropic 2D shapes. Since $Bi_4Ti_3O_{12}$ is one of the core materials in my research, its structure and properties are described in more detail. $Bi_4Ti_3O_{12}$ belongs to Aurivillius-type layered perovskites, which in their structures contain perovskite blocks, separated by another layer. Bismuth titanate, $Bi_4Ti_3O_{12}$, consists of pseudo-perovskite $(Bi_2Ti_3O_{10})^{2-}$ blocks and $(Bi_2O_2)^{2+}$ layers, which are alternatingly staked along the c-axis as shown in Figure 2 [56]. Two different crystal structures, orthorhombic (B2cb) and monoclinic (B1a1) are reported for the room temperature phase of $Bi_4Ti_3O_{12}$. The orthorhombic structure was determined by the powder X-ray diffraction (XRD). On the contrary, single crystal XRD, neutron diffraction, and electron diffraction studies supported the monoclinic structure. The physical properties are in accordance with the monoclinic symmetry since the spontaneous polarization was observed along the a- and c-axes. Namely, orthorhombic space group B2cb does not allow a component of spontaneous polarization along the c-axis [57]. Heating above the Curie temperature (675 °C) results in a first-order phase transition to a paraelectric tetragonal phase [58].

In the literature, many different synthesis approaches are described, including solid-state, molten-salt, and some other low-temperature methods, e.g. hydrothermal, sol-gel, co-precipitation [59]–[63]. For my research, the most relevant approaches for $Bi_4Ti_3O_{12}$ synthesis are molten salt and hydrothermal methods. However, particles produced by the hydrothermal method usually result in smaller particle size, and investigation of the topochemical conversion was assumed to be easier for larger particles (side length 1-2 microns). Therefore, the molten salt method was selected for the preparation of $Bi_4Ti_3O_{12}$ templates and is further explained below and in 1.1.2.1.

Bismuth titanate is widely investigated due to its diverse properties, including ferroelectricity, piezoelectricity, photocatalytic activity, doping (e.g. Fe) and also multiferroic behavior [61], [64]–[71]. It is a piezoelectric material, which means it can generate an electric charge or voltage in response to applied mechanical stress. As a piezoelectric material with a high Curie temperature (675 °C) it has the potential for use in high-temperature piezoelectric applications [72], [73]. As a ferroelectric material, it can undergo a reversible spontaneous polarization reversal under the application of an external electric field. This ferroelectric behavior makes it promising for applications such as memory devices, sensors, actuators, and ferroelectric random-access memory (FeRAM). With its high dielectric constant, it is also a candidate in capacitor applications. Lately, $Bi_4Ti_3O_{12}$ is raising attention also in photocatalysis for a variety of applications, including water splitting, solar energy conversion, and environmental remediation [61], [64]–[68]. Plate-like morphology with a large flat surface area provides an increased number of active sites for chemical reactions and enhanced exposure to light in photocatalytic applications.

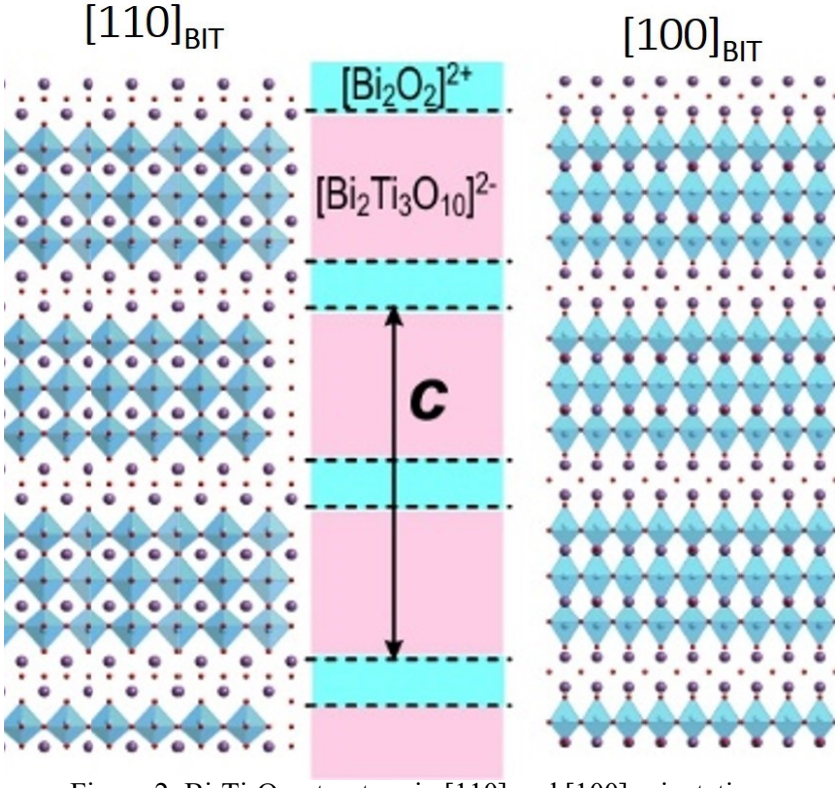

Figure 2: $Bi_4Ti_3O_{12}$ structure in [110] and [100] orientation.

1.1.2.1 $Bi_4Ti_3O_{12}$ by molten salt synthesis

The molten salt method using NaCl/KCl eutectic mixture was applied for the preparation of the $Bi_4Ti_3O_{12}$ platelets in my doctoral thesis research. Hence, the general description of this method is provided first and then some literature examples of different synthesis strategies for the formation of $Bi_4Ti_3O_{12}$ in other molten salts are given.

Generally, molten salt synthesis is employed for preparing complex oxide powders by a relatively simple procedure. As starting materials, oxides and carbonates are most used. The procedure consists of homogeneous grinding and mixing of reagents with salts followed by heat treatments above the melting temperature of the salts. The most used salts, mixtures, and their melting temperatures are listed in Table 2. The formation of product particles occurs in two stages. In the first stage, reactant particles dissolve in the molten salt, which acts as a solvent. Two mechanisms are reported for the reaction stage: dissolution-precipitation and dissolution-diffusion. The mechanism is determined by the relative dissolution rate. When the dissolution rates of reactants A and B are significant and comparable, both reactants dissolve in the molten salt and the product particles precipitate under a high degree of supersaturation. When the dissolution rate of one reactant is considerably higher than the dissolution rate of the other, then the dissolution-diffusion mechanism dominates. As all reactant particles are consumed, formed product particles start to grow by the Ostwald ripening mechanism, and final particle size increases with the prolongation of the annealing time. The material transport is faster in molten

salt than in solid-state systems. Covering the particles' surface molten salt also prevents their aggregation. This results in increased homogeneity and narrower particle size distribution [74].

Although great success has been achieved in the study of the reaction mechanisms in molten salt, it is still very challenging to control the morphology of formed materials [75]. Beside the concentration, the reaction temperature, duration of the reaction, precursor composition, and morphology of starting materials also affect the product particle shape [76]. The morphology of particles during the growth stage is associated with the free energy of the particle/molten salt interfaces. It decreases with the reduction of the surface area due to particle growth as well as with the disappearance of surfaces with high energy, which changes shape towards the equilibrium form [74].

Table 2: The most commonly used salts, mixtures, and their melting temperatures [77]–[80].

Salt	Composition	T_c
KCl	1	770 °C
NaCl	1	801 °C
KCl-NaCl	1:1 (mol)	657 °C
$SrCl_2$	1	866 °C
$NaNO_3$	1	308 °C
KNO_3	1	334 °C
$NaNO_3$-KNO_3	3:2 (wt)	130 °C
$LiNO_3$	1	253 °C
$LiNO_3$-$NaNO_3$-KNO_3	25.9:20.06:54.1 (wt)	118 °C
LiCl	1	610 °C
LiCl-KCl	58.2:41.8 (mol)	352 °C
CaCl2	1	772 °C
$CaCl_2$-NaCl	0.479:0.521 (mol)	499 °C

Several studies on $Bi_4Ti_3O_{12}$ plate-like particles preparation by solid-state reaction or molten salt synthesis are reported [80]–[84]. Summarized reaction conditions for some of them are presented in Table 3. Most commonly, Bi_2O_3 and TiO_2 are used as starting materials, but also other reagents (e.g. $Bi(NO_3)_3{\cdot}5H_2O$, $Ti(OC_4H_9)_4$) can be used [80]. In solid-state or molten-salt synthesis of $Bi_4Ti_3O_{12}$ from Bi_2O_3 and TiO_2 starting materials, secondary phases such as $Bi_{12}TiO_{20}$ or $Bi_2Ti_2O_7$ commonly formed [62], [85]–[87]. Moreover, secondary phases containing sodium can form during the process [81]. The secondary phases must be removed from the product prior to further use due to their detrimental effect on their properties. A eutectic mixture of salt is most used to lower the reaction temperature. The melting point of KCl and NaCl salt is 770 °C and 801 °C, respectively, while the melting point of the eutectic mixture KCl/NaCl is 657 °C [77]. The melting point of Bi_2O_3 is 820 °C [81]. Heating the reaction mixture close to this temperature accelerates the volatization of bismuth, which can lead to bismuth deficiency in the product. Thus, some authors decided to add Bi_2O_3 in excess or keep the temperature for some time at 660 °C to fully melt the salts, and then elevated the temperature for a shorter time to proceed with the formation of $Bi_4Ti_3O_{12}$ [81]. Those studies also confirmed that higher temperatures and longer reaction times lead to larger platelets due to the Oswald ripening effect [80]–[84]. Lowering the reaction temperature is not the only role of the molten salt. At the same time, it improves the degree of homogeneity but also helps to prevent particle agglomeration and to control the size and the shape of forming particles. Therefore, He and colleagues studied the influence of the ratio of salt and the reactants. They included a wide range of molar ratios NaCl:KCl:$Bi_4Ti_3O_{12}$=M: M:1 (M=4, 8, 16, 32, 40, 50 and 60) [84]. This study revealed that the average side length and the thickness of $Bi_4Ti_3O_{12}$ particles decrease with the increase of the molar ratio of the salt up to the ratio $Bi_4Ti_3O_{12}$:NaCl: KCl=1:60:60. A long mass transport distance between $Bi_4Ti_3O_{12}$ particles due to the high molar ratio lowers the growth rate of $Bi_4Ti_3O_{12}$, leading to the size reduction of the resulting particles [88].

Table 3: Summarized reaction conditions for the preparation of $Bi_4Ti_3O_{12}$ platelets in molten salt [80]–[84].

Materials	**Salt**	**Materials: Salt**	**Reaction conditions**	**Morphology**	**Phases**
Bi_2O_3(1-mol% excess.), TiO_2	NaCl	1:2 (wt.)	800°C/1h, 920°C/2h	N.A. (lower degree of anisotropy)	$Bi_4Ti_3O_{12}$, TiO_2, $Na_nTi_4O_8$
Bi_2O_3(1-mol% excess.), TiO_2	NaCl:KCl 1:1 (mol.)	1:2 (wt.)	660°C/1h, 920°C/2h	Plate-like particles (0.3×8×8)µm	$Bi_4Ti_3O_{12}$ (ortho.)
$Bi(NO_3)_3{\cdot}5H_2O$, $Ti(OC_4H_9)_4$	$CaCl_2$:NaCl 0.479:0.521 (mol.)	1:1(wt)	650°C/2h	Plate-like particles/flakes (1-3 µm	$Bi_4Ti_3O_{12}$ (ort. +tet.)
$Bi(NO_3)_3{\cdot}5H_2O$, $Ti(OC_4H_9)_4$	$CaCl_2$:NaCl 0.479:0.521 (mol.)	1:1(wt)	750°C/5h	Plate-like particles/flakes (3-10)µm	$Bi_4Ti_3O_{12}$ (ortho.)
Bi_2O_3, TiO_2	NaCl: KCl 1:1 (mol.)	1:1 (wt)	1100°C/6h	Plate-like (0.5-1×10-12)µm	$Bi_4Ti_3O_{12}$
Bi_2O_3, TiO_2	NaCl: KCl 1:1 (mol.)	1:1 (wt)	1100°C/1h	Platelets (N.A.)	$Bi_4Ti_3O_{12}$
α-Bi_2O_3, TiO_2 (P25), 1:1 (mol)	NaCl: KCl 1:1 (mol.)	NaCl:KCl: $Bi_4Ti_3O_{12}$ M:M:1 (M=4-60)	800°C/2h	Platelets (0.15-0.055×2.4-0.5)µm	$Bi_4Ti_3O_{12}$ (ortho.)

The mechanism of formation of $Bi_4Ti_3O_{12}$ in the molten salt is typically a two-step process: the dissolution of precursor materials in the molten salt and subsequent crystallization of $Bi_4Ti_3O_{12}$. The precursor materials are typically Bi_2O_3 and TiO_2 (nano)powders, which are added to the salt, which melts at higher temperatures and acts as a solvent. Thus, it provides a suitable environment for the dissolution of the precursors. As the precursors are dissolved in the molten salt, ion exchange reactions take place. Bismuth and titanium ions combine with oxygen species, leading to the formation of $Bi_4Ti_3O_{12}$. The reaction is driven by the higher thermodynamic stability of $Bi_4Ti_3O_{12}$ compared to dissolved precursor species. After the desired time, the reaction mixture is cooled down. In the meantime, molten salt becomes a solid matrix and $Bi_4Ti_3O_{12}$ crystals solidify inside the matrix. Separation of $Bi_4Ti_3O_{12}$ crystals from the solid matrix of the salt is done by washing them with water and acids (e.g. HNO_3) to remove byproducts.

1.2 Nucleation and Crystal Growth

The formation of any crystalline substance includes nucleation and crystallization (growth of crystals), which are responsible for the functionality of the material. Because the functional properties are influenced not only by the type of material but also by the material's shape, size, chirality, defects, etc., it is essential to understand how we can influence and direct crystal growth. Therefore, based on the understanding of nucleation and crystallization theory, we can plan experimental (reaction) conditions for the controlled growth of crystallites and thus also create their functional properties.

1.2.1 Nucleation

The formation of a new phase starts with nucleation. A new crystalline phase forms from a metastable solution and requires the appearance of small clusters of building units in the volume of the supersaturated ambient phase [89]. So, nucleation is defined as a series of atomic or molecular processes rearranging into the cluster of the product phase. A cluster needs to be large enough to grow irreversibly to larger size. A cluster is defined as a nucleus or critical nucleus. Supersaturation (S) is defined as the ratio of concentration C and solubility C^* ($S = C/C^*$) at the reaction conditions being adjusted to generate supersaturation and it is the driving force for the crystallization [89]. The classical theory is valid at small or moderate supersaturations, in contrast to the atomistic theory which is applicable at high supersaturations [40]. One must take into consideration that the solubility may change with the temperature, pH, solvent evaporation, crystal growth, etc. If the concentration exceeds the solubility ($S > 1$), the solution is supersaturated, and crystals can grow. If the concentration is lower than the solubility ($S < 1$), the solution is undersaturated and crystals tend to dissolve. The process of nucleation and growth according to the LaMer mechanism can be broken down into three main phases [90]. (I) The concentration of free monomers in the solution experiences a rapid increase. (II) Subsequently, the monomers undergo "burst nucleation," leading to a substantial decrease in the concentration of free monomers in the solution. This nucleation rate is described as "effectively infinite," and after reaching this stage, further nucleation is almost non-existent due to the low concentration of monomers. (III) The growth phase follows the nucleation stage, driven by the diffusion of monomers through the solution. These three stages are illustrated in (Figure 3 a), where the concentration of monomers is schematically plotted over time.

The crystals can be formed from a clear solution (primary nucleation) or parent crystals (secondary nucleation). Primary nucleation can take place in the absence of heterogeneous particles in a clear solution (homogeneous nucleation) or at surfaces such as dust, walls, interfaces, scratches on glassware, etc. (heterogeneous nucleation), which is commonly almost impossible to avoid [89].

Nucleation and crystal growth kinetics vary under thermodynamically metastable conditions and local deviations in thermodynamic systems increase the thermodynamic potential of the system. Hence, leading to the formation of small aggregates. If the initial phase is stable, these formed agglomerates are "lifeless". If the initial phase is unstable, the tendency to grow prevails after the agglomerates exceed the critical size. In this case, the system must overcome the activation barrier which is given by the work of formation of the critical nuclei (Figure 3 b). The nuclei form a thermodynamically favorable shape (requires minimal work for nuclei formation), usually it is the equilibrium shape [40], [91].

The rate of nucleation (J) is defined as the number of formed nuclei in a given time and volume. Theoretically, nucleation events are distributed evenly across the bulk fluid volume. However, it is more commonly the truth that local extreme conditions cause local nucleation events. The nucleation rate is defined as:

$$J = Ae^{-\frac{\Delta G^*}{kT}} \quad (2)$$

Arrhenius coefficient (A) is dependent on supersaturation and the nucleation rate is zero until the critical value of the supersaturation is reached. This is a so-called metastable zone. The control over the process can be exerted based on consideration of classical nucleation theory, which defines that the nucleation barrier (ΔG) is proportional to the third power of interfacial free energy (α) and inversely proportional to the square of natural logarithm of supersaturation (i.e. $(lnS)^2$) (Figure 3 b). The Gibbs free energy is a function of a cluster size (radius). The energetic barrier (ΔG^*, denoted also as Δg_n) at the formation of the nucleus with critical size (r^*) needs to be surpassed to promote the nucleation [40], [91].

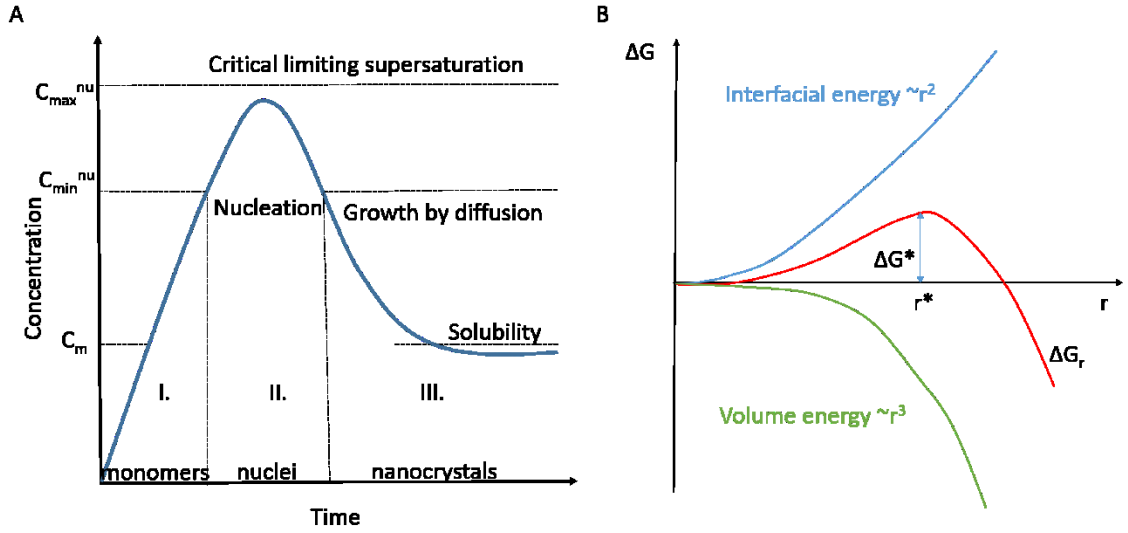

Figure 3: Simplified illustration of nucleation and crystal growth process according to LaMer (A) and the association of a free energy change with a radius r of a sphere in a homogeneous nucleation (B).

1.2.2 Crystal growth

Crystal growth is a series of processes occurring after nuclei reach the critical size. Atoms or molecules incorporate into the surface of a crystal, leading to increasing its size. First, atoms or molecules need to be transported through the solution to the atomic or molecule surface. An approaching atom can either be reflected or absorbed on the surface of the substrate. Which situation will occur depends on the incoming flux atom, the trapping probability, and the sticking coefficient. For successful physisorption, the atom must overcome the local energy barrier. After it is physiosorbed, it can be either chemisorbed or desorbed and therefore ejected from the surface. The balance between the growth and dissolution process of individual atoms or small clusters of atoms is governed by the total free energy of the atom or the cluster, relative to an assembly of individual atoms. Atoms or molecules that adsorb on the surface are not a part of the crystal as far as their chemical potential becomes equal to that of the crystal. On the contrary, after the atoms are more tightly bound to the crystal than the atoms in a kink position, they are already a part of a crystal. Considering the surface of a (100) facet of a cubic Kossel crystal (also valid for $SrTiO_3$) with a monoatomic step, atoms can occupy various positions. The most important atomic sites are the following: atom adsorbed on the crystal face, atom adsorbed at the step, an atom in a half-crystal (kink) position, atom embedded into the step edge, and atom embedded into the outermost crystal plane. Atoms in each of those positions are bound differently to the crystal surface, because of the different number of bonds with a crystal and unsaturated dangling bond. This means that those atoms or atomic sites differ in their surface energies (see Figure 4 and Figure 5). [40]

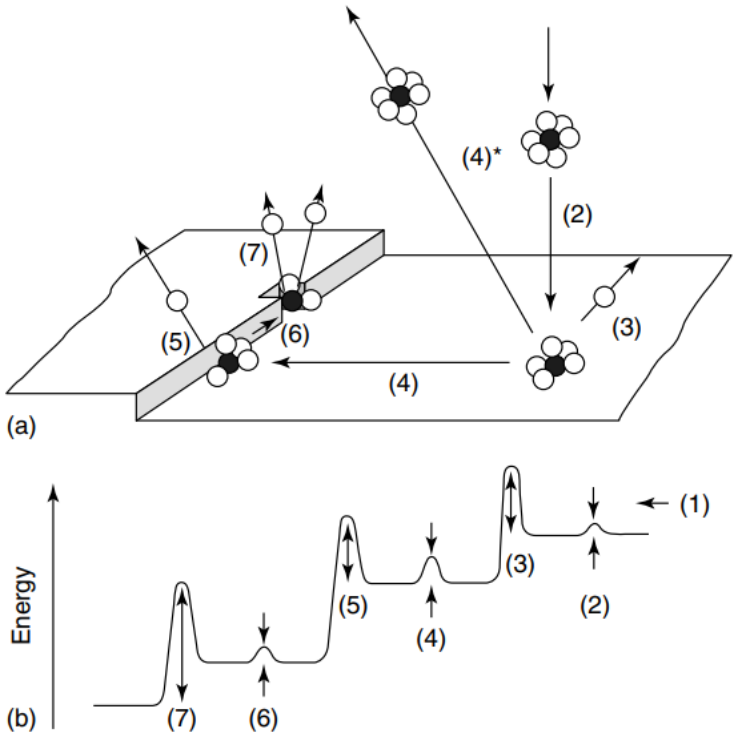

Figure 4: Schematic representation of processes involved in the crystal growth. (1) Transport of solute to the vicinity of the surface, (2) diffusion through the boundary layer, (3) adsorption onto a crystal surface, (4) diffusion over the surface (also desorption can occur at this stage/place), (5) attachment to the step or edge, (6) diffusion along the step or edge, (7) incorporation into the kink site or vacancy [91].

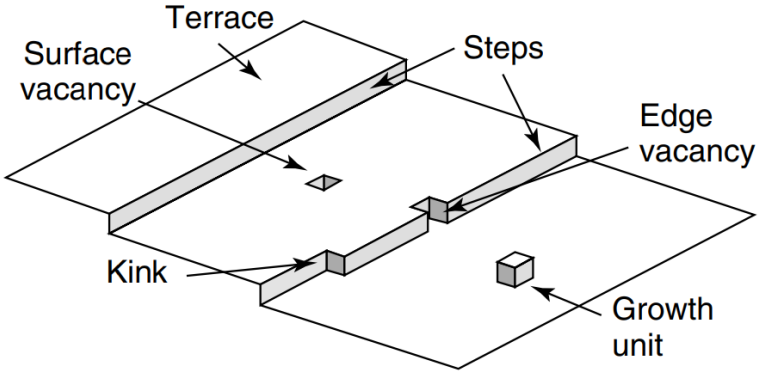

Figure 5: Illustration of atomic sites on the surface according to the Kossel model [91].

Once an atom sticks to the surface, it creates tension in the surface, which is a function of the broken bond energy of exposed surface atoms which depends on the crystal structure of the substrate. Overall surface energy is then minimized by surface diffusion of the adsorbed atom to a low-energy site. Atoms usually diffuse along the surface until they reach the kink site at the ledge or elsewhere [92]. As the ledges vary with the crystal face orientation, these processes also vary on different crystal faces thus forming different surface structures. Hartman introduced a classification of crystal faces into flat (F), stepped (S), and kinked (K) faces (Figure 6) [93]. In the ideal case, the F faces are atomically flat, the S faces consist of ledges and the K faces consist of kinks. Consequently, the slowest growth is expected on F faces and the fastest on the K faces. In $SrTiO_3$, F surfaces are represented with (100) facets, S surfaces are represented with (101) facets and K surfaces are represented with (111) facets. The crystal growth mechanism is influenced by the structure of crystal surfaces.

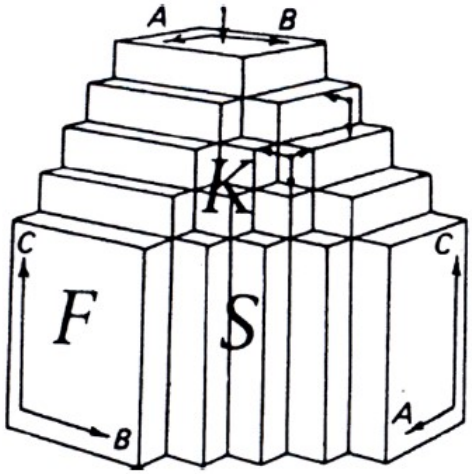

Figure 6: Classification of faces introduced by Hartman. F – flat faces, S – stepped faces, and K – kinked faces. Adopted from Hartman [93].

In the case that the crystal has flat faces, the growth rate is determined by the formation of steps and by the lateral moving of these steps. In the ideal crystal face with no defects, the growth is determined only by the frequency of formation of 2D nuclei, which is an energetically activated process. From the energetics point of view, relatively high supersaturation conditions are predicted to overcome the energy barrier associated with 2D nucleation so that growth can take place. However, from experiments it was determined that growth can occur also at lower supersaturation than predicted. Frank explained that crystal surfaces are intercepted by dislocations, which create steps, required for the 2D nucleation [94]. Present screw dislocations represent a valuable source of steps, and the growth is not limited by the formation of the step anymore (Figure 7 left). The theory of crystal growth by spiral dislocation was then further explained by Burton, Carbera, and Frank (*BCF theory*) [95]. The pyramid growth is observed when the 2D nucleation determines the growth rate (Figure 7 right) [40]. In terms of the mechanism, the growth of heterostructures might be considered as the growth of thin films.

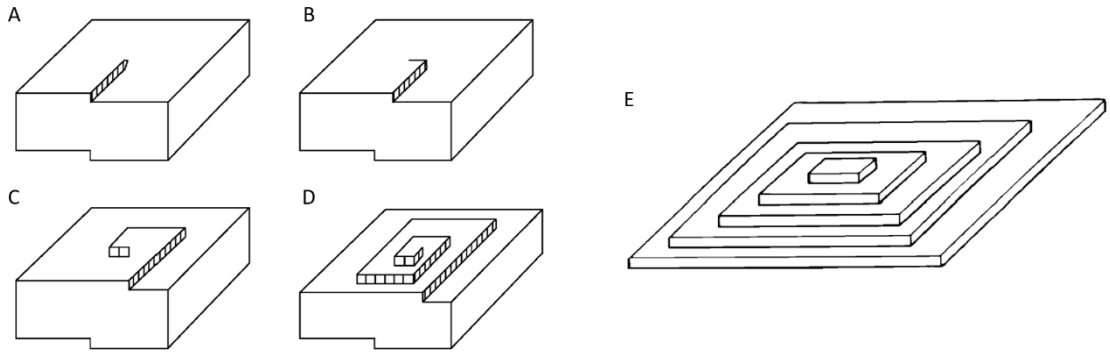

Figure 7: Illustration of the spiral growth (A-D) and pyramid growth (E) [40].

1.2.3 Nucleation and crystal growth control

Material's properties are commonly a consequence of the material's morphology. Therefore, in materials science, it is desired to control the nucleation and crystal growth processes. The control of nucleation and growth is a complex process. Optimization of synthesis parameters and synthesis design are crucial for the preparation of particles with desired morphology and properties. Different strategies are used for this purpose, including control of the reaction temperature, heating and cooling rates, varying the supersaturation, the addition of additives, surfactants, or seeds, stirring, using templates or substrates, and others.

The temperature strongly influences the nucleation and growth processes because the nucleation rates and growth kinetics are related to the temperature. Generally, higher reaction temperatures promote nucleation and lower reaction temperatures lead to the growth of larger

crystals. Additives or surfactants are chemicals that can modify crystal growth, due to their impact on surface energy, crystal morphology, and growth kinetics. As a consequence, with the addition of additives or surfactants, it is possible to impact the morphology of crystals (e.g. particles). Seeding means introducing small crystalline particles, i.e. seeds, into the solution, where those seeds represent nucleation sites and thus help to control the nucleation. By varying the size, composition, and number of seeds, it is possible to control the nucleation and crystal growth rates as well as the final size of the crystals. Stirring also has an impact on the nucleation process, because it enhances mass (and heat) transport and promotes heterogeneous nucleation. Stirring assures that the solute molecules and precursors (reactants) are evenly distributed in the reaction mixture. By mixing, it is also possible to prevent localized nucleation. Commonly used applied strategies are also using templates or substrates. Template and substrate with desired crystal structure impact on the growth of the new film. Thus, it is possible to direct the growth in certain unfavorable crystallographic directions or morphologies, leading to special/enhanced properties or possibilities for using the material in certain applications. In this dissertation, the focus was on using supersaturation to direct the growth and influence on the particle morphology.

Supersaturation is beneficial for nucleation because it provides the driving force, which is necessary for the formation of a new solid phase (particles). In other words, supersaturation is the concentration gradient in terms of available and needed constituents. When a system is supersaturated, it becomes thermodynamically unstable. The excess molecules seek to lower the overall free energy and it can be done by forming a new solid phase – new particles. Also, the higher the supersaturation, the higher the probability that molecules would collide and form clusters. This is a nucleation process, and the nuclei are formed. Those nuclei can still become unstable and dissolve or they reach the thermodynamic stability (overcome the energy barrier required for the formation of stable nuclei) and start to grow – a crystal growth process or the formation of a new phase. However, the highest supersaturation does not necessarily mean success. Too high supersaturation may result in rapid and uncontrolled nucleation, leading to the formation of numerous small particles with limited growth. On the other hand, moderate and controlled supersaturation allows controlled nucleation and subsequent growth, leading to the desired particle size and distribution. The reaction conditions for the nucleation and growth must therefore be evaluated and determined for each system individually.

Another use of introducing supersaturation for nucleation and crystal growth processes is that supersaturation can promote the growth of particles in morphologies that are not energetically favorable. Again, supersaturation provides a driving force for the system to overcome the energy barrier for the formation of those morphologies. Namely, certain morphologies are favorable under equilibrium conditions and by using supersaturation, the growth of less stable morphologies becomes more feasible. In the context of particle growth, an energy gradient enables the attachment of atoms to nuclei or surfaces, leading to the growth of particles. In the case of energetically unfavorable morphologies, supersaturation can provide the conditions for their growth by lowering the activation energy required for the formation of those structures. Higher collision probability also increases the chances of crystal growth and decreases the probability of nuclei/particle dissolution. Thus, the use of supersaturation might be helpful to direct the crystal growth towards energetically unfavorable morphologies under equilibrium conditions.

1.2.4 Epitaxial growth

Epitaxial growth is the oriented growth of a crystalline material on the surface of a single crystal. The first systematic investigation into epitaxy was conducted in 1928 by Royer. Later, in 1949, Frank and van der Merwe introduced a theory of epitaxy that relied on the concept of pseudomorphism [96]. In this process, the film maintains a consistent epitaxial relationship with the underlying substrate. This epitaxial alignment is typically described using Miller indices to represent crystal planes and directions. The process of epitaxial growth is influenced by the chemical bonds' nature and strength within both the film and the substrate, as well as the differences in their lattice parameters. The extent of this discrepancy is known as the lattice mismatch (denoted as *f*) between the crystal lattices of the film and the substrate and is defined as:

$$f = \frac{a_{film} - a_{substrate}}{a_{substrate}} \tag{3}$$

where a_{film} and $a_{substrate}$ are the lattice constant of the deposited film and the substrate, respectively. [40]

Epitaxial growth is usually used in MBE, CVD, PVD, or PLD for the preparation of thin films. However, the aspects of epitaxial growth in thin films can be translated to topochemical

conversion for the preparation of heterostructural platelets. Three primary mechanisms for the epitaxial growth are described and illustrated in (Figure 8): Stranski-Krastanov, Volmer-Weber, and Frank-van der Merwe [40], [97].

Volmer – Weber growth is also known as the island-plus-island (or 3D) growth. It prevails when the total surface energy of the film interfaces is larger than that of the substrate-vapor interface. Adatom – adatom interactions are stronger than those of adatom – surface which leads to the formation of three-dimensional adatom clusters or islands. To minimize the interface with the substrate, the material balls up. Such a type of growth is uneven. And the diffusion in this case is slow. For this type of growth, it is experimentally suggested that epitaxy is a postnucleation phenomenon involving rotation, migration, and rearrangement of "stable" clusters [40], [97].

Frank – van der Merwe growth is also known as layer-by-layer growth and dominates when the surface-adatom surface energy is larger than the other two combined and therefore leads to layer growth. Consequently, a smooth film will form. Frank – van der Merwe growth is two-dimensional (2D growth), indicating that complete films form before growth of subsequent layers. In this growth type, the epitaxy can be destroyed by influencing the growth process at a later stage incorporating impurities or defects into the growing film which can affect the nucleation process by changing the nucleation kinetics. [40], [97]

Stranski – Krastanov growth is a combination of both previously described mechanisms. First, a layer covers the substrate. After a few monolayers, the strain with the substrate is relaxed and the growth changes to island growth. Critical layer thickness is determined by the strain and the chemical potential of the film. [40], [97]

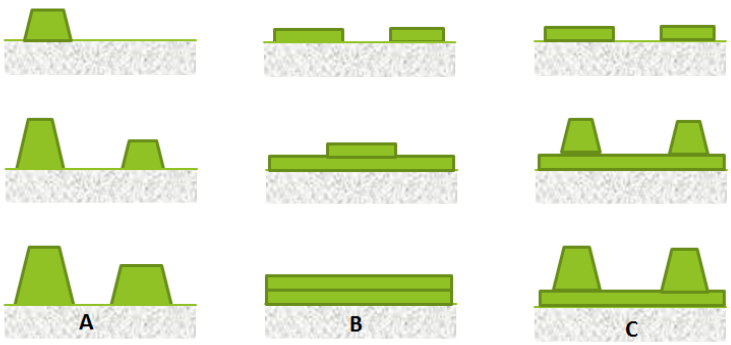

Figure 8: Illustration of three possible growth mechanisms for thin films including a) Volmer-Weber, b) Frank van der Merwe, and c) Stranski-Krastanov.

From a broad perspective, epitaxial orientation is established by seeking the lowest free energy state of the system. Epitaxial growth can be categorized into *homoepitaxy*, involving the same material for both the film and substrate, and *heteroepitaxy*, when they differ. The specific epitaxial orientation of the film is determined by the crystal structure, particularly the interaction between contacting crystal planes, as well as the characteristics of the chemical bonds at the epitaxial interfaces. The success of epitaxial growth depends on the compatibility of the film and substrate in terms of crystal structures and lattice parameters. For the coherent growth and adoption of the lattice arrangement, the lattice mismatch between the film and the substrate is usually relatively small – within a few percent. Larger mismatches usually lead to strain and the formation of defects [40]. To achieve that the epitaxial growth of a crystal results in the epitaxial layer perfection, surface smoothness, and well-defined interfaces, several factors have to be taken into account [98]. These factors encompass the method used for epitaxial layer growth, the interfacial energy between the substrate and epitaxial film, and the growth parameters (reaction parameters). The relation between the nucleation process and the occurrence of the epitaxy is not completely clear yet. However, it is assumed that the chemical potential of the first deposited layer determines the mechanism [40]. To be capable of better understanding the epitaxy, it would be needed to experimentally investigate how real crystals reach the equilibrium state, including studying the growth kinetics and reactions of lattice imperfections. Also, to gain a better understanding of parameters that influence the epitaxy, such as strength of interface interactions, surface topography of the substrate, diffusion processes and reactions at the interface, etc.

1.2.5 Tailoring the morphology of $MTiO_3$ by topochemical conversion

Several ABO_3-type perovskite particles tend to grow in isotropic shapes, e.g. spheres or cubes due to their rather symmetrical crystal structure. But recent findings about the importance of size [99], mesocrystallinity [24], [100], type of exposed facets [101]–[103], termination [104], [105] and preferential orientation [24], [43] for efficiency of catalytic and photocatalytic reactions increasingly promote the interest for morphological engineering of functional (nano)particles. On the contrary, Aurivillius-type layered perovskites such as $Bi_4Ti_3O_{12}$ with pseudo-perovskite $(Bi_2Ti_3O_{10})^{2-}$ units, which are sandwiched between the $(Bi_2O_2)^{2+}$ layers, crystallize in the plate-like shape. Based on these pseudo-perovskite units, which are good substrates for the epitaxial growth of other perovskite titanates, $Bi_4Ti_3O_{12}$ plates could be used as the template for the preparation of plate-like $MTiO_3$ particles. This could be achieved via topochemical transformation or topochemical conversion.

Topochemical conversion (TC; also known as topochemical transformation) is a reaction that involves the introduction of a guest species into a host structure (also called template) and that results in significant structural modifications to the host (template), for example, the breakage of bonds [106]. In other words, a topochemical conversion is a chemical reaction that occurs within a solid material, while maintaining its original morphology. The term "topochemical" arose from the words "topos", which means "place" and "chemistry", which refers to the chemical reaction and chemical changes within the material. During topochemical conversion, atomic/ionic rearrangement occurs, while the overall crystal structure and morphology are preserved. Consequently, the initial precursor is also called the host structure or the template [30], [47], [106]. An example of topochemical conversion is the transformation of one perovskite into another by replacing cations within the perovskite structure. In such a reaction, the precursor phase controls both the orientation and the morphology of the resulting phase, therefore, upon successful reaction, the final phase preserves the morphology of the initial precursor. The most studied topochemical conversion reactions are TC in molten salt (MS) and TC under hydrothermal conditions (HT) [30], [47], [48], [75], [82], [107]–[113]. Thus, the focus in this dissertation is on the reactions in molten salt and under hydrothermal conditions and other methods will not be discussed at this point.

Predicting the success of a topochemical conversion might be challenging, however, considering some general guidelines and factors can help to predict the reaction outcome. Before employing the transformation, the crystal structure and compatibility of the starting material and product material must be analyzed. Similarities in crystallographic parameters (symmetry, lattice constants, coordination environments) are indicators for higher chances for a successful topochemical conversion. Besides crystallographic factors, ionic radii must be similar. Large differences in ionic radio lower the probability that the reaction proceeds as topochemical conversion. To ensure molecular charge neutrality, valence states must also be considered so that the charge balance is maintained. If the valence states are incompatible, or the charge balance cannot be maintained, the conversion might not proceed as planned. Finally, the thermodynamic stability of the starting material (template) and final material (product) must be evaluated and predicted. If the product material has lower energy and higher stability than the starting material (template), it increases the chances of a successful topochemical reaction. Those are only general guidelines that might help to predict the success of a topochemical conversion, however, success is not always straightforward and often requires a combination of experimental validation and theoretical analysis.

However, it is not straightforward that the reaction will successfully lead to the desired morphology through topochemical conversion. Namely, the reaction conditions must be selected to ensure that the template particles do not dissolve into smaller molecules, intermediates, or ions. If not, the reaction that occurs is not considered topochemical conversion. This means that in the case of topochemical conversion in molten salt, the dissolution-diffusion process must be dominant to preserve the morphology of the template particles [40], [74]. Otherwise, in the case of the dissolution-precipitation mechanism, the precursor particles dissolve, and the objective material precipitates with an intrinsic shape, which is usually the equilibrium one. Successful topochemical conversion always includes elements of epitaxial growth. For this reason, the crystallographic orientation of the new phase is determined by the template and therefore adequate low lattice mismatch between both phases is crucial aside from the reaction condition. For the topochemical conversion under hydrothermal conditions, the reaction involves exclusively dissolution and epitaxial growth and if the process is interrupted before it is finished, heterostructural particles with epitaxial contact form.

Different precursor templates were reported for topochemical conversion to $SrTiO_3$ in molten salt. Firstly, $Sr_3Ti_2O_7$ with Ruddelsen – Popper type crystal structure was reported as template

particles for fabricating {100} oriented $SrTiO_3$ plates [114]. It is assumed that the nucleation and epitaxial growth of $SrTiO_3$ from the (001) surfaces of the $Sr_3Ti_2O_7$ precursor phase to $SrTiO_3$ occur due to the similar atomic configurations of both structures. However, complete conversion requires a high reaction temperature of above 1200 °C [115]. Watari prepared $Sr_3Ti_2O_7$ plates with the molten salt and used them in the subsequent step for the preparation of highly (100) oriented $SrTiO_3$ ceramics by reactive template grain growth [116]. Secondly, in molten salt prepared $SrBi_4Ti_4O_{15}$ (SBIT) plates were used for topochemical microconversion to $SrTiO_3$ in KCl salt, and the morphology was preserved. It was seen from XRD patterns that developed planes were {001} in $SrBi_4Ti_4O_{15}$ and {100} in $SrTiO_3$. The authors suggest that during conversion the {001} plane of $SrBi_4Ti_4O_{15}$ converts to {100} plane in $SrTiO_3$ [45]. The overall topochemical conversion from Aurivillius $SrBi_4Ti_4O_{15}$ platelike precursors to perovskite $SrTiO_3$ microplatelets is proposed to occur in two main stages: topochemical reactions and recrystallization and grain growth. Figure 9 shows the schematic illustration of the crystal structure conversion from Aurivillius phase $SrBi_4Ti_4O_{15}$ to perovskite phase $SrTiO_3$. During the conversion process, the $(Bi_2O_2)^{2+}$ slabs in $SrBi_4Ti_4O_{15}$ are removed during heat treatment. Sr^{2+} diffuses into pseudo-perovskite $(A_{n-1}B_nO_{3n+1})^{2-}$ blocks and replaces Bi^{3+} ions in the A-site and forms a $SrTiO_3$ perovskite phase [45]. A detailed study of the reaction process is necessary to fully understand the process and to be able to predict the reaction outcome at different reaction parameters. During the transformation from the $SrTi_4Bi_4O_{15}$ into $SrTiO_3$, the plate shape of the template was well preserved when the reaction took place in the molten salt. However, this transformation requires 3 steps, namely, the formation of $Bi_4Ti_3O_{12}$, its transformation to $SrBi_4Ti_4O_{15}$, and final conversion to $SrTiO_3$. The direct topochemical transformation from $Bi_4Ti_3O_{12}$ plates into $SrTiO_3$ was not reported before the start of this doctoral research, neither for the molten salt nor for the hydrothermal conditions.

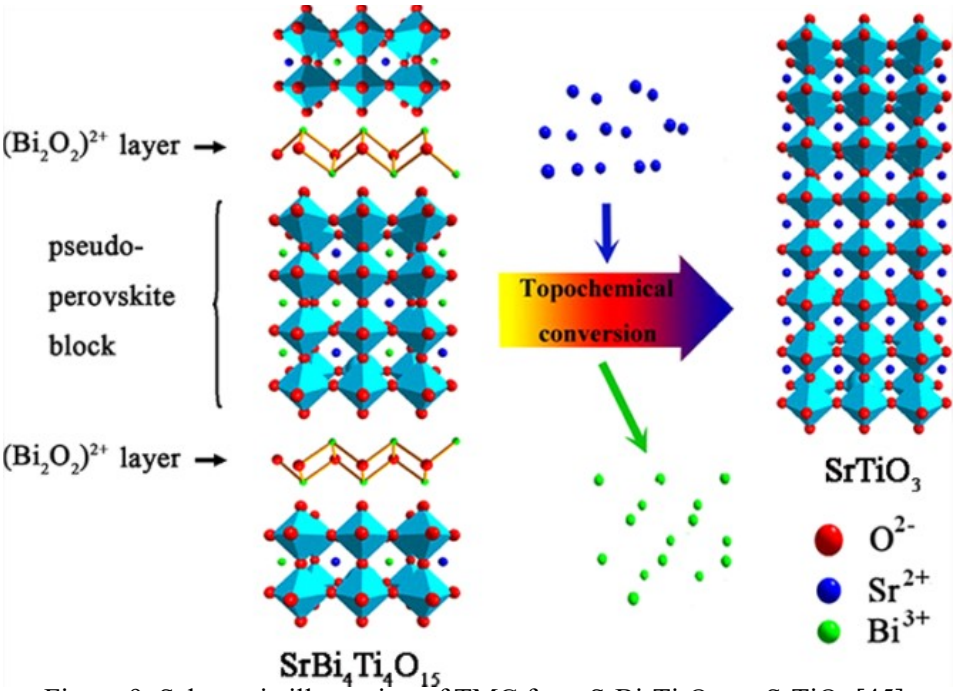

Figure 9: Schematic illustration of TMC from $SrBi_4Ti_4O_{15}$ to $SrTiO_3$ [45].

The conversion of $Bi_4Ti_3O_{12}$ to $SrTiO_3$ involves the replacement of bismuth cation (Bi^{3+}) in the crystal lattice with strontium cations (Sr^{2+}). At the same time, the $[Bi_2O_2]^{2+}$ layer must dissolve from the structure. Though, overall platelet is not allowed to dissolve, to be able to maintain the platelet morphology. The general approach for converting $Bi_4Ti_3O_{12}$ to $SrTiO_3$ contains the following steps: (i) preparation of starting material ($Bi_4Ti_3O_{12}$ template platelets) and characterization, (ii) topochemical conversion: molten-salt reaction at high temperatures, where strontium source (usually $SrCO_3$ or SrO) reacts with template platelets, (iii) heat treatment or annealing for promoting the conversion and ensuring the formation of $SrTiO_3$ (typically above 1000 °C), (iv) post-treatment, such as removing the byproducts, drying and finally (v) characterization. High energy input is required for performing the reactions at such high temperatures, therefore, it is cost-effective to perform the reaction at lower temperatures, e.g. hydrothermal reaction. Additionally, negligible diffusion in the solid-state lattice at the typical

hydrothermal temperatures and the facts that TC involves epitaxial growth enable the formation of heterostructures with a well-defined interface at the intermediate stage of the transformation.

The TC of the titanate template to $SrTiO_3$ under hydrothermal conditions expresses some particularities and might be challenging. Namely, hydrothermal synthesis involves the use of water or aqueous solutions at elevated temperature and pressure. Such conditions can promote the dissolution and precipitation of the materials, making it difficult to control the substitution of particular cations without destroying the crystal structure. That being said, such a method would require a thorough understanding of the reaction conditions, precursor materials, and reaction kinetics to control the reaction. While the creation of epitaxial thin film heterostructures using physical vapor deposition techniques has been extensively explored, the meticulous investigation of particulate epitaxial heterostructure formation from solutions has been lacking. However, both processes require similar considerations, including epitaxy, lattice misfit, and the formation of defects. Particularly, the transformation of particles under hydrothermal conditions can be intricate and highly responsive to changes in the conditions. This complexity arises because the template typically dissolves while simultaneously acting as a substrate for epitaxial growth [48]. Moreover, understanding the role and significance of supersaturation becomes crucial in directing such transformation processes. Presently, our comprehension of these transformation processes is relatively limited [117]. This study aims to fill this gap in knowledge by meticulously examining the hydrothermal topochemical transformation of $Bi_4Ti_3O_{12}$ platelets into $SrTiO_3$ while preserving the original shape.

Reaction processes and formation mechanisms of $SrTiO_3$ through topochemical conversion under hydrothermal conditions are even less understood with few studies of epitaxial growth of $SrTiO_3$ on mono metal oxides (e.g. TiO_2) [30], [32], [48]. In contrast to topochemical conversion in molten salt, the contribution of diffusion in solid state lattice is negligible under hydrothermal conditions and the transformation occurs mainly through dissolution and epitaxial growth process. Similar to molten salt, the preservation of the initial morphology is enabled by low solubility and slow dissolution rate of the precursor template and high structural matching of parent and newly growing phase. Low lattice mismatch together with appropriate high supersaturation leads to a low energy barrier for nucleation, which results in layer-by-layer growth and coverage (protection) of the precursor surface with the growing phase, and consequently the initial morphology is maintained. The extensive studies of hydrothermal topochemical conversion were performed by Kalyani and his colleagues who studied the formation of $SrTiO_3$ mesocrystal through topochemical reaction between the single crystal anatase nanowires (ANW) and Sr^{2+} ions in the alkaline solution under hydrothermal conditions [30], [48]. Kalyani reported about $SrTiO_3$ mesocrystal formation through a topochemical reaction between the single crystal anatase nanowires (ANW) and Sr^{2+} ions in the alkaline solution under hydrothermal conditions [30], [48]. $SrTiO_3$ was grown as cubic subunits of the mesocrystal. The growing $SrTiO_3$ cubic nanocubes on the ANW had a very uniform size distribution of 50 nm and were almost perfectly aligned through (100) lattice planes and tightly bound together, forming $SrTiO_3$ nanowires, which resembled very well the shape of ANW. For the comparison, the attempt of a similar reaction using single crystalline hydrogen titanate nanowires (HTNW) instead of ANW resulted in the loose $SrTiO_3$ particles. The difference in these two reaction mechanisms can be explained in the view of structural similarities and degree of lattice mismatch between the precursor particles (ANW or HTNW) and the newly formed phase ($SrTiO_3$).

It is widely known that the synthesis of alkaline earth titanates requires alkaline pH (pH > 10) for better stabilization of the product phase [118], [119]. Therefore, the NaOH or KOH solution is usually used as a mineralizer. Mineralizer and hydrothermal conditions influence the solubility of the reaction precursors, and it can increase their dissolution dramatically. In some cases, alkaline mineralizers can promote rapid hydrolysis of the precursor and hence the formation of amorphous titanium hydroxide gel. This gel is then an effective precursor of the hydrothermal reaction [48]. The mechanism of crystallization plays an important role in morphological evolution. The crystallization mechanism is a consequence of reaction potential. Various reaction parameters influence the morphology of nanoparticles such as temperature, pressure, reaction time, precursor concentration, mineralizer concentration, A: Ti ratio in the solution as well as stirring.

The calculated precursor solubility for $Ti(OH)_4$, anatase, and rutile in $SrTiO_3$ synthesis is presented in Figure 10. The aqueous species $Ti(OH)_n^{(n-4)-}$ (n = 4-6) predominate at pH ≥ 7. It can be seen from Figure 10 that the solubility of the rutile is the lowest in the whole temperature range. The addition of a small amount of ethanol slightly lowers the solubility of all three titanates. [48]

According to Kalyani's thermodynamic calculations, the $SrTiO_3$ is the predominant product phase in the temperature range 25-300 °C in NaOH solution 0.01-2 mol/kg, if the $[Sr^{2+}]$

concentration is in the range of 0.05-0.2 mol/L. However, in the presence of CO_2, the side-product, $SrCO_3$, is formed. It is known that the tendency of precipitation of $SrCO_3$ is correlated with NaOH concentration, but not much information is available [48].

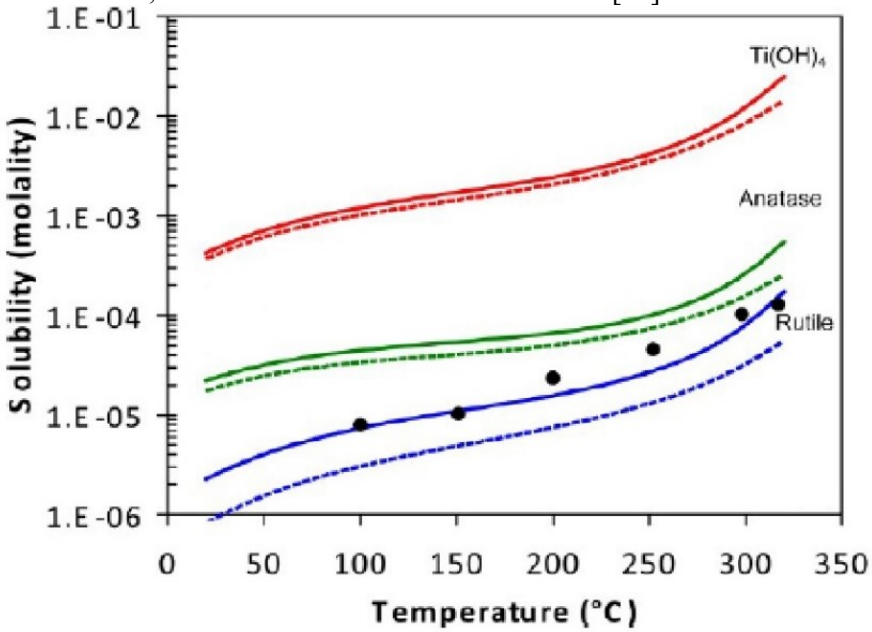

Figure 10: Calculated solubility of rutile, anatase, and $Ti(OH)_4$ in water in the temperature range 20-320 °C is presented with solid lines, and the solubility in the mixed water-ethanol with dotted lines [48].

For $SrTiO_3$ formation from anatase (TiO_2) through the dissolution-precipitation mechanism, equations (4)-(6) and overall reaction (7) were suggested [120].

$$Sr(OH)_2{\times}8H_2O \rightarrow Sr^{2+} + 2OH^- + 8H_2O \quad (4)$$

$$TiO_2 + 2OH^- + 2H_2O \rightarrow Ti(OH)_6^{2-} \quad (5)$$

$$Sr^{2+} + Ti(OH)_6^{2-} \rightarrow SrTiO_3 + 3H_2O \quad (6)$$

$$TiO_2 + Sr(OH)_2{\times}8H_2O \rightarrow SrTiO_3 + 9H_2O \quad (7)$$

The major and most obvious difference between topochemical conversion in molten salt and under hydrothermal conditions lies in the reaction medium and reaction conditions. The reaction media determine the solubility of the template particles and stability of the forming phases. The reaction medium in topochemical conversion in molten salt is molten salt (e.g. molten KCl, NaCl). The reaction occurs at high reaction temperatures (800 °C – 1200 °C). At such conditions, the diffusion of ions is possible within the solid material. Consequently, structural rearrangements occur, while the overall crystal morphology is preserved. On the other hand, under hydrothermal conditions, the reaction temperature is considerably lower (100 °C – 200 °C), and the reaction occurs in aqueous solution. High pressure and reaction temperature enhance the solubility, reactivity, and diffusion of ions in solution. The important difference between the mechanism of topochemical conversion in molten salt and under hydrothermal conditions is that in MSS TC three processes are involved: dissolution, epitaxial growth, and diffusion in a solid crystal lattice, while in HT TC, only dissolution and epitaxial growth occur, but no diffusion in solid material.

Preparation of a particular material in pre-defined controlled morphology different from the thermodynamic equilibrium shape represents a challenge and requires an in-depth understanding of reaction and crystal growth mechanisms [121]. Although a lot of effort has been put into synthesis control, it remains a great issue to prepare non-aggregated well-defined anisotropic perovskite nanoparticles with predefined crystal orientation and homogeneous particle size distribution [49]. In general, the most common synthesis strategies for control of particle shape are based on modification of the crystal facets' energy by additives, which selectively adsorb on particular facets and retard their growth rate; and topochemical conversion (in-situ transformation) of appropriate templates with defined shape [113].

1.3 Hydrogen Production for Energy

Nowadays, the whole world is facing energy shortages and global warming. At the same time, people have started to realize the value and importance of a clean and healthy environment in which we live. To become independent from fossil fuels and to achieve the EU goal related to zero emissions of CO_2 by 2050, intensive efforts are going on in searching for alternative energy sources [122]. Here, hydrogen fuel technology is extremely important. By the adopted European directive, Slovenia has thus committed itself to providing an adequate number of publicly accessible hydrogen charging points by December 31, 2025, both for local transport and for cross-border transport [123]. Utilization of solar energy for the production of renewable fuels through various catalytic (photocatalysis, piezo catalysis) or electrochemical processes is one of the sustainable approaches in addition to using other abundant free energy from the environment, e.g. wind and waste vibrations [124]–[126].

Total electricity supply in the EU in 2021 increased by 4.2 % compared to 2020 with fossil fuels as the leading source for electricity generation [127]. On the level of individual energy carriers, the biggest contributors to the EU electricity generation system in 2021 were nuclear with 731 terawatt-hours (TWh), natural gas (550 TWh), wind (386 TWh), hydro (370 TWh), lignite (227 TWh), other bituminous coal (193 TWh), and solar (163 TWh).

In Slovenia, we are supplied with various primary energy sources. In 2021, more than half of the energy was still obtained from fossil fuels: mostly from imported oil and oil products (transportation), imported natural gas (heating), and coal (electricity) [128]. Fossil fuels play an important role in the production of electricity, as approximately one-third of all electricity is obtained from them. Almost 20 % of it is produced from nuclear energy and 25 % from hydropower. Other sources (primarily biomass, solar, and geothermal energy) contribute less than 3 % to the structure of sources for electricity production in Slovenia. Primary energy consumption in Slovenia in 2021 was 113 kWh per day for each resident (per capita), which makes the total country energy consumption of 235 GWh/day or 86 TWh annually. Primary (total) energy use includes the use of energy for:

- all forms of transport (33 kWh/day/capita or 25 TWh annually),
- heating and heat in households and industry (28 kWh/day/capita or 21 TWh annually),
- use of electricity in households and industry (20 kWh/day/capita or 15 TWh annually),
- but also includes conversion losses, including waste heat.

The final use of energy, which does not consider losses, thus amounts to just under 82 kWh per day per capita for Slovenia. In Slovenian households, more than 80 % of energy is used for heating (62 %) and water heating (19.5 %). The remaining 20 % of energy is spent on the operation of small electrical appliances, the operation of large household appliances, cooking, and lighting [128].

Vehicles are a large source of greenhouse emissions at the moment [129]. There is no one-size-fits-all solution when it comes to the electrification of heavy commercial vehicles. One of the technological solutions that Scania is researching together with its partner ASKO are electrically driven trucks with fuel cells powered by hydrogen [130]. The Pipistrel Vertical Solution company is also aware that aviation is one of the major polluters of the atmosphere, which is why they started developing electric planes 20 years ago, and have been producing them in series since 2007 [131]. Because the electric plane has a limited range and usefulness due to the energy density of the batteries, they see it as an ideal solution for a hydrogen drive. Their first four-seater hydrogen-powered hybrid electric plane completed its first flight in 2020.

Hydrogen fuel stands out with its high energy density. At the same time, it is storable, easy to transport, and suitable for use in fuel cells and other engines for energy conversion. Additionally, hydrogen combustion results in water without the formation of environmentally harmful residuals or greenhouse emissions. However, hydrogen is not an energy source, but rather a portable energy storage medium, similar to electricity. It is used to convert, store, and release energy. Renewable energy sources are weather dependent, which may cause uneven production and thus uneven availability of energy over different time frames (days, weeks, months, even years). Accordingly, a hydrogen-based energy system (energy to hydrogen to energy) can be implemented as an intermediate to avoid fluctuations in energy availability. The hydrogen-based system comprises four stages: production, storage, safety, and utilization [132] and all these have to be considered. The advantage of hydrogen is its lightness, which gives hydrogen the potential to be used in specific applications such as aviation and maritime.

1.3.1 Hydrogen classification

Although hydrogen is colorless and odorless, a whole spectrum of colors is used to describe hydrogen according to its origin. The colors are connected to the sources and technologies for the production of hydrogen as a fuel [132]. *Grey* hydrogen is produced commercially from fossil fuels including steam methane reforming, autothermal reforming of natural gas, and partial oxidation of coal or heavy oil without capturing the greenhouse gases produced by the process. Unfortunately, the production of hydrogen in this way is accompanied by CO_2 emission. In steam methane reforming 8-10 kg of CO_2 is formed for each kg of hydrogen. In other words, on an annual basis, it means more than 800 million tons of CO_2 [133]. The process using coal or heavy oil is sometimes referred to also as black hydrogen production. *Blue* hydrogen is mainly produced from natural gas by steam reforming. Contrary to the gray hydrogen process, in this case, carbon dioxide and vapors that form during the process are captured and stored, thus reducing the greenhouse gas footprint of grey hydrogen. Hydrogen can also be generated by pyrolysis of a fossil fuel or natural gas, producing carbon as a side-product. This is so-called *turquoise* hydrogen. Hydrogen can be generated also by biomass fermentation, gasification, reforming, pyrolysis, and bio-photolysis processes. Due to the limited availability of biomass and conflict of interest between fuel and food production, the production of hydrogen from biogenic sources is fairly limited. EU's potential biomass resources have been estimated to be 10 % of EU energy consumption [134]. *Green* hydrogen is the most desirable one because it is produced without harmful emission of greenhouse gases. The process uses renewable energy sources (e.g. solar energy or wind energy) for water electrolysis or via photocatalytic hydrogen evolution. Now, green hydrogen is the rarest because its production is still very expensive, and the efficiency is still too low for commercial use. Therefore, the transition to hydrogen-based energy is not possible to hop directly to green hydrogen, but via blue hydrogen [132], [135]. Besides, great attention must be paid to the production processes and involved materials. Photocatalytic water splitting is one of the favorable routes to produce H_2 and perovskite materials are one of the promising photocatalysts. Recently, $SrTiO_3$-based composites (Al-doped $SrTiO_3$ containing 0.1 wt. % Rh and Cr) have gained more significance in photocatalysis, following their use in large-scale solar hydrogen generation plant, demonstrated by the Japanese group [136], [137]. Some other shades in the spectrum of hydrogen colors are used: *pink/purple* – for the hydrogen produced from electrolysis using nuclear power, and *yellow* – for the hydrogen, produced by electrolysis using solar energy [135], [138].

The current color classification model refers to the type of input energy for the production process and greenhouse gas emissions, rather than how pure obtained hydrogen is. Also, the carbon capture and storage (CCS) energy consumption and effectiveness in removing carbon must be included in the total emissions [135]. To indicate the purity of the obtained hydrogen, the term "number of nine" is used in the literature, like the classification of other gases. Namely, the purity of three nines means 99.9 % or 3.0 hydrogen purity. Accordingly, 4.6 indicates the purity of four nines followed by a 6, i.e. 99.996 % pure hydrogen [135]. The innovative approach uses the concept of the color spectrum with cleanness percentage; this is Hydrogen Cleanness Index (HCI) followed by the depth level number, e.g. 75 Green-2. In this case, it means that renewable energy was utilized to produce hydrogen (green) [135]. The process is 75 % green due to some emissions associated with this process. The number after the color (number 2 in this case) is referring to the described model in Figure 11, saying that indirect greenhouse-gasses emission (i.e. CO_2 emissions) associated with the production pathway has been considered.

Currently, there are several types of hydrogen storage technologies available, including compressed hydrogen gas, liquid hydrogen storage, metal hydride storage, and carbon absorption [139]. Hydrogen storage is often considered a bottleneck in the hydrogen economy obtained from non-renewable routes [139]. The place of hydrogen production can have a large influence on the price and the best method of delivery. For example, a large hydrogen production plant can produce hydrogen at a lower price because it produces more, but the delivery of hydrogen costs more if the place of use is far away. Today, hydrogen is transported from place to place of production to the place of use via pipeline and road in cryogenic trucks liquid tanks, or trailers with gas pipes [140]. Hydrogen is a colorless, odorless, and flammable gas [141]. As with all other fuels, hydrogen also has some safety concerns and a degree of danger. While it is a lighter element than the air, it dissipates rapidly in case of a leak, which makes hydrogen safer than other spilled fuels. However, the leak goes easily undetectable and if the gas collects in a confined space, it can eventually explode [135], [141]. The explosion limit for hydrogen in air is 18.3 % – 59.0 % in comparison to 1.1 % - 3.3 % and 5.7 % - 14.0 % for gasoline vapor and natural gas, respectively [142].

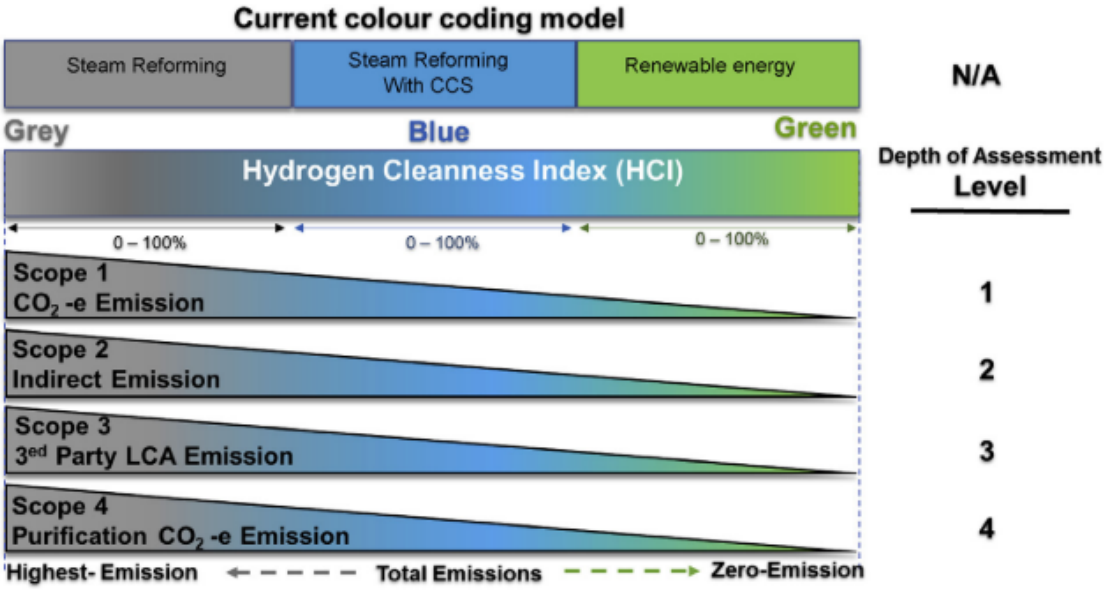

Figure 11: Innovative Hydrogen Cleanness Index (HCI), and depth assessments [135].

1.3.2 Methods for green hydrogen production

Currently, we are not able to produce hydrogen rapidly, efficiently, in an environmentally friendly manner, and at the same time assure enough energy. When obtaining energy from renewable sources, we are also tied to weather conditions, seasons, and (micro)locations. Additionally, consumption on different days of the week and even parts of the day is not the same. Therefore, the development of various sources of electricity is important, as well as the establishment of a good energy management system and the possibility of storing temporary surpluses. Green hydrogen is mostly obtained through water-splitting reactions, and there are a variety of different approaches to perform it. Overall water splitting is the chemical reaction ($H_2O \rightarrow H_2+1/2O_2$) in which the bonds in water molecules are broken so that the hydrogen is separated from oxygen. This is a thermodynamically uphill reaction ($\Delta G^o = 237$ kJ/mol), therefore it needs some help to happen. One possibility is to use electric current – in this case, the reaction is called electrolysis or electrocatalytic reaction [125], [143], [144]. Photoelectrochemical water splitting (Figure 12) is achieved by a combination of electricity and solar light and it is one of the processes, commonly named artificial photosynthesis [26], [145]–[147]. In this case, the electricity to split water comes from the photovoltaic system, and the H_2 and O_2 evolve in the cathode and photoanode compartments, respectively, of the photoelectrochemical cell (PEC). Another artificial photosynthesis approach is photocatalytic water splitting, where the water is split into H_2 and O_2 with the help of solar energy and photocatalyst [148]–[150]. Contrary to photoelectrochemical water splitting, this process can be performed in one step so that the photocatalyst is suspended directly in water without using an additional photovoltaic system (Figure 12a). The thermal decomposition of water is a process of breaking bonds by heating [151]. However, such a process requires high temperatures and therefore consumes high amounts of energy. Another approach to improve the efficiency of photocatalytic water splitting is piezo-photocatalysis. In this process, a catalyst is simultaneously an H_2-evolution photocatalyst and a piezo catalyst (piezoelectric material) and it can collect solar and mechanical energy (vibrational energy). In this way, waste vibrations in sunny places could be exploited to produce H_2 through the water-splitting process. Piezo-photocatalysis is a two-step process; first, the photons of appropriate energy excite the electrons from the valence band to the conduction band of the material; and second, mechanical energy (vibrations) induces a built-in-electric field that suppresses charge recombination and enables faster diffusion of photoelectrons from the bulk to the surface of the material. As a consequence, the efficiency of the photocatalytic reaction is higher [152], [153]. In the early ’80s, hydrogen photoproduction from water and various organic compounds (e.g. ethanol, methanol, lactic acid, ethylene, sugar, amino acids) in the presence of semiconductors was demonstrated [154]. The process is called photoreforming and its main advantage is in combination of two advantageous reactions, namely photocatalytic H_2 evolution and degradation of organic pollutants. The latter are sacrificial agents since their oxidation

proceeds more easily compared to oxidation of water. The nature of the sacrificial agent affects the mechanistic aspects and influences efficiency.

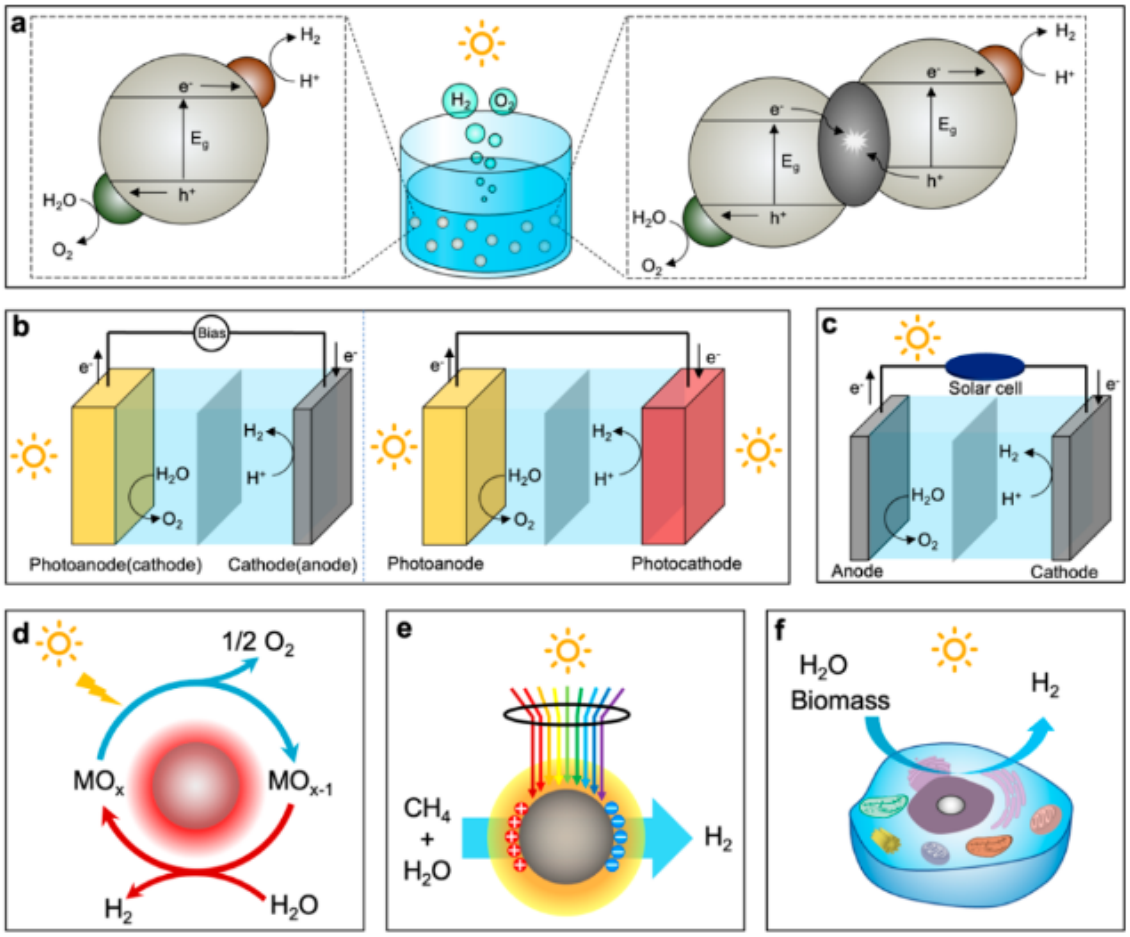

Figure 12: Illustrations of different approaches for solar hydrogen production: a) photocatalytic water splitting, b) photoelectrochemical water splitting, c) photovoltaic-electrochemical water splitting, d) solar thermochemical water splitting, e) photothermic hydrogen production and f) photobiological hydrogen production. Adopted from [155].

Hydrogen can also be produced biologically with the help of algae and different kinds of biomass. Photosynthetic microorganisms produce hydrogen from water splitting using sunlight [156]. The most important methods for production of H_2 by means of sunlight are described in [155]. There are also other approaches including radiolysis [157], nanogalvanic aluminum alloy powder [158], nuclear-thermal (next-generation nuclear plants, NGNP) [159], and solar-thermal [160]. The reverse reaction of water splitting is used in hydrogen fuel cells.

Among the above reactions, photocatalysis and electrocatalysis have emerged as the most widely explored processes. For comparison, electrocatalysis is a complex and costly process, which uses external bias, expensive electrodes, and complex reaction setup and requires precise catalyst preparation. However, the costs may be reduced by employing sunlight to support the electrocatalytic process. On the contrary, photocatalytic water splitting provides a cheaper and cleaner alternative as it uses sunlight. However, this process rather suffers from low efficiency. Photocatalytic water splitting is one of the artificial photosynthesis approaches for the production of new hydrogen fuel [153].

1.3.3 Photocatalytic hydrogen evolution

Photocatalytic hydrogen production is a chemical process that converts solar energy into chemical energy using a suitable photocatalyst [152]. A suitable photocatalyst must be efficient and stable. Additionally, to make the process commercially available, the photocatalyst must be easily available, cost-effective, and environmentally friendly.

Photocatalytic system for hydrogen production requires a photo-reactor, light source, photocatalyst, and water or water solution. As a light source, sunlight simulator sources are commonly used to demonstrate the natural conditions. As a solution, pure water or water mixed with a sacrificial agent can be used. To be able to measure the evolved hydrogen quantity, a coupled gas chromatography system is also required. The photocatalysis occurs in 4 steps: light harvesting, charge excitation, charge transfer and separation, and surface catalytic reactions or redox reactions.

First, light strikes over a photocatalyst's surface and absorbs it. The semiconductor material consists of a valence band (VB) and a conductive band (CB). Their separation is described as a band gap energy (E_g). An appropriate photocatalyst for H_2 evolution from water is a material with a conductive band more negative than the potential for hydrogen formation (-0.41 eV vs NHE) and a more positive valence band than the potential for O_2 formation (+0.82 eV vs NHE). Moreover, the band gap should be larger than the standard Gibbs free energy for the formation (237 kJ/mol, corresponding to the minimum requirement for water splitting 1.23 eV) and smaller than the incident light energy to make photoexcitation even possible (3.2 eV). The process consists of two half-reactions: water oxidation and hydrogen evolution. Together with the overall reactions it can be described with the following chemical reactions:

Oxidation: $2H_2O_{(l)} \rightarrow O_{2(g)} + 4H^+_{(aq)} + 4e^-$ $E_0 = 1.23$ eV
Reduction: $4H^+_{(aq)} + 4e^- \rightarrow 2H_{2(g)}$ $E_0 = 0.00$ eV
Overall reaction: $2H_2O_{(l)} \rightarrow O_{2(g)} + 2H_{2(g)}$ $E_0 = -1.23$ eV

Light absorption induces electronic transitions, which generate electrons and holes (electron-hole pairs or simply charges). Excitation of electrons from VB to CB results in leaving holes in VB and consequently in the separation of charges. Finally, redox reactions occur. Namely, the electrons are involved in the reduction of the protons, and the holes are involved in the oxidation of water. Consequently, holes decompose H_2O to O_2, and H^+ and H^+ form H_2 after gaining an additional electron. Photo-excited holes have great oxidizing potential to oxidize organic compounds, i.e. alcohols. The photocatalytic reaction is directly proportional to light intensity, however, the actual absorption depends on the photocatalytic material (band gap, morphology) as well as the photoreactor (design, conditions) [161].

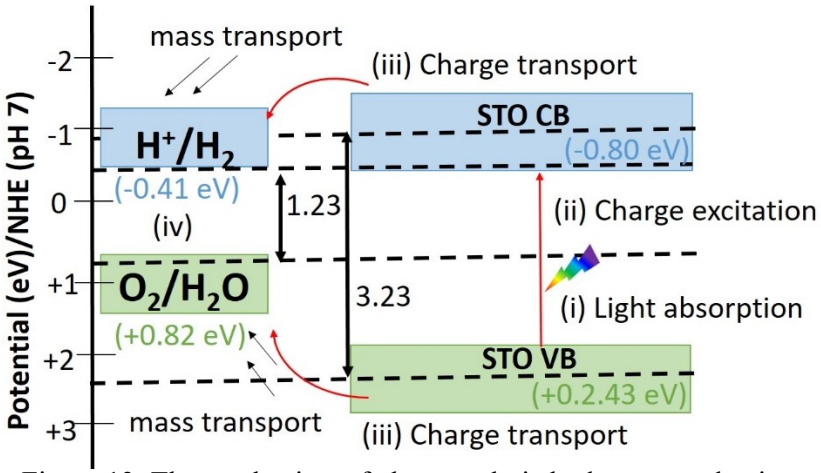

Figure 13: The mechanism of photocatalytic hydrogen production.

Photoreactor and reaction conditions for the photocatalytic hydrogen evolution need to be studied and optimized for each system individually to achieve the highest possible STH efficiency. On the other hand, it is hard to compare the photocatalytic efficiencies of different photocatalysts from different reports, because of using different light sources and reaction systems. Also, optimization of the photocatalyst amount, free space volume, etc. are not always optimized in the investigation. Similarly, solvents and sacrificial agents differ. This together with

the price, processing methods, and environmental impact of the photocatalyst gives us a very complex problem to solve. Two standard measures are used for reporting the results independently of the reactor system and light source: apparent quantum yield (AQY) and solar-to-hydrogen efficiency (STH) [162]. AQY describes the portion of the incident light of a certain wavelength that is effectively used to produce H_2. More precisely, AQY is defined by the equation:

$$AQY\ (h\nu) = \frac{nR}{I} \tag{8}$$

In the AQY equation, n is the number of involved electrons in the photocatalytic reaction, R is the evolution rate of water, and I is the number of incident photons. The disadvantage of the AQY is that it is determined at a certain wavelength. However, in real-life experiments, the whole solar spectrum is involved. Sometimes, internal quantum yield (IQY) is also given and is calculated as the ratio of the reacted electrons and incident photons. Less frequent use of this equation arises from the fact that it is hard to determine the number of absorbed photons by a photocatalyst.

STH represents the ratio of the energy converted into hydrogen gas to the energy input from solar radiation. As an absolute standard for measuring the performance of a photocatalyst, STH values are reported together with irradiance (number of photons and wavelength of used sunlight). STH is defined as the ratio between the output energy and the energy of incident solar light:

$$STH = \frac{r_{H2}\Delta G}{P_{sun}S} \tag{9}$$

In the STH equation, r_{H2} is the hydrogen evolution rate, ΔG is standard Gibbs energy for water dissociation (237 kJ/mol), P_{sun} is the energy flux of the sunlight and S is the area of the reactor. For the commonly used solar simulator, Xenon light AM 1.5 G, the energy flux is 1000 W/m^2. To date, the highest reported STH value of 9.3 % for photocatalytic water splitting (InGaN/GaN nanowires) was reported by Zhou et al. in 2023 [163]. United States Department of Energy suggested an appropriate commercial price for hydrogen fuel as 2-4 USD/kg H_2. 1.6 USD/kg H_2 would mean that in the 10-year lifetime of a photocatalyst, the STH value should be 10 %. The study of Zhou came very close to the targeted value. STH is related to AQY, and wavelength of the incident light as presented in Figure 14. To achieve an STH value of 10 %, AQYs of 62 %, 40 %, and 30 % are needed when using solar photons with wavelengths shorter than 600 nm, 700 nm, and 800 nm, respectively. The STH of a photocatalyst that absorbs only UV light with a wavelength shorter than 400 nm is limited to 1.7 %, due to the limitation of a photon number at this wavelength. Also, more than half of the energy of the UV photons dissipates as heat while producing H_2 [162]. Therefore, scientists seek to produce narrow-band-gap semiconducting photocatalysts. However, one must also have in mind scalability. A solar hydrogen plant with 10 % STH would need an area of 250,000 km^2 and required 50 million tons of water daily. According to energy consumption projections, this would cover approximately one-third of energy needs in 2050 [162].

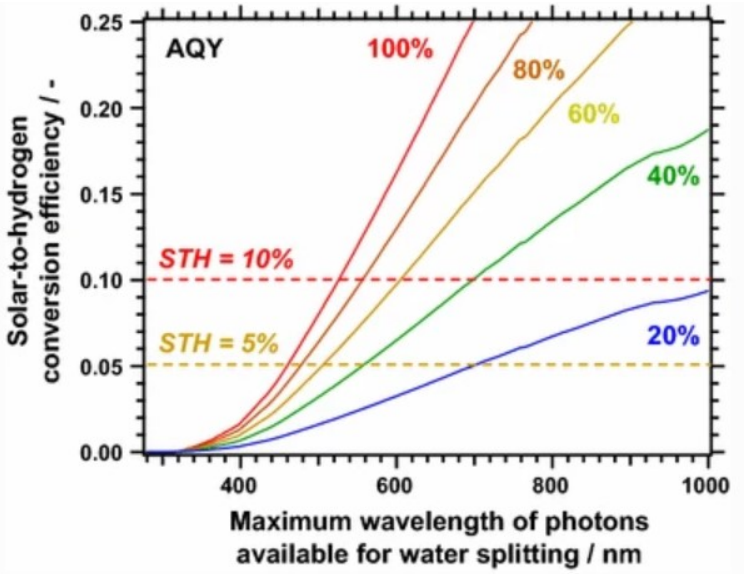

Figure 14: Relationship between STH and AQY for photocatalytic water splitting [162].

1.3.3.1 Materials for photocatalytic hydrogen evolution

Several materials have been investigated and used as photocatalysts in photocatalytic hydrogen evolution, but semiconductors are the most common among them [126]. This is a large group of materials containing various oxides, sulfides, ferrites, carbon-based materials, heterostructures, MOFs, etc. [148], [161], [164]–[166]. This group of materials has several advantages, however, most of them are active exclusively or predominantly in UV spectral range. The solar spectrum contains less than 10 % UV light, while the majority is the visible spectrum range. Consequently, the (theoretical) efficiency of such materials is very low and cost-consuming. There is a need to develop photocatalytic materials that would be efficient and cost-effective, environment and health-friendly, stable, and applicable in scale-up processes [161], [167]. The chemical composition, morphology, and electron band structure also influence the photocatalyst performance [148].

Among perovskite materials, titanate perovskites had been widely explored in photocatalysis due to their unique electronic and optical properties, extraordinary stability, and durability [6]. Primitive titanate, $SrTiO_3$, is one of the promising and consequently widely studied photocatalysts for hydrogen evolution due to its suitable band edge positions, flat band potential, possible surface defects, and high stability [24], [126], [168], [169]. However, the wide band gap hinders its visible light activity. The cubic crystal structure of $SrTiO_3$ is capable of accommodating most of the metallic ions from the periodic table due to various degrees of lattice distortion. The distortion in the crystal lattice changes the electronic band structures [170]. Therefore, it affects the electronic reactions, i.e. excitation, transfer, and redox reactions, and consequently influences the photocatalytic activity of the material. Another advantage of $SrTiO_3$ is that more than 90 % of the metals can be doped into the perovskite lattice without changing the structure and morphology [171]. To improve the reaction efficiency different strategies are commonly employed including band engineering [23], [28], [172], [173], usage of co-catalysts [174], and tailoring of morphology and exposed facets [101], [175]–[177]. For more details see 1.3.3.2.

1.3.3.2 Limitations and strategies to improve the efficiency

A great number of studies have been done in the past years on the topic of photocatalytic and photoelectrochemical H_2 generation which affirm the importance of greener technologies and processes [121], [124]–[126], [143], [144], [147], [178]–[182]. Still, hydrogen fuel (especially the one produced by solar energy) is not in everyday use yet. A fair number of factors limit the efficiency of photocatalytic hydrogen evolution to be too low for practical exploitation. Most oxide semiconductors are non-active in visible light or show only poor activity. As a consequence, such photocatalytic reactions have low usage of visible light [136], [3]. Besides, oxide semiconductors show low migration ability of photo-generated charges (electrons and holes), and short lifetimes of those charges (high recombination rates). Another problem is the long-term stability of photocatalysts. Some photocatalysts were found to be active only with limited reaction cycles [183], [184]. Different strategies to overcome the limitations of photocatalytic hydrogen evolution were developed through decades and the most important approaches are described in continuation.

Co-catalyst loading: Photocatalytic activity can be relatively easily enhanced with the loading of a scarce amount of noble metal (e.g. Au, Pd, Pt, Rh) which serves as a co-catalyst [185]–[190]. Co-catalysts are typically deposited onto the surface of the photocatalyst or incorporated into the reaction environment. Co-catalysts act as electron acceptors or electron donors and provide active catalytic sites, improve charge transfer processes, or facilitate reactant adsorption and activation. Co-catalysts affect the reaction kinetics and enhance the catalytic activity of the photocatalyst. From the standpoint of scale-up, the use of noble metals is not desired to produce hydrogen evolution from water splitting due to higher required amounts of the noble metals and related higher costs. Loading the noble metals is one of the most efficient methods for the enhancement of the photocatalytic activity for hydrogen evolution. This is true also for Al-doped $SrTiO_3$, which was intensively investigated in combination with Rh/Cr_2O_3 and CoOOH co-catalysts. The role of individual elements was thoroughly studied. Rh noble metal part promotes hydrogen evolution and also oxygen reduction reaction, but oxygen reduction reaction is blocked by the Cr_2O_3 shell over Rh metal nanoparticles. CoOOH nanoparticles that show a tendency to be deposited on the (110) facets of $SrTiO_3$ promote oxygen evolution reaction (oxidation of H_2O). Spatially selective photodeposition of Rh on the (100) facets and CoOOH on the (110) sites also explain high quantum efficiency (96 % at 350 nm-360 nm) of such $SrTiO_3/Rh(Cr_2O_3)$ CoOOH based photocatalytic system [191]. However, noble metals are rare and expensive and when it comes to large-scale production, this will increase the costs.

Doping: Important determinant for photocatalytic activity is the number of photoinduced charges generated in the photocatalyst by the light. The portion of the solar light that is absorbed

by the photocatalyst depends on its bandgap. Most oxide semiconductors, including $SrTiO_3$ (E_g=3.2 eV), exhibit a wide band gap and consequently utilize only the short wavelength part of the solar spectrum. Doping, co-doping, and self-doping (partial reduction of Ti^{4+} to Ti^{3+} and the formation of oxygen vacancies) can narrow the bandgap and improve the solar light absorption in $SrTiO_3$ and improve photocatalytic efficiency [192]. Namely, introducing dopant atoms with different electronic properties can improve the alignment of energy levels concerning the redox potential of reduction and oxidation reactions and therefore improve the light absorption and number of excited electrons leading to increased hydrogen evolution rate and higher efficiency. In contrast to co-catalysis, doping refers to the introduction of foreign elements into the crystal lattice of the photocatalytic material. However, it is not necessary that every doping improves photocatalytic efficiency through band gap narrowing. Incorporating Al^{3+} into $SrTiO_3$ (Al^{3+} ions replace Ti^{4+} ions in the B-site of the ABO_3 perovskite structure) significantly increases the material's activity for overall water splitting (OWS) reactions (oxygen and hydrogen (H_2:O_2 = 2:1) evolution), although this doping does not cause any significant change of the bandgap. The efficiency was proved to be enhanced by Al-doping by many different research groups, but the final photocatalytic efficiency also depends on co-catalyst deposition. The AQY value of 56 % at 365 nm was reported for Al-doped-$SrTiO_3$ loaded with $RhCrO_x$ co-catalyst by impregnation method [193]. The AQY value of this type of photocatalytic system was further improved to 96 % by optimized photodeposition of co-catalysts. In the literature, there are different explanations for why Al-doping so drastically improves the photocatalytic properties of $SrTiO_3$. According to Zhao et al. Al- doping in $SrTiO_3$ not only eliminates deep recombination sites associated with Ti^{3+} ions but also lowers the Fermi level of the compound by around 0.5 eV, resulting in a less n-type material [194]. The effect of Al^{3+} doping depends on its location relative to oxygen vacancies in the lattice. When the oxygen vacancy site is surrounded by fewer than two Al^{3+} ions, shallow acceptor states are formed near the vacancy, involving Ti^{4+} ions. These vacancy complexes, known as $\{Ti^{4+}–V_O\}$, contribute to the weak optical absorption and pale-brown color of Al-doped $SrTiO_3$ [194]. However, due to the lower Fermi level, these Ti^{4+} states are not continuously occupied by electrons and therefore only slightly promote electron-hole recombination. This is supported by the increased reversibility of surface photovoltage and electrochemical scans. These changes in the material's properties explain the significantly improved performance of Al-doped $SrTiO_3$ in overall water splitting, as observed in many studies [136], [194]–[199].

Plasmonic-cocatalysts: Photocatalytic properties can be significantly enhanced by the deposition of plasmonic metal nanostructures, showing a surface plasmon resonance (SPR) effect [150]. SPR is an optical phenomenon that occurs at the interface between a metal and dielectric material, which can be a thin film or nanoparticles. As a light with a specific wavelength interacts with the metal surface, it excites collective oscillations of electrons in a conductive band. These electrons are known as surface plasmons. When photocatalysts are combined with plasmonic metals, they can absorb a wider range of light, including visible and near-infrared light, which is usually not well utilized by regular photocatalysts. This increased light absorption helps the photocatalysts work better. Plasmonic metals also create strong electric fields near the metal surface. These localized electric fields can facilitate the separation and transport of photoexcited charge carriers within the photocatalyst. The localized electric fields can induce the charge transfer from the metal nanoparticles to the photocatalyst, allowing the electrons and holes to reach their intended reaction sites more easily. This efficient charge transfer reduces charge recombination and improves the overall performance of the photocatalyst. SPR effect is a characteristic phenomenon of small noble metal and non-noble plasmonic metal (NNPM) nanoparticles. NNPM group of materials has emerged as a compelling alternative to noble-metal photocatalysts, offering advantages such as earth-abundance, cost-effectiveness, and the potential for large-scale applications. Bi/TiO_2 photocatalyst displayed a dramatically higher photocatalytic H_2-production performance than pure TiO_2 [200]. In this case, Bi acts as an NNPM photocatalyst, which leads to increased light absorption due to the SPR effect. Another option to enhance light absorption are dye sensitizers, and defect-related color centers [201].

Self-doping (reduction): Next commonly used strategy includes reduction with the production of defect sites such as Ti^{3+} and O_v. Several research groups reported a large enhancement of solar-light absorption and visible light photocatalytic activity for H_2 evolution for reduced black TiO_2, $BaTiO_3$, and $SrTiO_3$ [202]–[204]. Typically, black TiO_2 has some degree of disorder, i.e. defects, on the surface. Studies have shown that the photoreactivity of TiO_2 is closely related to defect disorder [205]. Black coloration (or other, such as grey, brown, and opaque) has been ascribed to defect species like Ti–H bonds, surface hydroxide groups, oxygen vacancies, and Ti^{3+} species, that form during different synthesis methods [206]. Produced vacancies in black $BaTiO_3$ nanocubes contribute to the extended solar absorption and thus improve the separation ability of photogenerated carriers [204]. Similarly, Ti^{3+} cations and oxygen

vacancies are introduced into $SrTiO_3$ after reduction with aluminum, which results in enhanced absorption in both visible and near-infrared regions, and improved charge separation and charge transport [203]. Reduction of $SrTiO_3$ with other methods (i.e. reduction with $NaBH_4$ [207] or high-temperature hydrogenation treatment [208]) was also reported to result in significant improvement of photocatalytic hydrogen evolution rate.

Crystal facet engineering: The control of crystallographic orientation and facet engineering is a relatively novel and potentially powerful method to improve existing photocatalytic materials. The strategy of e^-/h^+ pair separation by crystal-facet engineering gained much attention because it enables the photo-excited e^- and h^+ to be collected on facets with different polarities. This prevents their recombination and spatially separates the reduction and oxidation reactions. As already mentioned, preparation of the particles with predefined exposed facets can be difficult, because during crystal growth, high-energy facets grow more quickly than low-energy facets, resulting in crystallites being terminated by the low-energy facets [42]. To modify the crystal facets' growth rates, species with functional groups or ions can be selectively adhered to those particular facets, leading to well-defined shape crystallites [187]. Mu reported that (001) and (110) facets of $SrTiO_3$ crystallites represent the separated reduction and oxidation catalytic sites, respectively [83]. It was shown for $SrTiO_3$ that the (001) facets favor the reduction, while (023) and (110) facets promote the oxidation reaction. In addition, it was shown that different co-catalysts can be deposited selectively: Pt deposition prefers the (001) facet and therefore promotes the reduction, while Co_3O_4 deposition prefers the (110) facet and therefore promotes the oxidation [38], [101].

Internal electric field: Fast recombination of photo-induced charge carriers (e^-/h^+ pairs) is one of the main reasons for the low photocatalytic efficiency of photocatalysts. Improvement of the charge separation by the internal electric field (built-in electric field), which can be present in the particles due to ferroelectric/piezoelectric polarization, flexoelectricity, or different polarities of the exposed facets is one of the strategies to improve photocatalytic efficiency. Diffusion of charge carriers competes with the built-in electric field [210]. The charge transfer within the crystal may not be as simple as the accumulation of charges on the surface [211]. However, experimentally observed charge accumulation on certain facets may reflect major charge recombination on other facets which suppresses most of the photoexcited electrons and holes. Presumably, photogenerated carriers first move towards the facets following the thermodynamic energy order and then reverse direction due to belt bending near the surface [212]. The controlled spatial separation of charges and redox reaction can be performed with specially designed nanostructures [148].

Morphology and surface modification: Charge recombination may be band-band recombination, trap-assisted recombination, or Auger recombination. Band-band recombination is a radiative transition occurring mostly in the direct band gap semiconductors in which electrons in a thin conductive band move to the valence band having holes. In trap-assisted recombination, an electron falls into the energy level within the band gap known as a trap formed due to a structural defect. Once the trap is filled up with electrons, it cannot accept more electrons. The electrons in the trap then move into the valence band and recombine. In Auger recombination, electrons and holes can recombine in a band-to-band transition [161]. So, for a successful hydrogen evolution reaction, the redox reaction and charge separation must occur within the lifetime of the photo-excited charge carriers. There is a tendency to prepare a photocatalyst with spatially separated reduction and oxidation sites. Additionally, the fast migration of photoinduced charge carriers to the surface of the photocatalyst where the reactions of H_2 and O_2 evolution take place is also important. From this standpoint, 2D structures with appropriate small thicknesses are more advantageous than larger 3D particles. Size, shape, and type of exposed facets can significantly affect the material's electrical, optical, and photocatalytic properties [213].

Photocatalytic reactions occur on the surface of the photocatalyst. Therefore, surface modification (e.g. increasing the surface area, particle size, porosity, and hierarchical structure) is an efficient approach to enhance photocatalytic activity. The photocatalytic activity of $MgTiO_3$ nanofibers was increased in comparison to $MgTiO_3$ nanoparticles in Wang's group as a consequence of higher surface area [214]. 2D structures have attracted a lot of interest in photocatalysis due to their low thickness which enables fast charge transfer to the surface. Additionally, a large surface area provides numerous active sites or large face contact with another material at the interface in the formation of 2D/2D heterostructures [215], [216]. Enhanced charge mobility at highly ordered atomically sharp interface in photocatalytic materials based on chemically bonded heterostructures with epitaxial contact is the reason for better performance and higher stability compared to physically mixed composite materials[216]–[218]. 1D structure and large surface area facilitated the charge carrier separation. Similarly, Guo et al. compared

$ZnO/SrTiO_3$ nanorod arrays to thin-film perovskite [219]. The latter showed better performance in photocatalytic hydrogen evolution.

Single-atom catalysts (SACs): This concept was introduced in the field of photocatalytic reactions in 2011 and became very popular among researchers in catalysis. The term SACs refers to the single metal atoms, which are distributed over the supports. It combines features of homogeneous (single active center and high selectivity) and heterogeneous catalysis (structural stability and facile separation) [183].

Heterostructures: Finally, a strategy for improvement of the photocatalytic efficiency is also the preparation of heterostructures. Designing heterostructures is one of the most efficient and recently well-studied approaches for the improvement of photocatalytic efficiency. Combinations of proper functional materials in single-component photocatalysts can improve the separation of photo-induced charge carriers, broaden the light-responsive range and enhance the stability of photocatalysts. The overall improvement of the photocatalytic efficiency depends on the band gap, relative band edge positions of the constituents, and interfacial contact between them. Considering the latter, large epitaxial 2D/2D contact areas are favorable, because of more effective charge transfer across the interface, which is usually higher in the case of highly structurally ordered (epitaxial) and chemically bonded interface than for the two constituents attached by physical forces (powder mixtures). The type of formed heterojunction depends on the relative band edge positions of the components. For the improvement of photocatalytic efficiency, the most beneficial is type II, p-n and direct Z-scheme heterojunction (Figure 15). In a type II heterojunction, the conduction band (CB) of one semiconductor is more negative than that of the other. This semiconductor has less positive valence band (VB) than the counterpart semiconductor. Under light illumination, the photoinduced electrons move from the semiconductor with more negative CB to that with less negative CB and the holes move from the semiconductor with more positive VB to that with less positive VB. The type II heterojunction favors photoinduced charge separation, however, the reduction and oxidation power are reduced. When different types of semiconductors (n- and p-type) are combined, then the heterojunction of p-n type can form. At the interface of p and n semiconductors, the space charge is formed already in the absence of light illumination. This internal electric field at the interface of the p-n junction is formed because electrons move from n-type to p-type and consequently, n-type and p-type semiconductor close to the interface becomes positively and negatively charged, respectively. Since there are two contributions (band alignment and internal electric field) that enable better separation of photoinduced charges, the recombination rate is decreased. Nevertheless, the redox ability is similar in type II heterojunction reduced.

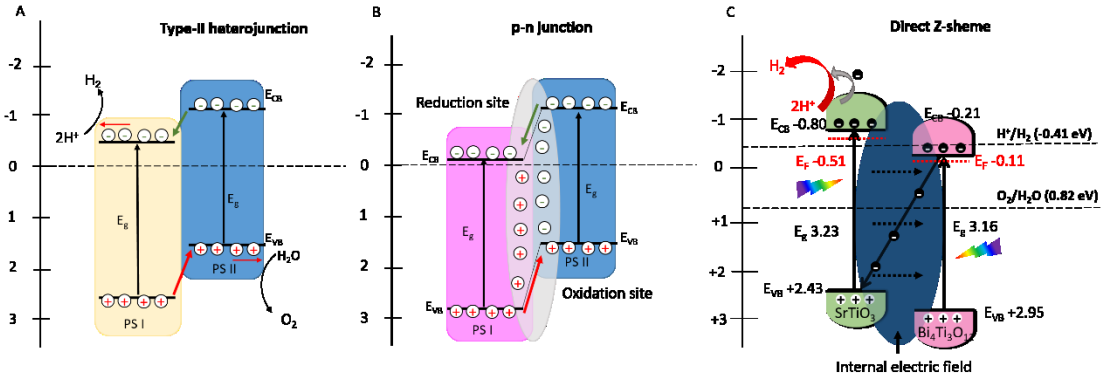

Figure 15: Illustrations of charge transfers in a) type-II heterojunction, b) p-n junction, and c) direct Z-scheme.

This is not the case for direct Z scheme heterojunction, in which photoinduced charge separation is improved due to the formation of an internal electric field, and the highest reductive and oxidative powers of both components are preserved. Direct Z-scheme heterojunction can for example form when two n-type semiconductors with different positions of CB are combined. In n-type semiconductors, the Fermi level is 0.1-0.3 eV below the CB. Due to the equalization of the Fermi levels at the interface of two semiconductors (e.g. both negative E_{CB} (vs. NHE), e.g. $Bi_4Ti_3O_{12}$ and $SrTiO_3$), the electrons from the semiconductor with more negative CB and more negative Fermi levels move to the semiconductor characterized by less negative CB and less negative Fermi levels and as a result, the semiconductors at the interface acquire positive and negative charges, respectively. Thus formed internal electric field can contribute to better photocatalytic performance in the following way: Under light illumination, the electrons from VB

of both semiconductors are promoted to the corresponding CBs. Due to the formed internal electric field, the electrons from the semiconductors with less negative CB move under this internal electric field over the interface to other semiconductors (with more negative CB) and there recombine with holes in VB. As a result, the reduction and oxidation capabilities of the semiconductor with more negative CB and the semiconductor with more positive VB, respectively, are preserved (Figure 15). The recombination rates within individual semiconductors are diminished because of the above-described charge flows caused by the formed internal electric field. From the band edge positions of two semiconductors that are combined in the heterostructure, it is difficult to predict which type of heterostructure, type II or direct Z-scheme, is formed. Since these types of heterostructures exhibit completely different charge flows, the reduction/oxidation reactions occur on different semiconductors. For example, in the case of direct Z-scheme charge transfer, the reduction reaction occurs on the semiconductor with more negative CB potential, while in type II heterojunction reduction occurs on the semiconductor with less negative CB. This can be verified with the photodeposition of noble metals, which in direct Z-scheme selectively deposit on the semiconductor with more negative CB, but it is the opposite for type II heterojunction. The other methods for verification of the charge transfer mechanism include sacrificial reagent testing, XPS, and radical trapping experiments [220].

There are a variety of reports of $SrTiO_3$ heterostructures with improved hydrogen evolution in comparison to pristine $SrTiO_3$. In the case of heterojunction $TiO_2/SrTiO_3$ improved photocatalytic water splitting was a consequence of spatial separation of charged particles [221]. Both materials in the respective heterostructure have a wide energy gap (~ 3.2 eV), but the conduction band of $SrTiO_3$ is slightly more negative than that of TiO_2. The authors explained that the electron-hole pair recombination was suppressed due to spatial interparticle charge separation and the highly stable reduced states of $TiO_2/SrTiO_3$. The formation of $SrTiO_3/TiO_2$ followed by nickel doping resulted in a reduced band gap shifted to the light absorption in the visible range [222]. It was proposed that doping with nickel reduced the electron-hole recombination as it trapped the photogenerated electrons, transferred the excited electrons to the adsorbed water, and induced oxygen vacancies. Zhang showed that $SrTiO_3$ monocrystal superstructure, synthesized by topotactic epitaxy from TiO_2 through hydrothermal treatment, exhibits greater efficiency, high quantum yield, and good durability in comparison to conventional systems [223].

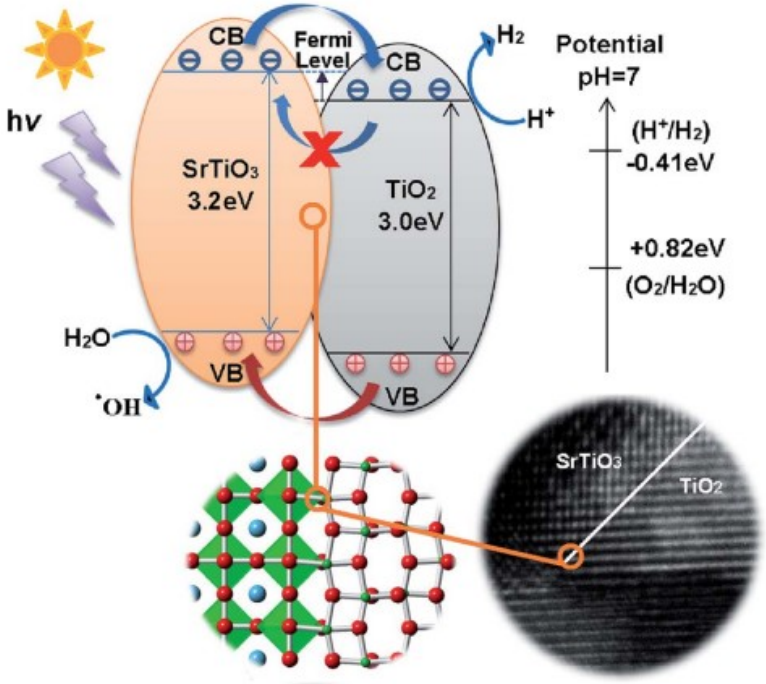

Figure 16: Visual presentation of photoexcited electron transfer and hydrogen evolution over $SrTiO_3/TiO_2$ nanoplatelets in the presence of CH_3OH as a sacrificial agent [223].

1.3.4 Future Perspectives on Solar-Driven Hydrogen Evolution

In response to the problems and disruptions in the global energy market caused by the Russian invasion of Ukraine, the European Commission presented the REPowerEU plan. The objectives of the REPowerEU plan are energy saving, clean energy production, and diversification of energy supply. It is supported by financial and legal measures to build the new energy infrastructure and system that Europe needs. Energy from renewable sources is the cheapest and cleanest energy available to us, and in addition, we can produce it in the EU and thus reduce energy consumption. The Commission proposes that the target for the share of renewable energy sources in the EU be increased from the current 40 % to 45 % by 2030. Under the REPowerEU plan, total renewable energy generation capacity would increase to 1.236 GW by 2030, instead of 1.067 GW, as envisaged in the 'Ready for 55' package. The EU Solar Energy Strategy will encourage the use of photovoltaic energy. This strategy under the REPowerEU plan aims to connect newly installed photovoltaic systems to the grid contributing more than 320 GW by 2025, more than double the current level, and by 2030, this figure is expected to reach almost 600 GW. With these additional early-acquired capacities, natural gas consumption will decrease by 9 billion cubic meters per year by 2027 [224].

Currently, the production of green hydrogen utilizing solar energy is considered to be one of the best renewable energy options, firstly because solar energy is huge, inexhaustible, and free energy potential, and secondly, this approach can solve the challenges of higher energy demands, fossil fuel depletion and greenhouse gasses limitations. Hydrogen is an energy carrier, suitable for transport and storage. This represents an advantage for the places and times with less convenient weather conditions (less sunshine). There are several solar-driven H_2 production technologies (Section 1.3.2), but most of these methods are still in the research stage. Table 4 summarizes the key benefits and critical challenges of different solar H_2 production approaches. Most of them suffer from high complexity, high costs, unsatisfactory stability, or too low efficiencies. All these fairly limit the potential of the approaches and their translation into everyday use. Photocatalytic hydrogen evolution from water is recognized as one of the most ideal methods for solar H_2 production due to its low complexity, sustainability, and suitability for scale-up. However, the commercialization of the approach is hindered by low light conversion efficiency, unsatisfactory stability, and complexity of H_2 and O_2 separation. From the standpoint of practical usage, it is important to pay attention to the selection of the photocatalyst material as well as the selection of other materials included in the production process. It is worth noting that the photocatalytic material is safe, non-toxic, and environmentally friendly, but also stable, efficient, available, and cost-effective, which are rather demanding terms and conditions.

Various strategies were used to achieve improved efficiency of H_2 evolution by the photocatalytic process (described in Section 1.3.3.2). The efficiencies of non-noble metal-based photocatalysts/cocatalysts systems are still too low for utilization in commercial processes. However, it should be noted that non-noble metal-based photocatalysts are the photocatalysts of choice for the commercialization of hydrogen production due to their low expenses. Nevertheless, at the research stage, the focus is on the understanding of phenomena and on the strategies to increase photocatalytic efficiency, while the costs and complexity of photocatalyst preparation are of secondary importance. To the best of my knowledge, the highest reported STH of 9.2 % (measured at 70 °C) has been reported recently for $Rh/Cr_2O_3/Co_3O_4$ loaded InGaN/GaN nanowires (NW). The most expensive element in this photocatalyst is Rh, but also In and Ga, which are the constituents of the main photocatalyst that are rather expensive. Among the photocatalysts, consisting of non-expensive and earth-abundant elements, $SrTiO_3$-based photocatalysts have attracted great attention. The other advantage of $SrTiO_3$ is high photo corrosion stability, but its wide bandgap (3.2 eV) and need of co-catalysts for notable photocatalytic H_2 evolution represent important drawbacks. Nevertheless, the largest scale-up of photocatalytic H_2-generation system on 100-m^2 was performed for Al-doped $SrTiO_3$ loaded with $Rh/Cr_2O_3/CoOOH$ co-catalysts. Due to the large size (100 m^2) of the demonstrator, this gave also the largest amount of hydrogen produced by sunlight, but the efficiency was low and the STH value much smaller compared to that achieved by photovoltaic-assisted water electrolyzers [225]. The role of H_2 energy produced by solar light in the future depends on many factors. Certainly, the fate of H_2 depends on how the challenges related to insufficient photoconversion efficiency, H_2 storage, and transport will be resolved.

Table 4: Summary of benefits and challenges of different approaches to hydrogen production.

The approach of H_2 production	Benefits	Challenges
Photocatalytic WS	low complexity, clean, sustainable	low efficiency, unsatisfactory stability, requires gas separation
Electrochemical WS	high efficiency, low environmental impact	high cost, high complexity, unsatisfactory stability
Photovoltaic-electrochemical WS	commercially available, long lifetime, high efficiency, easily scalable	high cost, high complexity, relatively high environmental impact (PV manufacturing)
Solar thermochemical WS	high efficiency, relatively low cost, reliable and viable	requires an effective solar collector, requires heat- and acid-resistant materials
Photothermal catalytic H_2 production (mainly fossil fuels)	high efficiency, high purity, feasible technology	high CO_2 emissions, high costs
Photobiological H_2 production	clean and sustainable, uses water or abundant organic substrates derived from waste	high cost, requires anaerobic photobioreactors, low efficiency

The development of other competitive renewable energy (e.g. nuclear) will also be decisive in how important solar H_2 will be in the future. Among the technologies (Table 4), those which will enable the production of H_2 in large quantities and at low costs will be commercialized. The future progress of the technology for H_2 generation from photocatalytic water splitting will depend on the development of non-expensive and stable photocatalysts with high efficiency (STH~10 %), optimized reactor designs in terms of efficient light harvesting, and H_2/O_2 separation. It is difficult to predict which materials will fulfill the requirements of adequately high STH, stability, and high costs. Till now there has been a lot of research done on Al-doped $SrTiO_3$ perovskites [137], [191], heterostructures, and g-C_3N_4 [220].

Perovskites and perovskite-based heterostructures have great potential in photocatalytic hydrogen production due to their high stability and low costs. However, hard work on the band gap tuning and band adjustments needed to be carried out to improve the efficiency of the process to be able to be up-scalable for commercial use and to meet our energy needs. Additional remaining challenges to be solved in the future are related to photocatalyst's stability, fast charge recombination, and too high costs. It is already well known that the synthesis approach and conditions are directly connected to the photocatalytic activity. However, a detailed understanding of the connections between morphology and photocatalytic activity is needed. In the future, more attention should be paid also to the optimization of the photocatalytic reaction environment and understanding of the mechanism of enhancing the reaction with sacrificial agents, etc. The world is seeking multi-disciplinary approaches such as the approach investigated and discussed in this research to design and produce novel solar-driven non-noble metal-based photocatalysts.

Chapter 2

Aims and Hypotheses

2.1 Aims of the Doctoral Dissertation

The main goal of the dissertation is to fill the gaps in the research field of reaction mechanisms under hydrothermal conditions, focused on topochemical conversion of Aurivillius-phase layer structure template particles into $MTiO_3$, with the emphasis on the transformation from $Bi_4Ti_3O_{12}$ to $SrTiO_3$. In addition to understanding the reaction conditions – reaction mechanism – particle morphology relationship, the research work in the dissertation is also application-oriented.

For that purpose, in the proposed doctoral dissertation, I would clarify the following issues:

- The influence of the $Bi_4Ti_3O_{12}$ template platelets' dimensions, initial aggregation, and their surface characteristic on the process of transformation and consequently on the morphology of the product.
- Determination of atomic-scale structure of the $Bi_4Ti_3O_{12}$ platelets (termination (with $[Bi_2O_2]^{2+}$ sheets or pseudoperovskite $[Bi_2Ti_3O_{10}]^{2-}$ blocks) and detailed microstructural examination of the $SrTiO_3/Bi_4Ti_3O_{12}$ interface (is the same layer in contact with grown $SrTiO_3$ phase?).
- The influence of hydrothermal reaction parameters (especially c_{NaOH}, c_{Sr2+}, temperature) on the growth mechanism, particle's morphology, and crystal structure.
- Determination of lattice mismatch that still allows layer-by-layer growth of $MTiO_3$ on $Bi_4Ti_3O_{12}$ and investigation of lattice defects caused by the misfit.
- The correlation between the reaction conditions and heteroepitaxial contact.
- The correlation between the reaction conditions, specific surface area, structure and composition of the $SrTiO_3$ and $SrTiO_3/Bi_4Ti_3O_{12}$ heterostructural platelets and photocatalytic hydrogen evolution rate.
- The effect of mesocrystallinity of $SrTiO_3$ and $SrTiO_3/Bi_4Ti_3O_{12}$ heterostructural platelets for higher hydrogen evolution rate.

2.2 Hypotheses of the Doctoral Dissertation

- Based on good structural matching, $Bi_4Ti_3O_{12}$ platelets can be transformed to $SrTiO_3$ platelets via topochemical conversion reaction under alkaline hydrothermal conditions.
- Transformation process, its kinetics, morphologies of formed $SrTiO_3$ and $SrTiO_3/Bi_4Ti_3O_{12}$ particles are governed by the "quality" of the initial $Bi_4Ti_3O_{12}$ platelets (aggregation, surface defects, platelet dimensions) and reaction conditions (Sr/Ti ratio, c_{NaOH}, T).
- Thorough understanding of the mechanism and significance of reaction parameters will enable us to control the target morphologies of heterostructures and final $SrTiO_3$ structures.
- Apart from different (higher) lattice mismatches, similar principles are valid for the growth of other $MTiO_3$ (M=Ba, Ca) perovskites on $Bi_4Ti_3O_{12}$.
- Based on the band-structure analysis it is anticipated that as-prepared $SrTiO_3$ particles and $SrTiO_3/Bi_4Ti_3O_{12}$ heterostructures can be used as a photocatalyst for hydrogen evolution.

Chapter 3

Materials and Methods

3.1 Chemicals

All chemicals (Table 5) were of analytical grade and were used as received without further purification. Water used for the study was purified with a system to produce ultra-pure water (Purelab Option-Q7, ELGA).

Table 5: Used chemicals.

Chemical	Manufacturer	Declared purity
$AgNO_3$	Alfa Aesar	99.9 %
$BaCl_2 \cdot 2H_2O$	Sigma Aldrich	99 %
Bi_2O_3 nanopowder	Alfa Aesar	99.8 %
$CaCl_2 \cdot 2H_2O$	Sigma Aldrich	≥99 %
C_2H_5OH, EMSURE®	Supelco	Absolute, ACS, ISO, Reag.
HF	Carlo Erba	96 %
HNO_3	VWR	68 %
KCl	Sigma Aldrich	≥99 %
NaCl	Merck	≥99.7 %
NaOH	Fischer Chemicals	≥98.7 %
Propan-2-ol	Carlo Erba	99.7 %
$(CH_3CO_2)_2Sr$	Sigma Aldrich	99.995 %
$SrCl_2 \cdot 6H_2O$	Sigma Aldrich, Roth	≥99.0 %
$Sr(NO_3)_2$	Fluka	≥99.0 %
TiO_2 anatase Hombitan	Sachtleben Pigments Oy	99 %
TiO_2 nanopowder P25	Degussa	≥99.5 %
TiO_2 rutile	Alfa Aesar	> 99 %

3.2 Processing Methods

3.2.1 Molten salt synthesis for $Bi_4Ti_3O_{12}$ template platelets preparation

$Bi_3Ti_4O_{12}$ template platelets were synthesized by the molten salt method. In the first part of the research (4.1), the processing parameters were optimized. The salts (KCl and NaCl) were weighted (Mettler Toledo, XS204) in 1:1 molar ratio (44 %wt NaCl) to ensure eutectic point composition ($T_{eut.}$= 657 °C [77]). The salts were grounded and mixed well in a mortar to achieve a homogeneous composition. Next, the required amount of Bi_2O_3 was added and the mixture was mixed well again. Finally, TiO_2 (P25, anatase or rutile) was added and mixed again. A homogeneous mixture of powder was subsequently transferred to the Al_2O_3 crucible with a diameter of 5 cm and a height of 7 cm and covered. The crucible with a lid was placed into a larger crucible (diameter 8 cm, height 9.5 cm), covered with a lid, and placed in the chamber furnace (Nabertherm LTH 16A). The heating rate was 10 °C/min, the reaction temperature was 800 °C. Holding time and cooling rate were varied. After the reaction, the product powder was washed with deionized water until all salts were removed (no AgCl precipitate in the filtrate after the addition of a few droplets of $AgNO_3$). For the identification of secondary phases and morphological observations, the product was dried at this point and XRD and SEM analyses were

performed. Next, 40 ml of different concentrations of HNO_3 was added to the powder, mixed well, soaked for 15 minutes, and subsequently washed with water to neutral pH (by centrifugation at 6000 rpm for 3-5 minutes/run; Eppendorf Centrifuge 5810 R), and finally dried at 80 °C or freeze-dried (Kambič LIO-5PLT) to obtain fine and pure powder product.

Based on the initial optimization (4.1), in the continued research (4.2), the procedure for preparation of the $Bi_3Ti_4O_{12}$ platelets was as follows: KCl and NaCl were weighed, grounded and mixed in a mortar, Bi_2O_3 nanopowder was admixed and lastly, TiO_2 nanopowder (0.500 g) was admixed as well. The molar ratio of starting materials KCl:NaCl:Bi_2O_3:TiO_2 was 50:50:2:3. The crucible with the reaction mixture was placed into a chamber furnace and heated up to 800 °C by the heating rate of 10 °C/min. After 2 hours at 800 °C, the furnace with its content was cooled down to room temperature naturally (step program). The product powder was washed with deionized water with suction filtration to remove the salt, followed by soaking in 40 ml of 2 mol/L HNO_3 for 15 minutes and washed with deionized water until neutral pH by centrifugation at 6000 rpm (Eppendorf Centrifuge 5810 R). The product powders were freeze-dried (Kambič LIO-5PLT).

3.2.2 Hydrothermal synthesis

3.2.2.1 Topochemical conversion of $Bi_4Ti_3O_{12}$ template platelets to $SrTiO_3$ particles

The topochemical conversion was performed under stirred hydrothermal conditions in high-pressure reactors Berghof BR100 and BR700 with Teflon (PTFE)-lined insert under stirring conditions (if not stated differently). For BR100, $SrCl_2{\times}6H_2O$ was dissolved in 2 ml (20 ml for BR700) of deionized ultrapure water and $Bi_4Ti_3O_{12}$ platelets (1 mmol/l) were admixed to the solution. The suspension was sonicated for 15 minutes in ultrasonic bath (Elmasonic P, Elma). Afterward, the suspension was quantitatively transferred to a PTFE-lined insert by washing the flask with a small amount of deionized water, and subsequently, 100 ml (250 ml for BR700) of NaOH was added. Finally, deionized water was added to the line mark in the PTFE insert, corresponding to the total volume of 120 ml (480 ml for BR700). If not stated differently, all solutions were cooled down to room temperature (25 °C) before admixing and the reactions were performed at 200 °C with stirring of 700 rpm (150 rpm for BR700). When some of the conditions (e.g. no stirring, different NaOH temperature) were changed for investigation purposes, this will be pointed out and discussed. After the reaction, the system cooled down naturally, while stirring. The product was washed with deionized water by centrifugation (until pH = 7), soaked in 30 ml of 1 mol/L HNO_3 for 5 min and washed again with water (again until pH = 7). In the end, the washed product was freeze-dried to obtain fine and soft product powder.

For the evaluation of reaction precursors influence in 4.1.1, also other strontium (strontium acetate and strontium nitrate) precursors were used in the same concentrations.

3.2.2.2 Topochemical conversion of $Bi_4Ti_3O_{12}$ template platelets to $BaTiO_3$ and $CaTiO_3$ particles

The topochemical conversion reactions to $BaTiO_3$ and $CaTiO_3$ were performed under the same stirred hydrothermal conditions in high-pressure reactor BR100 as described in 2.2.2.1. As a titanium precursor, $Bi_4Ti_3O_{12}$ platelets (1 mmol/l), obtained from nanopowder TiO_2 (P25), were used, and as barium and calcium precursors, corresponding chloride dihydrates $BaCl_2{\cdot}2H_2O$ and $CaCl_2{\cdot}2H_2O$ were used.

3.3 Characterization Methods

3.3.1 X-ray diffraction (XRD)

X-ray powder diffraction and X-ray diffraction for the platelets cast on Si-monocrystalline substrate were collected with X-ray Diffractometers Empyrean, Malvern PANalytical and Bruker AXS D4 Endeavor with CuKα radiation (λ = 1.5406 Å). For an estimation of the preferential orientation, a few drops of suspension of the particles in propan-2-ol were deposited on a Si-monocrystalline substrate (and left for the alcohol to evaporate). The typical measurement conditions are presented in Table 6. The diffractograms were analyzed using EVA software (Bruker AXS) and X'Pert High Score Plus software (PANalytical, HTK) to analyze the phase composition.

Table 6: Typical XRD recording conditions.

Diffractometer	Sample type	2θ range	Step	Time/step
Bruker	powder	10°-70°	0.04°	3 s
Bruker	suspension	20°-50°	0.04°	10 s
PANalytical	powder	10°-70°	0.026°	33 s
PANalytical	suspension	20°-50°	0.026°	100 s

3.3.1.1 Calibration curve for determination of $SrTiO_3$:$Bi_4Ti_3O_{12}$ ratio

For the preparation of calibration curve, appropriate amount of synthesized pure $SrTiO_3$ platelets and $Bi_4Ti_3O_{12}$ platelets were weighted (Mettler Toledo, XS 105), mixed and dissolved in propan-2-ol. The suspension was sonicated in ultrasonic bath at 37 Hz, 100 % for 15 minutes, mixed well again and few droplets of suspension were cast on Si-monocrystalline substrate. After natural drying, the XRD patterns were collected on PANalytical as stated in Table 6. Calculations, graphical presentation and data manipulation were done in OriginPro, OriginLab.

3.3.2 Scanning electron microscopy (SEM) with energy dispersive x-ray spectroscopy (EDXS)

Scanning electron microscopy (SEM) was used to determine morphological features of the samples and size determination. Two scanning electron microscopes were used for this purpose:

- FE-SEM, JSM 7600 F, JEOL, Japan; operated at 5 kV for imaging and 15 kV for EDXS.
- Schottky FEG, Verios HP 4G, Termo Fischer, USA; operated at 2 kV and 13 pA with beam deceleration (2 kV) for secondary electrons (SE) imaging, 5kV and 50 pA for backscattered electron (BSE) imaging and 20 kV and 50 pA for energy dispersive x-ray spectroscopy (EDXS).

EDXS analyses and elemental composition calculations were performed with the help of INCA (Jeol) and Aztec (Termo Fischer) software. Size parameters were measured on Verios, calculations and data manipulations were performed in Excel (Microsoft) and OriginPro (OriginLab). Surface coverage was estimated with ImageJ software.

3.3.2.1 Sample preparation for SEM analysis

A small amount of dry powder sample was dispersed in 3 ml of 2-propanol. The suspension was mixed and sonicated in ultrasonic bath for 20 minutes to obtain well dispersed non-aggregated particles. In the meantime, the sample holders (Al-polished) were warmed in a drier to 70 °C. A small droplet of suspension was cast on a warm holder (on the polished surface) and placed back into the drier to completely evaporate the alcohol.

Dried samples were then coated on a precision etching coating system (PECS, Model 682) with 5 nm of platinum for observations under FE-SEM and with 5 nm of carbon for observations under Schottky FEG. To achieve a better effect of coating, rotation and rocking were used while sputtering. For EDXS analyses on FE-SEM and FEG SEM, 7.5 nm and 6 nm of carbon, respectively, was sputtered in the presence of rotation and rocking.

3.3.3 Transmission electron microscopy (TEM) with energy dispersive x-ray spectroscopy (EDXS)

Microstructures and crystal structures in cross-sections were examined by scanning transmission electron microscopy using a probe Cs-corrected scanning transmission electron microscope (STEM Jeol ARM 200 CF, JEOL, Japan) operated at 200 kV.

3.3.3.1 Sample preparation for TEM analysis

Sample particles for the STEM analyses were prepared using two approaches. Sample particles are platelets with considerably larger side lengths than thickness. Such particles tend to align along the preferential orientation with their largest surface parallel to the substrate. For observations from the top-down view, the powder sample was sonicated in absolute ethanol and a droplet of the suspension was applied to the lacey, carbon-coated copper grid. The thickness of the platelets of up to 100 nm allowed STEM analyses without any further thinning.

For HR-TEM and HAADF-STEM analyses, the samples were prepared in cross section. Electron transparent lamellae were prepared by tripod polishing following the procedure by Voyles in an automatic tripod polisher [226]. A small amount of sample powder was mixed with

Cystal Bond thermoplastic wax and attached to pyrex specimen holder. As-prepared specimen was polished with a diamond-lapping film (DLF) with different grain sizes (15, 6, 3, 1, 0.5 and 0.1 μm) to ensure a planar surface. Final polishing was performed on polyurethane cloth using a silica solution with 20 nm-sized particles (Allied Colloidal Silica Suspension) to remove the scratches from the polished surface. The sample was removed from pyrex holder by heating the polishing block on a hot plate prior to polishing the other side and glued on the pyrex holder again with the opposite side. The process of thinning and polishing was then repeated on the other side. The samples were coated with 2 nm of carbon on PECS before the observations.

3.3.4 X-ray photoelectron spectroscopy (XPS)

X-ray photoelectron spectroscopy (XPS) was performed with the Versaprobe 3 AD (Phi, Chanhassen, US) using a monochromatic Al-Kα X-ray source. For each measurement, spectra were acquired on a 200 μm spot size with the charge neutralizer turned on, as the powders were put on a non-conductive double tape. Survey spectra were measured at 280 eV pass energy and step of 1 eV, while high-resolution spectra were measured at 55 eV pass energy and step of 0.05 eV. Charge neutralization was used, so the energy scale of XPS spectra was corrected by shifting the C1s peak of carbon to the binding energy of 284.8 eV. XPS spectra were analyzed with PHI Multipak software.

For ex-situ measurement after the H_2 evolution reaction, the solution of dispersed STO/BIT was centrifuged and vacuum dried. The powder was transferred to an argon-filled glovebox and put on a non-conductive double tape. XPS holder was then transferred to the spectrometer without exposure to air.

3.3.5 Brunauer-Emmet-Teller (BET) Specific Surface Area Analysis

The Brunauer-Emmet-Teller (BET) surface area measurements of prepared powders were performed by nitrogen adsorption with a Micromeritics Gemini II 2370 (Norcross, GA). The samples were degassed before the measurements overnight.

3.3.6 UV-VIS diffuse reflectance spectroscopy and Kubelka-Munk function for band-gap determination

Band-gap energies of the platelets were determined from the diffuse reflection spectra. The measurements in the UV-VIS spectral ranges were performed with an integrating sphere and $BaSO_4$ was used as a reference. The measurements were performed on UV-VIS spectrophotometer Shimadzu UV-3600, Tokyo, Japan.

3.3.7 Thermal analysis

Differential scanning calorimetry (DSC) measurements were performed on a Jupiter 449 simultaneous thermal analysis (STA) instrument (Netzsch, Selb, Germany). The heating rate was 20 °C/min. The atmosphere was Ar/O_2 (80/20). A TG/DSC-cp sample holder and platinum crucibles were used for analyses. Prior to the measurements, the temperature and enthalpy calibrations of the STA instrument were made with $BaCO_3$, CsCl, K_2CrO_4, $KClO_4$ and $RbNO_3$ standards.

3.3.8 Photocatalytic testing of the $Bi_4Ti_3O_{12}$ particles for Rhodamine B dye degradation

The decomposition of Rhodamine B (RhB) was measured in UV-A light. Sample powder (0.2 mg/mL) and RhB solution (10 mg/L) were mixed, sonicated (1 minute, pulse:pause = 2:1 second at 80 %), stirred in the dark at 500 rpm for 30 minutes and exposed to UV-A light. Degradation of the dye was checked before irradiation and after 1 h, 2 h, 3 h, 4 h and 24 hours of irradiation with UV-A light. The powder was removed by centrifugation. The absorbance was measured at $\lambda = 554$ nm using a Synergy Micro Plate Reader (BIOTEK). Two additional control measurements were performed: (i) reaction in the dark for suspension of sample and RhB and (ii) a parallel reaction under UV-A light irradiation for pure RhB (without sample).

3.3.9 Photocatalytic hydrogen evolution

The photocatalytic H_2-evolution measurements were carried out in a 50-ml quartz round-bottom flask at ambient temperature and atmospheric pressure using mixing to achieve the particle suspension. A commercial solar simulator equipped with a Xenon arc lamp (300 W, Newport) and an AM 1.5G filter was used as the light source. In a typical photocatalytic measurement, 20 mg of photocatalyst was suspended in 40 ml of aqueous solution containing 25 vol % of methanol and the suspension was sonicated for 30 min to obtain a well-dispersed particle suspension. Before the light irradiation, the quartz flask was sealed with a rubber septum and purged with a nitrogen flow for 40 minutes to remove the excess oxygen in the reaction mixture. Finally, the sealed quartz flask was placed under light irradiation. All the photocatalysts were subjected to 4 h of light irradiation, and the H_2 evolution was measured periodically every hour. The generated gas composition (1 ml) was analyzed with a gas chromatograph (GC, SRI-8610C) equipped with a thermal conductivity detector (TCD) and high-purity nitrogen was used as the carrier gas.

Chapter 4

Results and Discussion

4.1 $Bi_4Ti_3O_{12}$ Template Platelets

$Bi_4Ti_3O_{12}$ platelets were synthesized in molten KCl/NaCl salt at 800 °C from Bi_2O_3 and TiO_2 nanopowders. As-prepared platelets served as a template in the second part of the research, which is the hydrothermal topochemical conversion of $Bi_4Ti_3O_{12}$ platelets to $SrTiO_3$, $BaTiO_3$ and $CaTiO_3$ particles. To ensure uniform transformation speed, the template platelets should exhibit a uniform size distribution as much as possible (side length and thickness). The thickness and the side-length of particles depend on the reaction parameters. Therefore, the first step in my doctoral study was optimization of processing parameters for $Bi_4Ti_3O_{12}$ template platelets preparation.

4.1.1 The importance of morphology, crystal structure and aggregation stage of initial precursors (TiO_2) in the formation of non-aggregated, defect-free $Bi_4Ti_3O_{12}$ platelets with the narrow size distribution

In the process of hydrothermal topochemical conversion, $Bi_4Ti_3O_{12}$ platelets dissolve and at the same time serve as the substrate for the $ATiO_3$ (A=**Sr**, Ba, Ca) epitaxial growth. Thus, the quality (i.e. number of defects and aggregation stage) of the $Bi_4Ti_3O_{12}$ platelets is expected to play an important role in the transformation process. For example, defects are expected to influence the $Bi_4Ti_3O_{12}$ platelets' dissolution rate and increase the activation energy for $ATiO_3$ nucleation on the $Bi_4Ti_3O_{12}$ surface by increasing interfacial free energy, being larger than that arising only from the lattice mismatch.

Considering the "dissolution-precipitation" mechanism for $Bi_4Ti_3O_{12}$ formation in molten salt (see Section 4.1.2), the morphology and crystal structure of the starting materials (Bi_2O_3 and TiO_2) affect the quality of the $Bi_4Ti_3O_{12}$ platelets. Smaller nanoparticles as a starting material enable their faster dissolution and ensure more homogeneous concentration of dissolved species in the molten salt media. As a result, there is higher probability for $Bi_4Ti_3O_{12}$ homogeneous precipitation, while in the case of larger undissolved reagent particles, these serve also as the substrate for nucleation and growth of the product material. Fluctuations in the conditions are greater in the latter case. Thus, precipitated particles are expected to be more aggregated with broader size distribution and contain also more defects. To evaluate to which extent the characteristics of the reagents affect the morphology of precipitated $Bi_4Ti_3O_{12}$ particles, I synthesized $Bi_4Ti_3O_{12}$ using TiO_2 precursors with a different size and morphology: nanopowder P25, anatase and rutile (Figure 17, Figure 18 and Figure 19).

The XRD patterns of TiO_2 precursors were recorded (Figure 17) and their morphologies were examined by SEM (Figure 19). The P25 nanopowder is the mixture of anatase and rutile. This powder consists of small non-aggregated nanoparticles with average particle size of 20 nm and narrow size distribution (Figure 19A). The powder that is declared as anatase was confirmed to be anatase, while the TiO_2 powder that was declared as a rutile is not pure rutile but also contains some amount of anatase phase (Figure 17, black curve). However, the amount of anatase is lower than in P25 nanopowder. Anatase TiO_2 has crystallites with the size of 50-100 nm, which are aggregated forming μm-size aggregates (Figure 19B). TiO_2 rutile precursor consists of even larger particles with a wider size distribution and these crystallites are also aggregated (Figure 19C). The specific surface area of TiO_2 is by far the largest for the nanopowder P25, and smaller for the other two (Table 7). These differences between the TiO_2 precursors are manifested in the morphologies of formed $Bi_4Ti_3O_{12}$ platelets in the following manner: $Bi_4Ti_3O_{12}$ platelets formed from TiO_2 P25 exhibit well-defined platelet shapes with side lengths ranging from 0.25 μm to 3.62 μm, resulting in average value of 1.17 μm and median of 1.0 μm. Both statistical values are

larger compared to those of $Bi_4Ti_3O_{12}$, prepared with the other two TiO_2 precursors (Table 4). In the case of larger and more aggregated anatase and rutile TiO_2 precursors, the range of the formed $Bi_4Ti_3O_{12}$ platelets dimensions, was 0.10-5.23 microns and 0.13-2.75 microns, respectively (Figure 18 and Table 7). Anatase- and rutile-made $Bi_4Ti_3O_{12}$ consists of some significantly larger platelets, while the most frequent particle size group is that with platelet side lengths of smaller than 0.5 microns, resulting in average side lengths of 0.7 μm and 0.6 μm respectively. BET of $Bi_4Ti_3O_{12}$ synthesized from rutile and P25 are comparable, however, $Bi_4Ti_3O_{12}$ formed from rutile particles are smaller, but aggregated which together does not reflect the difference in BET value (Figure 18 and Figure 19). On the other hand, $Bi_4Ti_3O_{12}$ prepared from anatase has a larger BET because of a larger number of smaller $Bi_4Ti_3O_{12}$ particles, which are, as evident from the SEM image (Figure 19E), also aggregated, but at the end, the specific surface area is still larger in this case (Table 7). Also, the XRD patterns acquired from the powders cast on the single crystal silicon substrate confirmed that $Bi_4Ti_3O_{12}$ platelets obtained from nanopowder TiO_2 (P25) can be easily separated and oriented parallel to the substrate. This is evident from the high intensity of (00l) diffractions, while (117) diffraction exhibits very low intensity. On the contrary, other two TiO_2 precursors give $Bi_4Ti_3O_{12}$ with XRD patterns, in which (117)-crystal plane shows higher intensity, indicating random orientation of the platelets due to aggregation (Figure 20). The aggregated $Bi_4Ti_3O_{12}$ platelets formed from larger anatase and rutile are presumably a less ideal template for topochemical conversion to $SrTiO_3$. The findings of the conversion of different quality templates to $SrTiO_3$ under moderate and high supersaturation conditions are described in 4.2.2.1.

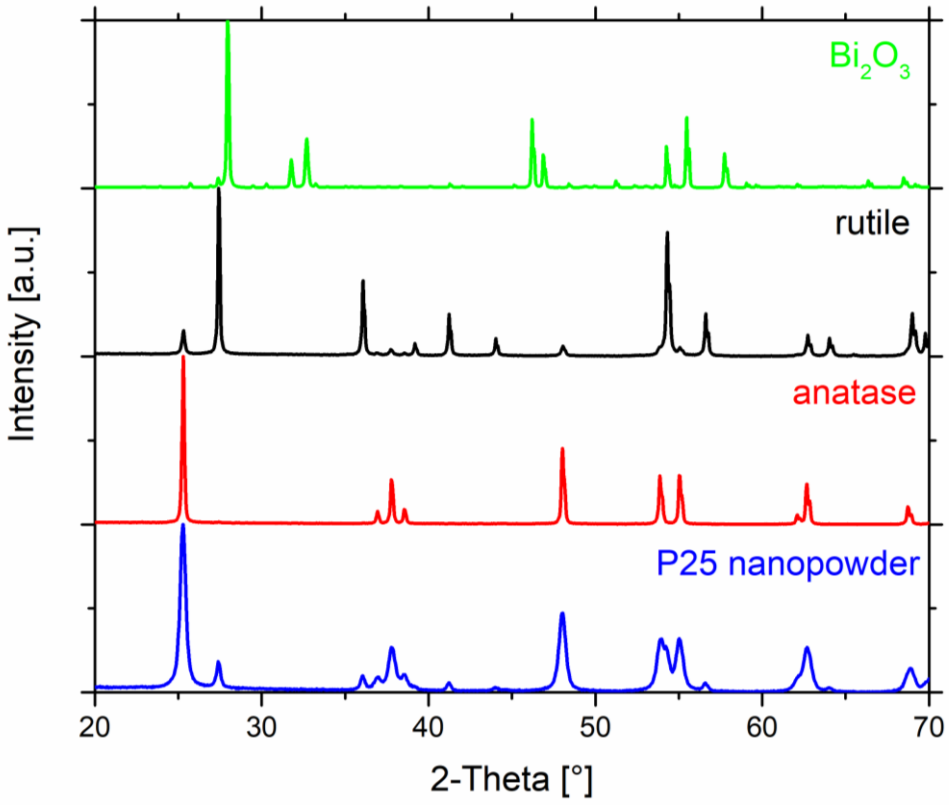

Figure 17: Powder XRD patterns of used TiO_2 and Bi_2O_3 raw materials.

Table 7: Comparison of the size ($Bi_4Ti_3O_{12}$: side length) and specific surface area (BET) values for TiO_2 sources and prepared $Bi_4Ti_3O_{12}$ platelets.

TiO_2 source	**P25 nanopowder**	**Anatase**	**Rutile**
Diameter[nm]	20	50-100	500-2000
Specific Surface Area [m^2/g]	54	11	8
$Bi_4Ti_3O_{12}$	**$Bi_4Ti_3O_{12}$ (P25)**	**$Bi_4Ti_3O_{12}$ (anatase)**	**$Bi_4Ti_3O_{12}$ (rutile)**
Side length [µm]	0.25-3.62	0.10-5.23	0.13-2.75
Mean [µm]	1.17	0.70	0.60
St. Dev. [µm]	0.57	0.60	0.33
Median [µm]	1.02	0.52	0.50
Specific Surface Area [m^2/g]	3	4	3

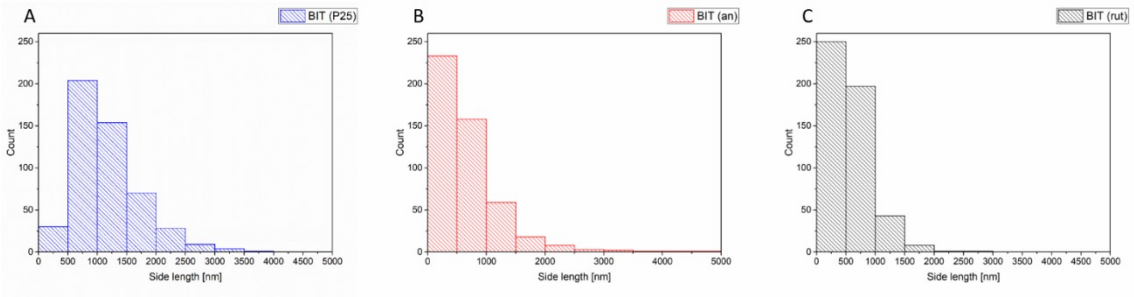

Figure 18: Side length distribution of $Bi_4Ti_3O_{12}$ particles prepared from three different TiO_2 precursors: P25 nanopowder (A), anatase (B) and rutile (C).

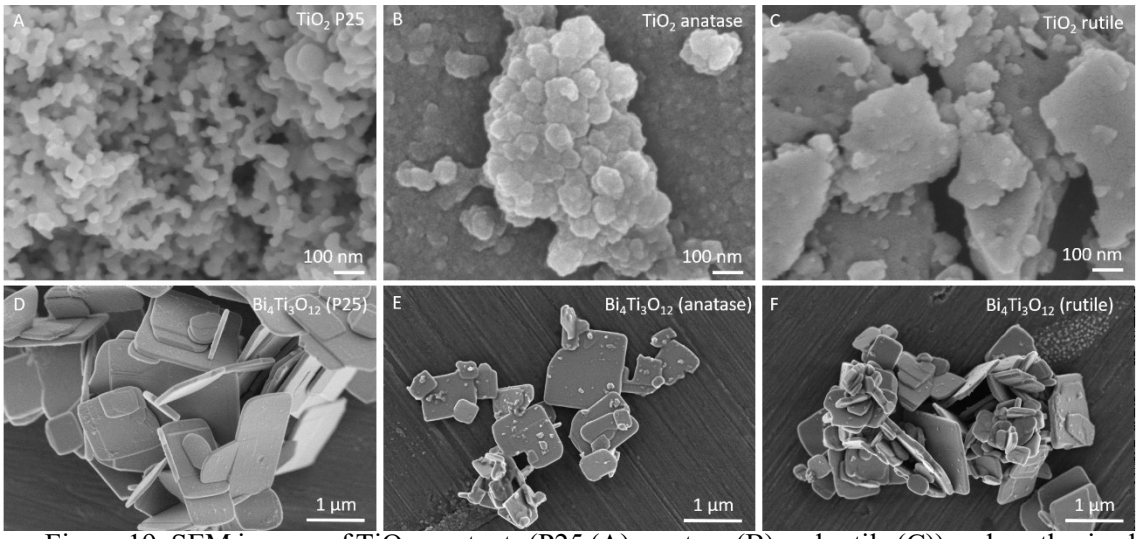

Figure 19: SEM images of TiO_2 reactants (P25 (A), anatase (B) and rutile (C)) and synthesized $Bi_4Ti_3O_{12}$ platelets prepared from P25 nanopowder (D), anatase (E) and rutile (F) TiO_2 powders in molten salt at 800 °C for 2 hours.

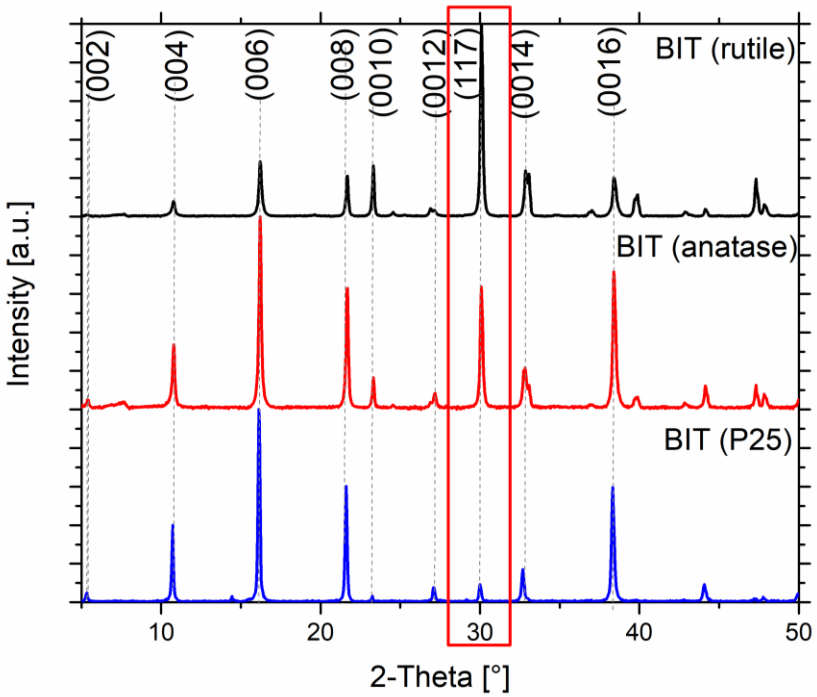

Figure 20: XRD patterns of $Bi_4Ti_3O_{12}$ prepared from different TiO_2 reagents: P25 nanopowder (blue), anatase (red) and rutile (black). XRD patterns were acquired for the $Bi_4Ti_3O_{12}$ samples, cast from the (iso-propanol) suspensions on the Si-monocrystalline substrate.

4.1.2 Optimization of processing parameters for preparation of the $Bi_4Ti_3O_{12}$ template platelets

According to the literature review, the reaction temperature of 800 °C was selected [84]. Based on the results presented in 4.1.1., TiO_2 nanopowder P25 was selected for further optimization of the conditions of $Bi_4Ti_3O_{12}$ template platelets preparation. The heating rate was selected according to the capability of our chamber furnace and was 10 °C/min. Holding time, salt:rectants molar ratio, Bi:Ti initial molar ratio and cooling rate were investigated. The reaction conditions for the investigation of the influence of processing parameters on the morphology are summarized in Table 8. In the beginning of the optimization study, the Bi_2O_3 was added in excess with respect to TiO_2 (Bi:Ti molar ratio 2.67, while the stoichiometric Bi:Ti molar ratio is 1.33) in order to provide a high concentration of Bi^{3+} for the formation of $Bi_4Ti_3O_{12}$ plates.

Table 8: The reaction conditions for the investigation of the influence of processing parameters on the $Bi_4Ti_3O_{12}$ morphology (TiO_2⇒P25 nanopowder).

Sample	Bi:Ti	NaCl:KCl:$Bi_4Ti_3O_{12}$	T(°C)	Time	Heating	Cooling
BIT1	2.67	50:50:1	800	20 min	10°/min	10°/min
BIT2	2.67	50:50:1	800	2 h	10°/min	10°/min
BIT3	2.67	25:25:1	800	2 h	10°/min	10°/min
BIT4	2.0	25:25:1	800	2 h	10°/min	10°/min
BIT5	1.33	25:25:1	800	2 h	10°/min	10°/min
BIT6	1.33	50:50:1	800	2 h	10°/min	10°/min
BIT7	1.33	25:25:1	800	2 h	10°/min	5°/min
BIT8	1.33	25:25:1	800	2 h	10°/min	natural

The XRD analysis confirmed the formation of the orthorhombic (S.G. B2cb) $Bi_4Ti_3O_{12}$ phase (PDF:01-072-1019) as the main phase in all experiments, summarized in Table 8. However, in some cases (BIT1, BIT2, BIT3, BIT4 and BIT7) also $Bi_{12}TiO_{20}$ secondary phase was present (Figure 21). The secondary phase was removed after washing with 2 mol/L HNO_3 (XRD for BIT1 in Figure 22).

The formation of $Bi_4Ti_3O_{12}$ platelets in the molten salt proceeds according to the dissolution-precipitation mechanism. First, Bi_2O_3 and TiO_2 dissolve in the molten salt, and afterwards, $Bi_4Ti_3O_{12}$ platelets precipitate. Further growth of the platelets is governed by Ostwald ripening. To tailor the size of the platelets, longer (2 hours, BIT2) and shorter (20 minutes, BIT1) reaction times were selected for the preparation of larger and smaller $Bi_4Ti_3O_{12}$ platelets, respectively. In both cases, product particles were formed as platelets (Figure 23). Platelets obtained after a shorter reaction time exhibited a smaller average side length and thickness in comparison to the platelets obtained after a longer reaction time. Moreover, particles obtained after a longer reaction time have a more defined plate-like shape and a more uniform size distribution. This can be ascribed to the Ostwald ripening process because in the second case, particles had more time to grow and achieve a more uniform size distribution.

In the next step, the nominal molar ratio of bismuth to titanium (denoted as Bi:Ti in Table 8) was investigated. The following nominal Bi:Ti molar ratios were selected: 2.67, 2.0 and 1.33 (stoichiometric) for BIT3, BIT4, and BIT5, respectively. The BIT5 platelets with stoichiometric Bi:Ti initial ratio, have a more defined shape and narrower size distribution than in other two cases. In cases with an excess of Bi_2O_3 (BIT3 and BIT4), a considerable amount of the secondary bismuth phases such as $Bi_{12}TiO_{20}$ was formed. On the contrary, when the stoichiometric ratio was used (BIT5), $Bi_4Ti_3O_{12}$ was the main phase already before washing with HNO_3 (Figure 21).

For the optimization of the amount of salt, the weight ratio of reactant to salt 1:6 was used (50:50:1 in molar ratio NaCl:KCl:$Bi_4Ti_3O_{12}$) according to the reports in the literature [84]. SEM observations showed some inhomogeneity in size distribution. Therefore, the ratio was lowered to 1:3 (25:25:1 molar) and the size distribution of product particles became narrower. With the lower amount of salt, the diffusion distance of reactant particles is smaller, therefore reaction occurs faster and more uniformly. Powder XRD patterns are comparable in both cases. $Bi_4Ti_3O_{12}$ is the main phase, however, there is some secondary $Bi_{12}TiO_{20}$ phase present before washing with HNO_3.

Cooling is an important part of the crystallization process and particle growth. Cooling rates of 10 °C/min (BIT5), 5 °C/min (BIT7) and natural cooling (BIT8) were compared. However, based on SEM observations there is no significant difference in the morphology when the cooling rates were 10 °C/min, 5 °C/min or natural cooling.

The processing conditions that were found to be optimal for the preparation of the $Bi_4Ti_3O_{12}$ template platelets in molten salt are presented in

Table 9. If not mentioned differently, the proposed reaction conditions were used for further template preparations.

Table 9: The optimal processing conditions for the preparation of $Bi_4Ti_3O_{12}$ platelets from TiO_2 nanopowder (P25).

Sample	**Bi:Ti**	**NaCl:KCl:$Bi_4Ti_3O_{12}$**	**T(°C)**	**Time**	**Heating**	**Cooling**
BIT5	1.33	25:25:1	800	2 h	10°/min	10°/min

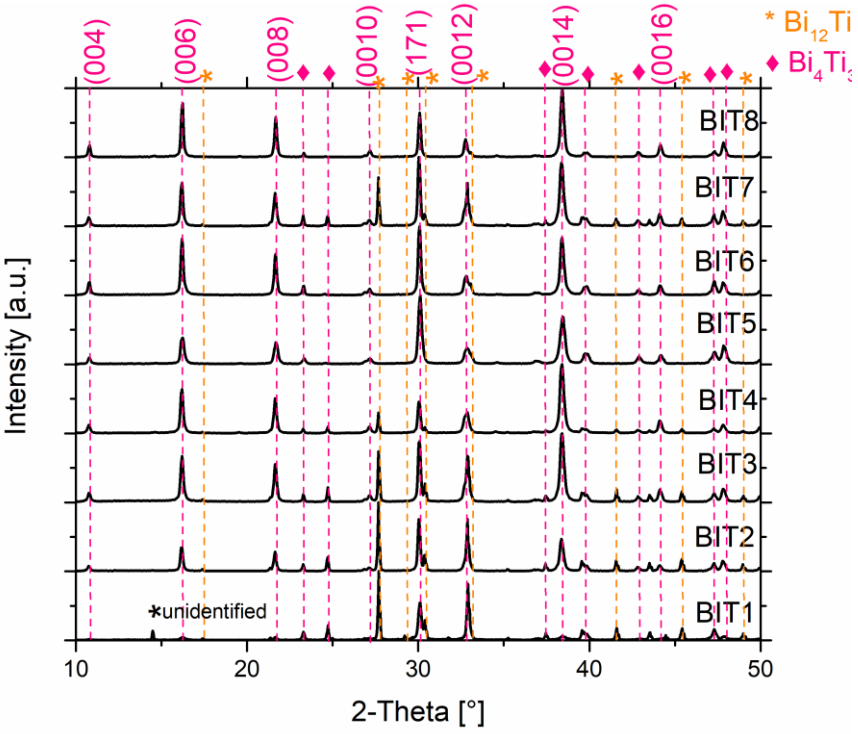

Figure 21: Powder XRD patterns of $Bi_4Ti_3O_{12}$ platelets prepared in molten salt under different reaction conditions as described in Table 8 and washed with water. Denoted lattice planes above the patterns belong to $Bi_4Ti_3O_{12}$ phase.

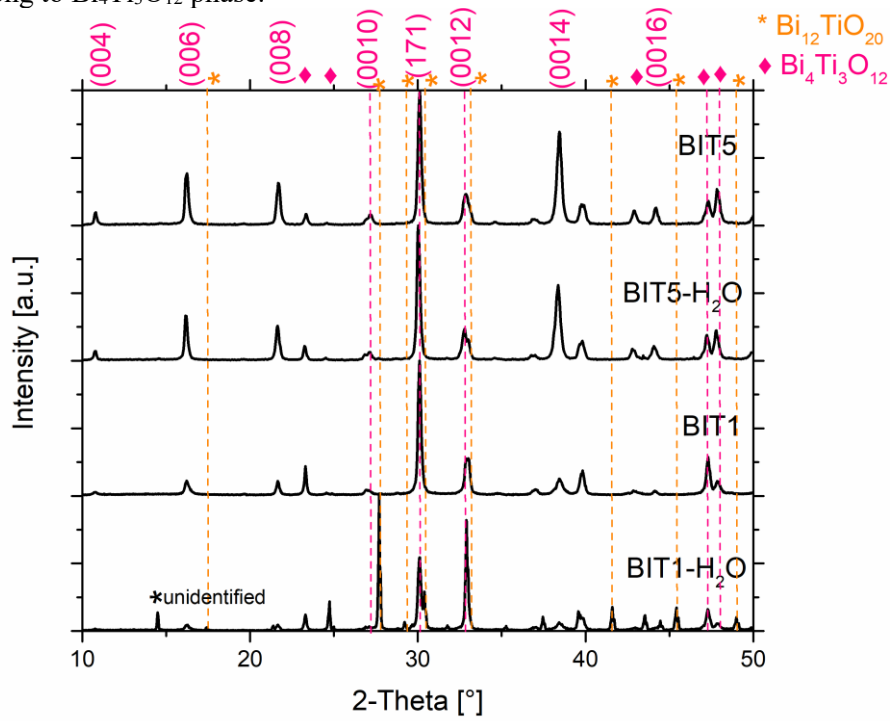

Figure 22: Powder XRD patterns of two different $Bi_4Ti_3O_{12}$ samples (BIT1 and BIT5) washed only with water and after additional washing in HNO_3 and removal of secondary phase. Denoted lattice planes above the patterns belong to $Bi_4Ti_3O_{12}$ phase.

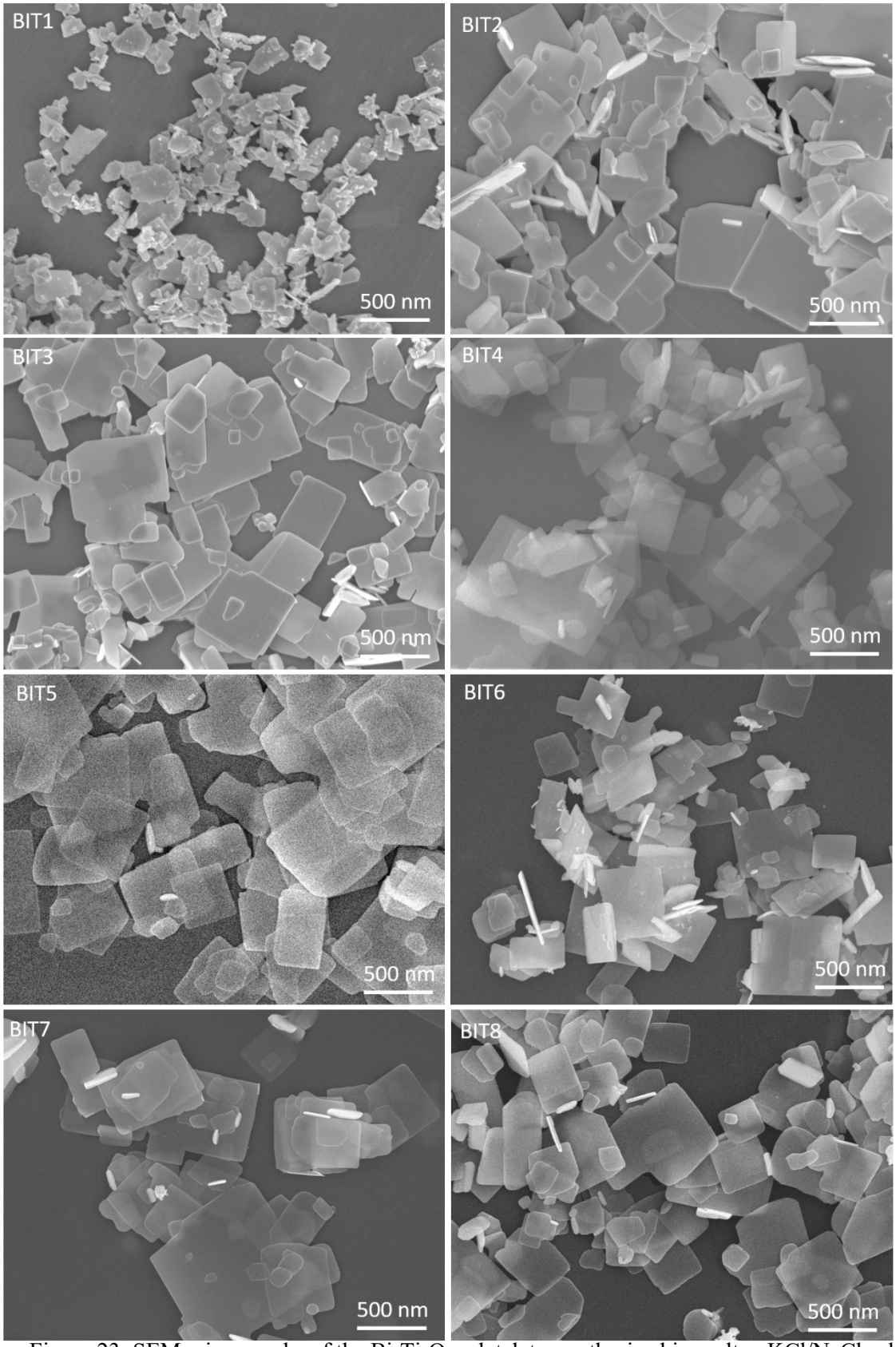

Figure 23: SEM micrographs of the $Bi_4Ti_3O_{12}$ platelets, synthesized in molten KCl/NaCl salt at 800 °C as described in Table 8.

4.1.2.1 Washing and drying procedure

After the formation of $Bi_4Ti_3O_{12}$ from Bi_2O_3 and TiO_2 in molten KCl/NaCl salt, this reaction product and eventual secondary phase (e.g. $Bi_{12}TiO_{20}$) must be separated from the salt. Considering the high solubility of NaCl (36 g/100 g H_2O) and KCl (35.5 g/100 g H_2O) in water at 25 °C, the salts can be easily removed by dissolving them in water. Two methods were used: suction filtration and centrifugation in 50 mL centrifugation tubes and Eppendorf 5810 R centrifuge.

I have found that the first step – removing the salt, is faster by suction filtration and the particles agglomerate less than in the case of multiple centrifugation rounds with high revs. However, one has to take care that the underpressure is not too high and that the particles on the filter paper are always wet and in the form of a suspension. If not, particles can agglomerate and it is difficult to separate them afterwards. Rinsing and washing with deionized water is carried out until all salt is removed – no white precipitate after the addition of a few droplets of 0.1 mol/L $AgNO_3$ to the filtrate.

Afterward, the product was washed with HNO_3 to ensure that all secondary phases are removed. The second step of the washing procedure was performed employing centrifugation, since it was faster and particles did not agglomerate strongly, because the centrifugation conditions with short times (1-2 min) at low speed (6000 rpm) are enough for sedimentation of the particles and their efficient separation from the solution. HNO_3 is a strong acid that can similarly to HCl or HF etch the surface of the materials [63], [227]–[230]. Therefore, I studied how the type of acid, concentration, and contact time of the acid with the platelets affect the efficiency of the secondary phases removal as well as how it influences the platelets' surface. A comparison between soaking in HNO_3 in ultrasonic bath and without ultrasonic support was also made. No significant difference was observed on particles with SEM and XRD analysis (not shown). Particles were also washed with HF instead of HNO_3 and by-products were also removed successfully, and the platelets did not appear damaged under SEM (not shown). Compared to HF, handling HNO_3 is easier from a health and environmental standpoint and therefore, HNO_3 was selected for further use.

The used concentrations and contact times for HNO_3 are presented in Table 10. The samples after HNO_3-treatment and water washing were examined by SEM (Figure 24) and XRD (Figure 25). For the systematic investigation of the effect of the washing agent (HNO_3), 3 batches of $Bi_4Ti_3O_{12}$ platelets were prepared and mixed (10 g). Afterwards, the powder was divided into 10 samples (approx. 100 mg each) and washed by soaking the powder in washing agent for a defined time as shown in Table 10. For the comparison of phase purity and morphology, one sample was washed only with deionized water. In this investigation, the reduced amount of the washing agent (20 ml instead of 40 ml) was used, because also the amount of $Bi_4Ti_3O_{12}$ platelets was lower in comparison to as-prepared batches, however, the concentration was still not the same as in further/normal/usual experiments. Using higher concentrations (4 mol/L HNO_3) caused the dissolution of the product particles, not only the removal of the secondary phases, so it was necessary to use a lower concentration of the acid. After HNO_3 treatment and water washing, the samples were freeze-dried, because the preliminary experiments showed fluffier and less agglomerated powders after freeze-drying in comparison to dying in the dryer chamber at elevated temperatures (60 °C – 100 °C).

Table 10: Used washing agents for the removal of secondary phases after $Bi_4Ti_3O_{12}$ synthesis in molten salt. Volume of added washing agent was 20 ml in all experiments.

Sample	Washing agent	Molarity (mol/l)	Contact time (min)	BET (m^2/g)
BIT-0-0	H_2O	/	15	3
BIT-1-5	HNO_3	1	5	3
BIT-1-15	HNO_3	1	15	3
BIT-2-1	HNO_3	2	1	3
BIT-2-10	HNO_3	2	10	2
BIT-2-30	HNO_3	2	30	3
BIT-3-15	HNO_3	3	15	3

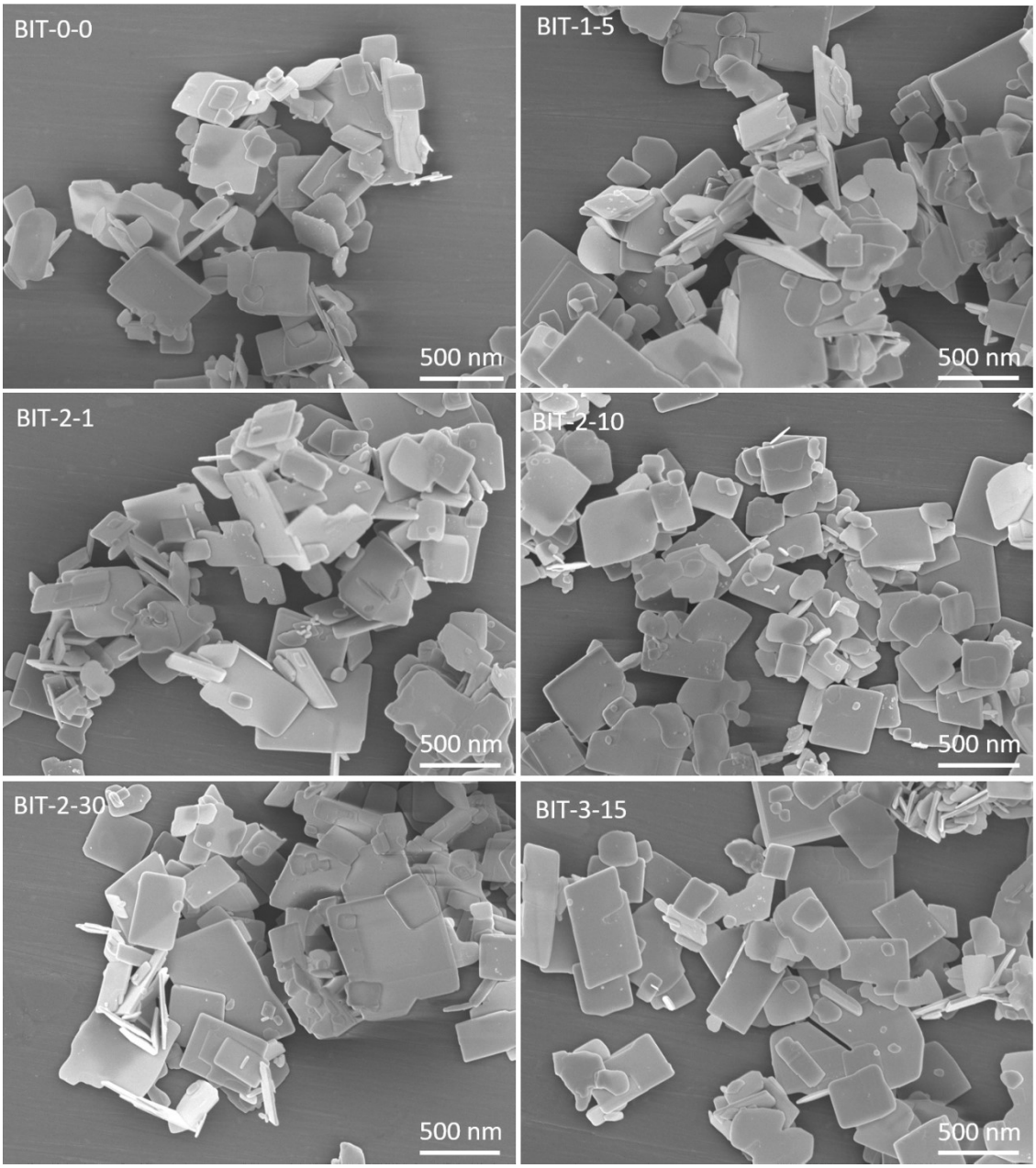

Figure 24: SEM micrographs of $Bi_4Ti_3O_{12}$ platelets after different washing procedures with HNO_3 acid as presented in Table 10.

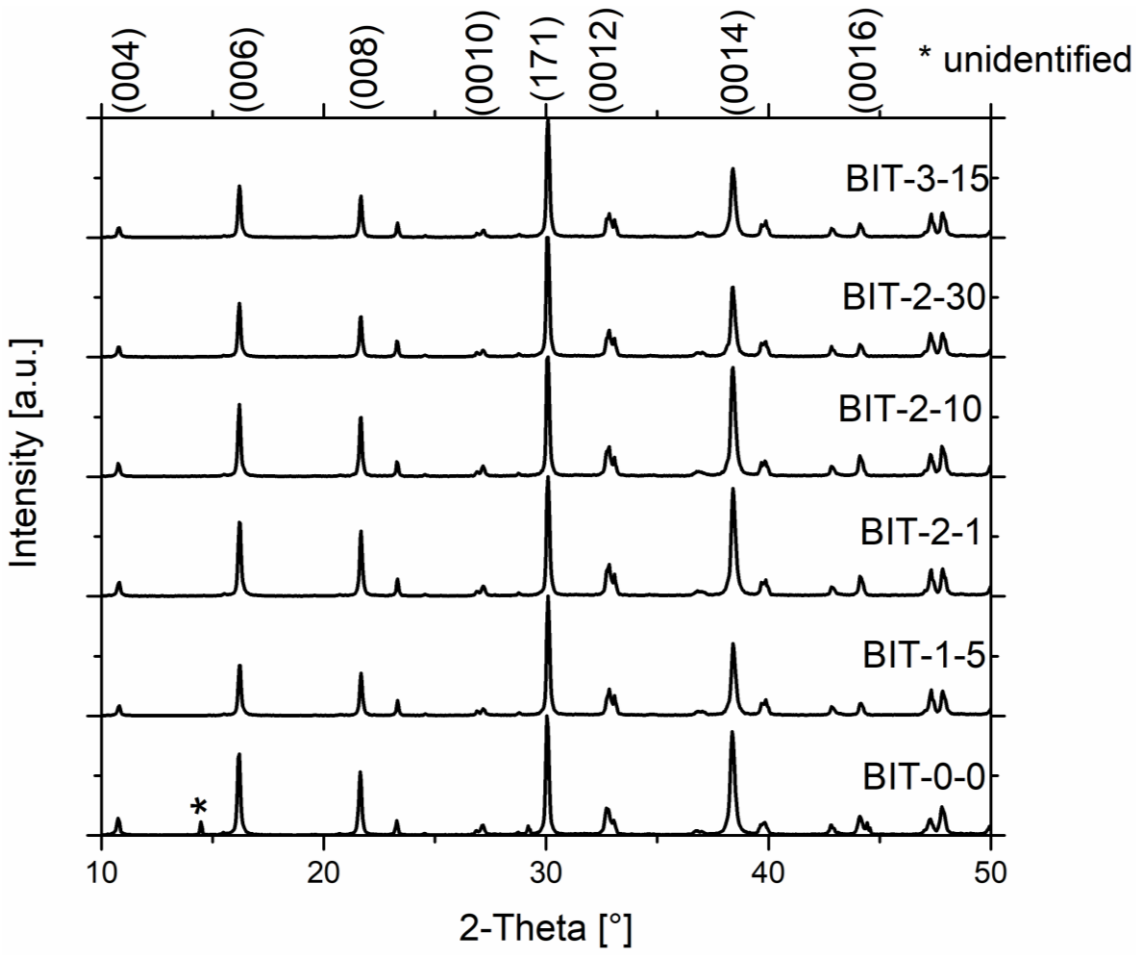

Figure 25: XRD patterns of $Bi_4Ti_3O_{12}$ platelets after different washing procedures with HNO_3 acid as presented in Table 10.

Template platelets were also examined under HR-STEM before and after washing with HNO_3 to observe the changes on the atomic scale. In Figure 26, typical $Bi_4Ti_3O_{12}$ platelets after H_2O washing (A) and after additional washing with 2 mol/L HNO_3 (B and C) in cross-sectional view are presented. STEM revealed that after washing the platelets only with water, the platelets are surrounded with an amorphous phase (Figure 26 A). The amorphous phase was not present anymore after the platelets were washed also with HNO_3. In addition, the platelets in both cases show bismuth oxide $[Bi_2O_2]^{2+}$ layer termination (described in more detail later in 4.1.3).

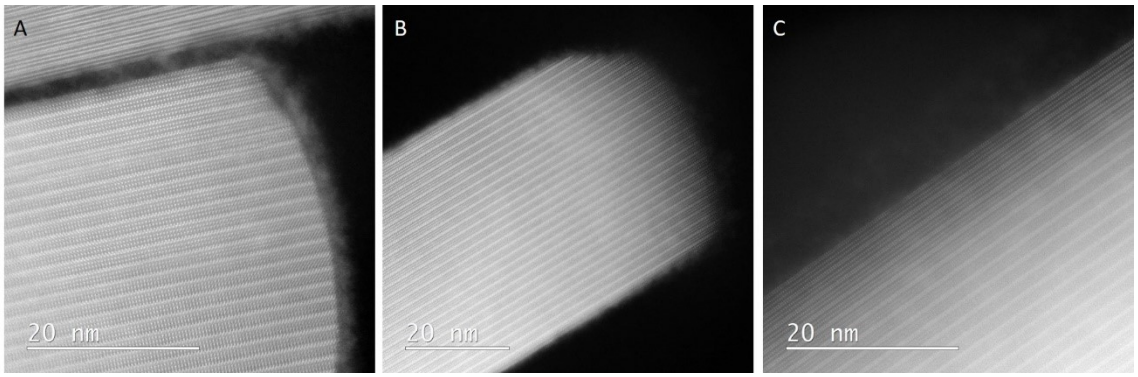

Figure 26: HR STEM micrographs of $Bi_4Ti_3O_{12}$ platelets in cross-sectional view after H_2O washing (A) and HNO_3 washing (B and C).

4.1.2.2 Some characteristics of the selected $Bi_4Ti_3O_{12}$ platelets: Photocatalytic activity for Rhodamine B dye degradation and phase transition behavior

The size of the $Bi_4Ti_3O_{12}$ platelets is expected to influence their functional properties. For two samples with significantly different size of the product platelets (BIT1 and BIT8 from Table 8), the specific surface area (BET), the photocatalytic activity (PA) and the DSC measurements were performed to evaluate how the size of the platelets influences these platelets' characteristics. For these measurements, BIT1 (smaller) and BIT8 (larger) $Bi_4Ti_3O_{12}$ plates were selected (Table 8). The BET results correlated with the SEM observations; the larger BET values were obtained for BIT1 than for BIT8 (Table 11). BIT1 particles were smaller, and consequently, the specific surface area was larger than for BIT8.

Factors such as surface defects, particle size, morphology, crystallinity, and band gap influence photocatalytic activity. Therefore, BIT1 and BIT8 were tested for their capability to degrade Rhodamine B (RhB) under UV-A light irradiation. For photocatalysis, defects are beneficial to some extent, because they introduce intermediate surface states that narrow the band gap. But a high density of defects, which act as recombination centers for photo-induced electrons and holes, lowered the photocatalytic activity. Moreover, high concentration is not beneficial for epitaxial growth, which we wanted to achieve in the next step. After 4 hours of irradiation with UV-a light, 88 % of RhB was degraded with BIT1 and 65 % with BIT8. This result confirmed the assumption that the photocatalytic activity of BIT1 is larger than that of BIT8, since smaller particles with a higher specific surface area provide a greater number of active sites for the photocatalytic reaction and consequently lead to higher degradation rates.

The same samples (BIT1 and BIT8) were used for the DSC study. The DSC measurements revealed that ferroelectric-to-paraelectric phase transition for both samples occurs at similar temperatures, i.e. 643.6 °C for BIT1 and 642.9 °C for BIT8 (Figure 27). However, the samples differed in absolute values of the phase-transition enthalpies, i.e. $|\Delta H_{FET}|$ for BIT was 1.457 J/g and for BIT8 it was 4.555 J/g (Table 11). The same correlation of the phase-transition enthalpy and particle size was also observed for $BaTiO_3$ [231]. Taking into account that the enthalpy of the phase transition is proportional to the polarization (P) ($\Delta H_{FET} = 2\pi P^2 T_c / C$ (Eq. 1), where C is the Curie-Weiss constant), the decrease of $|\Delta H_{FET}|$ could be explained by the decrease of P. It is also known that the phase-transition enthalpy is related to the domain structure [231], [232]. The larger $|\Delta H_{FET}|$ of BIT8 could correlate with larger particles and be expected to exhibit a multi-domain structure. Due to the domain clamping, the enthalpy of the phase transition was higher for larger platelets compared to the single-domain smaller platelets. In addition, with a decrease of the platelets' size, the ratio between the disordered surface and the ordered bulk is increasing, which additionally causes a destruction of the polar state, which consequently decreases the enthalpy of the ferroelectric-paraelectric phase transition [231].

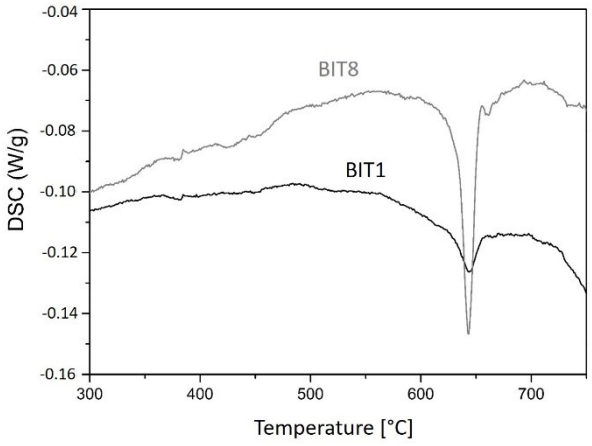

Figure 27: DSC curves of BIT1 (smaller platelets) and BIT8 (larger platelets) during heating.

Table 11: Summarized BET values and results of DSC and PA measurements for BIT1 and BIT8.

Sample	BET (m^2/g)	Tc (°C)	$\lvert\Delta H_{FET}\rvert$ (J/g)	PA4 hours
BIT1	3	643.6	1.457	88.6 %
BIT8	1	642.9	4.555	65.0 %

4.1.3 Compositional and structural studies of $Bi_4Ti_3O_{12}$ template platelets

$Bi_4Ti_3O_{12}$ in the hydrothermal topochemical conversion to $ATiO_3/Bi_4Ti_3O_{12}$ and $ATiO_3$ (A=**Sr**, Ba, Ca) serves as a template. For a better understanding of this transformation process, atomic-scale insight into template characteristics was needed. For this reason, $Bi_4Ti_3O_{12}$ platelets were characterized down to the atomic scale by scanning transmission microscope (STEM). The platelets were analyzed in cross-section to obtain information about the platelets' termination and distribution of the layers' parallel to the basal surface plane.

Observations of the thinned edge-on oriented $Bi_4Ti_3O_{12}$ platelets at lower magnifications showed that the thickness of the platelets varies from 50 nm-70 nm (Figure 28). Furthermore, it is also evident that the basal-plane surface of the $Bi_4Ti_3O_{12}$ platelets is quite well atomically flat on a large scale (Figure 28 C and D). High magnification STEM along [100] and [110] $Bi_4Ti_3O_{12}$ zone axes (Figure 28) disclosed single crystalline layered structure of the platelet with alternation of pseudoperovskite $[Bi_2Ti_3O_{10}]^{2-}$ blocks and bismuth oxide $[Bi_2O_2]^{2+}$ layers, whereby the latter exclusively terminates the basal surface planes of the as-prepared $Bi_4Ti_3O_{12}$ platelets. Termination with $[Bi_2O_2]^{2+}$ layer remains also after washing of the product powder with 2 mol/L HNO_3 to remove secondary phases. On the contrary, at the lateral surfaces of the platelets, both types of structural units ($[Bi_2Ti_3O_{10}]^{2-}$ and $[Bi_2O_2]^{2+}$) are exposed (Figure 28 D and E). These differences between the basal and lateral surfaces are the result of layer-by-layer growth and presumably influence different dissolution rates of the $Bi_4Ti_3O_{12}$ platelets along different crystallographic orientations. The hydrothermal topochemical conversion is performed in a highly alkaline solution (6 mol/L NaOH) under elevated pressure and temperature, which could modify the surface by etching or incongruent dissolution.

The solubility of $Bi_4Ti_3O_{12}$ platelets in 6 mol/L NaOH at 25 °C is not high. However, it is different at higher temperatures such as reaction temperature of 200 °C (Figure 29 and Figure 30). To investigate what happens to $Bi_4Ti_3O_{12}$ platelets in 6 mol/L NaOH at 200 °C, $Bi_4Ti_3O_{12}$ platelets were exposed to 6 mol/L NaOH and temperature of 200 °C for 1 hour in the high-pressure reactor (Figure 29). After SEM and XRD observations (Figure 31, blue curve), it could be concluded that the particles did not change. However, a closer look under HR STEM revealed some important changes. The most important information that is clear from HR STEM image is change of termination. While as-prepared $Bi_4Ti_3O_{12}$ platelets were exclusively terminated by $[Bi_2O_2]^{2+}$ layer, $Bi_4Ti_3O_{12}$ platelets exposed to 6 mol/L NaOH solution and 200 °C were terminated with pseudoperovskite $[Bi_2Ti_3O_{10}]^{2-}$ layer. To test the stability of such particles that are exposed to elevated pressure and 200 °C, the platelets were treated in 6 mol/L NaOH at 200 °C for 15 hours [233]. Even after that time, the platelets did not significantly change the dimensions. Small deterioration of the lateral surfaces was observed by SEM. All these indicate that the solubility of $Bi_4Ti_3O_{12}$ in 6 mol/L NaOH solution at 200° C is low [233], [234].

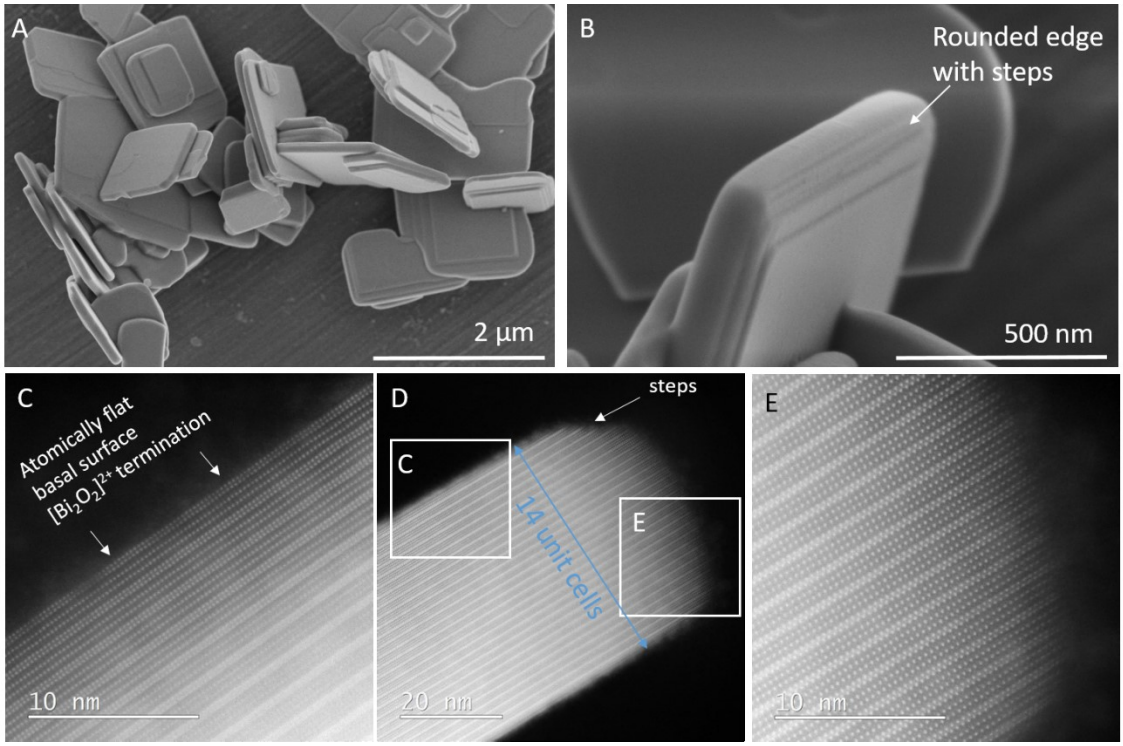

Figure 28: $Bi_4Ti_3O_{12}$ template platelets under scanning electron microscope (A and B) showing the typical morphology of particles and atomic-resolved microscope (C, D: atomically flat basal surface with bismuth oxide termination and the rounded edge with the steps and exposed both types of structural units: $[Bi_2Ti_3O_{10}]^{2-}$ and $[Bi_2O_2]^{2+}$ (D and E)).

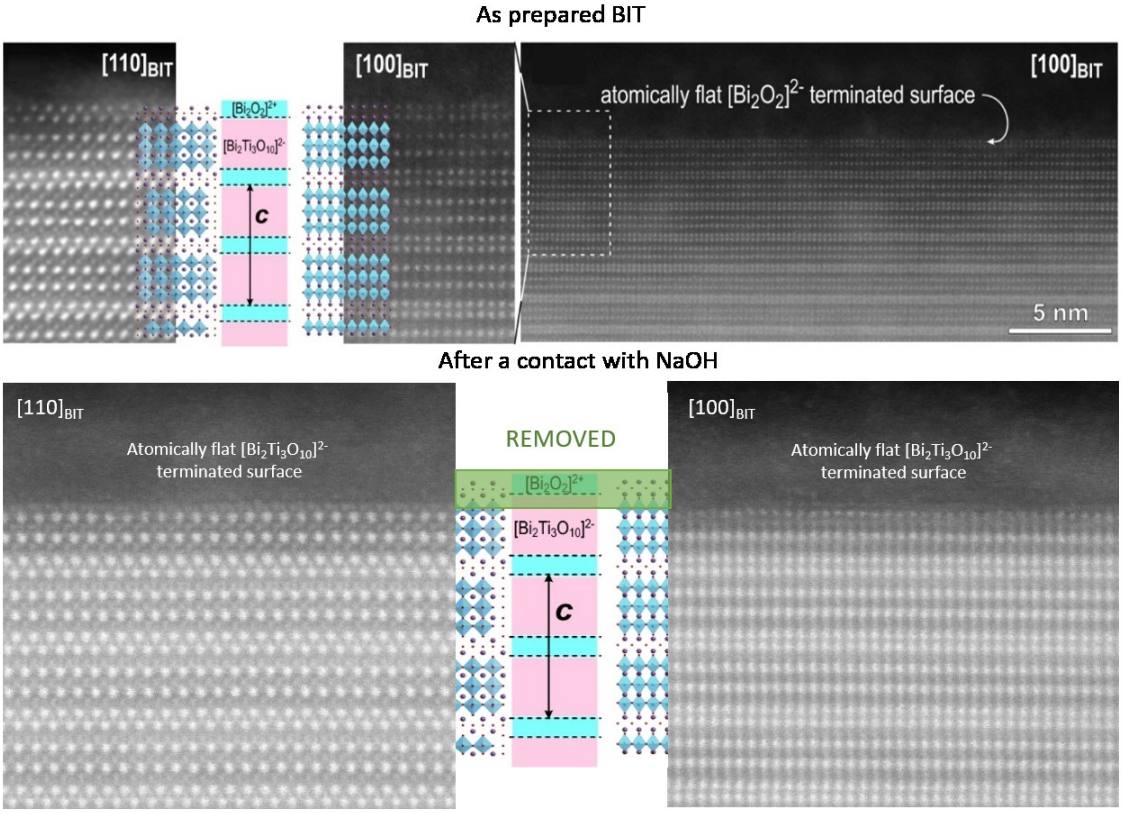

Figure 29: Termination of the $Bi_4Ti_3O_{12}$ platelets: as-prepared and after treatment in 6 mol/L NaOH at 200 °C.

Additionally, the system can also behave differently if strontium ions (Sr^{2+}) are present in the alkaline solution. Namely, as explained in Section 4.2.1, the $SrTiO_3$ formation is the driving force for further $Bi_4Ti_3O_{12}$ dissolution. To examine whether the change in termination occurs already at much lower temperature below 200 °C, an additional experiment was conducted. NaOH solution with the temperature of 70 °C was added to suspension of $Bi_4Ti_3O_{12}$ in water solution, containing high excess of $SrCl_2$ (Sr/Ti=12). The suspension was left in a sealed flask for 35 minutes in ambient conditions. Afterwards, the particles were washed with deionized water and 1 mol/L HNO_3. SEM and XRD examinations were done before and after HNO_3 washing. In this case, $SrCO_3$ was formed as a side-product and was removed after washing with nitric acid. The formation of $SrCO_3$ is undesirable during the transformation of $Bi_4Ti_3O_{12}$ to $SrTiO_3$ because it consumes strontium. The sample was examined also under STEM to see whether the $[Bi_2O_2]^{2+}$ layer is still the termination layer of the $Bi_4Ti_3O_{12}$ basal surface planes, or it is removed already at these mild conditions (70 °C, 6 mol/L NaOH, Sr/Ti=12). To get reliable information about the initial processes, several $Bi_4Ti_3O_1$ platelets that were previously dispersed in $SrCl_2$ water solution and added by hot (70 °C, 6 mol/L) NaOH solution, were examined by STEM from the cross-sectional view. HR-STEM disclosed partial dissolution of the $[Bi_2O_2]^{2+}$ termination layer. Some of the $Bi_4Ti_3O_{12}$ platelets still preserve $[Bi_2O_2]^{2+}$ termination, while the others are already terminated by pseudoperovskite block. Presumably, $[Bi_2O_2]^{2+}$ layer and pseudoperovskite $[Bi_2Ti_3O_{10}]^{2-}$ layer dissolve incongruently. The STEM examinations shown evidently prove that $[Bi_2O_2]^{2+}$ layer dissolves before the nucleation of $SrTiO_3$, therefore, in the process of the topochemical conversion $SrTiO_3$ starts to grow on the pseudoperovskite $[Bi_2Ti_3O_{10}]^{2-}$ layer. The majority of the $Bi_4Ti_3O_{12}$ platelets have mixed termination. This means that at some points on the surface, $[Bi_2O_2]^{2+}$ layer is removed, on the other part of the platelets' surface it is still present. Imperfections such as dislocations and steps were found to be the most common starting points for the dissolution of the $Bi_4Ti_3O_{12}$ platelets (Figure 30 G). Thus, the addition of hot NaOH solution (60 °C – 70 °C) in the presence of $SrCl_2$ significantly increases the surface roughness of growing $SrTiO_3$ compared to the synthesis procedure starting from cold (25 °C) NaOH solution (see Section 4.4). This result implies that the processes ($Bi_4Ti_3O_{12}$ dissolution, $SrTiO_3$ nucleation) start much below 200 °C.

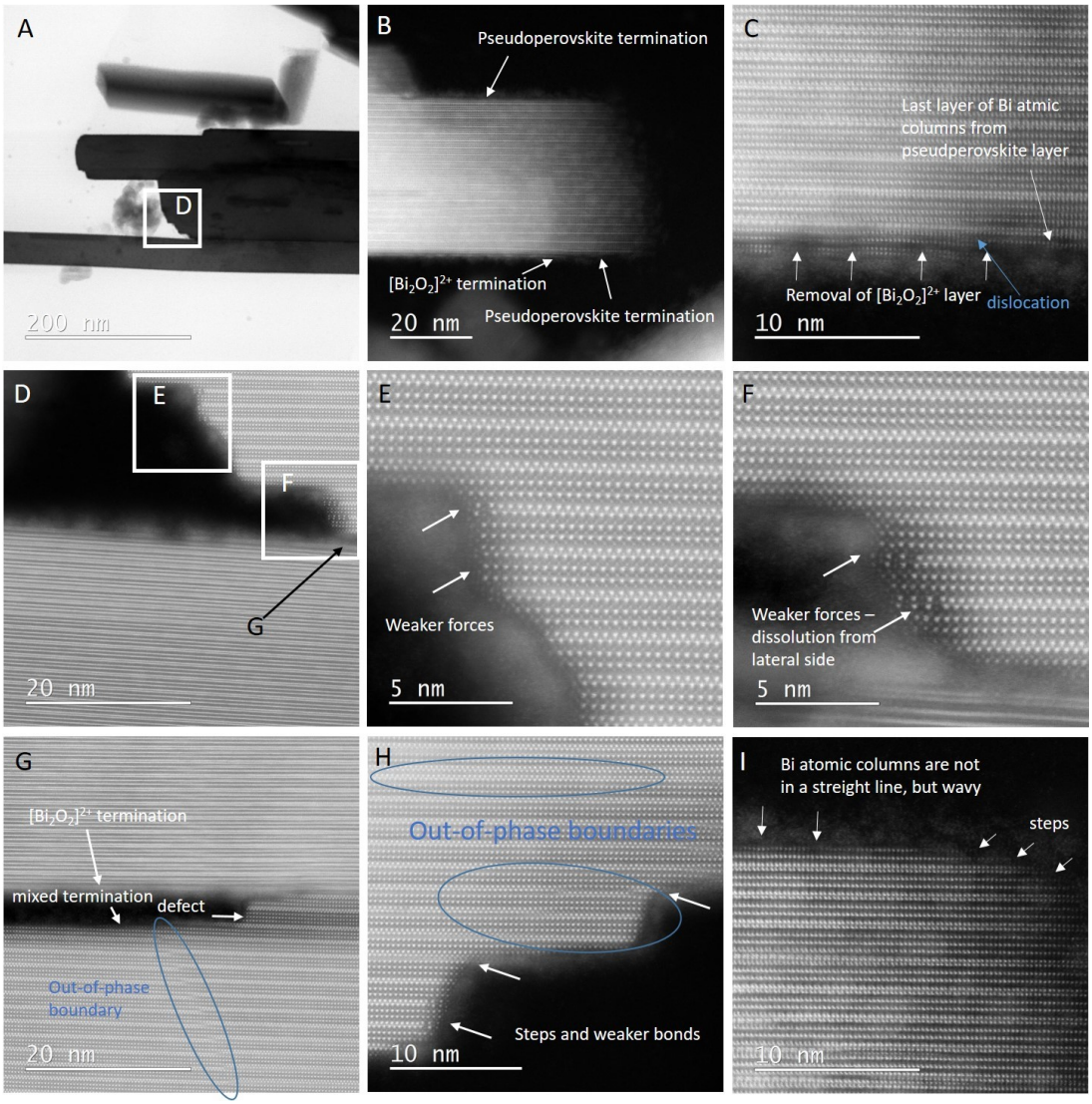

Figure 30: STEM images of cross-sectional analysis of $Bi_4Ti_3O_{12}$ platelets soaked in hot 6 mol/L NaOH solution in the presence of $SrCl_2$.

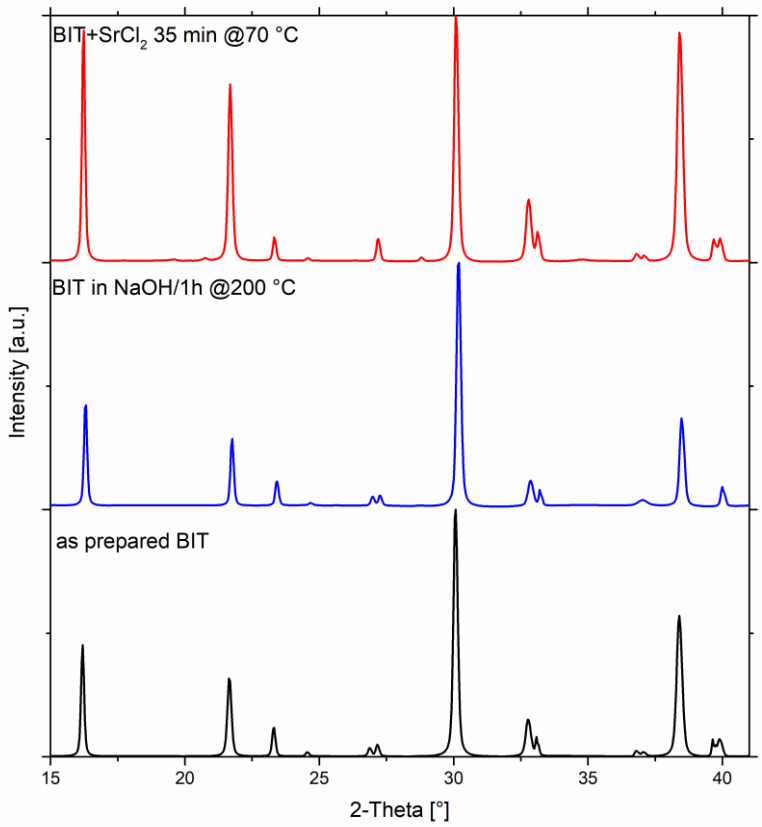

Figure 31: Powder XRD patterns of $Bi_4Ti_3O_{12}$ platelets: as-prepared (black), dispersed in 6 mol/L NaOH and heated to 200 °C for 1 hour in high pressure reactor (blue) and $Bi_4Ti_3O_{12}$ particles, soaked in 6 mol/L NaOH with the temperature of 70 °C for 35 minutes (red). All samples were washed with D.I. water and 1 mol/L HNO_3 after treatment and prior to XRD examination. All XRD diffractions correspond to $Bi_4Ti_3O_{12}$ (pdf: 01-072-1019).

4.2 Topochemical Conversion of $Bi_4Ti_3O_{12}$ Platelets to $SrTiO_3$ Platelets under Hydrothermal Conditions

$Bi_4Ti_3O_{12}$ and $SrTiO_3$ have similar structural elements that potentially allow epitaxial growth of one phase on the other. Therefore, $Bi_4Ti_3O_{12}$ platelets were selected as a template for the preparation of plate-like $SrTiO_3$ particles. Topochemical transformations from similar Aurivillius phase precursors to various perovskite titanates ($ATiO_3$, A= Ca, Sr, Ba) that were already reported in the literature were mostly performed in molten salt [45], [47], [82], [83], [113], [235]–[237]. Such reactions occur at higher temperatures (800 °C – 1200 °C) and consume more energy in comparison to reactions under hydrothermal and solvothermal conditions (100 °C – 200 °C). Also, most commonly, the reactions were performed in more steps to preserve the plate-like shape of the template. The presented one-step hydrothermal topochemical conversion is therefore the novelty in the field and is supported by a detailed study of the mechanism. Furthermore, we have explored the possibilities to control the reaction pathway and to tune the morphology.

4.2.1 The background of the $SrTiO_3$ formation and the selection of reaction conditions

Thermodynamic modelling for hydrothermal formation of $SrTiO_3$ from simple TiO_2 precursors was done by Lencka and Riman, who calculated a phase-stability diagram for the Sr-Ti-H_2O hydrothermal system of anatase and hydrous TiO_2 gel [118], [238]. The diagram was extended to rutile by Kalyani and colleagues [30], [48]. Knaus and colleagues measured the solubility of rutile over a pH range from 1 to 13 from 100 °C to 300 °C, modeled obtained data using different hydrolysis species and determined the hydrolysis constants [239]. Sr-Ti-H_2O stability diagram shows that the formation of $SrTiO_3$ requires alkaline pH. The required pH for $SrTiO_3$ formation increases with decreasing Sr concentration. TiO_2 solubility and the formation of the predominant aqueous titanium species is strongly dependent on the temperature and pH [55], [118], [239]. Excess mineralizer (typically KOH or NaOH) is used to ensure alkaline pH for $SrTiO_3$ formation. Additional impact on the pH comes from the strontium source. Namely, solubility of the salt also influences the pH of the solution. $Sr(NO_3)_2$ is easily soluble and nearly neutral to the pH changes [118]. On the contrary, the solubility of $Sr(OH)_2$ is lower, and it tends to precipitate to $Sr(OH)_2$ or $Sr(OH)_2{\cdot}8H_2O$. Moreover, high pH range promotes the formation of $SrCO_3$, therefore the use of glovebox or working in N_2 atmosphere are recommended. If the chemicals are not clean enough, the formation of $SrCO_3$ cannot be fully avoided with either of the approaches. Nevertheless, by providing excessive Sr^{2+} ions, formation of $SrCO_3$ in the synthesis of $SrTiO_3$ is not problematic, because $SrCO_3$ can be easily removed through dissolution with weak acid (e.g. diluted CH_3COOH).

Similar thermodynamic modelling for hydrothermal formation of $SrTiO_3$ from complex titanate precursors such as $Bi_4Ti_3O_{12}$ is hampered by the lack of thermodynamic data, which limits the theoretical predictions for $Bi_4Ti_3O_{12}$ dissolution and formation of equilibrium compounds ($SrTiO_3$, Bi_2O_3, $Bi_{12}TiO_{20}$) under hydrothermal conditions as a function of the physical-chemical conditions, i.e. pH, reaction temperature, ions concentrations. Based on the known chemistries of the initial precursors ($Bi_4Ti_3O_{12}$, $SrCl_2$) in alkaline media, the following reactions can be envisaged. $SrCl_2$ exhibits high solubility in aqueous media at room temperature. Under alkaline conditions, dissolved Sr^{2+} ions precipitate as $Sr(OH)_2$, but with the increase of temperature to 100 °C or even up to 300 °C, this compound becomes highly soluble [118]. $Bi_4Ti_3O_{12}$ platelets are expected to dissolve in alkaline hydrothermal media according to the equation:

$$Bi_4Ti_3O_{12} + 12H_2O + 6OH^- \rightleftharpoons 4Bi(OH)_3 + 3Ti(OH)_6^{2-} \quad (10)$$

In the presence of dissolved Sr^{2+} and $Ti(OH)_6^{2-}$ species, $SrTiO_3$ starts to precipitate according to the equation:

$$Ti(OH)_6^{2-}(aq) + Sr^{2+}(aq) \rightarrow SrTiO_3(s) + 3H_2O(l) \quad (11)$$

In the presence of dissolved CO_2, $SrCO_3$ also forms in small quantities:

$$Sr(OH)_2(aq) + CO_2(g) \rightarrow SrCO_3(s) + H_2O(l) \quad (12)$$

In general, the formation of $SrTiO_3$ is expected to be the main reaction. Considering structural similarities between $SrTiO_3$ and $Bi_4Ti_3O_{12}$, precipitation of $SrTiO_3$ on the $Bi_4Ti_3O_{12}$ might be foreseen. The first experimental conditions for the hydrothermal topochemical transformation of $Bi_4Ti_3O_{12}$ to $SrTiO_3$ were selected based on the existing literature, including thermodynamic modeling of the $SrTiO_3$ crystallization from TiO_2 and empirical studies of $SrTiO_3$ growth on

various titanate precursors [30], [48], [118], [238], [239]. $Bi_4Ti_3O_{12}$ platelets can serve as a template in the topochemical transformation when their dissolution is slow enough. At the same time, a low concentration of $Bi_4Ti_3O_{12}$ was used to keep the concentration of dissolved Bi-O-based species low and thus to avoid the supersaturation for precipitation of bismuth titanates. On the contrary, high excess of $SrCl_2$ was used in order to achieve that dissolved $Ti(OH)_6^{2-}$ were exclusively used for the nucleation of $SrTiO_3$. The crystallographic matching between the $Bi_4Ti_3O_{12}$ (template) and $SrTiO_3$ (product) together with the supersaturation plays an important role in reaction mechanism and consequently determines the morphology of the final particles [30], [48].

First, influence of the reaction parameters was investigated, followed by the mechanism of the hydrothermal topochemical conversion of $Bi_4Ti_3O_{12}$ platelets to $SrTiO_3$. Finally, the interplay of crystallographic matching and supersaturation in the steering of the transformation pathway was investigated.

4.2.2 The impact of reaction parameters

First, the effect of a single parameter on the investigated system was tested. More precisely, what trend is shown by the increase or decrease in the values of the reaction parameters. The initial conditions were determined based on thermodynamic studies and previous research on hydrothermal syntheses of $ATiO_3$ perovskite particles. $Bi_4Ti_3O_{12}$ platelets were used as a titanium source and $SrCl_2 \cdot 6H_2O$ as a strontium source. Reactions were performed in high-pressure reactor Berghof BR100 with 60 % filling capacity, which corresponds to 120 mL of the solution. The time required for heating up to 200 °C is 75 minutes, and cooling down to room temperature takes 3 hours. The reaction time that is compared and discussed within this thesis is the time of exposure to the target temperature and does not include heating and cooling. However, the reaction takes place to some extent also in this period of time. In the end, the washing and drying procedure was also optimized.

4.2.2.1 $SrTiO_3$ formation from $Bi_4Ti_3O_{12}$ platelets with different size and aggregation stage

In the topochemical conversion, $Bi_4Ti_3O_{12}$ platelets are anticipated to serve as a template and also the source of $Ti(OH)_6$ species that form through the platelets dissolution (Eq. (10)). From the standpoint that the most common goal of particles synthesis is preparation of non-aggregated well-defined particles, well-separated $Bi_4Ti_3O_{12}$ platelets prepared from TiO_2 (P25) and Bi_2O_3 nanopowders are expected to be a more suitable template for the hydrothermal topochemical transformation into $SrTiO_3$ than aggregated smaller and less uniform-sized $Bi_4Ti_3O_{12}$ platelets prepared from large aggregates of anatase and rutile (see Chapter 4.1.1). Despite this, I still decided to study the transformations employing various $Bi_4Ti_3O_{12}$ templates with different morphological characteristics to better understand the principles for the steering of the transformation pathway. As it is shown in 4.1.1, different types of the TiO_2 precursors result in $Bi_4Ti_3O_{12}$ platelets that differ in terms of size distribution, aggregation, and surface defects. It is expected that all these $Bi_4Ti_3O_{12}$ template properties could then affect the success of the topochemical conversion to $SrTiO_3$ in terms of inherited morphology. Transformation of non-aggregated defect free $Bi_4Ti_3O_{12}$ platelets is anticipated to lead to $SrTiO_3$ platelets with better preserved platelet shape. Nevertheless, the $Bi_4Ti_3O_{12}$ platelets with broader morphological characteristics were employed to find out whether it is possible to overcome the imperfections of $Bi_4Ti_3O_{12}$ platelets and maintain the platelet shape in the transformation process by selection of proper experimental conditions (e.g. higher excess of strontium ions). For this reason, two sets of experiments were performed for each type of the $Bi_4Ti_3O_{12}$ platelet. These templates were subjected to the transformation at moderate (i.e. Sr/Ti=3 and 4 mol/L NaOH) and high (i.e. Sr/Ti=12 and 6 mol/L NaOH) excess of strontium salt and base concentration. Considering Eq. (11) – that higher excess of Sr^{2+} and higher base concentration would lead to a higher concentration of dissolved Sr^{2+} and $Ti(OH)_6^{2-}$, respectively, the above-mentioned experimental settings could be denoted also as moderate (Sr/Ti=3, 4 mol/L NaOH) and high supersaturation (Sr/Ti=12, 6 mol/L NaOH) conditions.

For the nucleation of $SrTiO_3$ on the $Bi_4Ti_3O_{12}$ platelets, defect-free $Bi_4Ti_3O_{12}$ template platelets provide the lowest nucleation barrier due to the lowest interfacial free energy that originates from lattice mismatch without additional contributions due to defects. Among various $Bi_4Ti_3O_{12}$ platelets, prepared from different TiO_2 precursors, this ideal was best approached by the platelets that were synthesized from Bi_2O_3 and TiO_2 (P25) nanopowders (Figure 19D, Figure 23 (BIT8) and Figure 26 B, C). XRD and SEM in Figure 32 and Figure 33, respectively, show that under both moderate and high supersaturation conditions, this kind of $Bi_4Ti_3O_{12}$ transformed to (100)-oriented $SrTiO_3$ platelets with almost fully preserved shape of $Bi_4Ti_3O_{12}$ template platelets. The

highest intensities of the (100) and (200) $SrTiO_3$ diffractions in the XRD patterns of the platelets cast on Si-single-crystalline substrate (Figure 32, blue curves) show that the platelets are well separated and oriented with (h00) planes parallel to the substrate. In the XRD patterns of the 12-hour-transformation products obtained at moderate supersaturation conditions (Sr/Ti=3, 4 mol/L NaOH)from the other two $Bi_4Ti_3O_{12}$ (synthesized from aggregated anatase and rutile) also other diffractions of $SrTiO_3$ ((110), (111)) were present (Figure 32 A and B red and black curves). These diffractions are a clear indication for randomly oriented $SrTiO_3$ particles in the aggregates. This was confirmed by SEM, which showed the formation of aggregated $SrTiO_3$ nanocubes, which did not resemble the template platelet shape (Figure 33). Presumably, in the case of these less ideal $Bi_4Ti_3O_{12}$ templates, there is a larger interfacial contribution and therefore, activation energy for nucleation of $SrTiO_3$ on $Bi_4Ti_3O_{12}$ is larger. As a result, formation of $SrTiO_3$ layer over the basal surface planes of such $Bi_4Ti_3O_{12}$ platelets is not fast enough to protect the dissolution of the platelets from the top and consequently the platelet shape is not preserved during transformation from $Bi_4Ti_3O_{12}$ to $SrTiO_3$. Moreover, as evident in Figure 32G, defects present the starting points for the $Bi_4Ti_3O_{12}$ dissolution. What about if the supersaturation is increased? Is it possible to overcome the template imperfections with an increase of supersaturation and promote $SrTiO_3$ layer-by layer growth? XRD patterns (Figure 32) show that the transformation reaction is slower in case of more aggregated template particles (from anatase and rutile) and the $Bi_4Ti_3O_{12}$ remains are still present in the product powder after a 12-hour reaction. The product particles are also more aggregated, which is visible from SEM images (Figure 33) as well as from XRD spectra on Si-single-crystalline substrate, through the presence of high intensity (110)- and (111)-diffractions of $SrTiO_3$ (Figure 32 B). SEM clearly shows that under high supersaturation conditions (Sr/Ti=12, 6 mol/L NaOH), the platelets' shape of the template is preserved also in the case of aggregated $Bi_4Ti_3O_{12}$ templates (formed from anatase and rutile) (Figure 33). This indicates that larger interfacial free energy which arises from $Bi_4Ti_3O_{12}$ platelets with more defective surface can be overcome by higher supersaturation conditions and in this way, the initial morphology of aggregated template platelets is preserved.

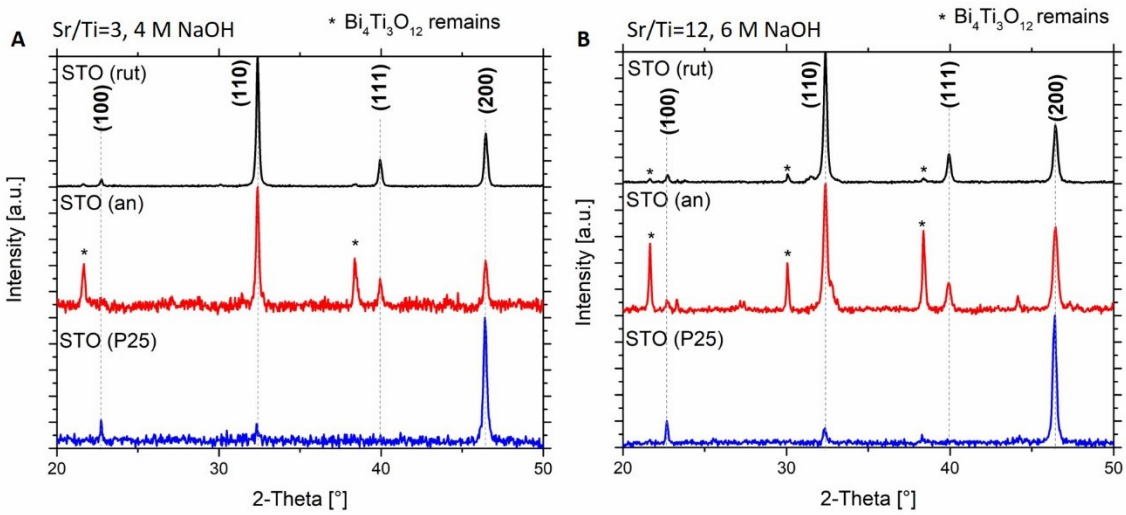

Figure 32: XRD of $SrTiO_3$ particles transformed from $Bi_4Ti_3O_{12}$ templates, obtained from different TiO_2 source – nanopowder P25 (blue), anatase (red) and rutile (black) at moderate supersaturation conditions (left: Sr/Ti=3, 4 mol/L NaOH) and high supersaturation conditions (right: Sr/Ti=12, 6 mol/L NaOH).

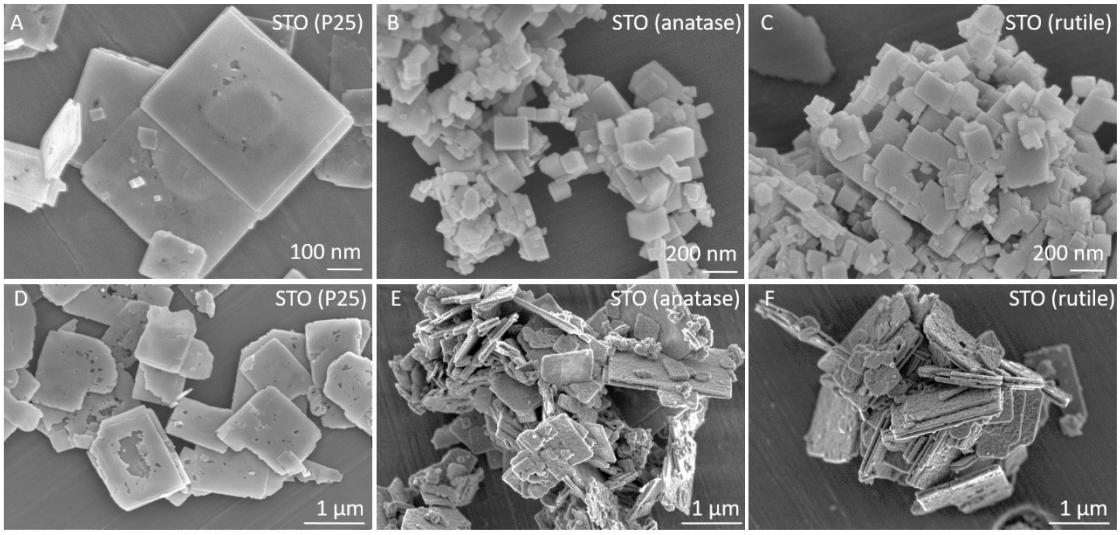

Figure 33: SEM of $SrTiO_3$ particles transformed from $Bi_4Ti_3O_{12}$ templates of different quality (different TiO_2 source) at moderate (Sr/Ti=3, 4 mol/L NaOH) supersaturation conditions (upper row) and high (Sr/Ti=12, 6 mol/L NaOH) supersaturation conditions (bottom row). Reaction conditions: 200 °C for 12 hours.

4.2.2.2 Strontium precursor

For the evaluation of the influence of strontium precursor, $SrCl_2$, $Sr(CH_3COO)_2$ and $Sr(NO_3)_2$ were used. The testing conditions for verification of the role of strontium precursor were performed at Sr/Ti=3, 4M NaOH and 200°C for 12 hours (Figure 34). In all the cases, $SrTiO_3$ particles resemble the templates shape. This indicates that all the tested salts can be used in the topochemical conversion of $Bi_4Ti_3O_{12}$ platelets to $SrTiO_3$ platelets. These experiments also show that anions (Cl^-, CH_3COO^-, NO_3^-) do not play any important role in the topochemical conversion reaction.

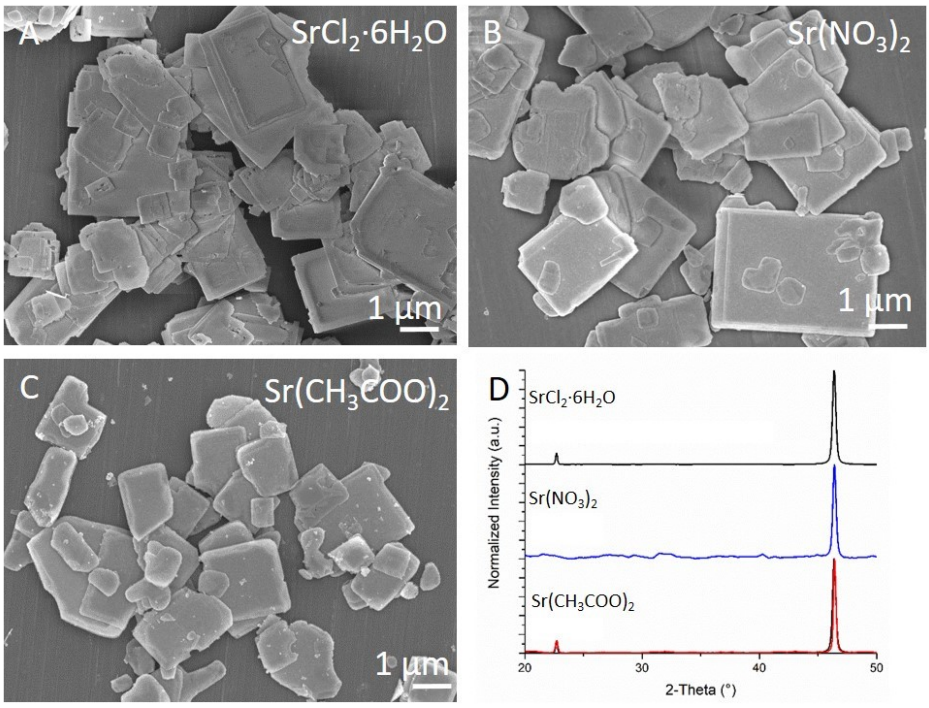

Figure 34: SEM micrographs of obtained $SrTiO_3$ platelets from different strontium sources: chloride (A), nitrate (B) and acetate (C) with their XRD patterns (D) of particles cast on Si-single crystalline substrate showing preferential (100) orientation. Samples were prepared with Sr/Ti=3 molar ratio, at 200 °C in 4 mol/L NaOH for 12 hours.

4.2.2.3 Stirring

Stirring is another important parameter, because it provides a more uniform concentration of all the solutes during the whole process. If the reaction mixture is not stirred during the reaction, the crystallization occurs under stagnant conditions. Thus, there is a higher probability that diffusion is the rate determining process of the transformation. Consequently, this can affect the reaction kinetics, mechanism, and product morphology. Therefore, the influence of stirring on the transformation from $Bi_4Ti_3O_{12}$ to $SrTiO_3$ was also investigated.

Two cases were compared: the first experiment was without stirring during the conversion, and the other was stirred for the whole time of the reaction with 250 rpm. All other conditions (reagent concentration, temperature) were the same. The results did not differ significantly, however the continuous stirring contributed to better preservation of the platelet morphology with a lower number of smaller holes.

4.2.2.4 Sr/Ti molar ratio

Presumably, it is important for the preservation of the template's shape that the nucleation of $SrTiO_3$ takes place rapidly and evenly over the entire basal surface. For this reason, an excess of strontium was used. The comparison of the reaction performed with stoichiometric Sr/Ti=1 initial molar ratio and with high excess of Sr (Sr/Ti=3, 6, 12 and 24) was performed. Results showed that when the reaction was done with stoichiometric ratio of Sr/Ti=1, the $SrTiO_3$ reaction product does not resemble the plate-like morphology. Most probably due to too low concentration of Sr^{2+} and in this case $Bi_4Ti_3O_{12}$ dissolves too fast. On the contrary, in the cases when Sr^{2+} excess was applied, the $SrTiO_3$ better resembled the plate-like morphology. The $SrTiO_3$ platelets prepared at different degrees of the Sr excess differ in the surface appearance. In the case of higher excess (Sr/Ti≥6), the platelets are rougher and more ruffled compared to the condition with Sr/Ti=3, when the platelets look smoother, but still not as smooth as original $Bi_4Ti_3O_{12}$ template platelets. The Sr/Ti molar ratio was found to have a significant (profound) influence on the conversion, therefore, it was separately investigated in more detail and this topic is presented in 4.2.4.

4.2.2.5 Reaction temperature

The temperature of hydrothermal reaction is also an important parameter, because it influences the $Bi_4Ti_3O_{12}$ dissolution rate (formation of $Ti(OH)_6^{2-}$) and also $SrTiO_3$ nucleation rate. To evaluate the effect of temperature on the transformation rate and morphological development, the reaction temperature was varied between 160 °C and 220 °C, while the other conditions were Sr/Ti=3 and 4 mol/L NaOH and the reaction time was 12 hours. At lower temperatures, the reaction was expected and confirmed with SEM and XRD (Figure 35) to proceed more slowly than at 200 °C – 220 °C. At the reaction temperature of 160 °C and 180 °C, the product did not result in pure $SrTiO_3$ particles even after 24 hours (not shown). On the other hand, reaction at 220 °C commonly produced frame-like $SrTiO_3$ particles even at shorter times, i.e. 3 hours or 6 hours (not shown). Due to the higher temperature, the dissolution of $Bi_4Ti_3O_{12}$ was too fast and the surface in the middle of the basal surface plane is not protected by $SrTiO_3$, and consequently, such product plate-like particles contain holes, resembling the frame-like shape.

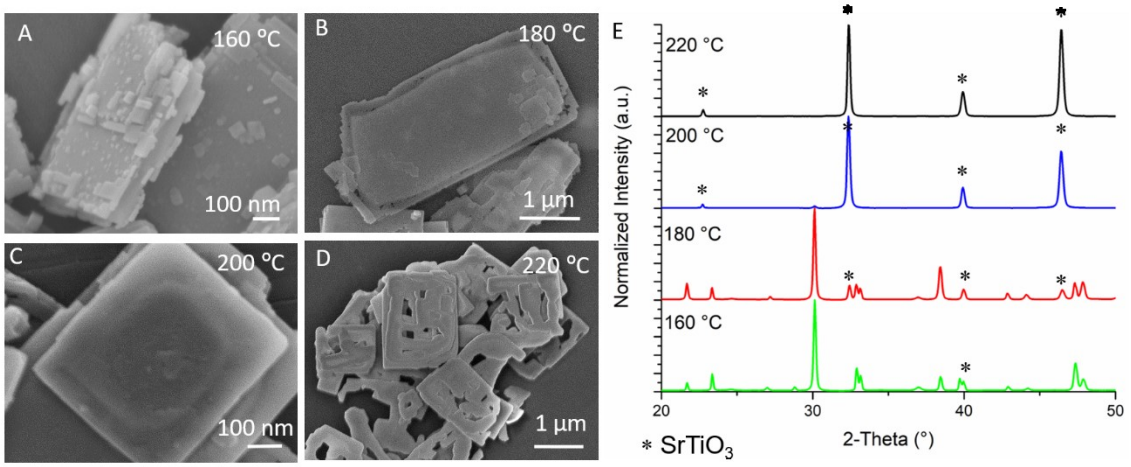

Figure 35: SEM micrographs (A-D) and powder XRD patterns of product particles of converted $Bi_4Ti_3O_{12}$ platelets to $SrTiO_3$ particles under hydrothermal conditions at 160 °C (A), 180 °C (B), 200 °C (C) and 220 °C, at Sr/Ti=3 molar ratio in 4 mol/L NaOH for 12 hours. $SrTiO_3$ diffractions are marked with a * sign, other belong to the $Bi_4Ti_3O_{12}$ phase.

4.2.2.6 NaOH concentration

As already explained in the beginning, the pH, (via NaOH concentration) plays an important role on the $Bi_4Ti_3O_{12}$ solubility. Therefore, different NaOH concentrations (2, 4 and 6 mol/L NaOH) were tested for the conditions with various Sr/Ti ratios (1, 3 and 12) at 200 °C. In 2 mol/L, NaOH $SrTiO_3$ was not pure phase nor after 24 hours with Sr/Ti=3. Moreover, the $SrTiO_3$ growth started at the edges of the $Bi_4Ti_3O_{12}$ platelets, but the frame breaks before the rest of the plate converted to $SrTiO_3$. The reaction products of the transformations in 4 mol/L and 6 mol/L NaOH were similar. In case of 4 mol/L NaOH negligible remains of $Bi_4Ti_3O_{12}$ were still present, while in 6 mol/L, the transformation into $SrTiO_3$ was complete with all selected Sr/Ti ratios. The influence of the NaOH concentration was found to be one of the two the most important factors that influence the conversion therefore, it was separately investigated in more detail and is presented in 4.2.4.

4.2.2.7 Addition of TiO_2

From the preliminary results, it was already obvious that nucleation of $SrTiO_3$ on the basal planes of the template must be rapid. Consequently, a large enough concentration of titanium ions must be present in the vicinity of the surface. Therefore, I tried to increase the concentration of available titanium ions in the solution by the addition of TiO_2 nanopowder to the reaction solution (2.5 %, 5 % and 10 % (molar) Ti excess with respect to needed Sr/Ti ratio in $SrTiO_3$). Unfortunately, these TiO_2 did not fully dissolve but acted like a seed which prefers the nucleation and growth of $SrTiO_3$ from the solution. As grown $SrTiO_3$ was in the shape of cubes and $SrTiO_3$ which anyway converted from $Bi_4Ti_3O_{12}$ was frame-like and rod-like (Figure 36).

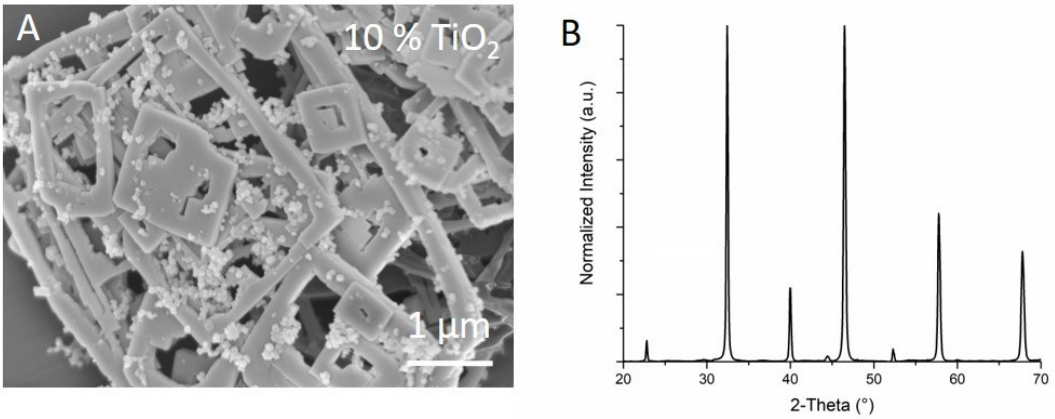

Figure 36: SEM micrograph (A) and powder XRD pattern (B) of product powder of $Bi_4Ti_3O_{12}$ template platelets converted to $SrTiO_3$ with the addition of TiO_2 nanopowder (10 % mol. excess Ti). Reaction conditions: 4 mol/L NaOH, temperature 200 °C and reaction time 12 hours.

4.2.2.8 Washing and drying

HNO_3 concentration, used for $SrTiO_3$ washing and the removal of the by-products (Bi_2O_3, $SrCO_3$) after the hydrothermal topochemical transformation, might influence the properties of $SrTiO_3$. Not enough concentrated HNO_3 may not remove all the by-products, while too concentrated acid may change the termination of $SrTiO_3$ plates and consequently modify the surface characteristics**.** Also, for drying two options were compared: air drying in the dryer and freeze drying. Powder obtained by freeze drying was fluffier and less aggregated. Therefore, it was the method of choice later in the research.

After hydrothermal reaction and natural cooling product particles were separated from the reaction solution by centrifugation at 7,500 rpm for 5 min/run and washed several times with distilled water. In the next step, the solid product was divided into 3 parts (into 3 centrifuges). Each part was soaked in 30 mL of HNO_3 with different concentrations (0.1 mol/L, 0.5 mol/L or 1 mol/L) for 5 min. Then, HNO_3-based solution was immediately separated from the particles by centrifugation and the remains of acid were removed by repeatable washing using distilled water. The particles were dried by freeze-drying according to the same procedure as $Bi_4Ti_3O_{12}$ particles. Dried $SrTiO_3$ samples were characterized by SEM (Figure 37) and XRD (Figure 38). As-prepared samples are denoted as STO1 (0.1 mol/L HNO_3), STO2 (0.5 mol/L HNO_3) and STO3 (1 mol/L HNO_3). The morphology of the $SrTiO_3$ particles is similar in all cases and it does not seem as if the 1 mol/L HNO_3 would harm/etched their surface more than 0.1 mol/L HNO_3. However, the XRD clearly shows that 0.1 mol/L and 0.5 mol/L HNO_3 does not remove $SrCO_3$ efficiently. Therefore, $SrTiO_3$ particles were treated in 1 mol/L HNO_3 to remove all by-products. In such a way, pure $SrTiO_3$ platelets were obtained.

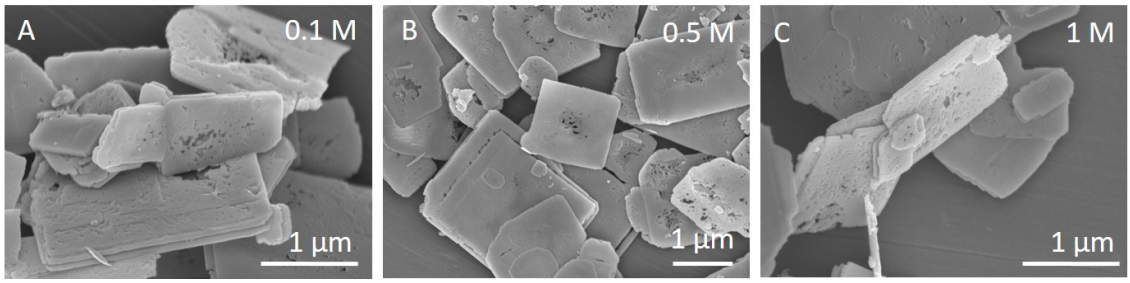

Figure 37: SEM micrographs of $SrTiO_3$ particles treated with different concentrations (0.1 mol/L, 0.5 mol/L and 1 mol/L) of HNO_3 after the synthesis.

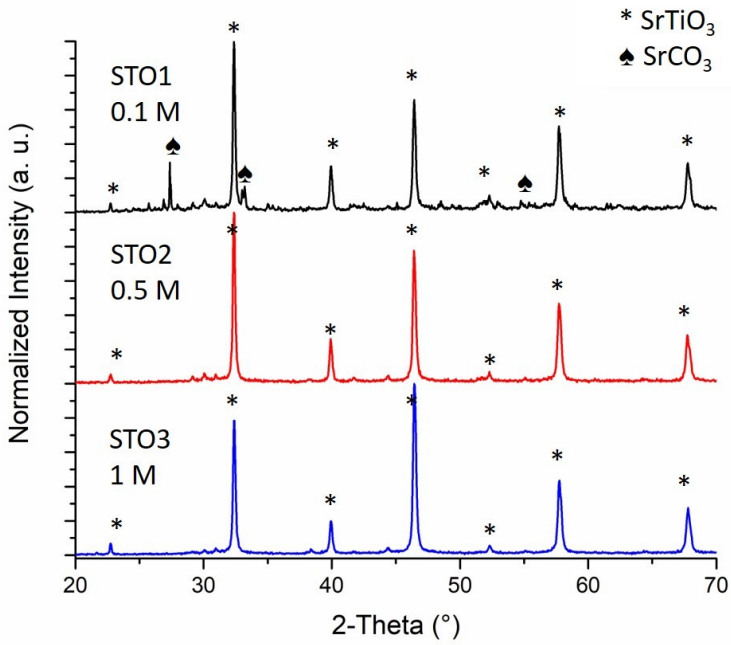

Figure 38: Powder XRD patterns of $SrTiO_3$ particles treated with different concentrations (0.1 mol/L, 0.5 mol/L and 1 mol/L) of HNO_3 after the synthesis. $SrCO_3$ diffractions were assigned with pdf card nr. 00-052-1526.

4.2.3 The topochemical conversion mechanism

In the hydrothermal topochemical conversion of $Bi_4Ti_3O_{12}$ to $SrTiO_3$, Ti^{4+} ions can be provided by $Bi_4Ti_3O_{12}$, and Sr^{2+} ions must be added by the other source – $SrCl_2 \cdot 6H_2O$ in this case. The epitaxial growth of $SrTiO_3$ on low-lattice-mismatch-single-crystalline $Bi_4Ti_3O_{12}$ substrate is expected to start taking place when the product of Sr^{2+} and $Ti(OH)_6^{2-}$ activities exceeds the solubility product, i.e. reaches the supersaturation conditions. The Sr^{2+} concentration is controlled by the amount of Sr-containing salt, i.e. $SrCl_2$ in this case. On the contrary, the concentration of $Ti(OH)_6^{2-}$ is controlled by the dissolution rate of $Bi_4Ti_3O_{12}$ in the reaction media.

To verify whether high enough $Ti(OH)_6^{2-}$ concentration for the precipitation of $SrTiO_3$ can be achieved already without the addition of a mineralizer, the experiment with aqueous solution of $SrCl_2$ and $Bi_4Ti_3O_{12}$ was performed. In this experiment, $Bi_4Ti_3O_{12}$ was dispersed in aqueous solution of $SrCl_2$ and heated to 200 °C for 15 hours. SEM analysis showed unchanged $Bi_4Ti_3O_{12}$ platelets (Figure 39). That the product was pure $Bi_4Ti_3O_{12}$ phase was confirmed also by XRD (Figure 39). It indicates that in aqueous solution (i.e. without the addition of the mineralizer), the dissolution of $Bi_4Ti_3O_{12}$ does not provide enough $Ti(OH)_6^{2-}$ to reach supersaturation for precipitation of $SrTiO_3$. This result is also supported by the study of Lencka and Riman who showed that $SrTiO_3$ precipitation requires alkaline pH [118].

The side-products carry valuable information about the reaction mechanism. Accordingly, powder XRD spectra (Figure 40) of water-washed reaction products provide information about the reactions occurring during the transformation.

The formation of $SrTiO_3$ is accompanied by the formation of $SrCO_3$ and Bi_2O_3 as the by-products of the reaction. These reaction products can also be envisaged from Equations (10) and (12) (page 59) $SrCO_3$ is the consequence of the reaction of $Sr(OH)_2$ with atmospheric CO_2. High excess of $SrCl_2$ and highly alkaline conditions (6 mol/L NaOH) lead to the formation of excessive $Sr(OH)_2$, which reacts with atmospheric CO_2 to $SrCO_3$. This reaction also takes place when the autoclave is opened after the synthesis and the content is exposed to air. Bi_2O_3 forms by condensation of $Bi(OH)_3$, which resulted from the $Bi_4Ti_3O_{12}$ dissolution [240]. By-products, Bi_2O_3 and $SrCO_3$, were removed by soaking the product powder in 1 mol/L HNO_3. No bismuth titanium compounds (e.g., $Bi_{12}TiO_{20}$) were detected, which proves that the dissolved titanium is consumed exclusively for the crystallization of $SrTiO_3$.

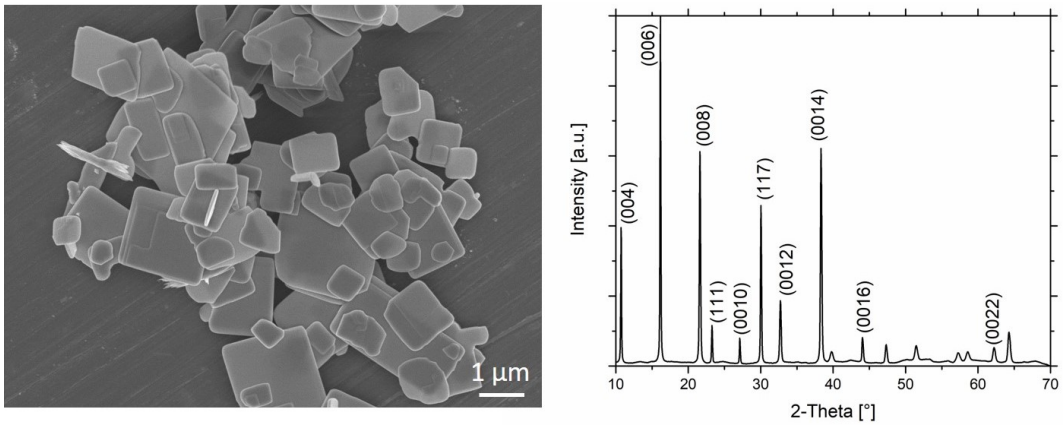

Figure 39: SEM image and powder-XRD pattern of the product powder obtained from $Bi_4Ti_3O_{12}$ platelets and $SrCl_2$ (Sr/Ti=12) in H_2O after 15 hours at 200 °C. According to PDF 01-072-1019 reference card, the product is pure $Bi_4Ti_3O_{12}$.

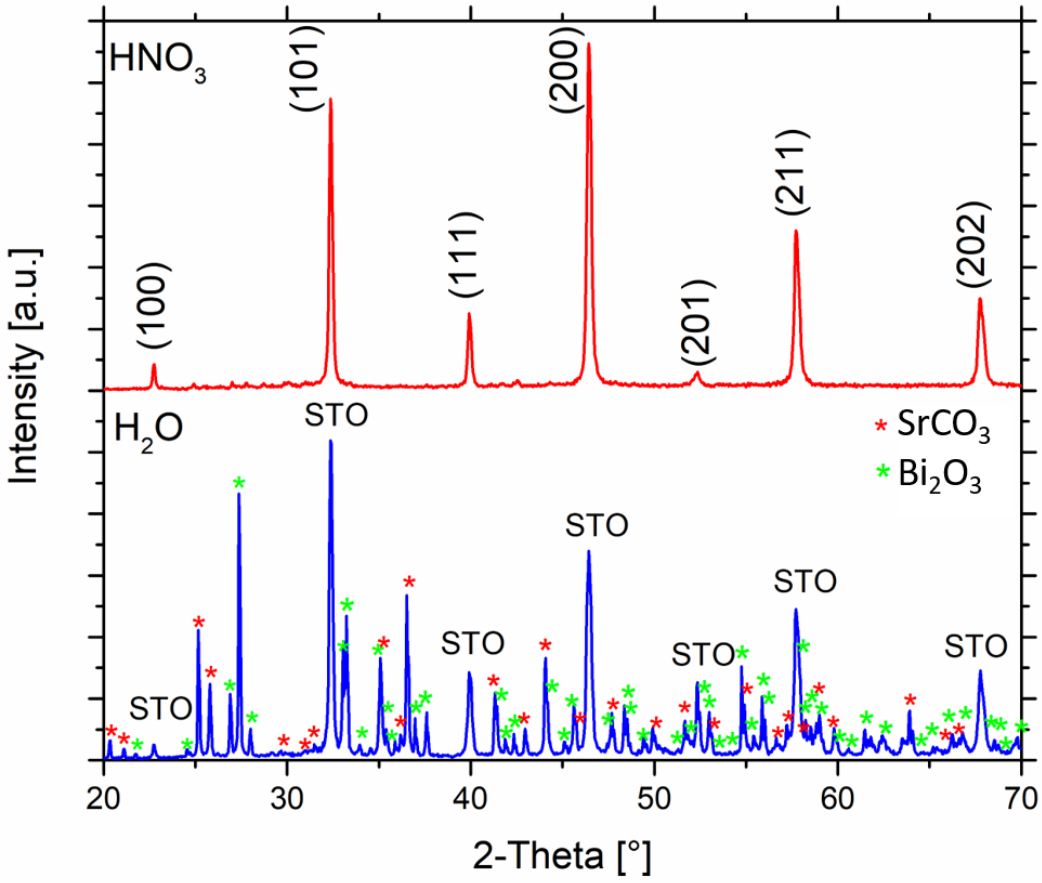

Figure 40: Powder-XRD patterns of $SrTiO_3$ (STO) sample after washing only with deionized water (blue) with identified by-products $SrCO_3$ and Bi_2O_3 and XRD pattern of the same sample after additional washing with 1 mol/L HNO_3 (red).

4.2.3.1 Time tracking of the conversion

To understand the mechanism of the hydrothermal topochemical conversion of $Bi_4Ti_3O_{12}$ platelets to $SrTiO_3$ platelets the reaction was interrupted at different reaction stages and the product was analyzed. The selected reaction conditions for this study are presented in Table 12. Holding time (might be referred to also as a reaction time) means the time of exposing the reaction mixture to the set reaction temperature (in this case 200 °C) and is not the actual reaction time, which includes also heating and cooling.

Table 12: The selected reaction conditions for the study of the mechanism of topochemical conversion of $Bi_4Ti_3O_{12}$ to $SrTiO_3$.

c($Bi_4Ti_3O_{12}$)	Sr/Ti	c(NaOH)	Temperature	Holding time
1.07 mmol/L	12	6 mol/L	200 °C	5 min – 30 h

To evaluate the behavior of the system during heating and cooling, the reaction was performed just to heat up the system to 200 °C and cool it back down to room temperature. The SEM image and powder-XRD pattern are shown in Figure 41. According to PDF 01-072-1019 reference card, the product is pure $Bi_4Ti_3O_{12}$, no $SrTiO_3$ was observed. Also, SEM examination confirmed that $SrTiO_3$ nucleation still did not proceed. From this experiment it was concluded that no significant progress of the topochemical reaction occurs during the heating stage.

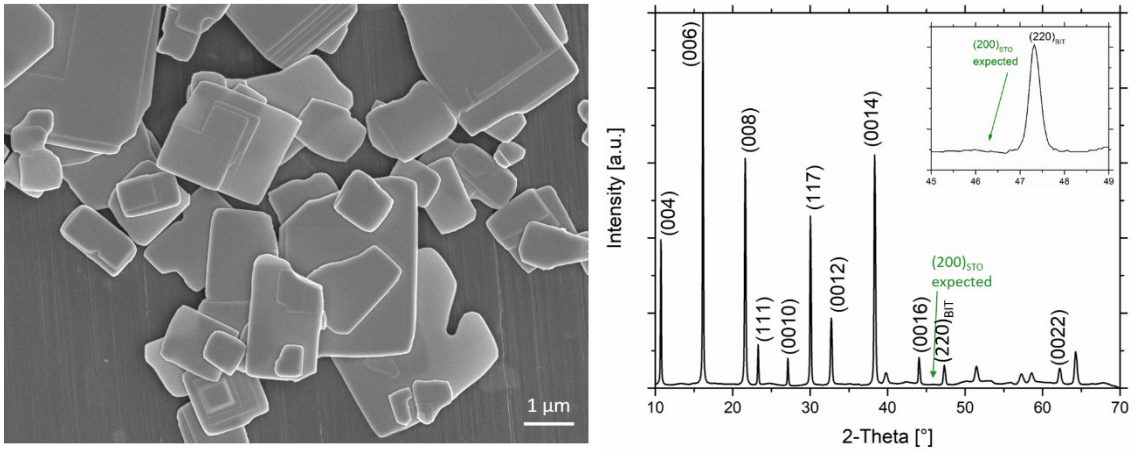

Figure 41: SEM image and powder-XRD pattern of the product powder obtained from $Bi_4Ti_3O_{12}$ platelets and $SrCl_2$ (Sr/Ti=12) in 6 mol/L NaOH after 5 minutes at 200 °C. According to PDF 01-072-1019 reference card, the product is pure $Bi_4Ti_3O_{12}$. The inset is zoomed-in part of the XRD with expected position of (200) peak of $SrTiO_3$.

The progress of the topochemical conversion was followed so that HNO_3-washed product particles were investigated by XRD, SEM and STEM. The XRD patterns and SEM images of morphological examinations of the initial $Bi_4Ti_3O_{12}$ platelets, intermediate $SrTiO_3/Bi_4Ti_3O_{12}$ products and pure $SrTiO_3$ particles are shown in Figure 42. The formation of the $SrTiO_3$ was observed already after 1 hour of the reaction and the ratio of $SrTiO_3$ to $Bi_4Ti_3O_{12}$ increases with the increased reaction time. The estimation of the amount of $SrTiO_3$ and $Bi_4Ti_3O_{12}$ present after each reaction was determined by the ratio of XRD intensities (200)$SrTiO_3$/(008)$Bi_4Ti_3O_{12}$ and (200)$SrTiO_3$/(0014)$Bi_4Ti_3O_{12}$ by the help of calibration curve as described in 3.3.1.1. The $SrTiO_3$ content is increasing with time from 24 % of $SrTiO_3$ after 1 hour to 73 % and 85 % after 3 and 6 hours, respectively. Pure $SrTiO_3$ was obtained after 15 hours. Obtained values for the $SrTiO_3/Bi_4Ti_3O_{12}$ ratio after the reaction are graphically presented in Figure 42 C. The XRD pattern of the platelets cast on Si-single-crystalline substrate revealed the (001) and (100) preferential orientations of $Bi_4Ti_3O_{12}$ and $SrTiO_3$ phases, respectively.

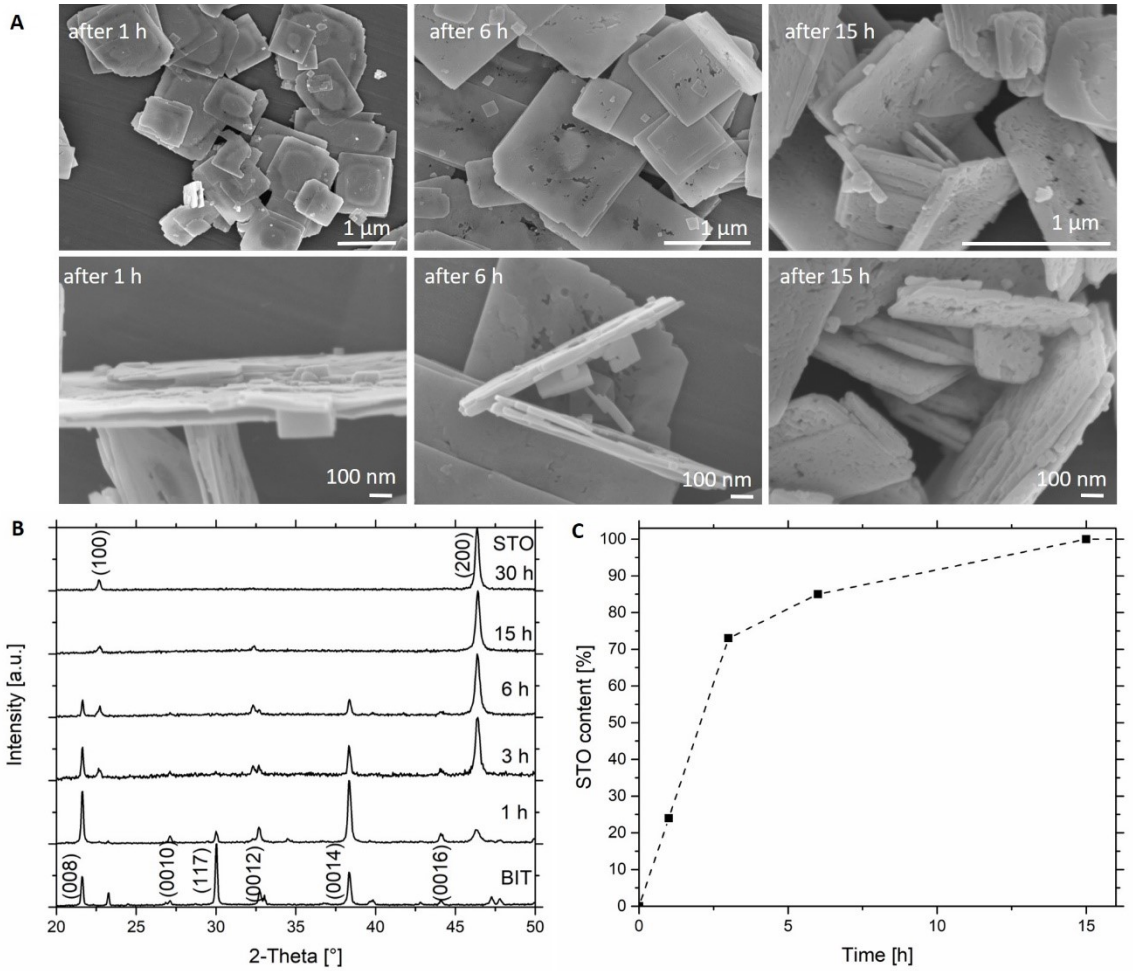

Figure 42: The monitoring of the transformation of $Bi_4Ti_3O_{12}$ to $SrTiO_3$. The SEM images of top-view and side-view of platelets after 1 hour, 6 hours and 15 hours of the transformation (A) with the XRD patterns (B) of the initial $Bi_4Ti_3O_{12}$ platelets, partially converted platelets after 1 hour, 3 hours and 6 hours of the reaction and completely transformed particles after 15 hours and 30 hours of the transformation in 6 mol/L NaOH with the Sr/Ti=12 initial molar ratio at 200 °C. The particles for XRD measurements were cast on Si-single-crystalline substrate. In C, the $SrTiO_3$ (STO) content in heterostructural particles is graphically presented.

Particles after 1 hour of synthesis remained the platelet morphology of the template with core-rim structure. The core and the rim give visible contrast in the BSE image (Figure 43B). This contrast may result either from the difference in the thickness of the platelets or because of the difference in the composition (atomic masses of the constituting elements). Various settings of the scanning electron microscope were used to get as much as possible entire information about the variation of the platelet's composition or morphological characteristics. When investigating the chemical composition of the sample using EDS, higher accelerating voltages are required to provide enough energy for electron ejection from the sample. But higher accelerating voltages also means lower surface sensitivity and resolution, because the signal for the image formation originates from deeper thickness of the sample. To obtain comparable SE and BSE images of the same platelet, accelerating voltage of 5 kV (50 pA) and no beam deceleration was used. The beam deceleration (2 kV) with low accelerating voltage (2 kV and 13 pA) was used to explore the surface of the platelets. The difference in obtained images (Figure 43, A in comparison to C and D) in terms of surface roughness is more than obvious and the selection of operation conditions of the microscope is of great importance not to mask the surface topography. From the plan-view, platelets seem almost flat, however, side-view together with the selection of milder operation conditions of the microscope shows differently. Basal plane is not smooth, but quite rough, with many nucleation sites and the groove is formed from the lateral sides.

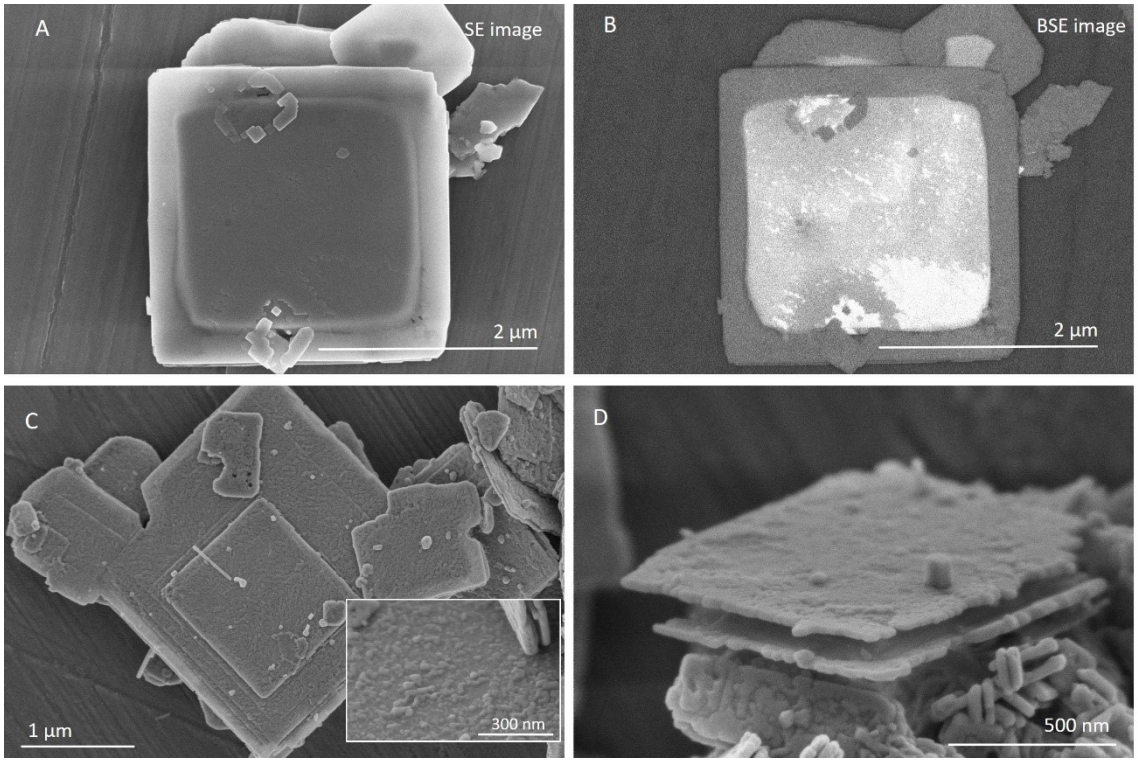

Figure 43: SEM micrographs of the heterostructural $SrTiO_3/Bi_4Ti_3O_{12}$ platelets after 1 hour of conversion. Images A and B are secondary electron (SE) and backscattered electron (BSE) images of a platelet, respectively. C with the inset is the SE image showing the surface of the platelet, which is not atomically flat. D is the SE image showing the rough surface and formed groove from all lateral sides. Higher accelerating voltage and no beam deceleration were used for A and B in comparison to C and D resulting in the difference in the surface smoothness on the images.

SEM and STEM images in Figure 43 and Figure 44, respectively, reveal that conversion proceeds from the lateral sides towards the platelet's center with decreasing the size of the phase contrast in the plate's center. After 6 hours of conversion, $SrTiO_3$ is already the main phase and after 15 hours almost pure $SrTiO_3$ is identified. However, negligible bismuth remains are still visible. EDXS analyses revealed less than 1 atomic % of Bi in $SrTiO_3$ after 15 hours of conversion.

To confirm that the origin of the contrast of SEM images between the core and the rim is a consequence of a difference in the molar mass of $Bi_4Ti_3O_{12}$ and $SrTiO_3$, the EDS mapping and EDS line profiling were performed on the partially converted particles after 1 hour of conversion (Figure 44).

EDS mapping revealed that the distribution of bismuth, exhibiting the largest atomic mass among the elements in the $SrTiO_3/Bi_4Ti_3O_{12}$ system, matches with the brighter platelet's core. Sr^{2+}, Ti^{4+} and O^{2-} are evenly distributed over the whole platelet. This is a confirmation that $Bi_4Ti_3O_{12}$ is dissolving from the edges towards the platelets' core, meaning that the "island" in the platelet's core is undissolved $Bi_4Ti_3O_{12}$. The darker "frame" (i.e. the rim), consisting of lighter elements, is $SrTiO_3$. The growth of the $SrTiO_3$ in the early stage of the transformation occurs on the whole basal surface of the $Bi_4Ti_3O_{12}$ platelet and later continues also on the inner side of $SrTiO_3$ in the groove. Minimums in the EDS line profile of Sr^{2+}, Ti^{4+} and O^{2-} coincide with the boundary of the core and the rim. At this spot of the platelets, darker areas are also observed in the EDS mapping. The dark color indicates a low concentration of detected ions (EDS line profile) due to lower thickness and holes, which most probably appear because of the disruption of the transformation process.

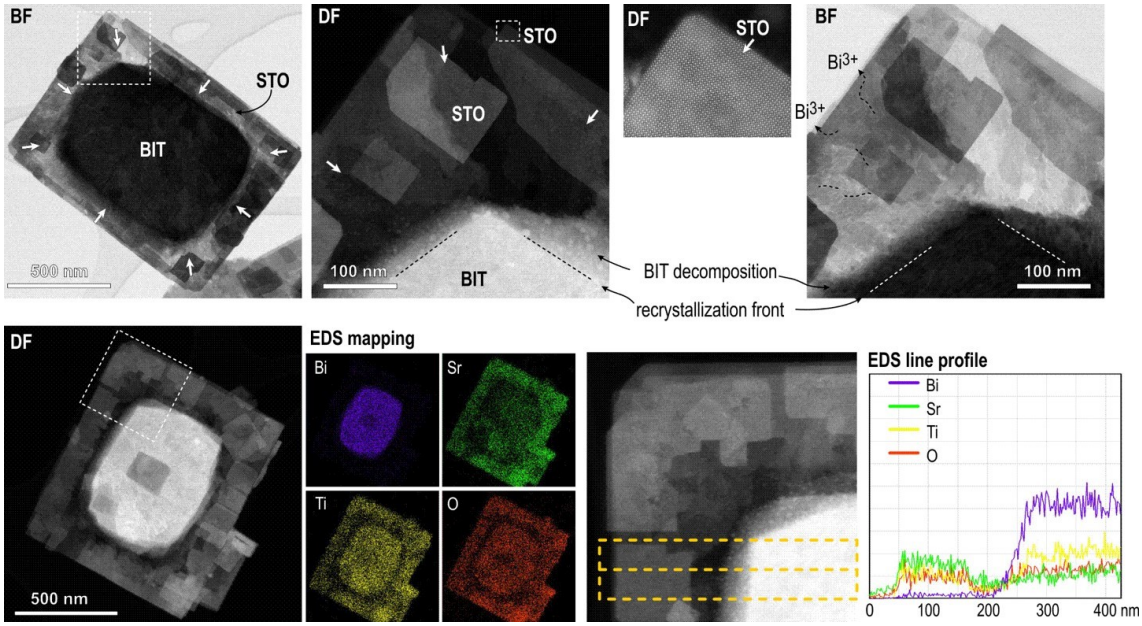

Figure 44: Heterostructural $SrTiO_3/Bi_4Ti_3O_{12}$ platelet after 1 h at 200 °C with Sr/Ti=12 in 6 mol/L NaOH under STEM observation in BF and DF with EDS mapping and EDS line profiling.

4.2.3.2 Microstructural and atomic-scale analysis of $SrTiO_3$ and $SrTiO_3/Bi_4Ti_3O_{12}$ platelets

A deeper insight into the microstructure was needed to understand the process of the transformation from the initial $Bi_4Ti_3O_{12}$ platelets to $SrTiO_3$. For this purpose, the partially and fully transformed platelets were examined by HAADF-STEM and HR-STEM from top and cross-sectional (edge-on) views.

First, completely converted pure $SrTiO_3$ particles were examined and are shown in Figure 45. The general plate-like shape of the initial $Bi_4Ti_3O_{12}$ template particles is well preserved, however, the integrity of the $SrTiO_3$ platelets reflects the mesocrystallinity of the final product (Figure 45 A and B). The final platelets consist of two intergrown $SrTiO_3$ platelets (Figure 45 D and E). The presence of $Bi_4Ti_3O_{12}$ in the central part of the $SrTiO_3$ platelets is not observed (nor in microscopic observations, nor in XRD analysis), indicating that all $Bi_4Ti_3O_{12}$ dissolved and consumed for the formation of $SrTiO_3$. In the edge-on-oriented platelets, the two parallel Bi-rich monoatomic layers were observed along the whole length of both $SrTiO_3$ platelet halves (Figure 45 E). The platelet is relatively dense at the edges, where the transformation starts, and the porosity of the platelet is increasing toward the central region of the platelet (Figure 45 B). A higher-magnification STEM image taken in the central part of the platelet with the FFT calculated from the whole area is shown in Figure 45 C. The matrix consists of epitaxially oriented nanocrystallites that formed (100)-oriented $SrTiO_3$ mesocrystalline platelets with some pores and nanosized inclusions with brighter contrast. The analysis showed that these are amorphous Bi-rich inclusions, which were trapped and overgrown by $SrTiO_3$ during the processes of $Bi_4Ti_3O_{12}$ dissolution and $SrTiO_3$ crystallization (Figure 45 F).

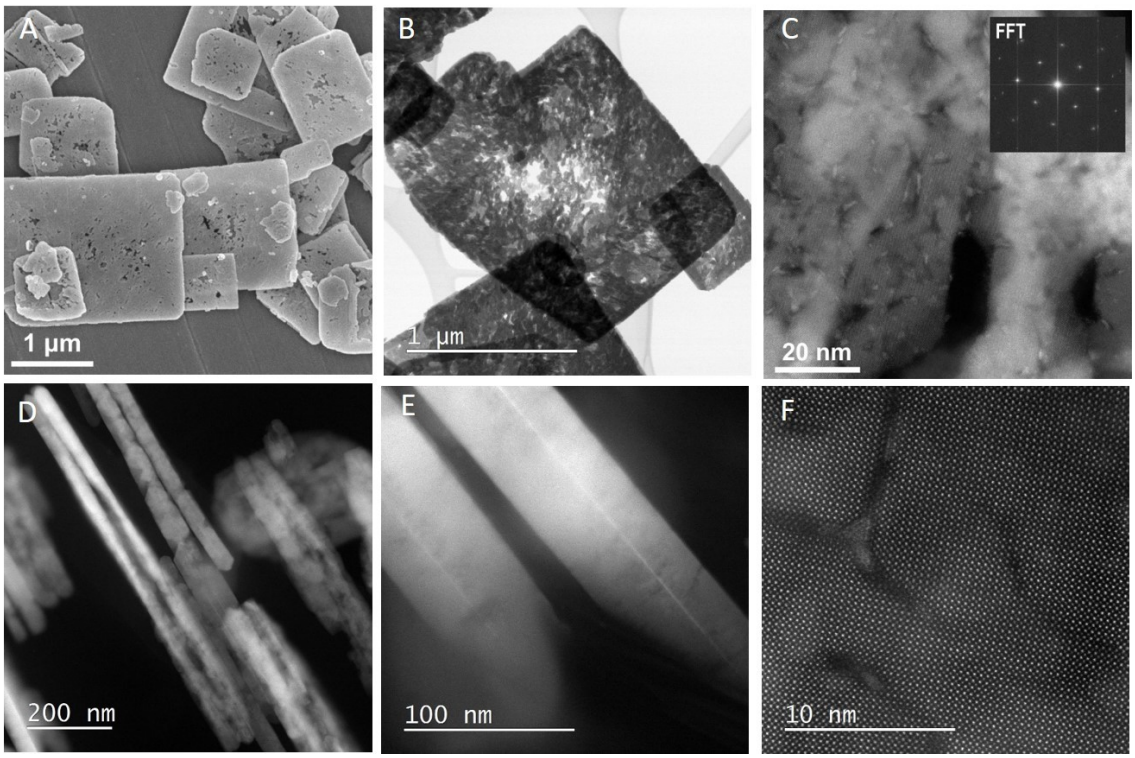

Figure 45: $SrTiO_3$ particles after complete transformation of $Bi_4Ti_3O_{12}$ template platelets (Sr/Ti=12, 6 mol/L NaOH, 15 h at 200 °C). SEM(A) and STEM-BF (B) images of platelets from top-down view. C: STEM-DF image of a platelet from top-down view from the central part of the platelet with a FFT in the inset, showing a (100) orientation of formed $SrTiO_3$. D and E are STEM-DF images of edge-on particles with visible Bi-rich layer (E). F is a STEM-DF image in top-down view showing the $SrTiO_3$ crystalline domains interrupted with some Bi-rich inclusions.

Even greater diversities are observed from the cross-sectional view of the partially transformed platelets (Figure 46), which can be assigned as a heterostructure of $Bi_4Ti_3O_{12}$ and $SrTiO_3$ ($SrTiO_3/Bi_4Ti_3O_{12}$ or STO/BIT). A typical heterostructural $SrTiO_3/Bi_4Ti_3O_{12}$ platelet possesses a core-rim structure (Figure 44) with a groove from the lateral sides to the inwards, splitting the platelet into two thinner parallel platelets (Figure 46 D, G and H). In the dark-field (DF) image, the core of the partially converted particles is much brighter, indicating a higher atomic density in the core region, whereas the rim is more electron transparent due to the lower average atomic density or thinner particle. The opposite is true for the images in the bright field (BF). High resolution STEM micrographs clearly show the formation of epitaxial contact between $SrTiO_3$ and pseudoperovskite layer of underlying $Bi_4Ti_3O_{12}$ (Figure 46 B). The $SrTiO_3$ grows in the form of a nanosized crystallites with a rectangular morphology (Figure 47 B). The presence of regions with distinctly different gray levels suggests that the crystallization of $SrTiO_3$ on the $Bi_4Ti_3O_{12}$ surface occurs in several layers and that the first layer consists of smaller nanocrystallites than upper layers (Figure 46 E).

A platelet was investigated in more detail in cross-sectional view in different platelet's regions. Images D-F in Figure 46 were taken in the central part, where the particle has a sandwich structure ($SrTiO_3/Bi_4Ti_3O_{12}/SrTiO_3$). A closer look at the $Bi_4Ti_3O_{12}$ layer in this part of the platelet (Figure 46 F) reveals that the atomic layers of the $Bi_4Ti_3O_{12}$ are subjected to intensive dissolution. $Bi_4Ti_3O_{12}$ disintegration is much faster from the lateral directions than from the top. This could be at the beginning a consequence of larger concentrations of kink sites at the $Bi_4Ti_3O_{12}$ lateral surface compared to that at the basal surface planes. But, with the continuation of the reaction, when the basal surface planes get protected by the $SrTiO_3$ layer, the dissolution of $Bi_4Ti_3O_{12}$ is enabled only from the unprotected lateral side. Figure 46 G was recorded in the region between the central part and the edge of the $SrTiO_3/Bi_4Ti_3O_{12}$ heterostructural platelet. The epitaxial orientation relationship between the $SrTiO_3$ and the $Bi_4Ti_3O_{12}$ is $[100]SrTiO_3||[001]Bi_4Ti_3O_{12}$ and shows that the orientation of the $SrTiO_3$ is governed by the structure of the underlying $Bi_4Ti_3O_{12}$ template. The fact that the $SrTiO_3$ growth on the $Bi_4Ti_3O_{12}$ is epitaxial confirms that the reaction is topochemical conversion [241].

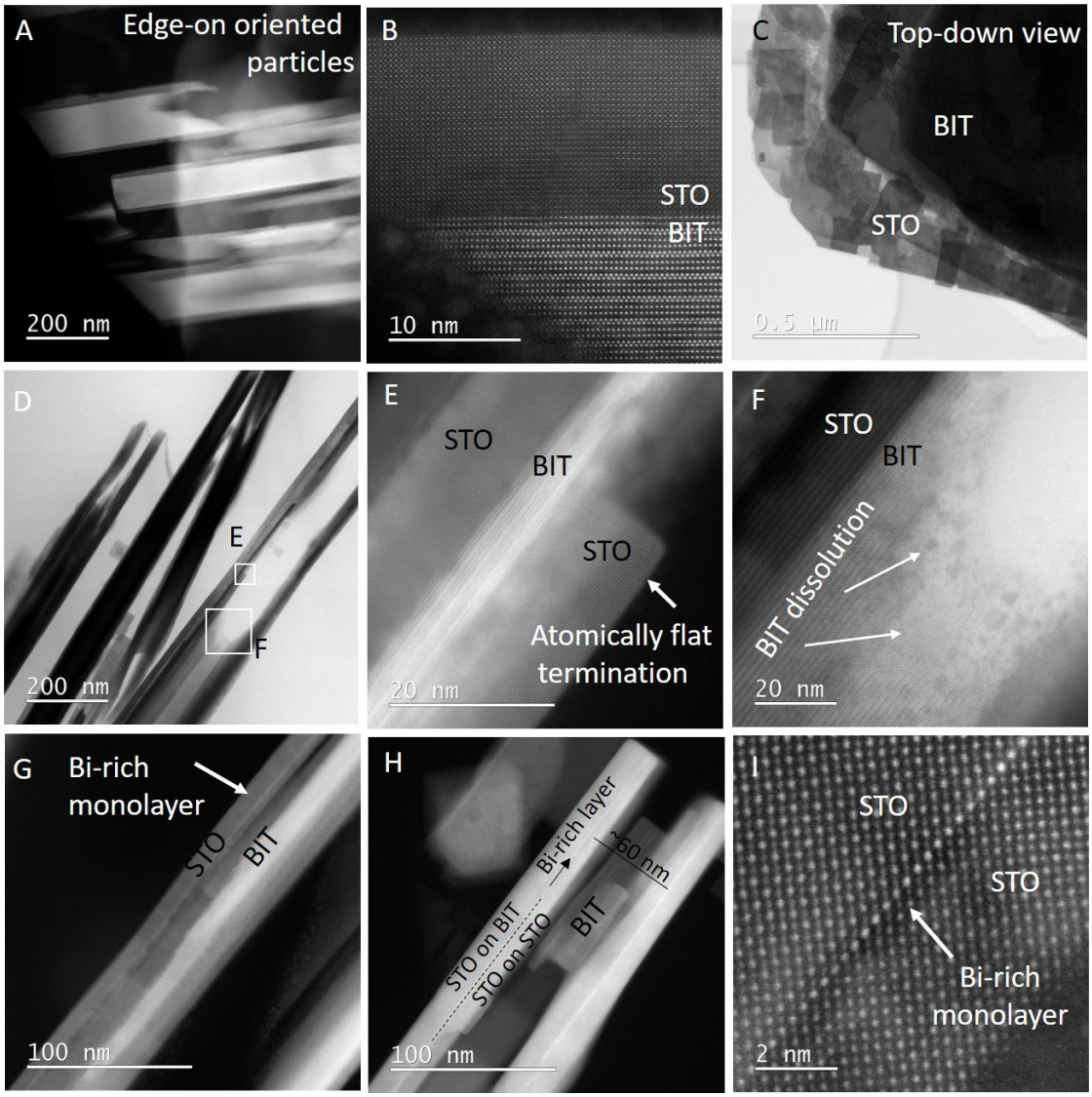

Figure 46: STEM images of partially converted $SrTiO_3/Bi_4Ti_3O_{12}$ particles after 1 h of conversion at 200 °C (Sr/Ti=12, 6 mol/L NaOH). A-C represents the early beginning of the conversion where $SrTiO_3$ grows mostly on both basal surfaces. D-I represents the continuation of the transformation with the dissolution of $Bi_4Ti_3O_{12}$ from lateral side and groove formation. H-I show the Bi-rich monolayer inside the $SrTiO_3$. All images except C are in cross-sectional view (edge-on orientation of the particles).

In the $SrTiO_3$ layer, one of the most interesting features of this conversion was revealed. Inside the $SrTiO_3$ platelet, a bismuth-rich monolayer (Bi-rich layer) is present (Figure 46 H and I). Similarly, the STEM image of the platelet close to the edge (Figure 46 H) revealed the formation of two parallel $SrTiO_3$ platelets that both contain the Bi-rich atomic layer running along both split platelets. Considering fast removal of terminating $(Bi_2O_2)^{2+}$ layer due to the presence of hot and concentrated NaOH, this Bi-rich monoatomic layer might be the remain of the Bi from the top pseudoperovskite layer. The Bi-rich monoatomic layer remains bonded to $SrTiO_3$ even after the progressive dissolution of the remaining $Bi_4Ti_3O_{12}$ template. When the dissolution front of $Bi_4Ti_3O_{12}$ (inside the groove) reaches this Bi-rich layer, it remains attached to the epitaxial $SrTiO_3$ layer and the growth of the $SrTiO_3$ also proceeds from the inner side and the Bi-rich layer becomes a coherent part of the newly formed $SrTiO_3$, where it is usually observed approximately in the middle of each $SrTiO_3$ platelet half (Figure 46 H). The presence of the Bi-rich layer seems as a consequence of the strong bonding between the terminating pseudoperovskite layer of the $Bi_4Ti_3O_{12}$ template and the growing $SrTiO_3$. However, it may also be important in terms of the template's shape preservation. It is obvious that the formation of two parallel platelets with an

incorporated Bi-rich layer is the consequence of $SrTiO_3$ epitaxial growth on the top pseudoperovskite layer of the basal-plane surfaces of the $Bi_4Ti_3O_{12}$ platelets.

4.2.3.3 Heteroepitaxial contact

Cross-sectional atomic-scale analysis of the $SrTiO_3/Bi_4Ti_3O_{12}$ interface provides the information needed for the complete understanding of the nucleation and growth process during studied hydrothermal topochemical conversion.

In the first part of the study (Chapter 4.1.3), it was identified that as-prepared $Bi_4Ti_3O_{12}$ platelets are terminated with $[Bi_2O_2]^{2+}$ layer. However, when the platelets come into contact with NaOH, the last $[Bi_2O_2]^{2+}$ layer is dissolved, so $Bi_4Ti_3O_{12}$ platelets become terminated with pseudoperovskite $[Bi_2O_3Ti_{10}]^{2-}$ layer. $Bi_4Ti_3O_{12}$, terminated with a pseudoperovskite layer is therefore the substrate for the nucleation and growth of $SrTiO_3$. This was also confirmed by the high-resolution STEM examination of the interfacial area (Figure 46B, Figure 47C-F). Despite structural similarities between $SrTiO_3$ and pseudo perovskite layer, there are some misfits between both structures. The lattice mismatches between different lattice planes of $Bi_4Ti_3O_{12}$ and $SrTiO_3$ of the relevant orientation relationships were determined by Rietveld structural refinements of the XRD patterns of both phases. Then, to understand how the misfit is manifested across the $SrTiO_3/Bi_4Ti_3O_{12}$ interface, HAADF-STEM examination of partially transformed platelet in edge on orientation was performed. The $SrTiO_3/Bi_4Ti_3O_{12}$ platelets formed after 1 hour at 200 °C in 6 mol/L NaOH with Sr/Ti=12 used for this investigation.

For determination of the unit cell parameters and relevant lattice spacings of $SrTiO_3$ and $Bi_4Ti_3O_{12}$, the XRD patterns were recorded at room temperature (R.T.) and at 200°C on a high-resolution X-ray diffractometer using high temperature heating stage. Through three heating-cooling cycles, four XRD patterns at room temperature and three measurements at 200 °C were collected. Measurements at room temperature for the initial sample and after cooling from 200 °C to R.T. are in good agreement, however, the results indicate that after first heating to 200 °C and cooling back to room temperature, the unit cell of $SrTiO_3$ shrinks a bit. The initial $SrTiO_3$ sample has a=3.9105(1) Å, and the final one at room temperature has a=3.9101(1) Å. At 200 °C, a=3.9171(2), which means an increase of 0.17 % (Table 13).

Table 13: XRD-determined unit cell parameters, lattice spacing and thermal expansion coefficients of $Bi_4Ti_3O_{12}$ and $SrTiO_3$ at room temperature and at 200 °C.

Material		25 °C	200 °C	Expansion	TCE (25 °C – 200 °C) (K^{-1})
$Bi_4Ti_3O_{12}$	a	5.4517(5)Å	5.4584(5)Å	0.12 %	$7.0 \cdot 10^{-6}$
	b	5.4143(5)Å	5.4239(5)Å	0.18 %	$1.0 \cdot 10^{-5}$
	c	32.796(2)Å	32.872(2)Å	0.23 %	$1.3 \cdot 10^{-5}$
$SrTiO_3$	a	3.9105(1)Å	3.9171(2)Å	0.17 %	$2.9 \cdot 10^{-5}$

From the unit cell parameters, inferred distances at room temperature and at 200 °C of the {110} plane in $Bi_4Ti_3O_{12}$ are 3.8417 Å and 3.8475 Å, respectively, while that of {100} plane in $SrTiO_3$ are 3.910 Å and 3.9171 Å, respectively. Due to the increase in the temperature (from room temperature to 200 °C h), the observed increase in the unit cell parameters of $Bi_4Ti_3O_{12}$ (~0.12 % to 0.23 %) and $SrTiO_3$ (~0.17 %) are in good agreement with the calculated TCE values reported in the literature ($(1.3 \pm 0.2) \cdot 10^{-5}$ for $Bi_4Ti_3O_{12}$ and $3.2 \cdot 10^{-5}$ for $SrTiO_3$ [242], [243]). At both temperatures, the lattice mismatch between {110} plane in $Bi_4Ti_3O_{12}$ and {100} in $SrTiO_3$ does not differ significantly and is calculated as ~1.78 %. For the comparison of d(100) $SrTiO_3$ and d(110) $Bi_4Ti_3O_{12}$, I have taken into account that in $Bi_4Ti_3O_{12}$ a and b are not the same. The misfits between the $Bi_4Ti_3O_{12}$ and $SrTiO_3$ lattice planes in other relevant orientation relationships at 200°C were calculated to be 1.48 % between (200) plane of $Bi_4Ti_3O_{12}$ and (110) of $SrTiO_3$ and 2.11 % between the (020) of $Bi_4Ti_3O_{12}$ and (110) of $SrTiO_3$. These misfits in the range from 1.48 % to 2.11 % are the unavoidable contribution to the interfacial free energy (Eq. (14)) for the nucleation of $SrTiO_3$ on the basal surface plane of $Bi_4Ti_3O_{12}$ platelet, which will be discussed in 4.2.4.

It is not easy to compare the Ti-O distances in the two structures with the above XRD data. The $SrTiO_3$ structure is cubic, and the space group Pm3m means that all atoms are locked in special positions. This means that all TiO_6 octahedra are perfectly symmetrical, and the Ti-O distance is exactly half of the distance a (at 200 °C it is 1.9586±1 Å and at room temperature 1.9551±1 Å). On the contrary, the symmetry for $Bi_4Ti_3O_{12}$ is lower, therefore the TiO_6 octahedra in the perovskite blocks are distorted; the oxygen atoms are not in specific positions, and it is not

possible to deduce the distance from the cell. To be able to fit the coordinates of the atoms, even more accurate data are needed.

In general, in the process of epitaxial growth, the misfit can be reduced by elastic strains or accommodated by misfit dislocations. The latter are formed when the misfit is too large to be eliminated by elastic strains. The HAADF-STEM analyses revealed that the misfit across the $SrTiO_3/Bi_4Ti_3O_{12}$ interface is compensated by missing lattice planes in the $SrTiO_3$ film, showing as misfit dislocations (Figure 47C-F). The average spacing between these misfit dislocations in an unstrained (relaxed) film is calculated from Eq. (13):

$$x_0 = \frac{a_f}{a_f - a_s} \tag{13}$$

where a_f and a_s are the lattice spacings of the film (f) and substrate (s), respectively [244], [245]. The expected number of planes separating two dislocations in $SrTiO_3$ film grown on $Bi_4Ti_3O_{12}$ substrate in $[100]_{STO}$ $(010)_{STO}$ II $[1\bar{1}0]_{BIT}$ $(110)_{BIT}$ orientation relationship is around 57 and 58 (100) $SrTiO_3$ lattice planes (Table 14 and Figure 47). The spacing between the dislocations observed in the experimental images was slightly smaller (approximately 18-19 nm) in comparison to calculated values (approximately 22 nm) (Table 14). Spacings between the misfit dislocations in the other investigated low-index zone axis with $[1\bar{1}0]_{STO}$ $(110)_{STO}$ II $[010]_{BIT}$ $(200)_{BIT}$ are irregular (depending on the sample cross-section).

Table 14: The misfits between different lattice planes pairs of $Bi_4Ti_3O_{12}$ (BIT) and $SrTiO_3$ (STO) at heteroepitaxial contact. The presented values were calculated from the experimentally determined (by STEM) unit cell parameters at room-temperature (R.T.) and at 200 °C obtained from Rietveld structural refinements of the XRD patterns.

	$(110)_{BIT}$ - $(100)_{STO}$		**$(200)_{BIT}$ - $(110)_{STO}$**		**$(020)_{BIT}$ - $(110)_{STO}$**	
	R.T.	200 °C	R.T.	200 °C	R.T.	200 °C
d_{BIT}, Å	3.842	3.848	2.726	2.729	2.707	2.712
d_{STO}, Å	3.911	3.917	2.765	2.770	2.765	2.770
Misfit, %	1.77	1.79	1.43	1.48	2.12	2.11
Period of misfit, Å	222	220	195	189	144	133
Period of misfit, lattice planes	57	56	70	68	52	48

Local contrast around the misfit dislocations is a bit blurred in magnified images (Figure 47 D and F). It indicates that the crystal structure of the last pseudoperovskite layer of the $Bi_4Ti_3O_{12}$ is slightly disturbed around the dislocation cores due to the strain imposed to the substrate by the larger $SrTiO_3$ film. On the other hand, the $SrTiO_3$ film seems to be relaxed already after a few atomic layers. These results also indicate that the formation of the first layer of $SrTiO_3$ film starts by deposition of Sr^{2+} ions from the solution followed by the deposition of the perovskite TiO_6^{2-} octahedra. The growth continues with the next layer of Sr^{2+} and so on.

The observations obtained from the top-down STEM examination (Figure 47 A and B) to some extent supplement the information obtained from the cross-sectional view. STEM image of high magnified area of the $SrTiO_3$ growing on $Bi_4Ti_3O_{12}$, shown in Figure 47 B, discloses that $SrTiO_3$ in the first layers (1-2 structural units) grow in small crystallites with the dimensions like the calculated distances between the dislocations. After 1–2-unit cells, the growth mode rather continues as layer-by-layer growth and $SrTiO_3$ starts to form larger islands.

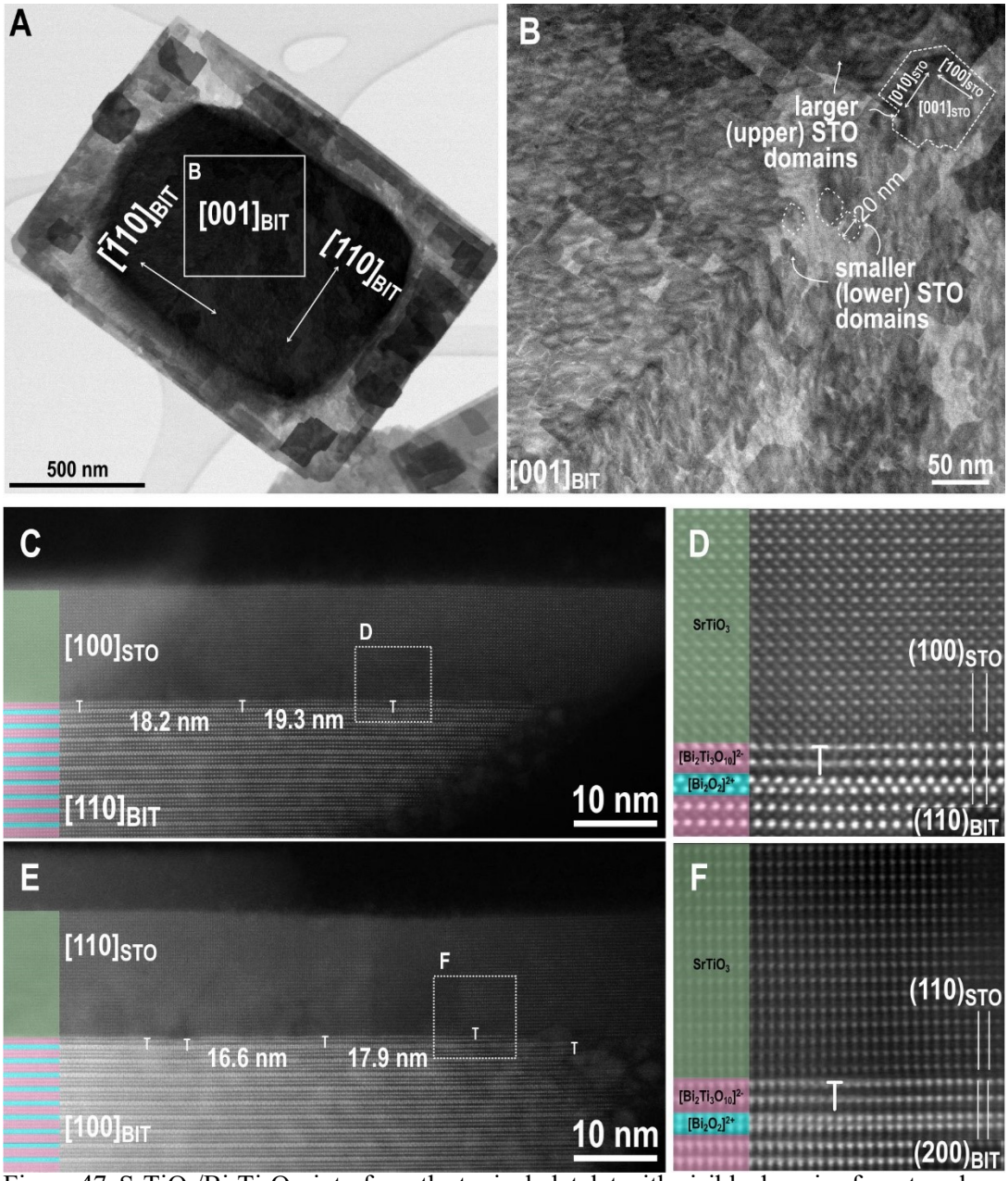

Figure 47: $SrTiO_3/Bi_4Ti_3O_{12}$ interface: the typical platelet with visible domains from top-down view (A, B) and HAADF-HRSTEM images of the $SrTiO_3/Bi_4Ti_3O_{12}$ interface ($[100]_{STO}$ $(010)_{STO}$ II $[110]_{BIT}$ $(1\bar{1}0)_{BIT}$ (C, D) and $[1\bar{1}0]_{STO}$ $(110)_{STO}$ II $[100]_{BIT}$ $(200)_{BIT}$ (E, F)). In the C-F the $[Bi_2O_2]^{2+}$ layers and pseudoperovskite $[Bi_2Ti_3O_{10}]^{2-}$ blocks are marked with blue and pink colors, respectively, and $SrTiO_3$ with green. The dislocations are marked with ⊤ sign (C-F). The $SrTiO_3/Bi_4Ti_3O_{12}$ heterostructural platelets were prepared with Sr/Ti=12 in 6 mol/L NaOH for 1 hour at 200 °C.

4.2.3.4 The proposed reaction mechanism

Based on the above results, the conversion mechanism of $Bi_4Ti_3O_{12}$ to $SrTiO_3$ under hydrothermal conditions is proposed. For better visualization it is schematically presented in Figure 48.

The dissolution of the initial $Bi_4Ti_3O_{12}$ platelets starts from the lateral surfaces where both types of structural units ($[Bi_2O_2]^{2+}$ layers and the pseudo-perovskite $[Bi_2Ti_3O_{10}]^{2-}$ blocks) are exposed. Additionally, the concentration of atomic steps is typically higher at the lateral surface and closer to the edge than in the middle of the basal surface planes. When the solution becomes locally saturated with Sr^{2+} and $Ti(OH)_6^{2-}$, nucleation of the $SrTiO_3$ occurs. The areas close to the edges are subjected to higher concentrations of $Ti(OH)_6^{2-}$ from the beginning of the reaction. Also, the $SrTiO_3$ nucleation occurs preferably in the areas with the lowest energy barrier (e.g. edge-atoms, kink sites). Therefore, $SrTiO_3$ nucleation starts at the $Bi_4Ti_3O_{12}$ platelet's edges and continues over the whole $Bi_4Ti_3O_{12}$ platelet's basal surfaces. By formation of this $SrTiO_3$ protection layer, dissolution of $Bi_4Ti_3O_{12}$ is restricted by the lateral side, which leads to the formation of a groove. With the progress of the reaction, the $SrTiO_3$ layer becomes thicker, while the groove deepens. As the $Bi_4Ti_3O_{12}$ inside the groove completely dissolves to the topmost pseudoperovskite block, the epitaxial growth of the $SrTiO_3$ also proceeds on the inner side and monoatomic Bi-rich layer gets captured within $SrTiO_3$. Consequently, the Bi-rich layer becomes coherently integrated into the $SrTiO_3$ platelet on both sides. The reactions of $Bi_4Ti_3O_{12}$ dissolution and $SrTiO_3$ epitaxial growth continue till pseudomorphic replacement of the $Bi_4Ti_3O_{12}$ platelet by two parallel and partially intergrown $SrTiO_3$ slabs. The monoatomic Bi-rich layer runs along each $SrTiO_3$ platelet half, and it is positioned approximately in the middle.

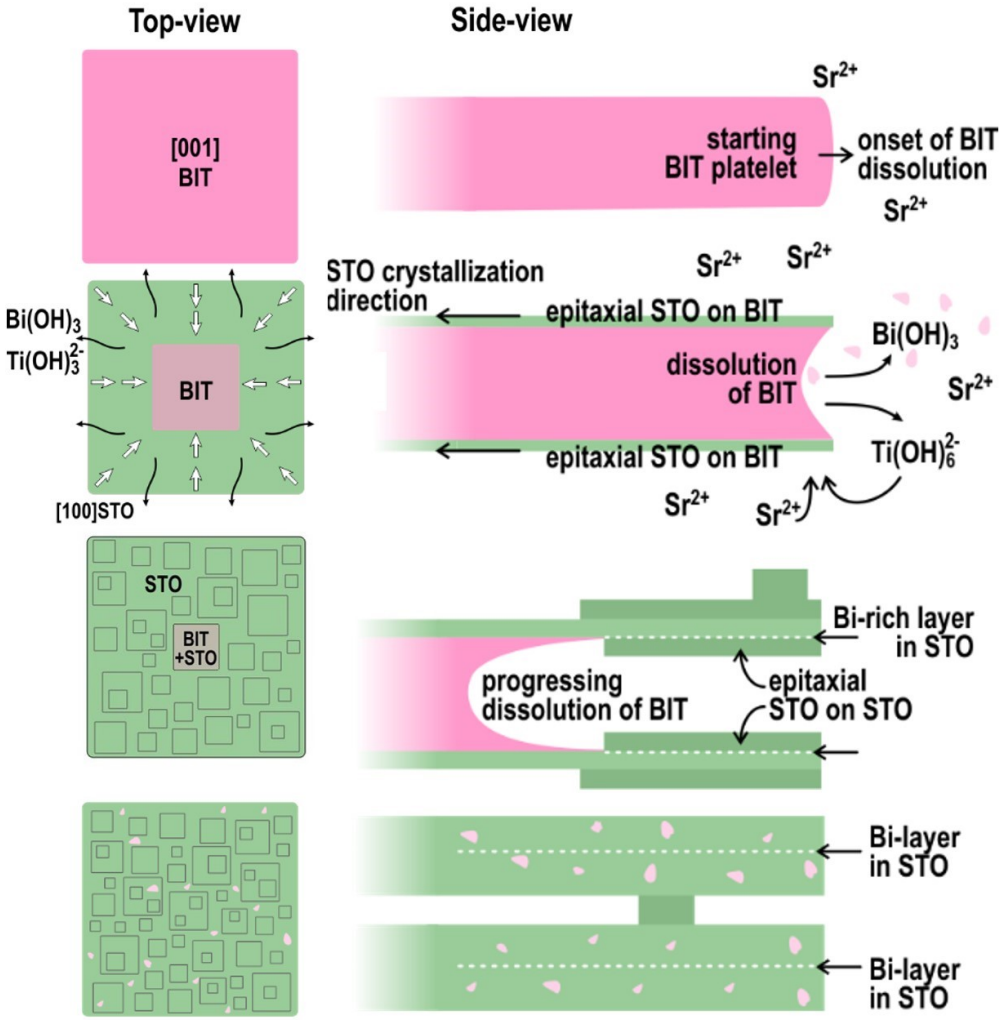

Figure 48: Schematically presented proposed mechanism (modified schemes from our articles [233], [234]).

4.2.4 Pathways of the reaction mechanism and morphology control

The precipitation of $SrTiO_3$ on $Bi_4Ti_3O_{12}$ platelets (heterogeneous nucleation) proceeds following Eq.(11): $Ti(OH)_6^{2-}(aq) + Sr^{2+}(aq) \rightarrow SrTiO_3(s) + 3H_2O(l)$. The classical nucleation theory defines that the nucleation barrier (Δg_n) is proportional to the third power of interfacial energy (α) and inversely proportional to the square of the natural logarithm of supersaturation (S) as defined in Eq. (14):

$$\Delta g_n \propto \frac{a^3}{(\ln(S))^2} \tag{14}$$

The structural mismatch is a constant and unavoidable contribution. The misfit between the relevant lattice planes of $Bi_4Ti_3O_{12}$ and $SrTiO_3$ was determined by Rietveld refinement (Table 14). How this misfit is manifested on the atomic level at the interface was examined by STEM (Figure 47). All these are described in more detail in previous sections. The second contribution to the activation energy for nucleation is supersaturation. Considering Eq. (14), higher supersaturation means lower activation energy for nucleation. The supersaturation (Eq. (15)) is in this system defined as the ratio between the product of the activities (activity of $Ti(OH)_6^{2-}$ species that form during $Bi_4Ti_3O_{12}$ dissolution and Sr^{2+} activity) and solubility product of $SrTiO_3$:

$$S = \frac{a(Ti(OH)_6^{2-})a(Sr^{2+})}{K_S} \tag{15}$$

Consequently, supersaturation is dependent on the concentration of $Ti(OH)_6^{2-}$ and Sr^{2+} that are present in the solution and available for the reaction. While the Sr^{2+} concentration can be easily controlled by the initial $SrCl_2$ concentration and therefore by Sr/Ti molar ratio, the $Ti(OH)_6^{2-}$ concentration is a complex function of the $Bi_4Ti_3O_{12}$ dissolution and $SrTiO_3$ precipitation. Consequently, controlling the reaction pathway in terms of $Ti(OH)_6^{2-}$ is more challenging than the control of Sr^{2+} concentration. So, the following subchapters describe how the transformation is guided by changing the molarity of NaOH and the initial Sr:Ti molar ratios which control the concentrations of dissolved titanium ($(Ti(OH)_6^{2-})_{aq}$) and strontium ($(Sr^{2+})_{aq}$) species, respectively.

For this study, the hydrothermal reactions at different concentrations of the $Sr^{2+}(aq)$ and $Ti(OH)_6)^{2-}(aq)$ were performed. As already explained in Chapter 4.2.4, the concentrations of $Sr^{2+}(aq)$ and $Ti(OH)_6)^{2-}(aq)$ are controlled by the nominal concentration of $SrCl_2$ and NaOH concentration. The minimal selected Sr/Ti molar ratio was 1, as at least stoichiometric Sr/Ti ratio is needed for complete transformation from $Bi_4Ti_3O_{12}$ to $SrTiO_3$. Higher $Sr^{2+}(aq)$ concentrations that significantly exceed the stoichiometric ratio (Sr/Ti=3, 12, 24) were used for the comparison. The influence of NaOH concentration was investigated at low (2 mol/L) and high (6 mol/L) NaOH concentration. The growth progress and phase composition were examined after 2.5 h and 12 h of each reaction at 200 °C.

4.2.4.1 Topochemical conversion in 2 mol/L NaOH

First, the nucleation and growth were investigated for four Sr/Ti nominal ratios (Sr/Ti=1, 3, 12 and 24) in 2 mol/L NaOH. Figure 49 represents the typical growth of $SrTiO_3$ on $Bi_4Ti_3O_{12}$ after 2.5 h of hydrothermal reaction at the lowest investigated supersaturating conditions (i.e. stoichiometric Sr/Ti ratio and 2 mol/L NaOH). In the beginning of the process, $Bi_4Ti_3O_{12}$ platelets are still mostly undissolved. This means that the concentration of available $Ti(OH)_6)^{2-}$ is still considerably lower in comparison to Sr^{2+} in the solution. Consequently, at the early stage of the reaction, the Sr/Ti ratio is much higher than stoichiometric. As seen from Figure 49, $SrTiO_3$ nucleates preferentially on the places of the $Bi_4Ti_3O_{12}$ template that enable lower nucleation energy [233], [246], i.e. kink sites in steps. $SrTiO_3$ grows as islands, reminiscent of island-by-island or Volmer-Weber growth mode. After 2.5 h, the islands have a side length of 20-50 nm and approximately 35 % of $Bi_4Ti_3O_{12}$ basal surface was covered with $SrTiO_3$ (Figure 49 and Figure 50A). The surface coverage was determined by the analysis of SEM micrographs of the particles by measuring 20 platelets and their $SrTiO_3$ islands in ImageJ and calculating the average coverage of the surface. According to XRD data, 90 % of the $SrTiO_3/Bi_4Ti_3O_{12}$ sample is still $Bi_4Ti_3O_{12}$.

For the comparison, the particles, obtained at conditions with higher Sr/Ti ratios, were analyzed (Figure 50 and Figure 51). At Sr/Ti=1, the $SrTiO_3$ islands are larger and thicker compared to those formed at higher Sr/Ti ratios. Moreover, islands are also more isolated and appear mostly close to the edge of the basal surface plane of the $Bi_4Ti_3O_{12}$ platelet (Figure 49). On the other hand, the islands appear smaller and closer together as the Sr/Ti ratio is increasing. Figure 50 shows the size of $SrTiO_3$ islands for all four Sr/Ti ratios and the $SrTiO_3$ coverage of the basal surface plane of $Bi_4Ti_3O_{12}$ platelets, that increases from 35 % for Sr/Ti=1 to 65 % for

Sr/Ti=3, 75 % for Sr/Ti=12 and to almost fully covered basal plane for Sr/Ti=24, For the latter, the size of the islands and surface coverage were not possible to determine based on SEM images. By increasing the Sr/Ti ratio, the growth appears more layer-by-layer than island-by-island. In Figure 51, the particles are presented at lower magnification, showing the distribution of $SrTiO_3$ over the basal surface of the $Bi_4Ti_3O_{12}$ platelets.

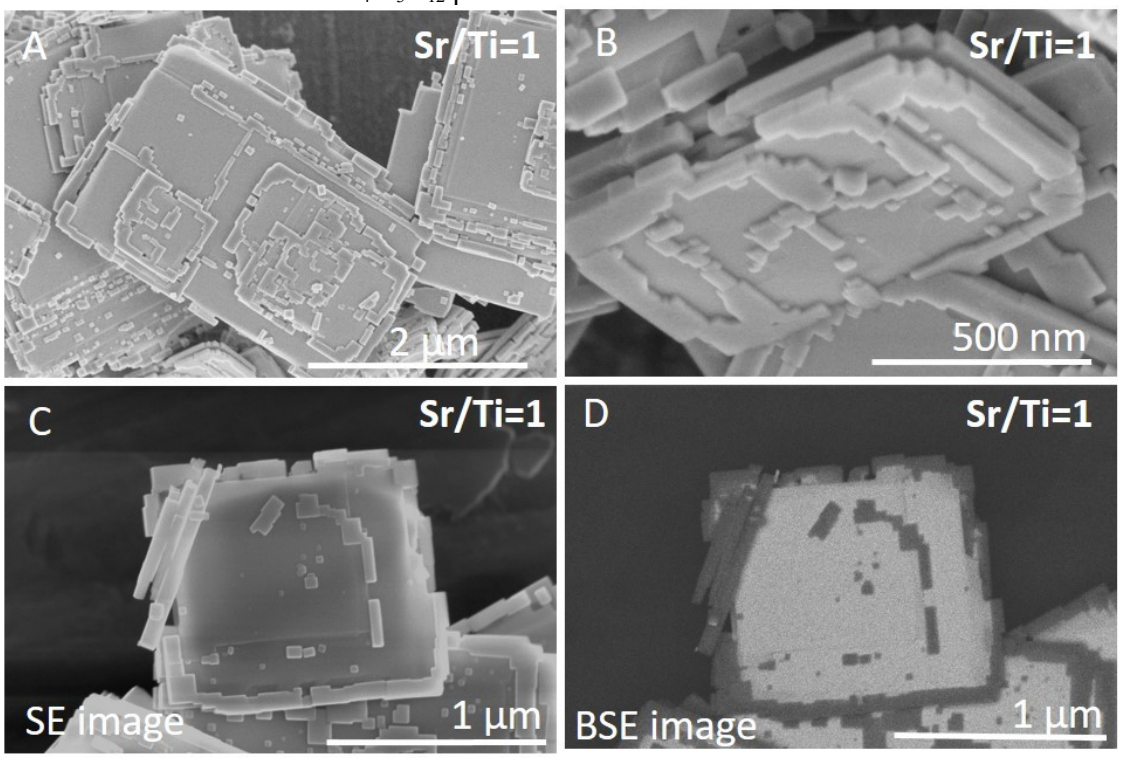

Figure 49: SEM micrographs of the $SrTiO_3$ growth on $Bi_4Ti_3O_{12}$ platelets after 2.5 h at 200 °C with the Sr/Ti=1 in 2 mol/L NaOH. $SrTiO_3$ primarily grows in islands on the edges and defect sites.

The observed morphological development is in accordance with the atomistic observation of the $Bi_4Ti_3O_{12}$ platelet 's morphology, as well as with nucleation and crystal growth theory. According to the classical nucleation-crystallization theory, the kink sites at the steps are the most favorable location for the incorporation and disincorporation of structural units [40], [247]. The steps in $Bi_4Ti_3O_{12}$ platelets were rarely present in the middle of the $Bi_4Ti_3O_{12}$ platelet. Instead, the steps are frequently present close to the edge (Figure 28B). The dissolution of the $Bi_4Ti_3O_{12}$ templates proceeds faster from the lateral side. As a result, the solubility product for $SrTiO_3$ formation at these places is exceeded earlier than in the middle of the basal surface plane. Moreover, in the case of Sr/Ti=1, larger $SrTiO_3$ islands are the biggest and the most distinct. On the other hand, tiny $SrTiO_3$ islands that are close to each other (in case of high supersaturation) provide better protection of the $Bi_4Ti_3O_{12}$ basal surface plane against the dissolution from the top of the basal surfaces. The explanation about better $SrTiO_3$ overgrowth over the basal surface planes of the $Bi_4Ti_3O_{12}$ platelet at higher c_{Sr2+} can be established based on the easier formation of the first Sr^{2+} and subsequent layers due to the abundance of Sr^{2+} ions in the solution. According to high resolution STEM (Figure 47D and F), the $SrTiO_3$ nucleation and growth over the pseudoperovskite layer of the $Bi_4Ti_3O_{12}$ platelets start with deposition of the Sr^{2+} layer, followed by the deposition of the layer of perovskite TiO_6 octahedra, next Sr^{2+} and so on. Additionally, faster $SrTiO_3$ nucleation and growth at higher c_{Sr2+} can also be explained based on Eq.(15) – a higher c_{Sr2+} ensures longer-term high supersaturation. As a result, the nucleation energy barrier is lower, which leads to a higher nucleation rate of $SrTiO_3$ on $Bi_4Ti_3O_{12}$ at larger Sr/Ti ratios.

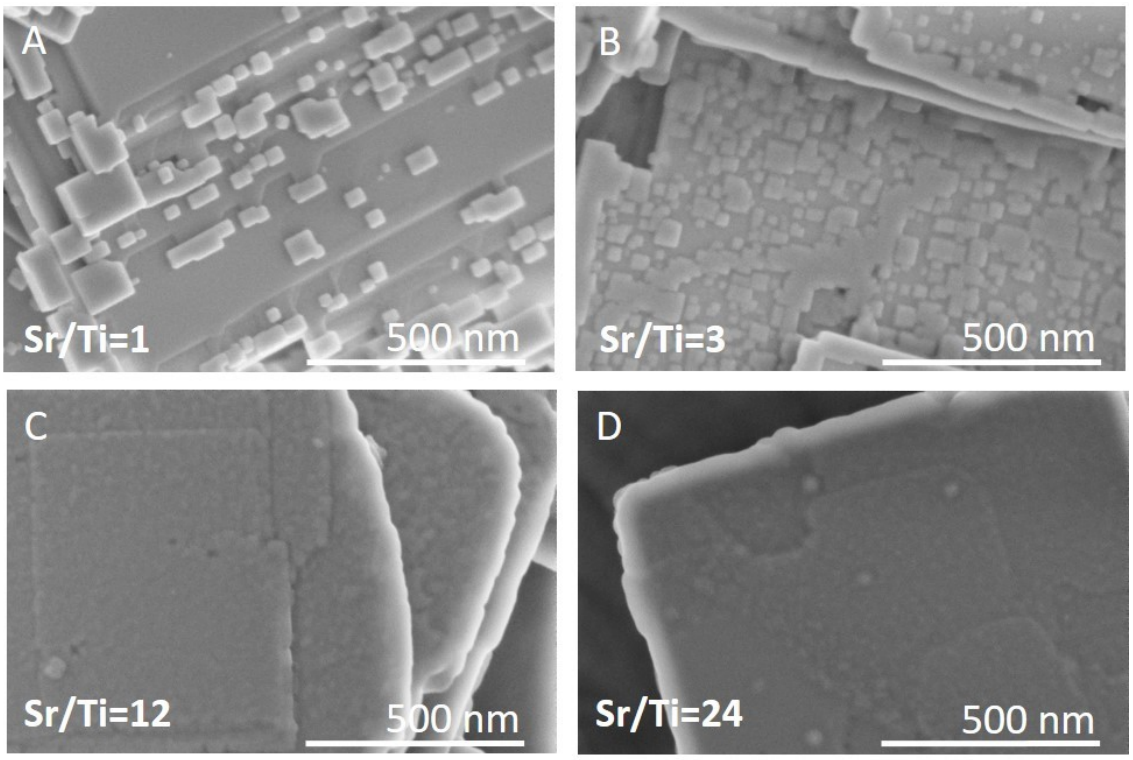

Figure 50: SEM micrographs of the part of the $SrTiO_3/Bi_4Ti_3O_{12}$ platelet after 2.5 h at 200 °C at different Sr/Ti ratios: (a) Sr/Ti=1, (b) Sr/Ti=3, (c) Sr/Ti=12, (d) Sr/Ti=24.

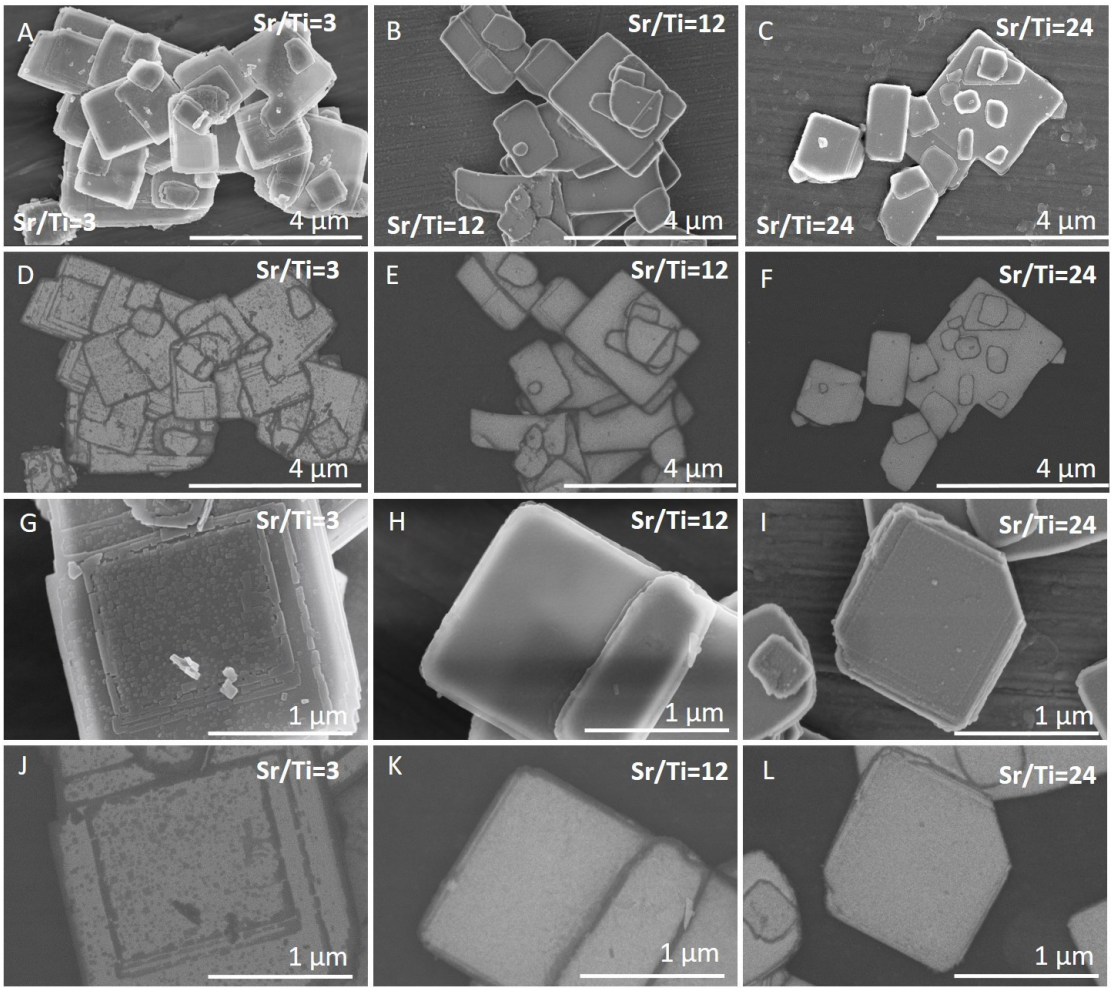

Figure 51: SEM micrographs showing the early stage of $SrTiO_3$ formation on $Bi_4Ti_3O_{12}$ at Sr/Ti= 3, 12 and 24. The SE (A-C, G-I) and corresponding BSE (D-F, J-L) images of $SrTiO_3/Bi_4Ti_3O_{12}$ particles after 2.5 h of reaction at 200 °C in 2 mol/L NaOH are present at lower (A-F) and higher magnification (G-L).

Regardless of the initial Sr/Ti ratios, the $Bi_4Ti_3O_{12}$ diffractions in the XRD patterns are highly dominating over those of $SrTiO_3$ (Figure 53), since the $SrTiO_3$ layer on the $Bi_4Ti_3O_{12}$ is still thin and the major part of $Bi_4Ti_3O_{12}$ remained unreacted after 2.5 h. Significant advancement of the transformation to $SrTiO_3$ was observed after 12-hour-reaction (Figure 52 and Figure 53). Almost pure $SrTiO_3$ was obtained at Sr/Ti=1 (~98 % $SrTiO_3$ and 2 % $Bi_4Ti_3O_{12}$ remains), whereas the amount of unreacted $Bi_4Ti_3O_{12}$ increased with Sr excess: the remains of $Bi_4Ti_3O_{12}$ are 27 % at Sr/Ti=3, 42 % at Sr/Ti=12 and 58 % at Sr/Ti=24. The unreacted $Bi_4Ti_3O_{12}$ phase appears as the brighter core in the BSE images (Figure 52). These results indicate that higher Sr concentrations impede the conversion from $Bi_4Ti_3O_{12}$ to $SrTiO_3$. This is a consequence of a high surface coverage at higher Sr/Ti ratios and the only remaining possibility for $Bi_4Ti_3O_{12}$ dissolution is from the lateral side. Hence, the supply of $Ti(OH)_6)^{2-}(aq)$ is restricted to a long diffusion path from the formed groove. The conditions with higher Sr/Ti ratio (Sr/Ti=12 and Sr/Ti=24) enable the best preservation of morphology, but the sluggishness of the reaction significantly extends the time needed for complete conversion to $SrTiO_3$. On the contrary, the preservation of the platelet morphology in the case of stoichiometric Sr/Ti=1 or low excess of Sr (Sr/Ti=3) is impaired. All these observations confirm that higher Sr concentrations (Sr/Ti=12, 24) are needed to direct the nucleation and growth of $SrTiO_3$ over the whole basal surface planes of the $Bi_4Ti_3O_{12}$ platelets.

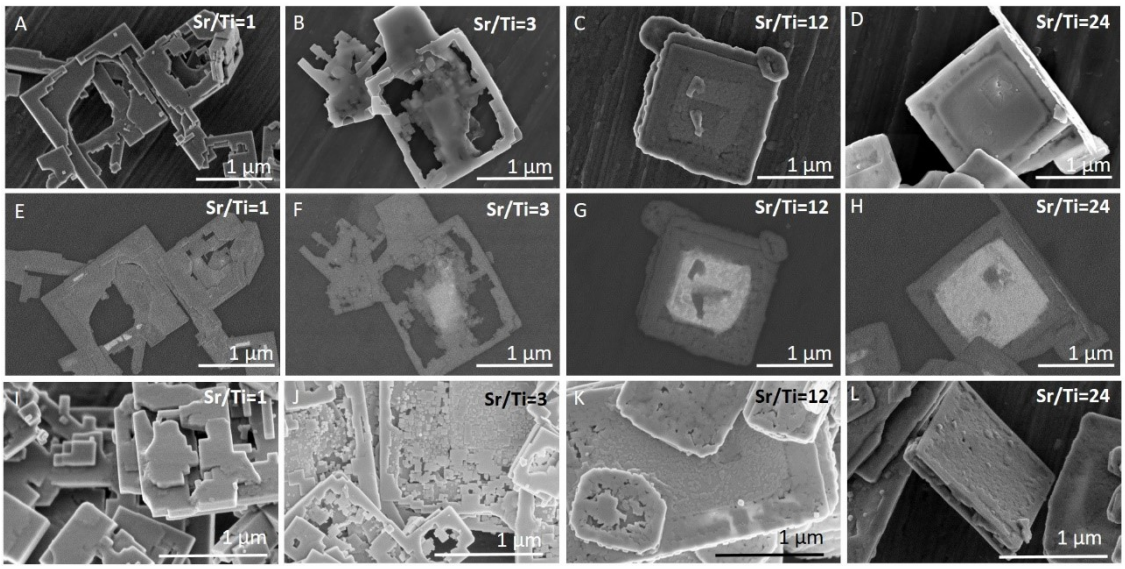

Figure 52: SEM micrographs showing the proceeding of $SrTiO_3$ formation from $Bi_4Ti_3O_{12}$ template platelets with nominal Sr/Ti= 1, 3, 12 and 24. The SE (A-D) and corresponding BSE (E-H) images of $SrTiO_3/Bi_4Ti_3O_{12}$ particles after 12 h of reaction at 200 °C in 2 mol/L NaOH showing the unreacted $Bi_4Ti_3O_{12}$ (brighter platelet's core) and $SrTiO_3$ edge (darker). SE images in I-L represent product particles obtained in 6 mol/L NaOH at 200 °C for 12 hours at nominal Sr/Ti=1, 3, 12 and 24.

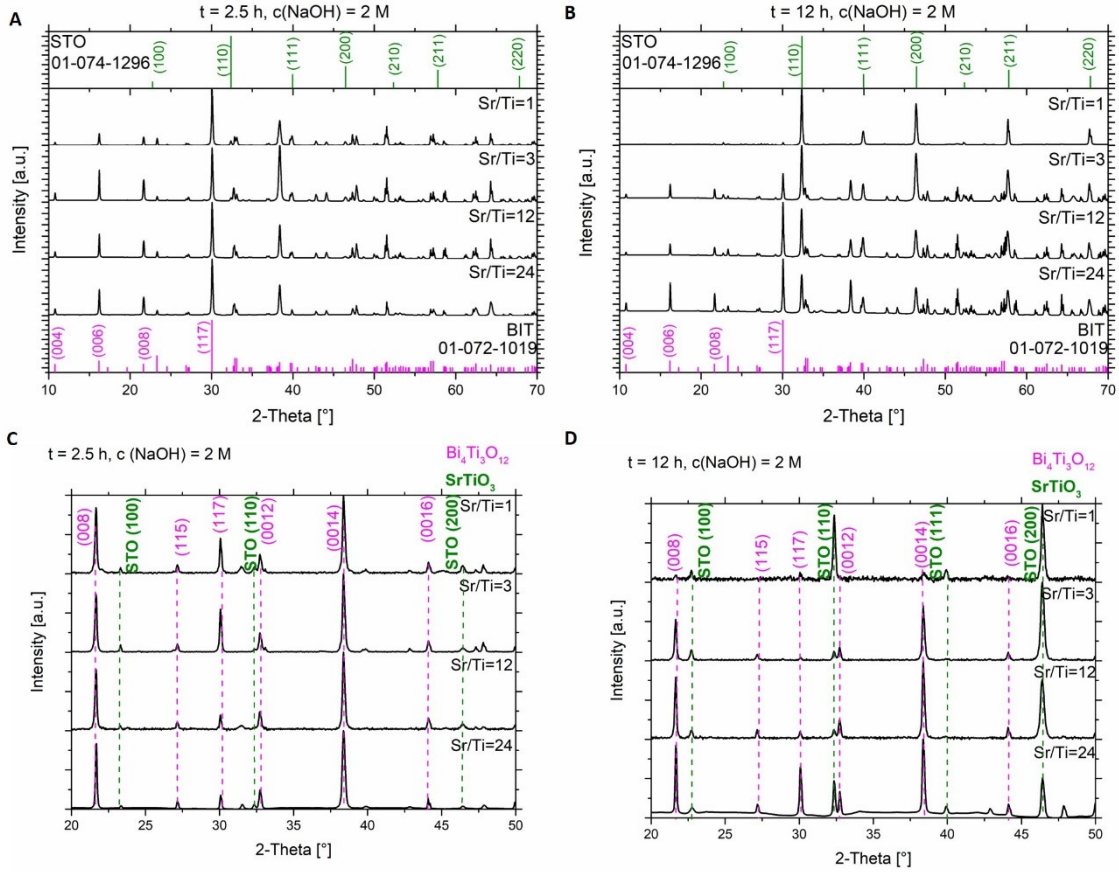

Figure 53: XRD patterns of the $SrTiO_3/Bi_4Ti_3O_{12}$ and $SrTiO_3$ platelets (A and B: powder samples, C and D: particles, cast on Si- single-crystalline substrate) formed in 2 mol/L NaOH at 200 °C with different nominal Sr/Ti ratio after 2.5 hours (A and C) and after 12 hours (B and D).

4.2.4.2 Topochemical conversion in 6 mol/L NaOH

The reactions in 2 mol/L NaOH at higher Sr/Ti ratios than stoichiometric did not completely transform $Bi_4Ti_3O_{12}$ to $SrTiO_3$ within 12 hours. To accelerate the reactions to accomplish the complete transformation in a reasonable time, the concentration of NaOH was increased for this study from 2 mol/L to 6 mol/L. According to Eq. (10): $Bi_4Ti_3O_{12} + 12H_2O + 6OH^- \rightleftharpoons 4Bi(OH)_3 + 3Ti(OH)_6^{2-}$, $Bi_4Ti_3O_{12}$ is expected to dissolve faster in 6 mol/L NaOH, providing a higher concentration of $Ti(OH)_6)^{2-}_{(aq)}$ in comparison to 2 mol/L NaOH. On the other hand, the dissolution of $Bi_4Ti_3O_{12}$ should still be slow enough to preserve the shape and to serve as the substrate for the epitaxial growth of $SrTiO_3$. The nucleation and growth progress were observed similar as in case of using 2 mol/L NaOH: for Sr/Ti= 1, 3, 12 and 24 after 2.5 h and 12 h of the reaction at 200 °C.

The XRD patterns of the $SrTiO_3/Bi_4Ti_3O_{12}$ and $SrTiO_3$ platelets (powder samples and particles cast on Si-single-crystalline substrate) are shown in Figure 54. Obviously, the transformations of $Bi_4Ti_3O_{12}$ to $SrTiO_3$ are significantly faster in 6 mol/L NaOH than previously in 2 mol/L NaOH. For easier visualization, the $SrTiO_3$ content after 2.5 h and after 12 h of the reaction is graphically presented in Figure 55.

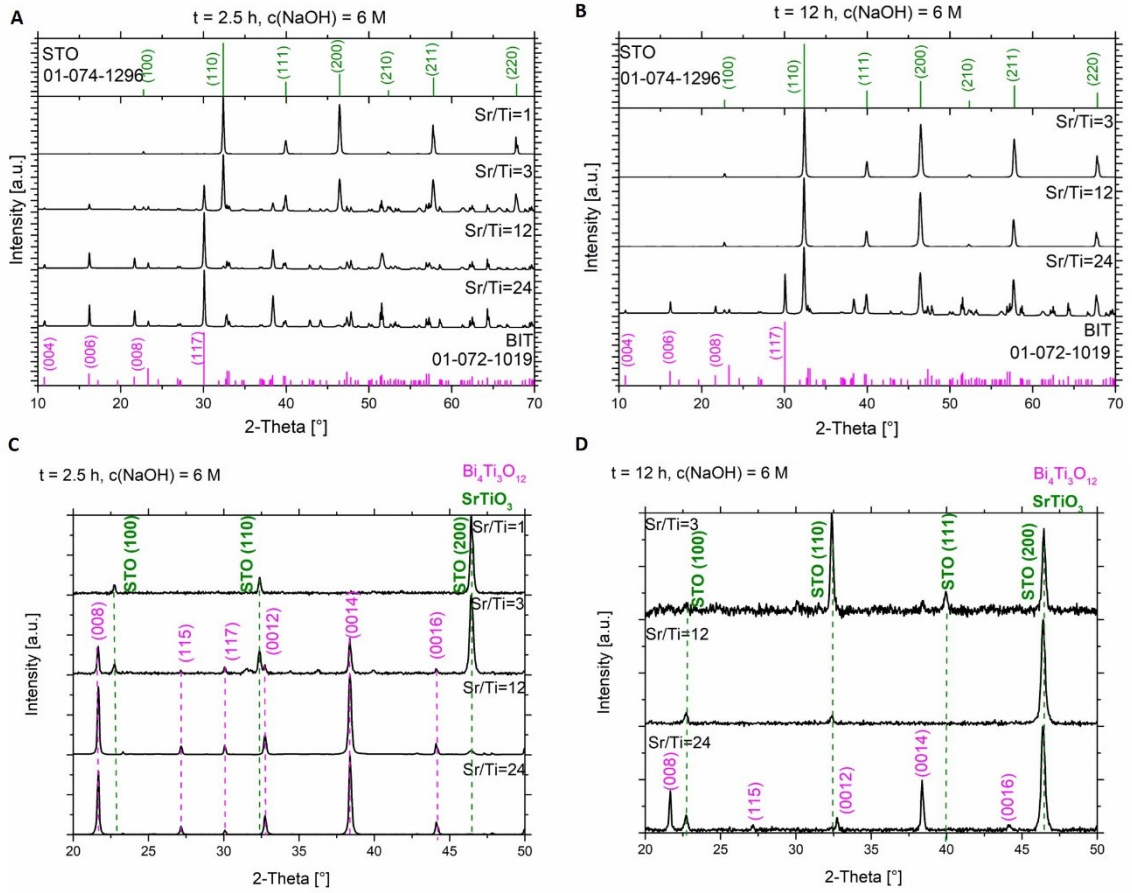

Figure 54: XRD patterns of the $SrTiO_3/Bi_4Ti_3O_{12}$ and $SrTiO_3$ platelets (A and B: powder samples, C and D: particles, cast on Si-single-crystalline substrate) formed in 6 mol/L NaOH at 200 °C with different nominal Sr/Ti ratio after 2.5 hours (A and C) and after 12 hours (B and D).

Like the reactions in 2 mol/L NaOH, also in 6 mol/L NaOH the transformation rate is decreasing with the increased Sr/Ti ratio. After 2.5 h of the reaction, pure $SrTiO_3$ is obtained in case of Sr/Ti=1. Under SEM examinations it was observed that the morphology of the template platelets is not preserved also in this case (Figure 56). Therefore, the reaction with Sr/Ti=1 in 6 mol/L NaOH was not performed for 12 h at 200 °C. For the Sr/Ti ratios higher than stoichiometric, Sr/Ti=3, 12 and 24, the presence of the $SrTiO_3$ after 2.5 h of the reaction at 200 °C was approximately 82 %, 3 % and 1%, respectively. After increasing the reaction time to 12 hours, the presence of the $SrTiO_3$ was approximately 98 % for Sr/Ti=3 and 12, and about 80 % for Sr/Ti=24.

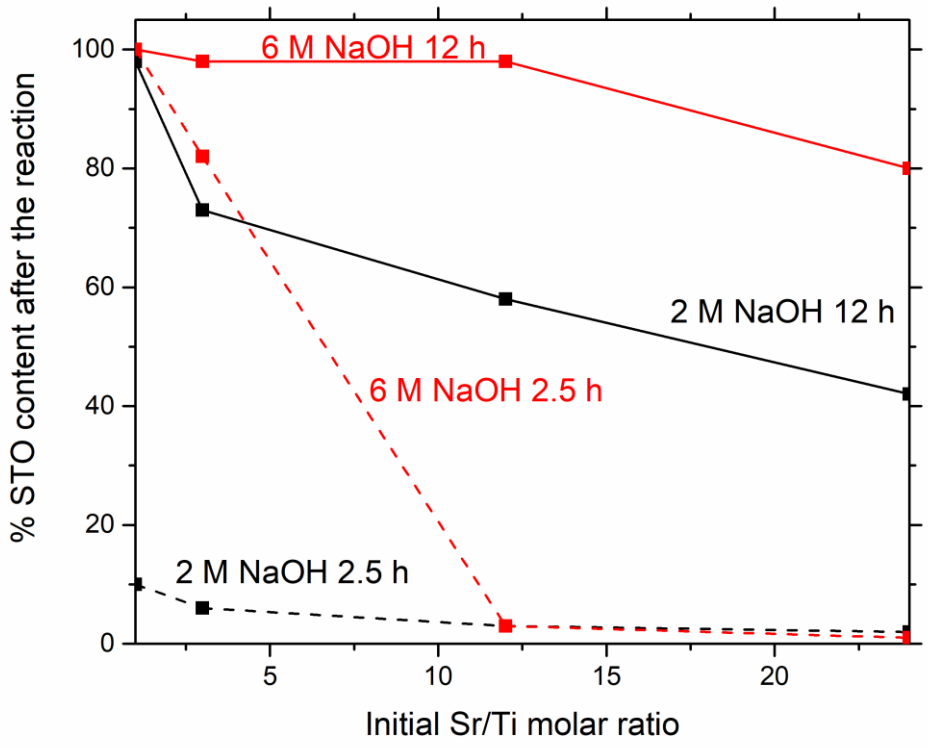

Figure 55: Graphical presentation of $SrTiO_3$ (STO) content in the platelets as a function of initial Sr/Ti ratios (Sr/Ti=1, 3, 12 and 24) at lower (2 mol/L – black lines) and higher (6 mol/L – red lines) NaOH molarity after 2.5 h (dashed lines) and after 12 h (solid lines) of the reaction at 200 °C. The STO content was determined according to the average ratio of the diffractions (200)STO/(008)BIT and (200)STO/(0014)BIT with the help of the calibration curve.

The experimental conditions with Sr/Ti=1 provide the lowest supersaturation. Together with 6 mol/L NaOH, these conditions do not allow fast enough protection of the basal surfaces of the $Bi_4Ti_3O_{12}$ template due to too low supersaturation and too fast template dissolution. Therefore, the morphology of the template is not inherited after the transformation. The $SrTiO_3$ particles obtained after the transformation reminiscent of various plate-like irregular morphologies like broken platelets, frame-like particles, or even distorted rods. The groove from the lateral side that is typical for the conditions with higher supersaturation and leads to the morphology preservation was not observed in any of the above $SrTiO_3$ nanostructures (Figure 56: A and E). This indicates that the dissolution of $Bi_4Ti_3O_{12}$ was not restricted exclusively from the lateral side, because the basal surfaces were not covered with $SrTiO_3$ nuclei (and therefore protected). Due to higher NaOH concentration (6 mol/L), the solubility of $Bi_4Ti_3O_{12}$ was even higher and the template dissolved intensively also from the top of the basal planes leading to previously described morphologies. Similar to 2 mol/L NaOH experiments, also under higher NaOH concentrations, better $SrTiO_3$ coverage and protection of the basal surface planes was observed at conditions with higher Sr/Ti ratios leading to better morphology preservation of the template (Figure 56 and Figure 57).

For the Sr/Ti ratios that exceed the stoichiometric, the particles morphology is preserved to great extent. However, for the Sr/Ti=3, it is the borderline molar ratio whether the morphology of the template will be preserved after the transformation or not. Supersaturation together with the quality of the template are the decisive elements (factors). In the case of Sr/Ti=3, the template morphology is preserved if the template is of great crystallinity with a low number of defects. In this case, the supersaturation can balance the influence of the lattice mismatch and the minor irregularities in the structure. The opposite is true for the case when the $Bi_4Ti_3O_{12}$ template batch does not show great crystallinity or possesses a very defective surface. Namely, the $Bi_4Ti_3O_{12}$ particles are very sensitive during their preparation for accurate weighting and good homogenization of reactant powders. As already mentioned earlier, this is the reason that the

$Bi_4Ti_3O_{12}$ templates were prepared in more batches and approved batches were then mixed together as a starting powder (mixture) for the systematic study of the transformations to $SrTiO_3$. In such a way, the uniformity of the template for all systematic studies was ensured. Before mixing, each $Bi_4Ti_3O_{12}$ batch was separately analyzed under SEM and XRD as well as tested under moderate hydrothermal conditions (Sr/Ti=3 in 4 mol/L NaOH for 12 h at 200 °C) to see the morphological outcome. Only $Bi_4Ti_3O_{12}$ batches that under this condition lead to satisfactory preservation of the platelet morphology, were used for further systematic studies. In this way, the only source of the difference in the morphology are the reaction conditions (so, the difference cannot be ascribed to the characteristics of the template).

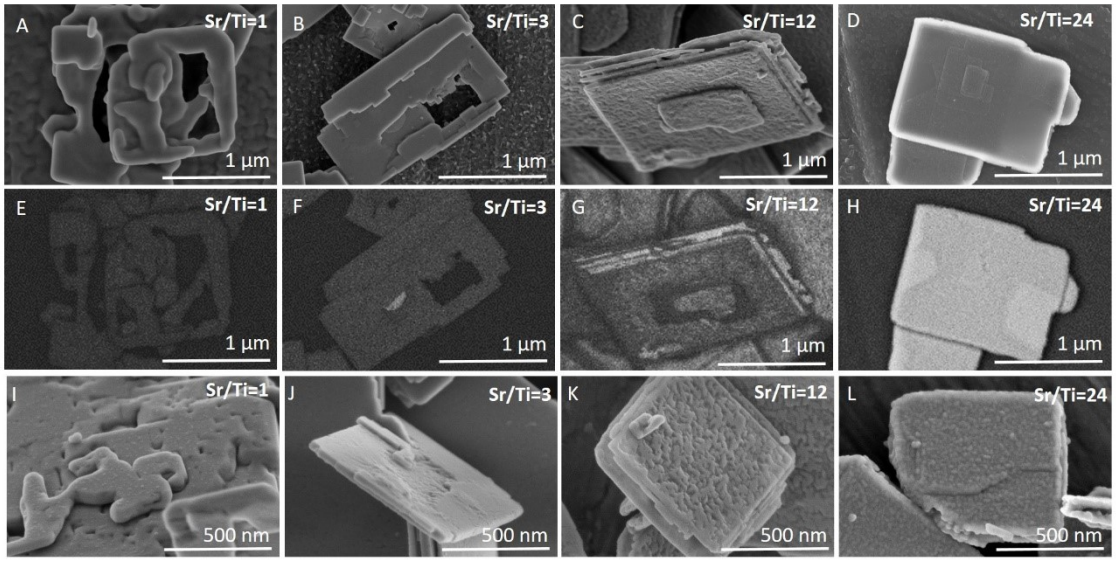

Figure 56: SEM micrographs showing the formation of $SrTiO_3$ from $Bi_4Ti_3O_{12}$ template platelets with nominal Sr/Ti= 1, 3, 12 and 24. The SE (A-D) and corresponding BSE (E-H) images of $SrTiO_3/Bi_4Ti_3O_{12}$ particles after 2.5 h of reaction at 200 °C in 6 mol/L NaOH showing the unreacted $Bi_4Ti_3O_{12}$ (bright) and formed $SrTiO_3$ (dark).

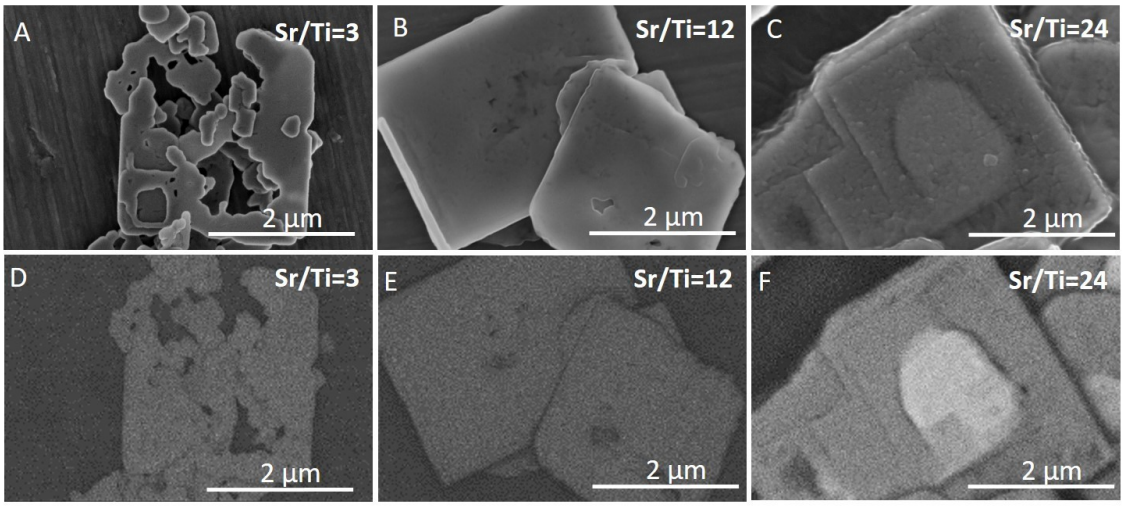

Figure 57: SEM micrographs showing the formation of $SrTiO_3$ from $Bi_4Ti_3O_{12}$ template platelets with nominal Sr/Ti= 3, 12 and 24. The SE (A-c) and corresponding BSE (D-F) images of $SrTiO_3/Bi_4Ti_3O_{12}$ particles after 12 h of reaction at 200 °C in 6 mol/L NaOH showing the unreacted $Bi_4Ti_3O_{12}$ (bright) and formed $SrTiO_3$ (dark).

The results demonstrate that the transformation from $Bi_4Ti_3O_{12}$ to $SrTiO_3$ performed in alkaline (2 mol/L or 6 mol/L NaOH) aqueous solutions at 200 °C with Sr/Ti=12 under hydrothermal conditions leads to well-preserved morphology of the initial $Bi_4Ti_3O_{12}$ template for intermediate $SrTiO_3/Bi_4Ti_3O_{12}$ as well as for the final $SrTiO_3$ structures. It is true also for higher

nominal Sr/Ti ratio (Sr/Ti=24), but the benefit of higher supersaturation does not exceed the costs of time and energy due to the deceleration of the reaction with higher supersaturation.

The comparison of the reaction pathways that can be directed by changing the reaction conditions (namely supersaturation) is schematically presented in Figure 58. The conditions with higher Sr/Ti ratios enable better protection of the basal surface planes against dissolution from the top at the beginning of the process, because the $SrTiO_3$ nucleation and growth occurs over the entire basal surface planes, while consequently the $Bi_4Ti_3O_{12}$ dissolution proceeds from the lateral sides. The process of $Bi_4Ti_3O_{12}$ dissolution and $SrTiO_3$ epitaxial growth continues till the complete transformation and formation of $SrTiO_3$ nanoplatelets. In the end, it consists of two parallel partially intergrown platelets. The groove that extends in the middle of the platelet and is parallel to the platelet's basal surface planes is the result of the $Bi_4Ti_3O_{12}$ dissolution from the lateral sides. The combination of high-quality template nanoplatelets, Sr/Ti=12 and 6 mol/L NaOH, provides the conditions for the complete transformation of $Bi_4Ti_3O_{12}$ into $SrTiO_3$ nanoplatelets in less than 12 hours. The presented procedure can also serve as some kind of general strategy for controlling hydrothermal transformations that proceed through dissolution and epitaxial growth processes.

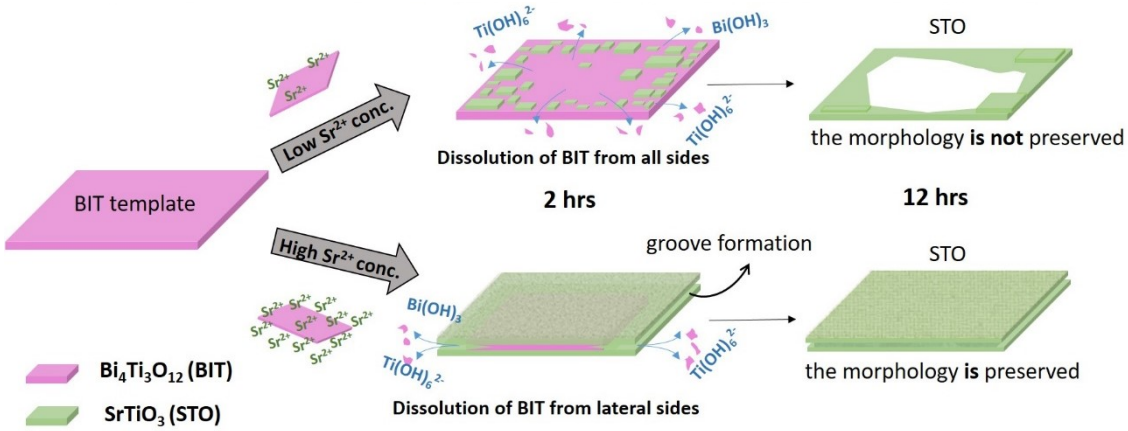

Figure 58: Schematic presentation of the reaction pathways depending on the level of the supersaturation depending on the concentration of Sr^{2+} (low and high). Modified scheme from Graphical abstract of our article [234].

4.3 Topochemical Conversion of $Bi_4Ti_3O_{12}$ Platelets to Other $MTiO_3$ Platelets Under Hydrothermal Conditions

4.3.1 $BaTiO_3$

Barium titanate ($BaTiO_3$, also BT or BTO) is a ferroelectric perovskite oxide. The key applications of barium titanate are in multilayer ceramic capacitors [248], thermoelectric and piezoelectric applications [249], energy harvesters [250], and (piezo)catalysis [251]–[253]. Lately, $BaTiO_3$ has also been investigated in cancer therapy, aids for faster healing and drug delivery systems [254]. $BaTiO_3$ with a larger A-site cation in comparison to $SrTiO_3$ has some limitations in the efficiency of topochemical conversion hydrothermal heteroepitaxial growth starting from $Bi_4Ti_3O_{12}$ template platelets [251]. However, due to the great application potential of $BaTiO_3$, it would be interesting to prepare this material in a 2D platelet shape. Great potential also has various 2D heterostructures containing the $BaTiO_3$ phase.

For the study of the transformation from the $Bi_4Ti_3O_{12}$ to $BaTiO_3$, similar strategies (various excess of Ba) and reaction conditions (200 °C, different NaOH concentrations) were used as previously for the research of topochemical conversion from $Bi_4Ti_3O_{12}$ template platelets to $SrTiO_3$. With respect to $Bi_4Ti_3O_{12}$-to-$SrTiO_3$-transformation, where the lattice spacing of (110) in $Bi_4Ti_3O_{12}$ (3.842 Å) and (100) $SrTiO_3$ (3.905 Å) corresponds to lattice mismatch of 1.8 %, the corresponding lattice spacing ((110) in $Bi_4Ti_3O_{12}$ (3.842 Å) and (100) $BaTiO_3$ (4.006 Å)) results in much larger misfit, around 4 %. Due to this greater misfit, the complete $BaTiO_3$ overgrowth of the $Bi_4Ti_3O_{12}$ basal surface planes and consequently the formation of $BaTiO_3$ platelets with inherited platelet shape of the $Bi_4Ti_3O_{12}$ template is under question whether it is possible under normal hydrothermal conditions without special additives. The reactants and synthesis procedure for the $Bi_4Ti_3O_{12}$-to-$BaTiO_3$-transformation are described in the methods section 3.2.2.2.

The reaction temperature, time, stirring, NaOH concentration, and nominal Ba/Ti molar ratio were changed and their effect on the morphology of the product particles and composition was studied.

First, NaOH concentration of 6 mol/L was selected and experiments with Ba/Ti=1, 3 and 12 were performed at 200 °C for 12 hours with stirring. Aditionally, the experiment with shorther reaction time (3 hours) was performed for Ba/Ti=12 to evaluate the reaction time, needed for the complete transformation and to track the morphology evolution. SEM and XRD results are shown in Figure 59. It is evident that after a 12-hour reaction the amount of $BaTiO_3$ increased with the increase of Ba excess (Ba/Ti ratio). At Ba/Ti=1 and 3, $Bi_4Ti_3O_{12}$ phase was still present after 12 hour reaction and its amount decreased when Ba/Ti icreased from Ba/Ti=1 to Ba/Ti=3. At Ba/Ti=12, the transformation to $BaTiO_3$ was nearly completed after 3 hours. Under conditions with a high excess of Ba (Ba/Ti=3 and 12) $BaTiO_3$ particles exhibit clear tetragonal crystal structure, while stoichiometric Ba/Ti ratio results in pseudocubic $BaTiO_3$ phase. For the stoichiometric Ba/Ti nominal ratio, $BaTiO_3$ particles formed in a octahedral morphology. On the contrary, when Ba was added in excess, cubic $BaTiO_3$ particles formed. None of the above conditions (C_{NaOH}=6 mol/L, Ba/Ti=1-12) enabled preservations of the platelet morphology. These results clearly show, that the nucleation rate of $BaTiO_3$ over the basal surface planes of the $Bi_4Ti_3O_{12}$ platelet is not so high to protect the dissolution of the platelet from the top, what is essential that the platelet morphology is preserved.

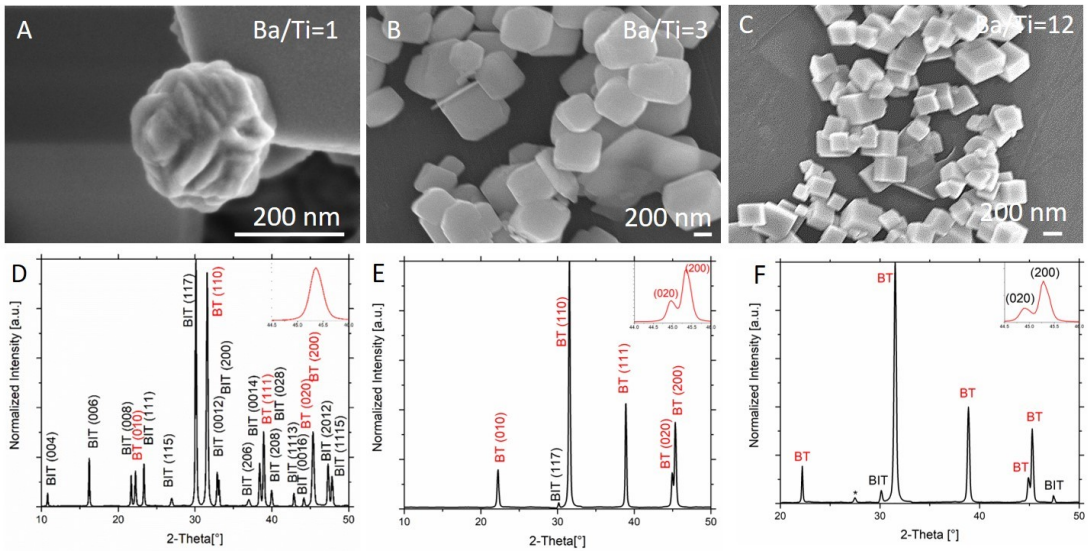

Figure 59: SEM micrographs and XRD patterns of particles during the topochemical conversion of $Bi_4Ti_3O_{12}$ platelets to $BaTiO_3$ under hydrothermal conditions in 6 mol/L NaOH. Initial molar Ba/Ti ratios were 1 (A and D), 3 (B and E) and 12 (C and F). The reaction time was 12 hours for Ba/Ti=1 and Ba/Ti=3, and 3 hours for Ba/Ti=12. The reaction temperature was 200 °C in all cases. The reaction was performed under stirring conditions.

The same was not observed for Ba/Ti ratios of 3 and 12 when the reaction was also performed in 2 mol/L NaOH. By increasing the initial Ba/Ti ratio to 12, $BaTiO_3$ still grows on $Bi_4Ti_3O_{12}$ in islands, while the shape of $BaTiO_3$ particles changed to cubes. According to XRD, both ($BaTiO_3$ and unreacted $Bi_4Ti_3O_{12}$) phases were present after 1 hour of the reaction (Figure 60E), but after 12 hours almost all $Bi_4Ti_3O_{12}$ template transformed to $BaTiO_3$ cubes. This result again confirms that larger excess of Ba ions promotes the higher rate of $BaTiO_3$ formation. Namely, at lower Ba excess (Ba/Ti=1 and 3), great part of the $Bi_4Ti_3O_{12}$ template remained untransformed after 12 hours. In contrast to $Bi_4Ti_3O_{12}$-to-$SrTiO_3$-transformation, the misfits between the corresponding lattice planes of $BaTiO_3$ and $Bi_4Ti_3O_{12}$ are too large to facilitate high nucleation rate of $BaTiO_3$ over the whole basal surface planes of $Bi_4Ti_3O_{12}$ platelets. This is a prerequisite to protect $Bi_4Ti_3O_{12}$ dissolution from the top and thus enable preservation of the platelet shape in the course of transformation. Presumably, $BaTiO_3$ nucleates on energetically most favorable sites of $Bi_4Ti_3O_{12}$ basal surfaces (edges, corners, kink sites at steps) and then the growth continued on the formed $BaTiO_3$ islands rather than on the unprotected $Bi_4Ti_3O_{12}$ sites. $Bi_4Ti_3O_{12}$ in the vicinity of $BaTiO_3$ particles dissolved and provided $Ti(OH)_6^{2-}$ for further $BaTiO_3$ growth. As a consequence, $BaTiO_3$ cubes and tetrahedrons with the side length around 150-300 nm formed. Additionally, from SEM micrographs A and B in Figure 60 it is seen how $BaTiO_3$ particles grew in layer by layer manner, accompanied by the formation of polyatomic steps. Polyatomic steps typically form by bunching of monoatomic steps due to local fluctuations in supersaturation or impurities. The steps with higher height advance at a lower rate due to the needs for greater flux of ions [40]. The steps are only visible in the case of lower Ba/Ti ratios of 1 and 3, while larger excess of Ba (Ba/Ti=12) leads to the formation of cube-like islands without visible steps.

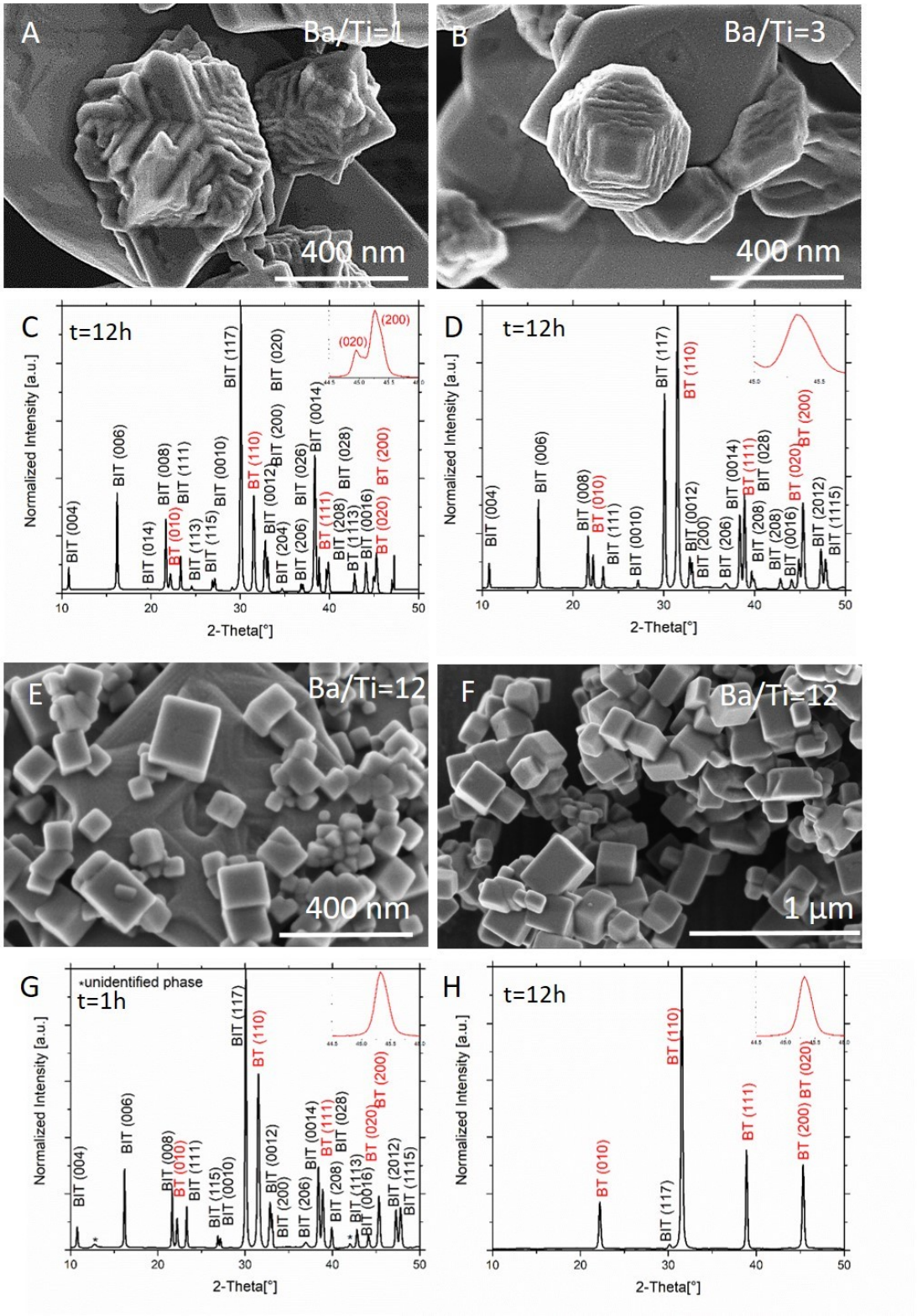

Figure 60: SEM micrographs and powder XRD patterns of particles during the topochemical conversion of $Bi_4Ti_3O_{12}$ platelets to $BaTiO_3$ under hydrothermal conditions in 2 mol/L NaOH. Initial molar Ba/Ti ratios and reaction times are written on every image. The reaction temperature was 200 °C. The reaction was performed under stirring conditions.

None of previously examined reaction conditions combinations was sufficient to be able to provide conditions for $BaTiO_3$ layer-by-layer growth over the entire basal surfaces of $Bi_4Ti_3O_{12}$, which would result to formation of $BaTiO_3$ with inherited platelet morphology. For this reason, some additional synthesis trials at higher temperature of 220 °C were performed. The highest reaction temperature in this study was 220 °C, because this is the limit temperature according to the recommendations of the autoclave manufacturer. The reactants were added in amounts corresponding to Ba/Ti nominal molar ratio 24, concentration of NaOH was 8 mol/L, the reaction temperature was 220 °C, stirring was 150 rpm, the reaction time was 1 hour to see the transformation in early stage and after 12 hours to see the final products. For this case, $BaTiO_3$ formed in cube-like and platelet-like morphologies. Nevertheless, the anisotropic 2D $BaTiO_3$ structures typically do not represent the entirely preserved shape of the template platelets (Figure 61A). Side products were also evaluated. XRD analysis of product particles washed only with deionized water revealed that besides $BaTiO_3$ and $Bi_4Ti_3O_{12}$ also $Bi_{12}TiO_{20}$, $Bi_{20}TiO_{32}$, $BaCO_3$ and Bi_2O_3 formed (Figure 61B). Secondary phases were removed after washing with 1 mol/L HNO_3.

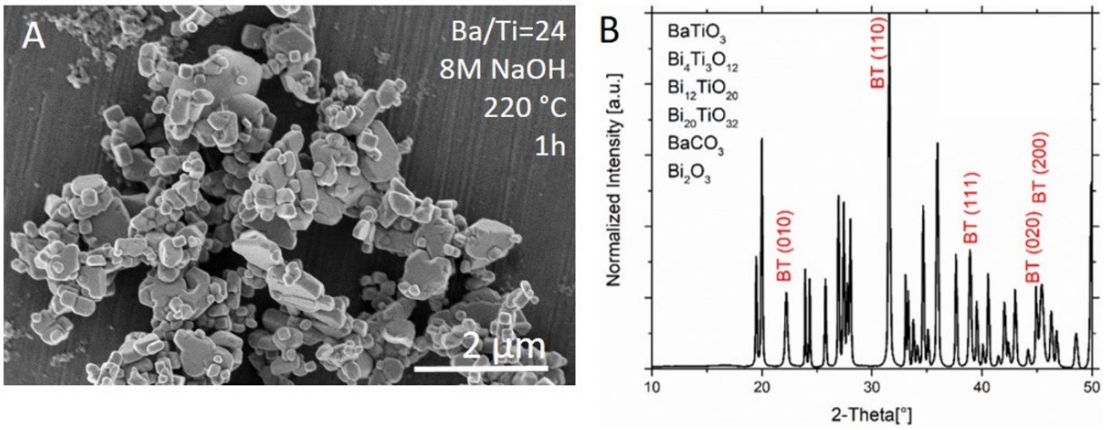

Figure 61: SEM micrograph (A) and powder XRD pattern (B) of product particles after 1 hour of the conversion of $Bi_4Ti_3O_{12}$ platelets to $BaTiO_3$ with Ba/Ti=24, 8 mol/L NaOH, 220 °C with stirring. Product powder was washed only with water to determine side products.

Some experiments were also performed under non-stirring conditions. Again, various morphologies were obtained, however, none of the selected reaction conditions lead to $BaTiO_3$ platelets after the reaction (Figure 62). Like stirring conditions, also under non-stirring conditions, higher Ba excess (Ba/Ti=12) leads to $BaTiO_3$ cubes and the transformation is nearly completed within 12 hours with negligible remains of the $Bi_4Ti_3O_{12}$ present (XRD patterns shown in Figure 63). At stoichiometric Ba/Ti ratio (Ba/Ti=1) and lower excess of Ba (Ba/Ti=3) in 1 mol/L NaOH, elongated $BaTiO_3$ nanostructures were grown from the $Bi_4Ti_3O_{12}$ platelet templates. Under these (i.e. the lowest used in this study) supersaturations conditions, $BaTiO_3$ starts to nucleate on the small area on the $Bi_4Ti_3O_{12}$ platelet and then $BaTiO_3$ continues to grow, forming elongated rods. At higher NaOH concentration (i.e. 4 mol/L), different rose-like and propeller-like morphologies were obtained (Figure 62 A, B and D). Also in this case, $BaTiO_3$ starts to grow on energetically most favorable sites of $Bi_4Ti_3O_{12}$ and not over the entire basal surface planes. The unprotected surface of the $Bi_4Ti_3O_{12}$ platelets dissolves and the product $BaTiO_3$ particles do not resemble the template morphology. The main reason for such reaction pathway and morphological development could be attributed to large lattice misfit (4 %) between the phases. From XRD patterns (Figure 63), it is seen that $BaTiO_3$ is the main phase after 12 h-24 h under experimental conditions combining Ba/Ti=12 with 1 mol/L or 4 mol/L NaOH (Figure 63 C), and Ba/Ti=3 with 4 mol/L NaOH (Figure 63 B). These results confirm that the Ba excess and NaOH concentration play the most important role in morphological development, while stirring conditions do not have significant impact.

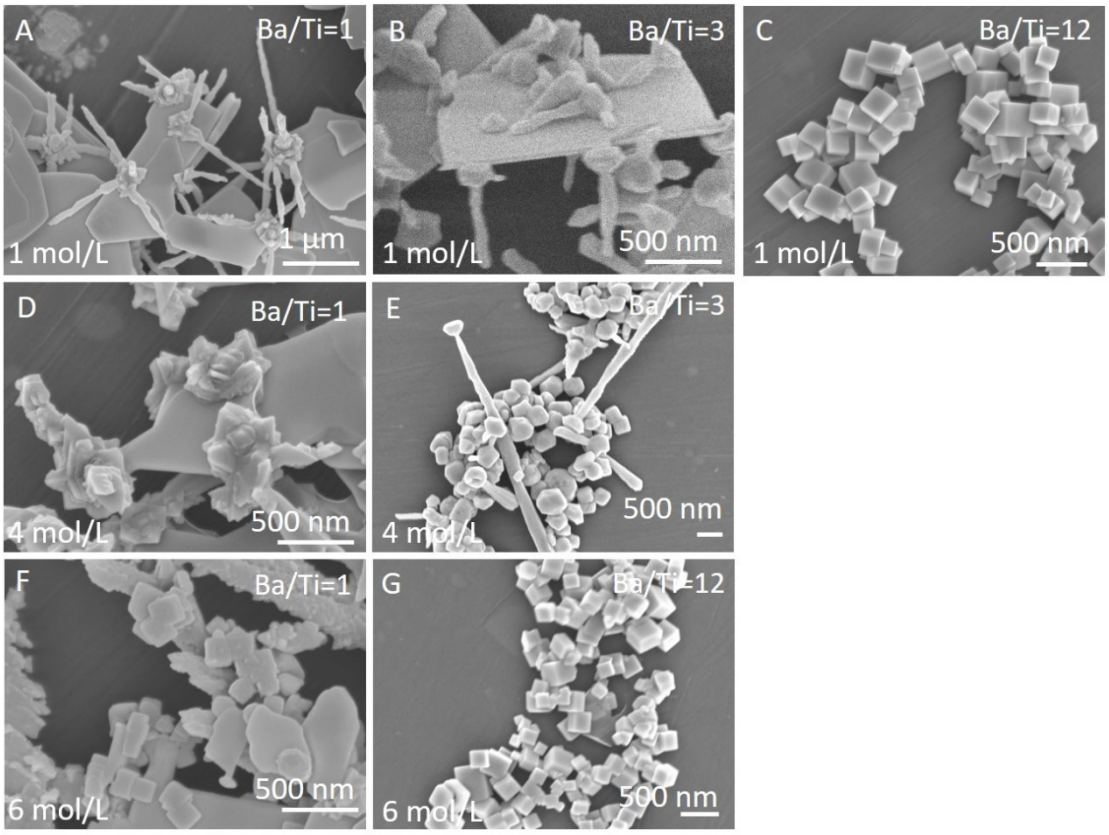

Figure 62: SEM micrographs of product particles after the hydrothermal transformation of $Bi_4Ti_3O_{12}$ platelets to $BaTiO_3$ in 1 mol/L NaOH (A-C), 4 mol/L NaOH (D, E) and 6 mol/L NaOH (F, G). Nominal Ba/Ti ratios and NaOH concentrations are written on images. The reaction temperature was 200 °C, reaction time 12 hours (all, except A and D). The reaction time in A and D was 24 hours.

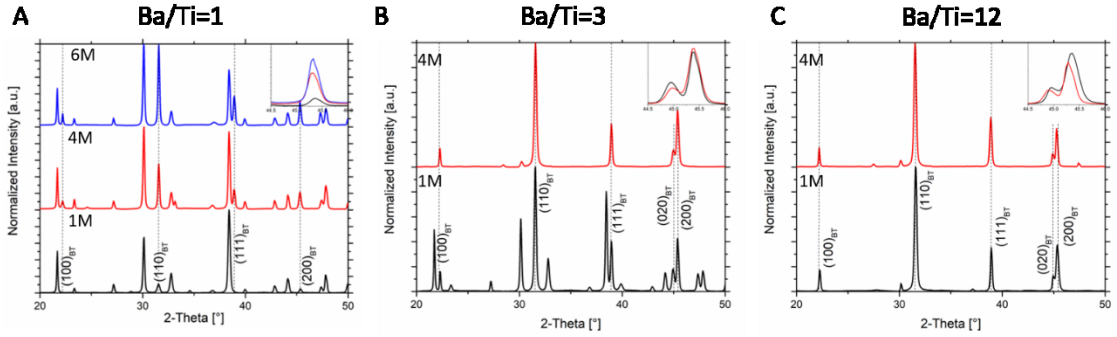

Figure 63: XRD patterns of product particles after the hydrothermal transformation of $Bi_4Ti_3O_{12}$ platelets to $BaTiO_3$ for nominal molar ratio Ba/Ti =1 (1, 4 and 6 mol/L NaOH), Ba/Ti=3 (1 and 4 mol/L NaOH) and Ba/Ti=12 (1 and 6 mol/L NaOH). The reaction temperature was 200°C, reaction time 12 hours, except for BaTi=1 with 1mol/L and 4 mol/L NaOH, the reaction time was 24 hours. Non-denoted peaks belong to $Bi_4Ti_3O_{12}$.

From SEM micrographs of partially converted particles, formed at higher Ba excess (Ba/Ti=12), it is evident that the cube formation starts already at the beginning of the conversion. The growth starts on the sites on basal surface of $Bi_4Ti_3O_{12}$ that are energetically most favorable. $Bi_4Ti_3O_{12}$ template in the vicinity of these sites dissolves and provides titanium ions ($Ti(OH)_6^{2-}$ octahedra) for the formation of $BaTiO_3$. Unfortunately, for the $BaTiO_3$, the lattice mismatch between $BaTiO_3$ and $Bi_4Ti_3O_{12}$ is too big to be overcome just by changing the Ba/Ti ratio and NaOH concentrations. In all cases, no matter how large excess of Ba was used (the highest Ba/Ti nominal molar ratio was 24 and concentration of NaOH 8 mol/L, Figure 61), the island formation

growth prevails over layer-by-layer growth. The shapes of growing $BaTiO_3$ strongly depend on the Ba/Ti ratios and NaOH concentration and changed from elongated rods, stars, flowers to octahedrons and cubes (Figure 59, Figure 60 and Figure 62).

Recently, a research group from ETH Zürich prepared well-defined $BaTiO_3$ nanosheets with highly exposed {001} polar facets according to our procedure [153]. The difference in experimental parameters in comparison to this study is higher temperature (240 °C), higher concentrations of $Bi_4Ti_3O_{12}$ (0.002133 mol/L) and NaOH (12 mol/L), while Ba/Ti nominal molar ratio was 8.8. The main distinction was the usage of sodium oleate to additionally help regulate the morphology. The role of sodium oleate was not explained. Their particles were tested for piezocatalytic organic pollutant degradation and hydrogen evolution and achieved 3- and 2-times higher rates in comparison to $BaTiO_3$ nanoparticles.

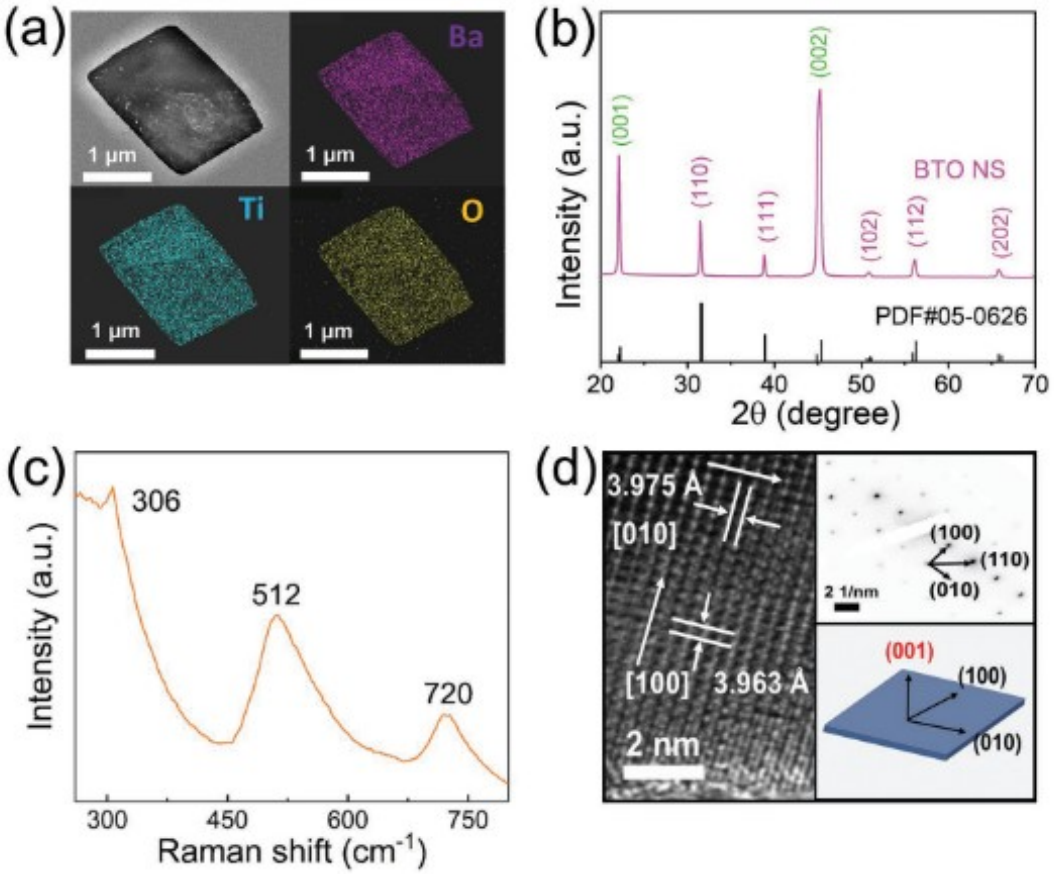

Figure 64: $BaTiO_3$ nanosheets prepared by hydrothermal topochemical transformation of $Bi_4Ti_3O_{12}$ platelets with the addition of sodium oleate (Adopted from Tang et al. [153]).

4.3.2 $CaTiO_3$

Calcium titanate ($CaTiO_3$, also CT or CTO) is a ceramic material with a perovskite structure, which naturally does not show high anisotropy. This dielectric material is widely used as a capacitor in electronic circuits, for microwave resonators, high-frequency filters and radioactive waste detectors. In the last decade, $CaTiO_3$ is investigated as a photocatalyst for water purification to replace TiO_2, or in solar cells [7], [29], [255], [256]. For microwave dielectric-resonator applications, dielectric ceramics materials should have high relative permittivity, low dielectric loss and a temperature-stable resonant frequency [257]. $CaTiO_3$ undergoes three phase transitions: above 1307 °C it is cubic, between 1227 °C and 1107 °C it is tetragonal and under 1107 °C it is orthorhombic [258]. Most commonly, $CaTiO_3$ is prepared by solid state reaction and sintering [258], [259] or hydrothermal/solvothermal method [176], [260]–[262]. The main disadvantage of the former approach is that this reaction needs high calcination temperature. Topochemical microcrystal conversion method was used for fabrication of textured microwave dielectric $CaTiO_3$ ceramics [107]. Plate-like $CaBi_4Ti_4O_{15}$ was used as a template precursor. The reaction was performed at 950 °C for 8 hours in molten KCl flux. Reaction was as follows: $CaBi_4Ti_4O_{15} + 3CaCO_3 \rightarrow 4CaTiO_3 + 2Bi_2O_3 + 3CO_2$. Precursor particles were plates with a thickness of approximately 0.3 µm, and a width of 2-6 µm. (00l) plane of the precursor was converted into the (h00) plane of the $CaTiO_3$.

In the literature, various $CaTiO_3$ morphologies were reported, including cubes, cuboids, blocks, rods, flower-like particles etc. [262]–[269]. As for other $MTiO_3$ (M for Ba and Sr) perovskites, preparation of highly anisotropic 1D and 2D $CaTiO_3$ nanostructures is not an easy task. To the best of my knowledge, hydrothermal synthesis of $CaTiO_3$ nanoplatelets has not been reported yet. Results of my work on the preparation of anisotropically shaped $SrTiO_3$ particles showed that it is possible to perform topochemical transformation of $Bi_4Ti_3O_{12}$ template platelets into $SrTiO_3$ platelets. Due to the similarity of crystal structures of $SrTiO_3$ and $CaTiO_3$ I decided to perform this preliminary study to verify whether $Bi_4Ti_3O_{12}$ platelets can be topochemically transformed to $CaTiO_3$ platelets under hydrothermal conditions. In the designing of the synthesis conditions, I have taken into account the findings obtained in the study of the $Bi_4Ti_3O_{12}$-to-$SrTiO_3$ transformation. According to my previous work, $Bi_4Ti_3O_{12}$ platelets have to be well dispersed in the reaction mixture in order to ensure optimal conditions for the topochemical transformation. The selected temperature range for $CaTiO_3$ formation was 180 °C – 200 °C, Ca/Ti equals 1-3 and C_{NaOH} varied from 2 mol/L to 6 mol/L. In order to evaluate the role of the titanate precursor, $CaTiO_3$ was also synthesized using other TiO_2 precursors (TiO_2 nanopowder P25 and TiO_2 anatase) in addition to $Bi_4Ti_3O_{12}$ platelets (Table 15).

Table 15: Reaction parameters for the preparation of $CaTiO_3$ particles by hydrothermal topochemical conversion from $Bi_4Ti_3O_{12}$ (BIT) platelets.

Sample	Temperature	Holding time	Ca/Ti ratio	c(NaOH)	Ti - source	c(BIT)
A	200 °C	12 h	1	4 mol/L	**TiO_2 P25**	N.A.
B	200 °C	12 h	1	4 mol/L	**TiO_2 anatase**	N.A.
C	180 °C	**6 h**	3	6 mol/L	BIT	1.423 mmol/L
D	180 °C	**12 h**	3	6 mol/L	BIT	1.423 mmol/L
E	180 °C	12 h	3	6 mol/L	BIT	**0.711 mmol/L**
F	180 °C	12 h	3	6 mol/L	BIT	**2.846 mmol/L**
G	180 °C	12 h	3	**2 mol/L**	BIT	1.423 mmol/L
H	**200 °C**	12 h	3	**4 mol/L**	BIT	1.423 mmol/L
I	**220 °C**	12 h	3	**6 mol/L**	BIT	1.423 mmol/L

Figure 65 shows the morphology of the hydrothermal reaction product using P25 TiO_2 (A), anatase TiO_2 (B) and $Bi_4Ti_3O_{12}$ template plates (C and D). For hydrothermal synthesis of $CaTiO_3$ A and B the reaction conditions were the same: Ca/Ti=1, 6 mol/L NaOH was used as a mineralizer, reaction temperature was 200 °C and the reaction time was 12 hours.

For the topochemical reaction as a way to prepare $CaTiO_3$ platelets from $Bi_4Ti_3O_{12}$ template platelets, the reaction conditions were varied by changing the reaction temperature (180 °C, 200 °C) reaction time (6 hours, 12 hours), molarity of NaOH (from 2 mol/L to 6 mol/L) and the

concentration of $Bi_4Ti_3O_{12}$ templates (see Table 1). For the preparation of $CaTiO_3$ from $Bi_4Ti_3O_{12}$, the nominal molar ratio of Ca and Ti (Ca/Ti ratio) was in all experiments the same – Ca/Ti=3. This means that Ca was added in the 3-times higher amount than stoichiometrically needed. It can be seen that in case of using TiO_2, the morphology of particles resulted in block-like shape, while in case of using plate-like $Bi_4Ti_3O_{12}$ templates, the shape of plates was preserved to some extent, depending on the reaction conditions (Figure 65, Figure 67, and Figure 69). Moreover, $CaTiO_3$ blocks are significantly smaller when using P25 TiO_2 in comparison to anatase TiO_2 precursor. This difference could arise from different sizes of TiO_2 nanoparticles, which influences TiO_2 dissolution and $CaTiO_3$ nucleation rates. In accordance to widely known reports from the literature, these results confirm that the size and the morphology of the precursor as well as reaction conditions influence the size and morphology of the product particles. In Figure 66, XRD patterns for samples A-D are presented. Phases that were identified and matched for each sample are denoted above the corresponding XRD patterns.

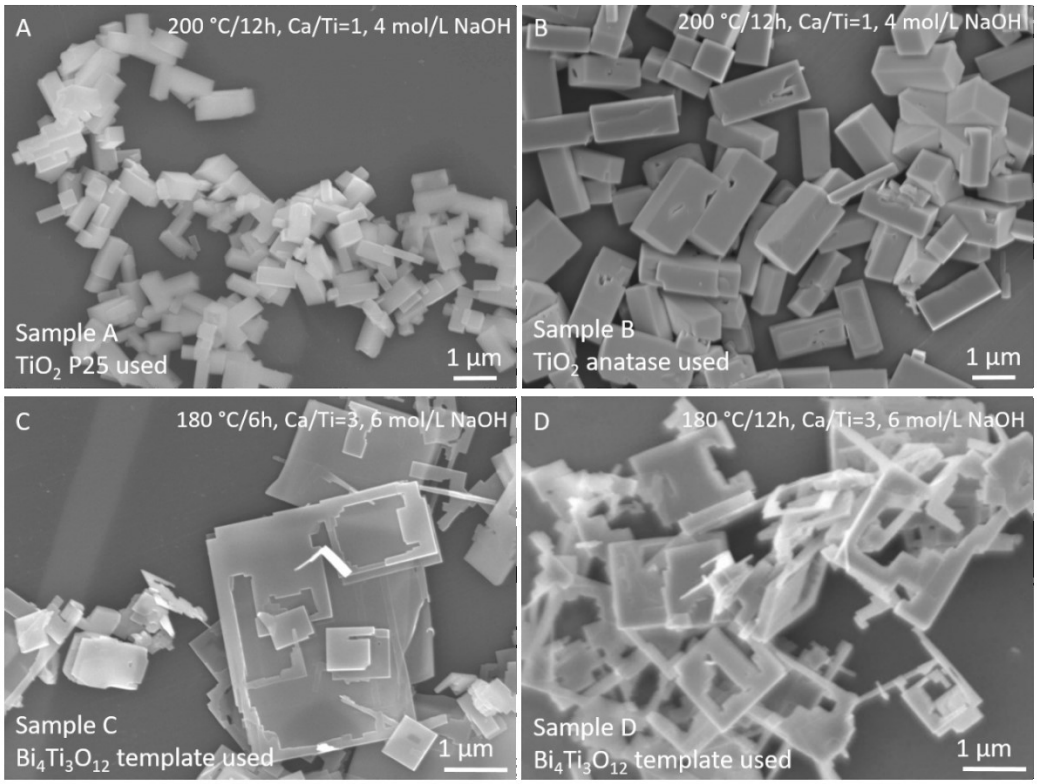

Figure 65: The morphology of prepared $CaTiO_3$ particles. Particles were prepared from TiO_2 P25 (A), TiO_2 anatase (B), $Bi_4Ti_3O_{12}$ template platelets (C and D) at different reaction conditions.

.

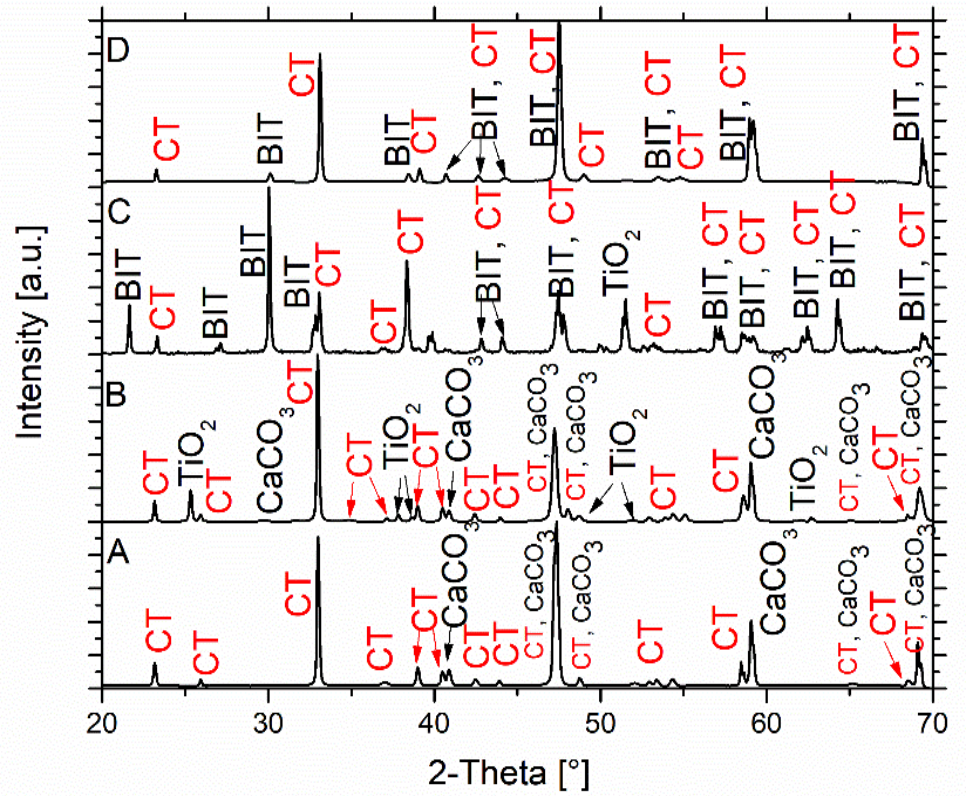

Figure 66: Powder XRD patterns for $CaTiO_3$ particles prepared from A: TiO_2 -P25 nanopowder, B: TiO_2 – anatase, C and D: $Bi_4Ti_3O_{12}$ platelets. Reaction conditions for A and B: nominal molar ratio Ca/Ti=1, 6 mol/L NaOH, 200 °C, 12 hours. For C and D: Ca/Ti=3, 6 mol/L NaOH, 180 °C, 6 hours (C) and 12 hours (D).

In reaction C, the reaction time was shorter in comparison to reaction D and the transformation did not occur completely. There are still clearly seen patterns for the remains of a $Bi_4Ti_3O_{12}$ template. As the reaction time was prolonged to 12 hours, the transformation was almost concluded and orthorhombic $CaTiO_3$ was the main phase (Figure 66). From SEM images C and D in Figure 65 it can be seen that the platelet shape is to some extent preserved, indicating that the transformation proceeds through dissolution and epitaxial growth. Based on this result it could be inferred that $Bi_4Ti_3O_{12}$ platelets are an appropriate template for the topochemical conversion into $CaTiO_3$ platelets, however, it is not necessary that optimal reaction conditions would be found easily.

During the study of topochemical conversion of $Bi_4Ti_3O_{12}$ to $SrTiO_3$ it was observed that reactant mass also influences the morphology of prepared particles. Therefore, the next parameter that was investigated for the $Bi_4Ti_3O_{12}$-to-$CaTiO_3$ transformation was the influence of the reactant's concentrations. For this experiment, the mass of $Bi_4Ti_3O_{12}$ was set to 0.1 g, 0.2 g and 0.4 g. SEM images and XRD patterns of the reaction products are presented in Figure 67 and Figure 68, respectively. From Figure 67A (sample E, using 0.1 g $Bi_4Ti_3O_{12}$) and Figure 67B (sample D, using 0.2 g $Bi_4Ti_3O_{12}$) we cannot see any significant difference in particle morphology. From XRD pattern it is also seen that the reaction with 0.2 g of $Bi_4Ti_3O_{12}$ is completed. Due to the lack of product powder, it was not possible to obtain powder XRD pattern for the experiment with 0.1 g $Bi_4Ti_3O_{12}$ (sample E). Based on SEM micrographs of particles obtained from 0.1 g and 0.2 g of $Bi_4Ti_3O_{12}$ and the XRD pattern for the 0.2 g experiment, it can be assumed that the reaction with 0.1 g $Bi_4Ti_3O_{12}$ was completed and the $CaTiO_3$ was the main phase. Unfortunately, the particle shape was not preserved. Moreover, the platelets were broken into smaller particles, some of them retained the platelet shape, other parts were in different morphologies, including rods and frames. Some individual preserved platelets and frames with the dimensions of the initial template indicate that the transformation includes the elements of topochemical conversion (epitaxial growth). Nevertheless, the results disclose that under experimental conditions of the samples D-F, the nucleation rate of $CaTiO_3$ was not high enough to protect the basal surface planes of the $Bi_4Ti_3O_{12}$ platelets against dissolution from the top. Product particles in the experiment F (0.4 g of $Bi_4Ti_3O_{12}$) still maintain the plate-like shape of the template, but as seen from its XRD pattern in Figure 68, there is a great amount of unreacted $Bi_4Ti_3O_{12}$ still present.

From SEM micrographs and XRD patterns in Figure 65-Figure 68, it is evident that shorter reaction time and higher reactant mass show similar influence on the transformation rate and product morphology. Higher mass and shorter time resulted in lower degree of transformation (lower amount of $CaTiO_3$).

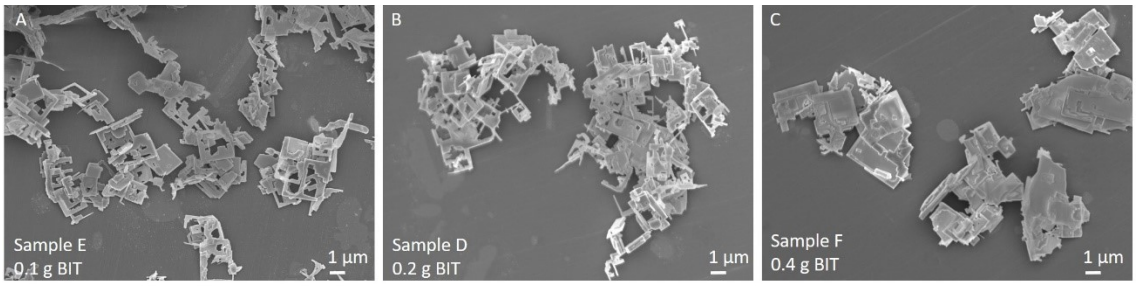

Figure 67: SEM images for the comparison of the influence of the mass of $Bi_4Ti_3O_{12}$ template platelets: a) 0.1 g, b) 0.2 g and c) 0.4 g with the reaction parameters: 6 mol/L NaOH, reaction temperature 180 °C, and holding time 12 h. Nominal molar ratio Ca/Ti was 3.

.

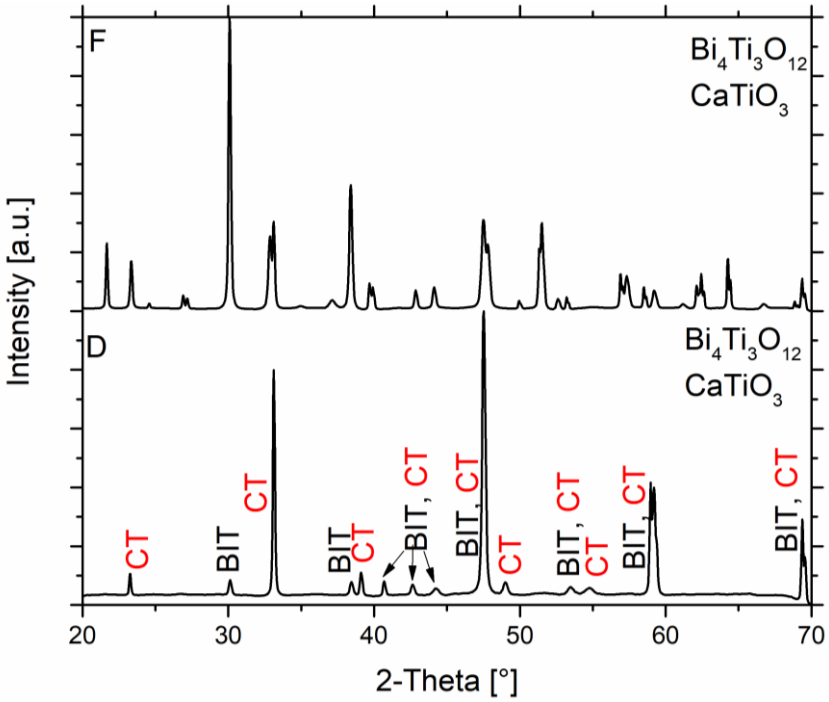

Figure 68: XRD pattern for the comparison of the influence of the $Bi_4Ti_3O_{12}$ mass. Sample E: 0.1 g is not shown due to lack of product powder, D: 0.2 g and F: 0.4 g template platelets for the topochemical conversion at same reaction conditions (6 mol/L NaOH, 180 °C 12 hours)

Afterwards, I investigated the influence of the mineralizer concentration in combination with temperature. SEM micrographs and powder XRD patterns are shown in Figure 69 and Figure 70, respectively. Reaction in 2 mol/L NaOH and at 180°C (Sample G) resulted in well-preserved plate-like shape, however the reaction did not complete in 12 hours at these conditions, because there is still $Bi_4Ti_3O_{12}$ phase present in the product as it is evident from the XRD pattern. On the other hand, the reaction is nearly completed after 12 hours when using 4 mol/L NaOH and 200 °C (sample H). Despite the plate-like shape of the template not being completely preserved in these two cases – in some cases it resembles frame-like shape, the morphology looks very promising in terms of being able to prepare $CaTiO_3$ platelets with some further optimization, including the Ca/Ti ratio. The latter optimization has not been done so far, but as it was observed from the $Bi_4Ti_3O_{12}$-to-$SrTiO_3$ transformation, the increase in Ca/Ti ratio is expected to be essential so that $CaTiO_3$ better preserves the $Bi_4Ti_3O_{12}$ template morphology. In the last experiment (sample I), the temperature was increased to 220 °C together with the NaOH concentration (6 mol/L) and it seems to be beneficial. The morphology of the $CaTiO_3$ particles of sample I appears

similar to $SrTiO_3$ platelets prepared in this thesis by topochemical conversion of the $Bi_4Ti_3O_{12}$ platelets.

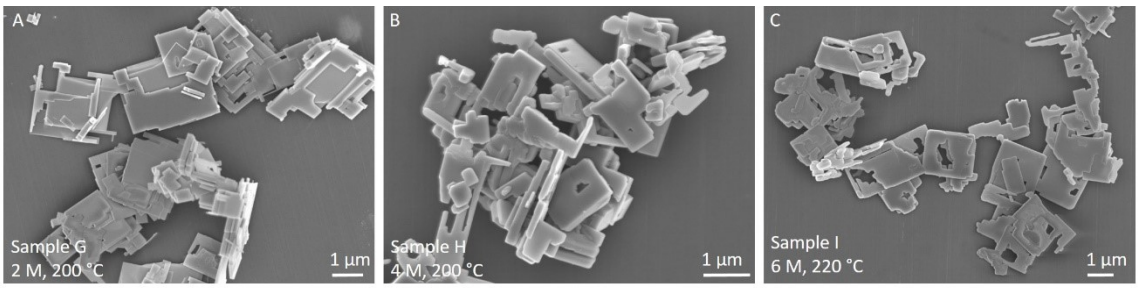

Figure 69: The morphology of $CaTiO_3$ particles obtained from $Bi_4Ti_3O_{12}$ templates by topochemical conversion using a different concentration of NaOH and temperature: 2 mol/L NaOH with 200 °C (A, sample G), 4 mol/L NaOH with 200 °C (B, sample H), and 6 mol/L NaOH with 220 °C (C, sample I). All samples were prepared from 0.2 g $Bi_4Ti_3O_{12}$ template platelet's powder and the holding time at selected temperature was 12 hours.

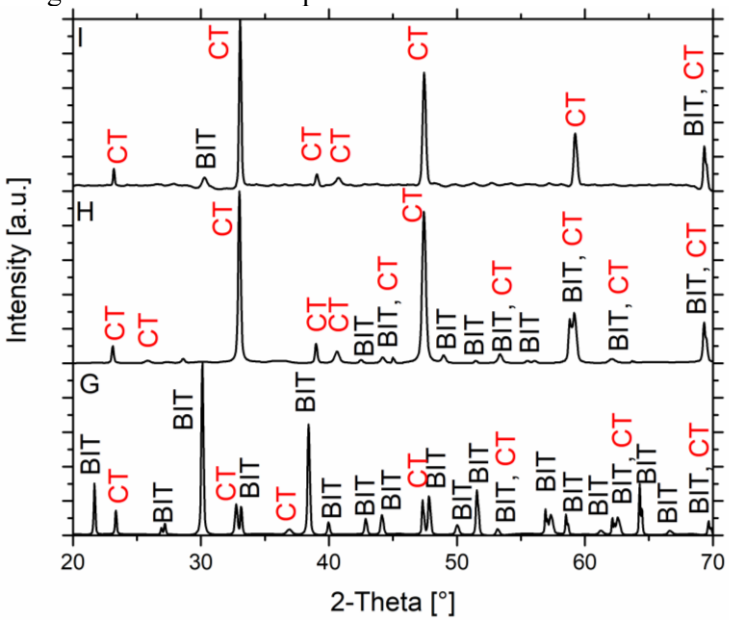

Figure 70: Powder XRD of $CaTiO_3$ particles obtained from $Bi_4Ti_3O_{12}$ templates by topochemical conversion using a different concentration of NaOH and temperature: 2 mol/L NaOH with 200 °C (sample G) and 4 mol/L NaOH with 200 °C (sample H). Powder XRD for sample I was not obtained due to the lack of product powder. Samples were prepared from 0.2 g $Bi_4Ti_3O_{12}$ template platelet's powder and the holding time at selected temperature was 12 hours.

In this study I showed that it is possible to prepare $CaTiO_3$ particles with defined shape under hydrothermal conditions. I observed block-like shaped particles produced from TiO_2 and $CaCl_2{\times}2H_2O$ and plate-like or frame-like shaped particles produced with topochemical conversion from plate-like $Bi_4Ti_3O_{12}$ templates. In both cases, I performed reactions under stirring conditions. Similar correlations between reaction conditions and transformation rate have been observed for the conversion of $Bi_4Ti_3O_{12}$ platelets to $CaTiO_3$ and to $SrTiO_3$. The results indicate that the transformation rate is faster at higher temperature, higher NaOH concentrations and lower concentrations of the $Bi_4Ti_3O_{12}$ platelet. However, some additional experiments are needed to confirm the trend. I believe that reaction conditions exist where the shape of the template would be nicely preserved in $CaTiO_3$, which would also be the main phase. To achieve this, some further experimental optimization is needed. Furthermore, thorough investigation of the reaction mechanism is still needed. According to these preliminary investigations there are some differences between the $Bi_4Ti_3O_{12}$-to-$SrTiO_3$ and $Bi_4Ti_3O_{12}$-to-$CaTiO_3$ transformation. This is expected already based on the differences in the lattice mismatches of the corresponding perovskite pairs ($Bi_4Ti_3O_{12}/SrTiO_3$ and $Bi_4Ti_3O_{12}/CaTiO_3$), different solubility of $Ca(OH)_2$ compared to that of $Sr(OH)_2$ and different solubility product for the formation of $CaTiO_3$ and $SrTiO_3$.

4.4 Photocatalytic Hydrogen Evolution

Previously described $SrTiO_3/Bi_4Ti_3O_{12}$ heterostructural platelets are new materials and therefore, it is worth evaluating their application potential. Considering that $SrTiO_3$ is an important H_2 evolution photocatalyst, the $SrTiO_3$ and $SrTiO_3/Bi_4Ti_3O_{12}$ platelets obtained after different hydrothermal reaction times were tested for photocatalytic hydrogen evolution. This photocatalytic testing was performed in pH-neutral water/methanol solution (H_2O/CH_3OH = 75/25 vol.), without the addition of any noble-metal co-catalyst. Different $SrTiO_3$:$Bi_4Ti_3O_{12}$ ratios were achieved by varying the reaction time, however, the reaction times and ratios were not always proportionate in a way that longer reaction time means higher $SrTiO_3$ content. Other reaction parameters, like the temperature of the initial NaOH solution, can also influence the transformation rate. Therefore, the prediction of the $SrTiO_3$:$Bi_4Ti_3O_{12}$ ratio was not always straightforward. The temperature of the NaOH solution before the start of the hydrothermal reaction was found to influence the surface roughness of the growing $SrTiO_3$ and consequently specific surface area of the heterostructures and $SrTiO_3$. The H_2 evolution photocatalytic activities of the heterostructures were compared to pure $Bi_4Ti_3O_{12}$ platelets (as used as a template for the topochemical conversion), pure $SrTiO_3$ platelets (completely transformed), and commercial $SrTiO_3$ nanopowders. All samples were evaluated under the same conditions. Emission spectrum of the light source used in photocatalytic experiments in shown in Figure 71 [270]. Xenon lamps are known for producing a broad and continuous spectrum of light that spans from ultraviolet to visible and near-infrared regions. The sun-like emission spectrum of Xenon arc lamps makes them a popular choice for solar simulation experiments. AM 1.5 G filter was also applied. In our experiments, the 6258 Ozone Free lamp was used. The light energy flux (1000 W/m^2) was achieved by adjustment the distance between the sample and light source.

I have attempted to estimate the contribution of surface area (Figure 72, right Y axe) and $SrTiO_3$:$Bi_4Ti_3O_{12}$ ratio to the photocatalytic performance. The $Bi_4Ti_3O_{12}$ platelets with the smallest specific surface area (2–3 m^2g^{-1}) show the lowest H_2-evolution rate among the studied materials, only 7.5 μmol $g^{-1}h^{-1}$. Low H_2 evolution photocatalytic activity of the $Bi_4Ti_3O_{12}$ is expected, because its conduction band is not negative enough. Slightly higher H_2 evolution rates were noticed for low $SrTiO_3$ content $SrTiO_3/Bi_4Ti_3O_{12}$ heterostructures (up to 37 μmol $g^{-1}h^{-1}$). The highest H_2 evolution rate, which was 15 times higher compared to that of commercial $SrTiO_3$ powder, was observed for the heterostructure, containing around 63 % of $SrTiO_3$ (1264.5 μmol $g^{-1}h^{-1}$). The H_2 evolution rate drops again with increasing the ratio of $SrTiO_3$ (724.5 μmol $g^{-1}h^{-1}$ at 95 % $SrTiO_3$) in the heterostructure and further decreases as the topochemical conversion is complete to pure $SrTiO_3$ (up to 130 μmol $g^{-1}h^{-1}$). Commercial nanocrystalline $SrTiO_3$ powder reached 81 μmol $g^{-1}h^{-1}$ (BET 24 m^2g^{-1}). As it can be seen from Figure 73, there is no clear correlation between $SrTiO_3/Bi_4Ti_3O_{12}$ ratio and H_2 evolution rate. The great differences of the H_2 evolution rates of the $SrTiO_3/Bi_4Ti_3O_{12}$ and $SrTiO_3$ platelets, that roughly follow the variation of BET values, imply that higher H_2 evolution rates are related to their higher BET.

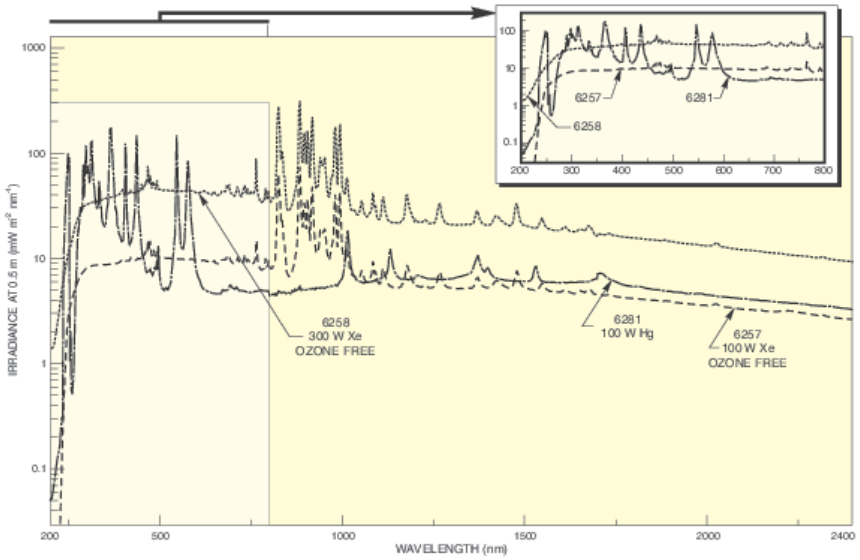

Figure 71: Emission spectrum of the light source used in photocatalytic experiments (6258 300 W Xe Ozone Free) [270]

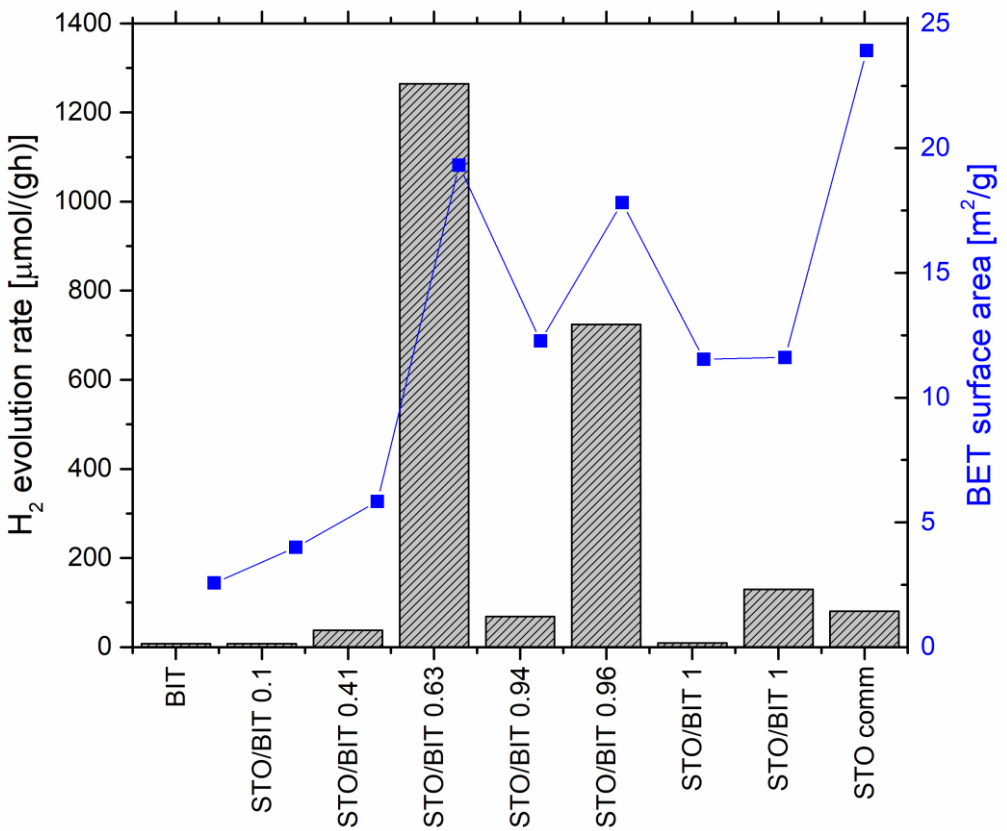

Figure 72: H_2 evolution rates (left Y axe) over the photocatalytic particles (20 mg) in 40 mL of aqueous solution with 25 vol % of methanol without noble-metal co-catalysts and BET values (right Y axe). Studied particles were pure $Bi_4Ti_3O_{12}$ (BIT), heterostructural $SrTiO_3/Bi_4Ti_3O_{12}$ (STO/BIT) particles with different $SrTiO_3$ (STO) contents, and commercial $SrTiO_3$ nanopowder (STOcomm).

It took quite some time to recognize that the experimental parameter that crucially determines the BET value is the temperature of NaOH, which is added to the suspended $Bi_4Ti_3O_{12}$ platelets in $SrCl_2$ water solution before the hydrothermal reaction. When using the solution of NaOH cooled down to room temperature, obtained platelets after the hydrothermal reaction were smooth with BET values lower than 10 m^2/g. On the other hand, the addition of a warm or hot solution of NaOH yielded platelets with a rough surface, showing BET values between 20 and 70 m^2/g. Figure 73 shows the H_2 evolution rate of the samples with comparable $SrTiO_3/Bi_4Ti_3O_{12}$ ratio (0.41 and 0.46), but different BET values. It is clear that the sample with higher BET (23 m^2/g) shows 30-times higher photocatalytic activity compared to the sample with 4-times lower BET (6 m^2/g).

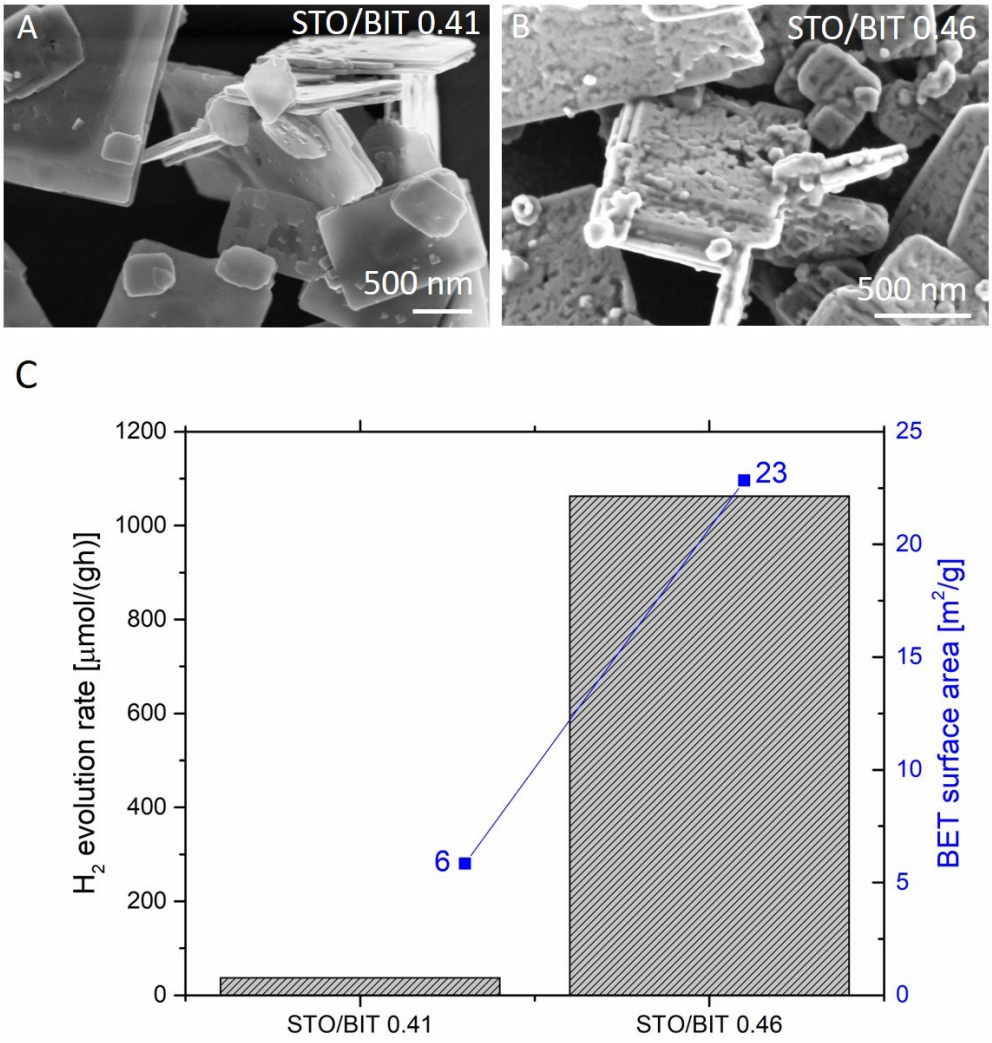

Figure 73: SEM micrographs of photocatalytic heterostructures with similar $SrTiO_3/Bi_4Ti_3O_{12}$ ratio, but different surface roughnesses (A-smooth surface, BET 6 m^2/g, and B- rough surface, BET 23 m^2/g), measured H_2 evolution rates and corresponding BET values (C).

To better understand the effect of BET on the photocatalytic activity some additional $SrTiO_3/Bi_4Ti_3O_{12}$ heterostructural and $SrTiO_3$ platelets with a rough surface (higher BET) were prepared using the same approach of adding hot NaOH (temperature between 65 °C and 70 °C) to the suspension of $Bi_4Ti_3O_{12}$ platelets in $SrCl_2$ water solution. Figure 74 presents the results of H_2 evolution rates, including those already shown in Figure 72 – Figure 74. The highest hydrogen evolution rate (2950 µmol/gh) among prepared and studied platelets was observed for $SrTiO_3/Bi_4Ti_3O_{12}$ heterostructures with $SrTiO_3$ content of 56 % and BET value of 52 m^2/g. With this synthesis strategy (using hot NaOH) also higher H_2 evolution rate for pure $SrTiO_3$ particles was achieved (STO/BIT-1 NEW, Figure 74). In terms of H_2 production rate, our heterostructures demonstrate better performance than several other noble-metal-loaded photocatalysts [195], [271]–[276].

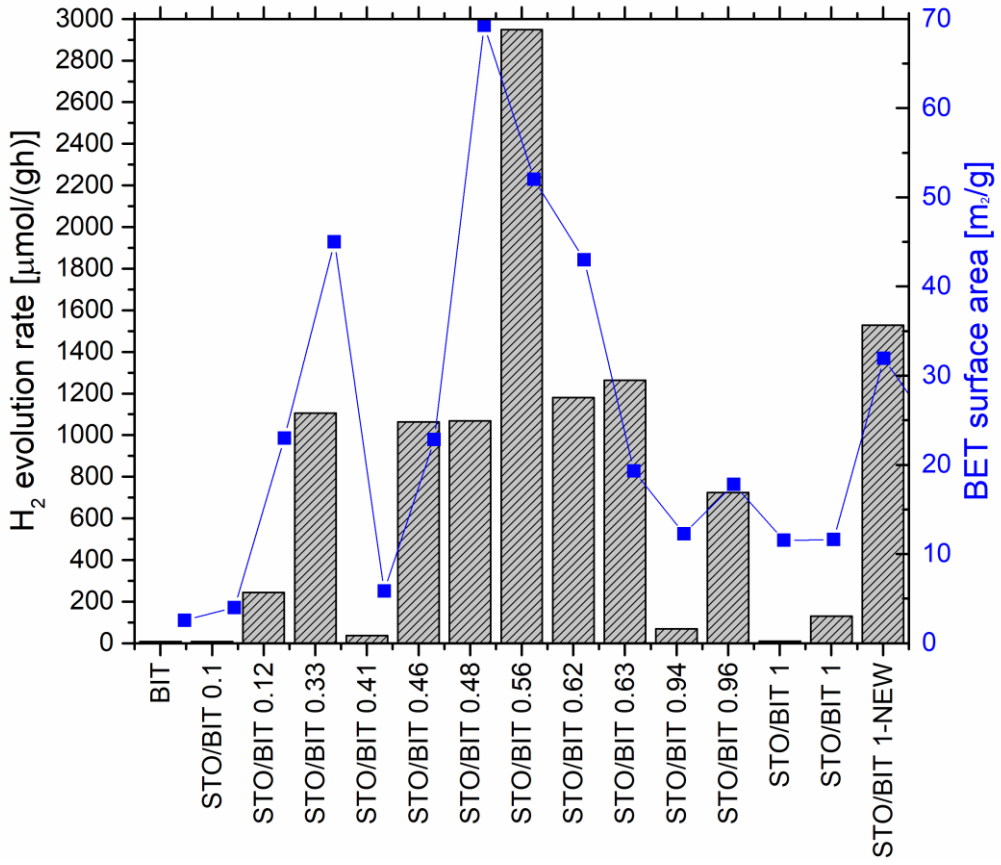

Figure 74: H_2 evolution rates (left Y axe) over the photocatalytic particles (20 mg) in 40 ml of aqueous solution with 25 vol % of methanol without noble-metal co-catalysts and BET values (right Y axe). Studied particles were pure $Bi_4Ti_3O_{12}$ (BIT), heterostructural $SrTiO_3/Bi_4Ti_3O_{12}$ (STO/BIT) particles with different STO contents and commercial $SrTiO_3$ nanopowder (STOcomm). $SrTiO_3/Bi_4Ti_3O_{12}$ and $SrTiO_3$ platelets with BET higher than 15 m^2/g were prepared with the addition of hot NaOH solution.

Band structural analysis is a prerequisite to understand photocatalytic properties of the material. The optical band gap energy (Eg) is an important optical parameter, defined as the energy difference between the bottom of the conduction band (ECB) and the top of the valence band (EVB). The Eg energies of the $Bi_4Ti_3O_{12}$, $SrTiO_3/Bi_4Ti_3O_{12}$ and $SrTiO_3$, were calculated using the well-known Tauc method from the UV-VIS diffuse reflectance spectra (DRS) and Kubelka-Munk (K-M) function F(R) [277], [278] as shown in Eq (16):

$$F(R) = \frac{K}{S} = \frac{(1-R)^2}{2R} \tag{16}$$

where K is the K-M absorption coefficient, S is the K-M scattering coefficient. Kubelka-Munk coefficients K and S are dependent on the illumination geometry and do not represent physical properties of the material [279]. However, K and S are dependent on the intrinsic absorption coefficient (α) and scattering coefficient (s) of the material. R is defined as the ratio of reflectance of the sample and the standard ($BaSO_4$ in this work):

$$R = \frac{R_{sample}}{R_{standard}} \tag{17}$$

R is dependent on the sample powder thickness, which has to be between 1 and 3 mm according to Murphy [280] or larger than 2 mm according to Escobedo-Morales [281] to avoid the contribution of the substrate.

Combination of F(R) into Tauc equation provides Eq (18):

$$\sqrt{F(R) \cdot h\nu} = B(h\nu - E_g) \tag{18}$$

where h is the Planck constant, ν is the incident frequency and B is a constant. More details on the measurements, calculation and derivations of the equations can be found elsewhere [277], [282]. The $(F(R) \cdot h\nu)^{1/2}$ vs. hν plots are shown in Figure 75. The band gaps (Eg) of $SrTiO_3$, $Bi_4Ti_3O_{12}$ and heterostructure $SrTiO_3/Bi_4Ti_3O_{12}$ were determined by extrapolation of the linear part of the function at F(R)=0. Eg values are 3.16 eV, 3.23 eV and 3.20 eV for $Bi_4Ti_3O_{12}$, $SrTiO_3$, and $SrTiO_3/Bi_4Ti_3O_{12}$ heterostructure, respectively.

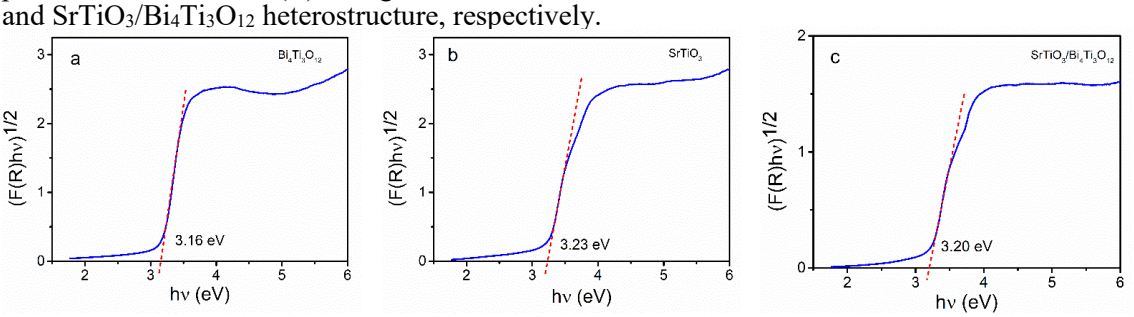

Figure 75: Determination of the band-gap energy from the Tauc plot for (a) $Bi_4Ti_3O_{12}$, (b) $SrTiO_3$ and (c) $SrTiO_3/Bi_4Ti_3O_{12}$ platelets.

The E_{CB} and E_{VB} were calculated by using Eq. (19) and Eq. (20) [283]–[285]:

$$E_{CB} = \chi_{mol} - E_e - 0.5E_g \tag{19}$$

$$E_{VB} = E_{CB} + E_g \tag{20}$$

where E_e is the free-electron energy vs. hydrogen (4.5 eV) and χ_{mol} is the geometric mean of Mulliken's electron negativities of constituent atoms, calculated according to Eq. (21) [284]:

$$\chi_{mol} = [\chi_A^a \cdot \chi_B^b \cdot \chi_C^c]^{\frac{1}{a+b+c}} \tag{21}$$

where the molecular formula is $A_aB_bC_c$. χ_A (χ_B, χ_C) is Mulliken's absolute electronegativity of the corresponding atom (in eV) and it is defined as the arithmetic mean of the electron affinity and the first ionization energy of that atom [286], [287]. For $SrTiO_3$ and $Bi_4Ti_3O_{12}$, the calculations give χ_{SrTiO3}=5.29 and $\chi_{Bi4Ti3O12}$=5.84. Considering this, the E_{CB} and E_{VB} of $SrTiO_3$ are -0.80 eV and 2.43 eV, respectively, and for $Bi_4Ti_3O_{12}$ E_{CB}=-0.21 eV and E_{VB}=2.95 eV (Figure 75).

For $SrTiO_3$, the calculated E_{CB} (-0.8 eV) matches the reported E_{CB} value (-0.81 eV[288], [289]), determined by the Mott-Schottky method for the single-crystalline $SrTiO_3$ [288]. In contrast, in the case of $Bi_4Ti_3O_{12}$, a larger deviation was observed between the calculated E_{CB} (-0.21 eV) and those E_{CB} values obtained from the Mott-Schottky plot (-0.1 eV[290], -0.41 eV[66]). The deviations are expected, because experimental values in the literature were determined for two different $Bi_4Ti_3O_{12}$ nanostructures [66], [290]. It is known that the experimental determination of the fundamental characteristics of nanostructural materials is related to a high degree of uncertainty [291]. The same applies also to the determination of E_{CB} from the Mott-Schottky relationship, which is based on several assumptions and ideal conditions (not completely fulfilled for nanostructures) [291], [292].

Considering the position of the Fermi energy in n-type semiconductors (0.3 to 0.1 eV below E_{CB}), the Fermi energy levels of $SrTiO_3$ and $Bi_4Ti_3O_{12}$ were estimated to be -0.51 eV and -0.11 eV, respectively (Figure 76). Due to the Fermi energy level equalization at the $SrTiO_3/Bi_4Ti_3O_{12}$ interface, electrons tend to move from $SrTiO_3$ to $Bi_4Ti_3O_{12}$ side. Consequently, $SrTiO_3$ and

$Bi_4Ti_3O_{12}$ at the interface become positively and negatively charged, respectively. The formation of such an internal electric field at the interface could be important for the decrease of the recombination rate of the photoinduced charges. Under simulated-light irradiation, both $SrTiO_3$ and $Bi_4Ti_3O_{12}$ absorb photons and the electrons from E_{VB} are promoted to $E_{CB,}$ leaving holes in E_{VB}. This results in the generation of the electron/hole pairs (Figure 76), which are prone to recombine. Due to the formation of internal electric field at the interface (positive charged $SrTiO_3$ side, negative charged $Bi_4Ti_3O_{12}$ side), some photoexcited electrons from E_{CB} of $Bi_4Ti_3O_{12}$ move to positive charged $SrTiO_3$ side and recombine with the holes in E_{VB} there. As a result, these holes at $SrTiO_3$ side are not recombined by the photoinduced electrons from $SrTiO_3$, which can be thus available for the reduction of H_2O (H_2 generation). On the $Bi_4Ti_3O_{12}$ side of the heterostructure, the holes oxidize the methanol [293]. The band structure of $SrTiO_3$ and $Bi_4Ti_3O_{12}$ supports the possible execution of direct Z-scheme charge transfer (Figure 76), by which the recombination rate is decreased and high redox ability is preserved [220], [294]. Highly ordered epitaxial contact between $SrTiO_3$ and $Bi_4Ti_3O_{12}$ enhances charge mobility at the interface, which is also expected to contribute to better efficiency.

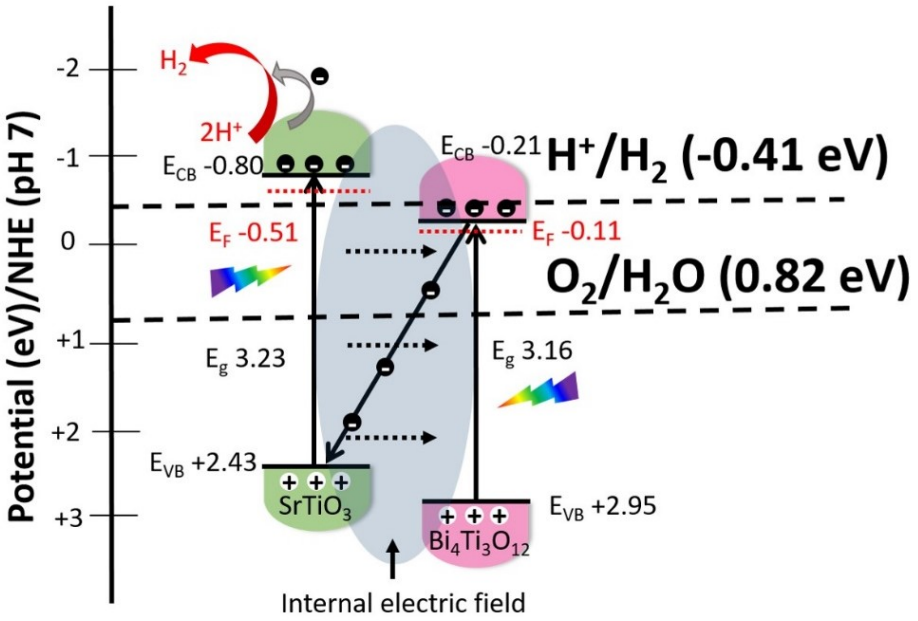

Figure 76: Band structure of $SrTiO_3$ and $Bi_4Ti_3O_{12}$.

Considering above-described band structure analysis, one possible explanation for better photocatalytic properties of the $SrTiO_3/Bi_4Ti_3O_{12}$ heterostructures could be established based on the direct Z-scheme charge transfer and formation of epitaxial $SrTiO_3/Bi_4Ti_3O_{12}$ heterojunction. However, it has to be pointed out that a high hydrogen evolution rate was achieved also with completely transformed $Bi_4Ti_3O_{12}$ to $SrTiO_3$ (STO/BIT-1 NEW). This result implies that the heterojunction may not be the only and the main reason for enhanced photocatalytic performance.

The color change of the samples after illumination implies that some metallic species can form by in-situ reduction and act as co-catalysts and improve photocatalytic performance through surface plasmon resonance (SPR). Therefore, the other reason for higher photocatalytic performance of the $SrTiO_3/Bi_4Ti_3O_{12}$ and $SrTiO_3$ platelets could be related to the presence of such kind metallic species. In our system, Bi^{3+} could be potentially captured in the porous structure of the platelets and under illumination and H_2 generation reduced to metallic Bi^o. Based on the literature report, similar improvement was observed for TiO_2 loaded with metallic Bi^o co-catalysts [200]. During our procedure, Bi^{3+} ions could form during dissolution of Bi_2O_3 side product with HNO_3 and get captured on the rough platelet surface. Those Bi^{3+} are more easily reduced than Bi^{3+} in the oxide network (or Ti^{4+} in oxide network). XPS revealed that in as-prepared platelets most Bi-remains are in the form of Bi^{3+}, but small amount is also in the form of metallic Bi^o (Figure 77). We assumed that even more Bi^o can form in-situ during photocatalytic hydrogen evolution reaction as it was also reported for Bi/TiO_2 [200]. To prove this, the sample after the photocatalytic reaction was immediately examined by XPS, which revealed that the amount of metallic bismuth significantly increased (Figure 78). Therefore, we believe that this is important evidence that Bi^o plays an important role in the improvement of H_2 evolution. It could be that the Bi^o plays an even more important role than the direct Z-scheme heterojunction.

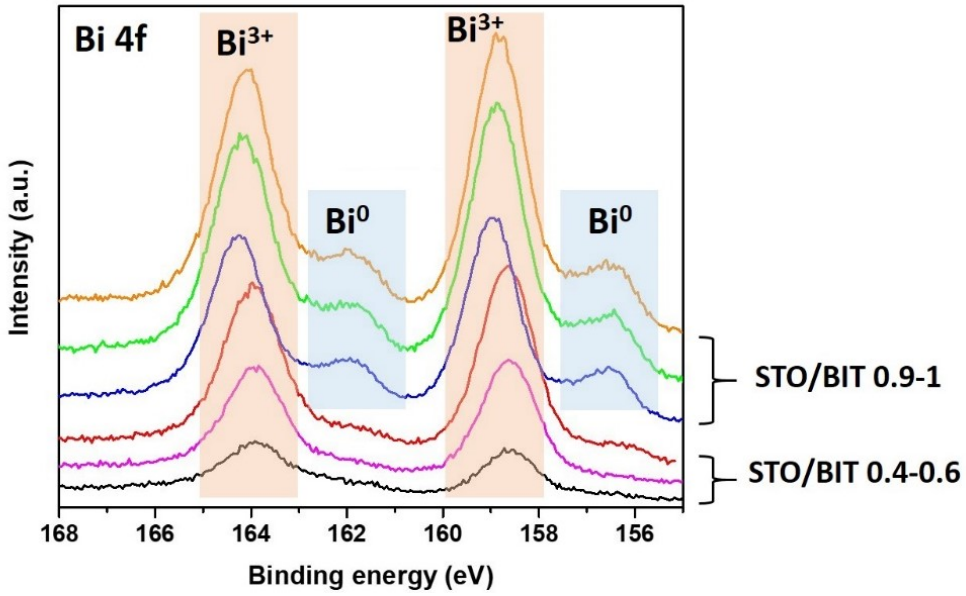

Figure 77: XPS spectra of as-prepared $SrTiO_3/Bi_4Ti_3O_{12}$ heterostructural platelets with lower and higher $SrTiO_3$ ratio. The majority of Bi-remains are in the form of Bi^{3+}, some metallic bismuth signal is present as well in samples with higher $SrTiO_3$ ratios.

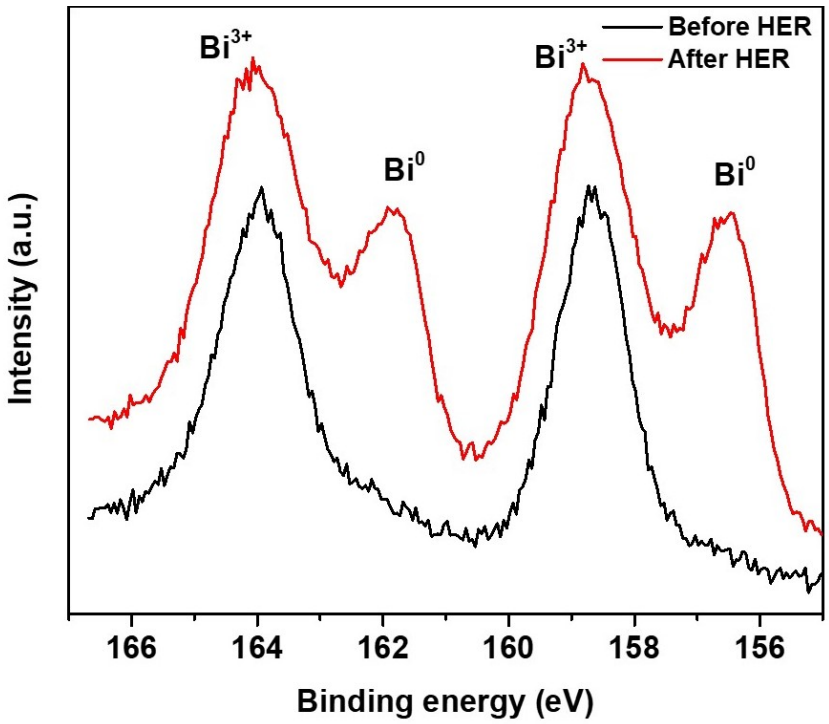

Figure 78: XPS before and immediately after hydrogen evolution reaction for the sample with the highest hydrogen evolution rate.

Based on the change of the color of the photocatalyst during the photocatalytic reaction the optical properties (in UV-VIS spectral range) of the photocatalysts after the HER were verified and compared with that of the initial photocatalysts. For the optical and XPS characterization of the platelets after the photocatalytic experiment, the following procedure was applied: powder was separated from the water-methanol solution by centrifugation, dried under vacuum and then kept under an inert atmosphere of N_2. The contact of the sample with air and oxidation of metallic Bi was avoided as much as possible during all procedures. Diffuse reflectance spectroscopy (DRS) analysis revealed (Figure 79) a considerable increase in absorption at 350-700 nm for the

photocatalysts after HER, while both samples (before and after HER) showed similar strong absorption in the UV region. The latter can be attributed to the absorption due to the bandgap of $SrTiO_3$. The higher light absorption of the black-colored STO/BIT platelets after HER in the visible part of the spectra compared to that of pristine STO/BIT agrees with the literature reports, dealing with photocatalysts containing metallic Bi° nanoparticles [295]–[298]. In these studies, it was typically observed that the presence of Bi gives continuous absorption in the spectral range 400-800 nm. A weak peak around 560 nm was observed in the spectrum of the photocatalysts after HER, and this peak matches with the reported broad SPR absorption of 10-70 nm Bi nanoparticles at 550 nm [299]. Nevertheless, this needs to be confirmed by additional experiments (e.g. determination of the size of Bi°).

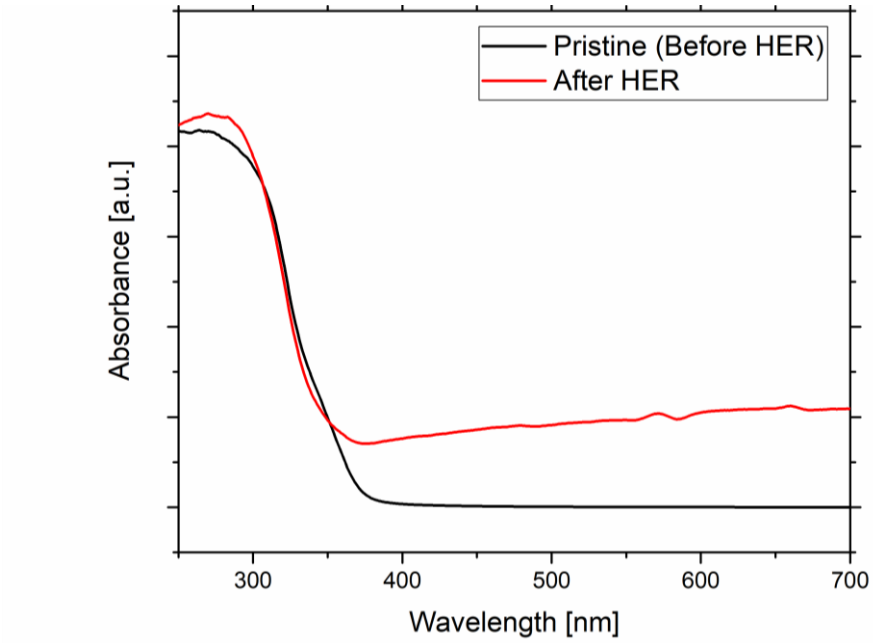

Figure 79: DRS in dependence of wavelength of pristine STO/BIT (before) and after HER

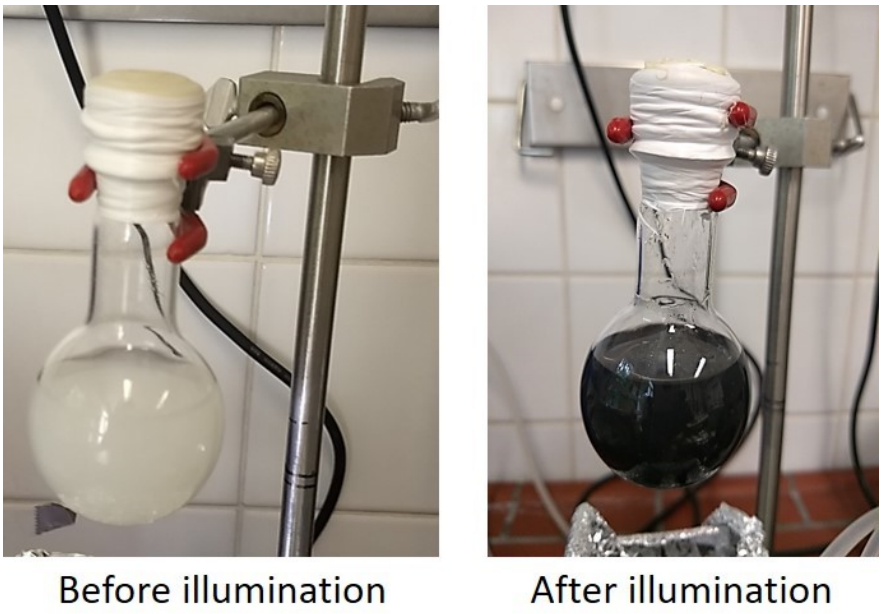

Figure 80: Color changed from white to black after the illumination and hydrogen evolution reaction in samples that showed greater hydrogen evolution values.

Long-term stability of the photocatalyst is important for its practical application. Cycled measurements of the H_2 evolution revealed good repeatability and reusability of the nanoheterostructural $SrTiO_3/Bi_4Ti_3O_{12}$ platelets. The stability of the H_2 evolution over the tested 24-hour reaction time is similar to that reported for other $SrTiO_3$-based photocatalysts (Figure 81) [136], [299], [300].

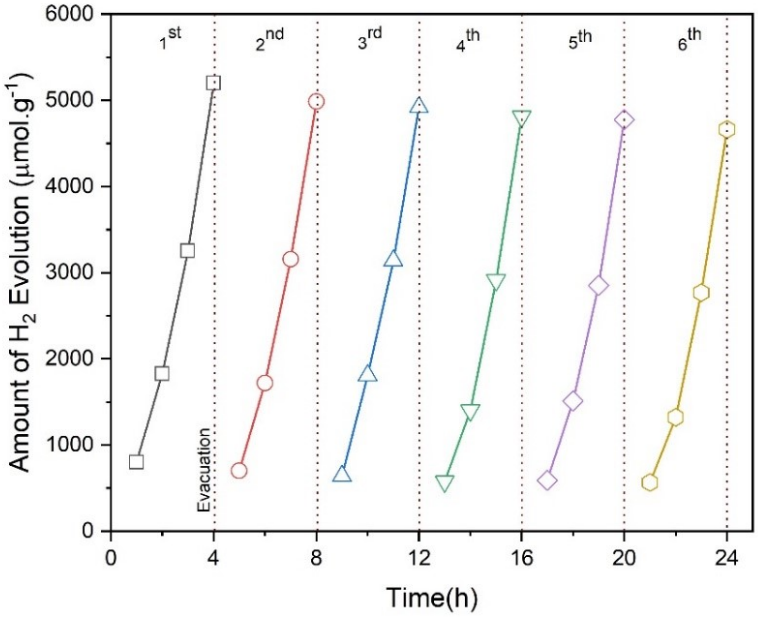

Figure 81: Stability test of H_2 evolution for $SrTiO_3/Bi_4Ti_3O_{12}$ heterostructural platelets obtained after 6-hour hydrothermal reaction (sample STO/BIT 0.63). After every 4 hours of photocatalytic reaction, the formed H_2 was evacuated.

For comparison with other photocatalysts, it is very convenient to express the photocatalytic efficiency in the form of solar-to-hydrogen (STH). STH efficiency is calculated by Eq. (22):

$$STH\ (\%) = \frac{r_{H2} x \Delta G_{H2O}}{P_{Sun} x S} x 100 \qquad (22)$$

where, $r_{H2,}$ ΔG_{H2O}, P_{sun} and S represent the H_2 production rate, the reaction Gibbs free energy (237 kJ/mol), the light energy flux ($1.0 \cdot 10^3$ Wm^{-2}) and irradiation area (9 cm^2), respectively.

Due to the small portion of UV light in the incident light spectra, the $SrTiO_3$-based photocatalysts do not show a high solar-to-hydrogen (STH) efficiency. It has been reported that a modification of the $SrTiO_3$ by doping and/or co-catalyst deposition led to a variation of the STH from 0.037 % to 0.65 % [25], [26], [136], [193], [276], [300], [301]. The highest STH efficiency (0.65 %) was reported by the group of Domen and co-workers [136] for Al-doped $SrTiO_3$ loaded with Rh/Cr_2O_3 and CoOOH co-catalysts. A STH greater than 1 % was demonstrated for La- and Rh-codoped $SrTiO_3$ (H_2 evolution) combined with Mo-doped $BiVO_4$ (O_2 evolution) and Au in the Z-scheme based photocatalysts [25]. To the best of my knowledge this was for quite a long time the highest STH obtained for the suspended photocatalysts powders in water. However, in 2023, Zhou et al. published the work about photocatalytic water splitting system with STH higher than 9%. In their work, the photocatalysts were InGaN/GaN nanowires (NW) grown on silicon wafer by molecular-beam-epitaxy technology. Actually, these were not particles suspended in water, but the InGaN/GaN NW exhibit columnar growth perpendicular to silicon substrate and the NW were deposited with $Rh/Cr_2O_3/Co_3O_4$ co-catalysts. Actually, this material did not show high STH (~0. 5 %) at 30 °C, but the STH increased above 9 % at 70 °C [163].

In the current study, $SrTiO_3/Bi_4Ti_3O_{12}$ heterostructural platelets without any noble-metal doping or co-catalyst loading exhibit an STH efficiency of 0.19 %-0.44 %, which is moderate, but comparable to several other reported STH values for noble-metal decorated $SrTiO_3$ photocatalysts [25], [26], [136], [193], [276], [300]. Considering that the $SrTiO_3/Bi_4Ti_3O_{12}$ heterostructure was evaluated for the first time in terms of photocatalytic H_2 evolution, we believe that there is still room for an improvement of the photocatalytic efficiency.

Chapter 5

Conclusions

Research and development are commonly strongly focused on the improvement of functional properties. At the same time, in terms of designing new nanostructured materials and tailoring their functional properties, the understanding of nucleation and crystal growth mechanisms is important as well. However, many gaps exist in understanding these processes and reaction mechanisms. With this work, we wanted to fill some of these gaps in the field of hydrothermal topochemical conversion (TC) reactions. Specifically, I studied the TC approach for the low-temperature hydrothermal preparation of functional 2D perovskite $ATiO_3$ (A=Ca, Sr, Ba) particles, which naturally do not grow in an anisotropic shape due to their symmetric crystal structure. The layered Aurivillius titanate phases, which spontaneously grow in a 2D morphology, can make it possible to bridge this natural feature of $ATiO_3$ perovskites by my means of topochemical reactions, enabling preservation of the 2D shape of the initial template. This is possible because of similar perovskite units in both phases. Till recently, this kind of transformation was mainly studied in molten salt media. The most common Aurivillius phases for the formation of $ATiO_3$ (M=Sr, Ca, Ba) in molten salt were $Bi_4Ti_3O_{12}$ and $ATi_4Bi_4O_{15}$. In my thesis, I attempted to translate the topochemical transformation from $Bi_4Ti_3O_{12}$ to $ATiO_3$ to much lower temperature ranges in the hydrothermal media. In many aspects, my research represents the pioneering work in the field of hydrothermal topochemical transformations of Aurivillius titanate phases to $ATiO_3$ perovskites. I have investigated the mechanisms and described them in view of nucleation crystallization theory.

In this thesis, the main emphasis is on the study of transformation from the $Bi_4Ti_3O_{12}$ platelets into $SrTiO_3$ platelets. The synthesis process was performed in two steps. In the first step, $Bi_4Ti_3O_{12}$ platelets were prepared in molten salt. Therefore, the preparation of $Bi_4Ti_3O_{12}$ templates was first studied and optimal reaction conditions were determined. Different reactants were used and compared. In the second step, the $Bi_4Ti_3O_{12}$ platelets were used as a template for the conversion under alkaline hydrothermal conditions into different $SrTiO_3/Bi_4Ti_3O_{12}$ heterostructures and pure $SrTiO_3$. X-ray diffraction and electron microscopy helped me to understand these processes. Atomic scale analysis of the $Bi_4Ti_3O_{12}$ template platelets, intermediate $SrTiO_3/Bi_4Ti_3O_{12}$ heterostructures, and final $SrTiO_3$ platelets was performed to be able to understand and control the transformation pathway. $Bi_4Ti_3O_{12}$ platelets that were used for the topochemical conversion exhibited an average side length of 1-2 μm and thickness of 60 nm. STEM examination of the $Bi_4Ti_3O_{12}$ platelets showed their layered structure with alternation of pseudo perovskite ($[Bi_2Ti_3O_{10}]^{2-}$) blocks and bismuth oxide ($[Bi_2O_2]^{2+}$) layers. The basal surface planes of the as-prepared platelets were exclusively terminated with $[Bi_2O_2]^{2+}$ layer, while both types of structural units were exposed at the lateral surfaces. Typically, platelets are single crystalline, (001) oriented containing a few or no planar defects and have atomically flat basal surface planes. As the template platelets are exposed to a highly alkaline NaOH solution, the outermost $[Bi_2O_2]^{2+}$ layer dissolves and the pseudo perovskite layer is exposed.

Next, the background of hydrothermal topochemical conversion of $Bi_4Ti_3O_{12}$ to $SrTiO_3$ was studied. The mechanism of the transformation was inferred from the atomic scale analysis of the platelets at different transformation stages, performed at high supersaturation conditions (Sr/Ti=12, 6 mol/L NaOH, 200 °C). The $Bi_4Ti_3O_{12}$ platelets are the source of $Ti(OH)_6^{2-}$ and also serve as the substrate for the nucleation of $SrTiO_3$. Already at the beginning and also after the formation of the protective $SrTiO_3$ layer, the dissolution of the $Bi_4Ti_3O_{12}$ platelets is faster from the lateral side and $SrTiO_3$ grows over both basal surface planes of the template. The process leads to the formation of a groove that extends along the platelet and deepens with the progress of the transformation. When $Bi_4Ti_3O_{12}$ inside the groove dissolves till the top layer of TiO_6 octahedra of the surface pseudo perovskite block of the $Bi_4Ti_3O_{12}$ platelet, $SrTiO_3$ starts to grow also from the

inner side and monoatomic Bi-O layer remains captured in the forming $SrTiO_3$. Through this process, the $Bi_4Ti_3O_{12}$ platelets become gradually pseudomorphically replaced by two $SrTiO_3$ partially intergrown parallel platelets, each of which contains approximately in the middle monoatomic Bi-O layer. The (100) $SrTiO_3$ orientation is dictated by the (001) orientation of the $Bi_4Ti_3O_{12}$. Since the $Bi_4Ti_3O_{12}$-to-$SrTiO_3$ topochemical conversion proceeds by the epitaxial growth, we accurately examined the lattice mismatches between the phases in all relevant orientation relationships (ORs). This was determined by Rietveld refinement of the XRD patterns of both materials at R.T. and at 200 °C. Depending on the orientation relationship, the misfit was between 1.4 % and 2.8 %. By STEM we examined the heteroepitaxial interface and confirmed that $SrTiO_3$ grows epitaxially on the pseudo perovskite layer of the template, and we also found that the misfit between $SrTiO_3$ and $Bi_4Ti_3O_{12}$ is manifested through the formation of dislocations.

Furthermore, I investigated how the misfits can be balanced by supersaturation and how the transformation can be steered by reaction conditions, particularly by reagents' concentrations and temperature. The supersaturation is in the reaction of $SrTiO_3$ formation defined by the concentration of $Ti(OH)_6^{2-}$ species that form during $Bi_4Ti_3O_{12}$ dissolution and Sr^{2+} concentration that is present in the solution and available for reaction. The NaOH concentration determines the dissolution rate of the $Bi_4Ti_3O_{12}$ platelets and consequently, the concentration of $Ti(OH_6)^{2-}$, which is also the function of $SrTiO_3$ precipitation. The nucleation rate depends on the supersaturation – higher supersaturation means lower activation energy for nucleation. I thoroughly investigated how the Sr concentration (Sr/Ti molar ratio) at a certain NaOH concentration influences the transformation kinetics and the manner of $SrTiO_3$ growth. With increasing the Sr/Ti nominal molar ratio, the $SrTiO_3$ islands on the basal surfaces of $Bi_4Ti_3O_{12}$ became smaller, but the $SrTiO_3$ surface coverage was higher. This indicates that by increasing the strontium excess (Sr/Ti ratio), the growth can be promoted from island 3D to layer-by-layer-like 2D growth over the whole basal surface planes. At the same time, with an increased Sr/Ti ratio and increased surface coverage, the conversion to $SrTiO_3$ is slower and $SrTiO_3$ content after a certain time and at a particular NaOH concentration decrease. On the contrary, a decrease of Sr excess (Sr/Ti=1 and 3) results in the $SrTiO_3$ island growth and the great part of the $Bi_4Ti_3O_{12}$ basal surface planes is not protected against dissolution from the top, and consequently, this leads to faster $Bi_4Ti_3O_{12}$ dissolution providing more $Ti(OH)_6^{2-}$ for the formation of $SrTiO_3$ which continues to grow on the already formed $SrTiO_3$ islands. Consequently, the transformation from $Bi_4Ti_3O_{12}$ to $SrTiO_3$ is faster, but the platelet morphology of the $Bi_4Ti_3O_{12}$ template is not preserved. $SrTiO_3$ particles, depending on the conditions (Sr/Ti=1 or 3, C_{NaOH}) and template quality (number of defects), adopt the shape of frames, cubes, or partially preserved platelets. The concentration of NaOH determines the rate of $Bi_4Ti_3O_{12}$ dissolution and $SrTiO_3$ formation. Optimal conditions for the complete transformation in a reasonable time of 12 hours from the $Bi_4Ti_3O_{12}$ to $SrTiO_3$ with preserved platelet morphology are the following: Sr/Ti=12, 6 mol/L NaOH, 200 °C. Shorter reaction times (<12 hours) lead to $SrTiO_3$/$Bi_4Ti_3O_{12}$ heterostructural platelets with various ratios of the components.

The developed hydrothermal topochemical conversion procedure is new and enables the preparation of unique $SrTiO_3$ platelets and novel $SrTiO_3$/$Bi_4Ti_3O_{12}$ heterostructural platelets and therefore it was worth evaluating their application potential. Platelets were tested for photocatalytic hydrogen evolution from pH-neutral water/methanol solution without the addition of any noble-metal co-catalyst. Also, a new approach for the preparation of platelets with higher surface area was developed and incorporated into the synthesis procedure. $SrTiO_3$/$Bi_4Ti_3O_{12}$ heterostructure with $SrTiO_3$ content of 56 % and BET value of 52 m^2/g produced the highest hydrogen evolution rate among prepared $SrTiO_3$/$Bi_4Ti_3O_{12}$ and $SrTiO_3$ platelets along with $SrTiO_3$ nanopowder. One possible explanation for better photocatalytic properties of the heterostructures could be established based on the formation of epitaxial $SrTiO_3$/$Bi_4Ti_3O_{12}$ heterojunction. $Bi_4Ti_3O_{12}$ and $SrTiO_3$ exhibit appropriate relative positions of band edges that enable the formation of direct Z-scheme. Another reason for higher photocatalytic performance could be related to the presence of Bi° metallic species, which can form by in-situ reduction of Bi^{3+} ions and act as co-catalysts and improve photocatalytic performance through surface plasmon resonance of Bi°. It could be that Bi° plays an even more important role than the heterojunction itself.

The same approach with topochemical conversion was used also for the preparation of other $ATiO_3$ perovskites. For $BaTiO_3$, the lattice mismatch was too big to handle at similar reaction conditions. In all cases, no matter how large supersaturation was used, the island formation growth prevails. However, the shapes strongly differed in almost every case from stars and flowers to octahedrons and cubes. On the contrary, the morphological studies of the topochemical conversion of $Bi_4Ti_3O_{12}$ platelets to $CaTiO_3$ particles showed that it is possible to apply the approaches from the $Bi_4Ti_3O_{12}$-to-$SrTiO_3$ conversion and also for transformation to $CaTiO_3$.

The detailed insight into the mechanism of epitaxial growth of $SrTiO_3$ on $Bi_4Ti_3O_{12}$ by hydrothermal topochemical conversion of $Bi_4Ti_3O_{12}$ platelets to $SrTiO_3$ expands the possibilities for using the hydrothermal topochemical reaction concept in the design of highly preferentially oriented heterostructures or mesocrystallites, involving other template particles and growing phases for the preparation of new, efficient, photocatalytic systems. An understanding of this transformation process provides general guidelines for the engineering of other epitaxial heterostructures or defined (anisotropic) nanostructures via hydrothermal topotactic epitaxy.

References

[1] D. G. Nocera and N. S. Lewis, “Powering the planet: Chemical challenges in solar energy utilization,” *Proc Natl Acad Soc*, 103, 43, 15729–15735, 2006.

[2] R. J. D. Tilley, “The ABX_3 Perovskite Structure,” in *Perovskites: Structure-Property Relationships*, John Wiley & Sons, Ltd., 1–41, 2016.

[3] S. B. Kumar, Dinesh; Sagar, Ram; Yadav, Monika; Kumar Singh, Akhilesh; Rai, “Synthesis Techniques and Applications of Perovskite Materials,” in *Perovskite Materials, Devices and Integration*, T. He, Ed. 2020.

[4] A. R. West, *Basic Solid State Chemistry*, Second Edi. Wiley, 1988.

[5] B. Y. R. D. Shannon, M. H, N. H. Baur, O. H. Gibbs, M. Eu, and V. Cu, “Revised Effective Ionic Radii and Systematic Studies of Interatomic Distances in Halides and Chalcogenides" *Acta Cryst*., A32, 751, 1976.

[6] L. Paramanik, S. Subudhi, and K. M. Parida, “Visible light active titanate perovskites: An overview on its synthesis, characterization and photocatalytic applications,” *Mater. Res. Bull.*, 155, 4, 111965, 2022.

[7] A. Alizadeh, M. Roudgar-Amoli, S. M. Bonyad-Shekalgourabi, Z. Shariatinia, M. Mahmoudi, and F. Saadat, “Dye-sensitized solar cells go beyond using perovskite and spinel inorganic materials: A review,” *Renew. Sustain. Energy Rev.*, 157, 11, 2021, 112047, 2022.

[8] L. Zhang *et al.*, “Lithium lanthanum titanate perovskite as an anode for lithium-ion batteries,” *Nat. Commun.*, 11, 1, 1–8, 2020.

[9] J. Y. Kim, J. W. Lee, H. S. Jung, H. Shin, and N. G. Park, “High-Efficiency Perovskite Solar Cells,” *Chem. Rev.*, 120, 15, 7867–7918, 2020.

[10] P. Zhang, M. Li, and W. C. Chen, “A Perspective on Perovskite Solar Cells: Emergence, Progress, and Commercialization,” *Front. Chem.*, 10, 4, 1–9, 2022.

[11] J. George, A. P. Joseph, and M. Balachandran, “Perovskites: Emergence of highly efficient third-generation solar cells,” *Int. J. Energy Res.*, 46, 21856–21883, 2022.

[12] J. Cao, Y. Ji, and Z. Shao, “Perovskites for protonic ceramic fuel cells: a review,” *Energy Environ. Sci.*, 15, 6, 2200–2232, 2022.

[13] S. S. Won *et al.*, “Flexible vibrational energy harvesting devices using strain-engineered perovskite piezoelectric thin films,” *Nano Energy*, 55, 10, 182–192, 2019.

[14] F. Jiang *et al.*, “Stretchable, Breathable, and Stable Lead-Free Perovskite/Polymer Nanofiber Composite for Hybrid Triboelectric and Piezoelectric Energy Harvesting,” *Adv. Mater.*, 34, 17, 2200042, 2022.

[15] “Energy harvesting based on environmentally-friendly perovskite piezoelectric nanofibers - Mohammad Bagher - The University of New South,” 5, 1, 2021.

[16] L. F. da Silva *et al.*, “Long-range and short-range structures of cube-like shape $SrTiO_3$ powders: microwave-assisted hydrothermal synthesis and photocatalytic activity.,” *Phys. Chem.* 15, 12386–93, 2013.

[17] B. L. Phoon, C. W. Lai, J. C. Juan, P. L. Show, and W. H. Chen, “A review of synthesis and morphology of $SrTiO_3$ for energy and other applications,” *Int. J. Energy Res.*, 43, 10, 5151–5174, 2019.

[18] J. H. Haeni, P. Irvin, W. Chang, R. Uecker, P. Reiche, and Y. L. Li, “Room-temperature ferroelectricity in strained $SrTiO_3$,” 430, 8, 583–586, 2004.

[19] A. Rothschild, W. Menesklou, H. L. Tuller, and E. Ivers-tiffe, “Electronic Structure, Defect Chemistry, and Transport Properties of $SrTi_{1-x}Fe_xO_{3-y}$ Solid Solutions,” *Chem. Mat.*. 18, 3651–3659, 2006.

[20] H. Fujioka, J. Ohta, H. Katada, T. Ikeda, Y. Noguchi, and M. Oshima, “Epitaxial growth of semiconductors on $SrTiO_3$ substrates,” 229, 1-4, 137–141, 2001.

[21] S. T. Huang, W. W. Lee, J. L. Chang, W. S. Huang, S. Y. Chou, and C. C. Chen, “Hydrothermal synthesis of SrTiO3 nanocubes: Characterization, photocatalytic

activities, and degradation pathway," *J. Taiwan Inst. Chem. Eng.*, 45, 4, 1927–1936, 2014.
[22] H. Shen *et al.*, "Low-temperature hydrothermal synthesis of $SrTiO_3$ nanoparticles without alkali and their effective photocatalytic activity," *J. Adv. Ceram.*, 5, 298-307, 2016.
[23] C. Wang, H. Qiu, T. Inoue, and Q. Yao, "Band gap engineering of $SrTiO_3$ for water splitting under visible light irradiation," *Int. J. Hydrogen Energy*, 39, 24, 12507–12514, 2014.
[24] P. Zhang, T. Ochi, M. Fujitsuka, Y. Kobori, T. Majima, and T. Tachikawa, "Topotactic Epitaxy of $SrTiO_3$ Mesocrystal Superstructures with Anisotropic Construction for Efficient Overall Water Splitting," *Angew. Chemie - Int. Ed.*, 56,19, 5299–5303, 2017.
[25] Q. Wang *et al.*, "Scalable water splitting on particulate photocatalyst sheets with a solar-to-hydrogen energy conversion efficiency exceeding 1%," *Nat. Mater.* 15, 6, 611–615, 2016.
[26] Y. Goto *et al.*, "A Particulate Photocatalyst Water-Splitting Panel for Large-Scale Solar Hydrogen Generation," *Joule*, 2, 3, 509–520, 2018.
[27] J. Liu, Z. Wei, and W. Shangguan, "Enhanced photocatalytic water splitting with surface defective $SrTiO_3$ nanocrystals," *Front. Energy*, 15, 700-709, 2021.
[28] S. Burnside, J.-E. Moser, K. Brooks, M. Grätzel, and D. Cahen, "Nanocrystalline Mesoporous Strontium Titanate as Photoelectrode Material for Photosensitized Solar Devices: Increasing Photovoltage through Flatband Potential Engineering," *J. Phys. Chem. B*, 103, 43, 9328–9332, 1999.
[29] J. H. Pan *et al.*, "Self-template synthesis of porous perovskite titanate solid and hollow submicron spheres for photocatalytic oxygen evolution and mesoscopic solar cells," *ACS Appl. Mater. Interfaces*, 7, 27, 14859-69, 2015.
[30] V. Kalyani, B. S. Vasile, A. Ianculescu, M. T. Buscaglia, V. Buscaglia, and P. Nanni, "Hydrothermal Synthesis of $SrTiO_3$ Mesocrystals: Single Crystal to Mesocrystal Transformation Induced by Topochemical Reactions," *Cryst. Growth Des.*, 12, 9, 4450–4456, 2012.
[31] F. A. Rabuffetti *et al.*, "Synthesis-dependent first-order Raman scattering in $SrTiO_3$ nanocubes at room temperature," *Chem. Mater.*, 20, 17, 5628–5635, 2008.
[32] G. Canu and V. Buscaglia, "Hydrothermal synthesis of strontium titanate: Thermodynamic considerations, morphology control and crystallization mechanisms," *CrystEngComm*, 19, 28, 3867–3891, 2017.
[33] Z. Zheng, B. Huang, X. Qin, X. Zhang, and Y. Dai, "Facile synthesis of $SrTiO_3$ hollow microspheres built as assembly of nanocubes and their associated photocatalytic activity," *J. Colloid Interface Sci.*, 358, 1, 68–72, 2011.
[34] Y. Wang *et al.*, "Formation of single-crystal $SrTiO_3$ dendritic nanostructures via a simple hydrothermal method," *J. Cryst. Growth*, 311, 8, 2519–2523, 2009.
[35] H. Xu, S. Wei, H. Wang, M. Zhu, R. Yu, and H. Yan, "Preparation of shape-controlled $SrTiO_3$ crystallites by sol-gel-hydrothermal method," *J. Cryst. Growth*, 292, 1, 159–164, 2006.
[36] Y. Li, X. P. Gao, G. L. Pan, T. Y. Yan, and H. Y. Zhu, "Titanate nanofiber reactivity: Fabrication of $MTiO_3$ (M = Ca, Sr, and Ba) perovskite oxides," *J. Phys. Chem. C*, 113, 11, 4386–4394, 2009.
[37] X. Wei, G. Xu, Z. Ren, C. Xu, G. Shen, and G. Han, "PVA-Assisted Hydrothermal Synthesis of $SrTiO_3$ Nanoparticles with Enhanced Photocatalytic Activity for Degradation of RhB," 91, 3795–3799, 2008.
[38] B. Wang, S. Shen, and L. Guo, "$SrTiO_3$ single crystals enclosed with high-indexed {023} facets and {001} facets for photocatalytic hydrogen and oxygen evolution," *Appl. Catal. B Environ.*, 166–167, 320–326, 2015.
[39] H. Kato, M. Kobayashi, M. Hara, and M. Kakihana, "Fabrication of $SrTiO_3$ exposing characteristic facets using molten salt flux and improvement of photocatalytic activity for water splitting," *Catal. Sci. Technol.*, 3, 7,1733–1738, 2013.
[40] I. V Markov, *Crystal Growth for Beginners: Fundamentals of Nucleation, Crystal Growth and Epitaxy*. World Scientific, 2003.
[41] Y. Lee *et al.*, "Photocatalytic Water Splitting of Al-Doped $Rh_xCr_{2-x}O_3/SrTiO_3$ Synthesized by Flux Method : Elucidating the Role of Different Molten Salts," *J. Phys. Chem. C*, 127, 21, 9981-91, 2023.
[42] L. Dong, H. Shi, K. Cheng, Q. Wang, W. Weng, and W. Han, "Shape-controlled growth of $SrTiO_3$ polyhedral submicro/nanocrystals," *Nano Res.*, 7, 9, 1311–1318, 2014.
[43] G. S. Foo, Z. D. Hood, and Z. Wu, "Shape Effect Undermined by Surface Reconstruction : Ethanol Dehydrogenation over Shape-Controlled $SrTiO_3$ Nanocrystals," *ACS Catal.* 8, 556-565, 2018.

[44] S. Gupta *et al.*, "Effects of Al Doping on Hydrogen Production Efficiency upon Photostimulated Water Splitting on $SrTiO_3$ Nanoparticles," *J. Phys. Chem. C.*, 126, 50, 21223-21233, 2022.
[45] Y. Chang *et al.*, "Formation mechanism of (001) oriented perovskite $SrTiO_3$ microplatelets synthesized by topochemical microcrystal conversion," *Inorg. Chem.*, 53 20, 11060–11067, 2014.
[46] J. Wu *et al.*, "Topochemical transformation of single crystalline $SrTiO_3$ microplatelets from $Bi_4Ti_3O_{12}$ precursors and their orientation-dependent surface piezoelectricity," *CrystEngComm*, 20, 22, 3084–3095, 2018.
[47] S. F. Poterala, Y. Chang, T. Clark, R. J. Meyer, G. L. Messing, and G. L. Messinge, "Mechanistic interpretation of the aurivillius to perovskite topochemical microcrystal conversion process," *Chem. Mater.*, 22, 6, 2061–2068, 2010.
[48] V. Kalyani *et al.*, "Hydrothermal Synthesis of $SrTiO_3$: Role of Interfaces," *Cryst. Growth Des.*, 15, 12, 5712–5725, 2015.
[49] K. Byrappa and M. Yoshimura, *Handbook of Hydrothermal Technology, Technology for Crystal Growth and Materials Processing*. 2001.
[50] J. Yu and P. E. Savage, "Decomposition of Formic Acid under Hydrothermal Conditions," *Ind. Eng. Chem. Res.*, 37, 1, 2–10, 1998.
[51] H. Pińkowska, P. Wolak, and A. Złocińska, "Hydrothermal decomposition of alkali lignin in sub- and supercritical water," *Chem. Eng. J.*,. 187, 410–414, 2012.
[52] A. Hu, X. Zhang, K. D. Oakes, P. Peng, Y. N. Zhou, and M. R. Servos, "Hydrothermal growth of free standing TiO_2 nanowire membranes for photocatalytic degradation of pharmaceuticals," *J. Hazard. Mater.*, 189, 1–2, 278–285, 2011.
[53] C. Wang and L. A. Johnson, "Functional properties of hydrothermally cooked soy protein products," *JAOCS, J. Am. Oil Chem. Soc.*, 78, 2,189–195, 2001.
[54] A. T. Getachew and B. S. Chun, "Influence of hydrothermal process on bioactive compounds extraction from green coffee bean," *Innov. Food Sci. Emerg. Technol.*, 38, 24–31, 2016.
[55] J. Livage, M. Henry and C. Sanchez, "Sol-ge chemistry of transition metal oxides" *Prog. Solid. S. Chem.* 18, 4, 259-341, 1989.
[56] S. E. Cummins and L. E. Cross, "Electrical and optical properties of ferroelectric $Ba_4Ti_3O_{12}$ single crystals," *J. Appl. Phys.*, 39, 5, 2268–2274, 1968.
[57] D. Urushihara, M. Komabuchi, N. Ishizawa, M. Iwata, K. Fukuda, and T. Asaka, "Direct observation of the ferroelectric polarization in the layered perovskite $Bi_4Ti_3O_{12}$," *J. Appl. Phys.*, 120, 14, 2016.
[58] Q. Zhou, B. J. Kennedy, and C. J. Howard, "Structural Studies of the Ferroelectric Phase Transition in $Bi_4Ti_3O_{12}$," *Chem. Mater.*, 15, 26, 5025–5028, 2003.
[59] F. Zhang, T. Karaki, and M. Adachi, "Coprecipitation Synthesis of Nanosized $Bi_4Ti_3O_{12}$ Particles," *Jpn. J. Appl. Phys.*, 45, 9B, 7385–7388, 2006.
[60] M. Villegas, C. Moure, J. F. Fernandez, and P. Duran, "Preparation and sintering behaviour of submicronic $Bi_4Ti_3O_{12}$ powders," *J. Mater. Sci.*, 31, 4,949–955, 1996.
[61] Y. G. Zhang *et al.*, "Photovoltaic effects in $Bi_4Ti_3O_{12}$ thin film prepared by a sol-gel method," *Mater. Lett.*, 125, 65,25–27, 2014.
[62] M. G. Navarro-Rojero, J. J. Romero, F. Rubio-Marcos, and J. F. Fernandez, "Intermediate phases formation during the synthesis of Bi_4Ti3O_{12} by solid state reaction," *Ceram. Int.*, 36, 4, 1319–1325, 2010.
[63] T. Jardiel, A. C. Caballero, J. F. Fernández, and M. Villegas, "Domain structure of $Bi_4Ti_3O_{12}$ ceramics revealed by chemical etching," *J. Eur. Ceram. Soc.*, 26, 2823–2826, 2006.
[64] Z. Xie, X. Tang, J. Shi, Y. Wang, G. Yuan, and J. M. Liu, "Excellent piezo-photocatalytic performance of $Bi_4Ti_3O_{12}$ nanoplates synthesized by molten-salt method," *Nano Energy*, 98, 1, 107247, 2022.
[65] D. Makovec *et al.*, "Ferroelectric bismuth-titanate nanoplatelets and nanowires with a new crystal structure," *Nanoscale*,14, 9, 3537–3544, 2022.
[66] Y. Liu *et al.*, "A novel $CeO_2/Bi_4Ti_3O_{12}$composite heterojunction structure with an enhanced photocatalytic activity for bisphenol A," *J. Alloys Compd.*, 688, 487–496, 2016.
[67] W. Zhao, Z. Jia, E. Lei, L. Wang, Z. Li, and Y. Dai, "Photocatalytic degradation efficacy of $Bi_4Ti_3O_{12}$ micro-scale platelets over methylene blue under visible light," *J. Phys. Chem. Solids*, 74, 11, 1604–1607, 2013.
[68] J. Wu, N. Qin, E. Lin, B. Yuan, Z. Kang, and D. Bao, "Synthesis of $Bi_4Ti_3O_{12}$ decussated nanoplates with enhanced piezocatalytic activity," *Nanoscale*, 11, 44, 21128–21136, 2019.
[69] X. Q. Chen *et al.*, "Enhanced multiferroic characteristics in Fe-doped $Bi_4Ti_3O_{12}$ ceramics,"

Solid State Commun., 150, 27–28, 1221–1224, 2010.
[70] J. Chen, Z. Tang, Y. Bai, and S. Zhao, "Multiferroic and magnetoelectric properties of $BiFeO_3$/ $Bi_4Ti_3O_{12}$ bilayer composite films," *J. Alloys Compd.*, 675, 257–265, 2016.
[71] T. Jardiel, A. C. Caballero, and M. Villegas, "Aurivillius ceramics: $Bi_4Ti_3O_{12}$-based piezoelectrics," *J. Ceram. Soc. Japan*, 116, 1352, 511–518, 2008.
[72] Z. Lazarevic, B. D. Stojanovic, and J. A. Varela, "An approach to analyzing synthesis, structure and properties of bismuth titanate ceramics," *Sci. Sinter.*, 37, 3, 199–216, 2005.
[73] Z. Ž. Lazarevic, N. Ž. Rom, M. Todorovic, and B. D. Stojanovic, "Structural and Ferroelectrical Properties of Bismuth Titanate Ceramic Powders Prepared by Mechanically Assisted Synthesis," *Sci. Sinter.*, 39, 2,177–184, 2007.
[74] T. Kimura, "Molten Salt Synthesis of Ceramic Powders," *Adv. Ceram. - Synth. Charact. Process. Specif. Appl.*, 75–100, 2011.
[75] L. Li, J. Deng, J. Chen, and X. Xing, "Topochemical molten salt synthesis for functional perovskite compounds," *Chem. Sci.*, 7,2, 855–865, 2016.
[76] K. H. Yoon, Y. S. Cho, and D. H. Kang, "Molten salt synthesis of lead-based relaxors," *J. Mater. Sci.*, 33, 12, 2977–2984, 1998.
[77] M. Broström, S. Enestam, R. Backman, and K. Mäkelä, "Condensation in the KCl – NaCl system Condensation in the KCl – NaCl system," *Fuel Process. Technol.*, 105, 1, 142–148, 2011.
[78] A. S. Basin, A. B. Kaplun, A. B. Meshalkin, and N. F. Uvarov, "The LiCl-KCl binary system," *Russ. J. Inorg. Chem.*, 53, 9, 1509–1511, 2008.
[79] T. Wang, D. Mantha, and R. G. Reddy, "Thermal stability of the eutectic composition in $LiNO_3$-$NaNO_3$-KNO_3 ternary system used for thermal energy storage," *Sol. Energy Mater. Sol. Cells*, 100, 162–168, 2012.
[80] W. Sui, H. Yu, S. Luan, and L. Wang, "Preparation and characterization of $Bi_4Ti_3O_{12}$ platelets by a novel low-temperature molten salt system," *J. Wuhan Univ. Technol. Sci. Ed.*, 24, 2, 241–244, 2009.
[81] J. F. Cao and Y.-X. Ji, "Morphology-controlled synthesis of $SrTiO_3$ micro-scale particles," *Chinese Phys. B*, 23,12, 128104, 2014.
[82] S. Su, R. Zuo, D. Lv, and J. Fu, "Synthesis and characterization of (001) oriented $BaTiO_3$ platelets through a topochemical conversion," *Powder Technol.*, 217,11–15, 2012.
[83] D. Liu, Y. Yan, and H. Zhou, "Synthesis of Micron-Scale Platelet $BaTiO_3$," *J. Am. Ceram. Soc.*, 90, 4, 1323–1326, 2007.
[84] H. He *et al.*, "Size controllable synthesis of single-crystal ferroelectric $Bi_4Ti_3O_{12}$ nanosheet dominated with {001} facets toward enhanced visible-light-driven photocatalytic activities," *Appl. Catal. B Environ.*, 156–157, 35–43, 2014.
[85] M. Villegas, A. C. Caballero, C. Moure, P. Duran, and J. F. Fernandez, "Factors Affecting the Electrical Conductivity of Donor-Doped $Bi_4Ti_3O_{12}$ Piezoelectric Ceramics," *J. Am. Ceram. Soc.*,. 82, 9, 2411–2416, 1999.
[86] T. Zaremba, "Investigation of synthesis and microstructure of bismuth titanates with TiO_2 rich compounds," *J. Therm. Anal. Calorim.*, 93, 3, 829–832, 2008.
[87] T. Zaremba, "Anisotropic grain growth of bismuth titanate in molten salt fluxes," *Zeitschrift fur Krist. Suppl.*, 30, 30, 477–482, 2009.
[88] Y. Kan, X. Jin, P. Wang, Y. Li, Y. B. Cheng, and D. Yan, "Anisotropic grain growth of $Bi_4Ti_3O_{12}$ in molten salt fluxes," *Mater. Res. Bull.*, 38, 4, 567–576, 2003.
[89] H. Joop and J. Sefcik, *The Handbook of Continuous Crystallization*. The Royal Society of Chemistry, 2020.
[90] V. K. LaMer and R. H. Dinegar, "Journal of the," *J. Am. Ceram. Soc.*, 72,11, 4847–4854, 1950.
[91] P. Cubillas and M. W. Anderson, *Synthesis Mechanism: Crystal Growth and Nucleation*, 1. 2010.
[92] K. Sangwal and R. Rodrigez-Clemente, "Surface Morphology of Crystalline Solids," *Trans Tech Publ.*, Zurich, Switzerland, 1991.
[93] P. Hartman, *Crystal growth- an introduction*. North Holland, Amsterdam, 1973.
[94] F. C. Frank, "The influence of dislocations on crystal growth," *Discuss. Faraday Soc.*, 5, 48–54, 1949.
[95] W. K. Burton, N. Cabrera, and F. C. Frank, "The growth of crystals and the equilibrium structure of their surfaces," *Philos. Trans. R. Soc., A*, A243, 299, 1951.
[96] F. C Frank and J. H. van der Merwe, "One dimensional dislocations. I. Static Theory" *Proceedings of the Royal Society A*, 198, 1053, 205–216, 1949.
[97] A. M. Visinoiu, "Growth mechanism and structure of epitaxial perovskite thin films and superlattices," 2003.

[98] K. R. Dixit, “Epitaxial growth of thin films,” *Proc. Indian Acad. Sci. - Sect. A*, 48, 6, 330–335, 1958.
[99] M. Klusáčková, R. Nebel, K. M. Macounová, M. Klementová, and P. Krtil, “Size control of the photo-electrochemical water splitting activity of $SrTiO_3$ nano-cubes,” *Electrochim. Acta*, 297, 215–222, 2019.
[100] D. Hu, H. Ma, Y. Tanaka, L. Zhao, and Q. Feng, “Ferroelectric Mesocrystalline $BaTiO_3$/$SrTiO_3$ Nanocomposites with Enhanced Dielectric and Piezoelectric Responses,” *Chem. Mater.*, 27, 14, 4983–4994, 2015.
[101] L. Mu *et al.*, “Enhancing charge separation on high symmetry $SrTiO_3$ exposed with anisotropic facets for photocatalytic water splitting,” *Energy Environ. Sci.*, 9, 7, 2463–2469, 2016.
[102] H. Y. Wang, J. Chen, F. X. Xiao, J. Zheng, and B. Liu, “Doping-induced structural evolution from rutile to anatase: Formation of Nb-doped anatase TiO_2 nanosheets with high photocatalytic activity,” *J. Mater. Chem. A*, 4, 18, 6926–6932, 2016.
[103] B. Shi, H. Yin, J. Gong, and Q. Nie, “Ag/AgCl decorated $Bi_4Ti_3O_{12}$ nanosheet with highly exposed (001) facets for enhanced photocatalytic degradation of Rhodamine B, Carbamazepine and Tetracycline,” *Appl. Surf. Sci.*, 419, 614–623, 2017.
[104] F. Polo-Garzon *et al.*, “Controlling Reaction Selectivity through the Surface Termination of Perovskite Catalysts,” *Angew. Chemie - Int. Ed.*, 129, 33, 9952–9956, 2017.
[105] Y. Liu, G. Zhu, J. Gao, and M. Hojamberdiev, “Applied Catalysis B : Environmental Enhanced photocatalytic activity of $Bi_4Ti_3O_{12}$ nanosheets by Fe^{3+}-doping and the addition of Au nanoparticles : Photodegradation of Phenol and bisphenol A,” *"Applied Catal. B, Environ,*. 200, 72–82, 2017.
[106] IUPAC, “IUPAC Compendium of Chemical Terminology,” *IUPAC Compend. Chem. Terminol. Gold B.*, 2, 1997.
[107] T. Watanabe, M. Watanabe, T. Suzuki, and S. Yamabi, “Platelet $NaNbO_3$ grown by single-step molten salt synthesis : Study on bismuth migration in topochemical conversion reaction Platelet $NaNbO_3$ grown by single-step molten salt synthesis :,” *Jpn. J. Appl. Phys.*, 53, 1–5, 2014.
[108] Y. Chang *et al.*, “Formation Mechanism of (001) Oriented Perovskite $SrTiO_3$ Microplatelets Synthesized by Topochemical Microcrystal Conversion,” 53, 20, 11060-11067, 2014.
[109] R. E. Schaak and T. E. Mallouk, “Topochemical synthesis of three-dimensional perovskites from lamellar precursors,” *J. Am. Chem. Soc.*,122, 12, 2798–2803, 2000.
[110] H. X. Wu, J. Fu, Y. Hou, M. Zheng, and M. Zhu, “Topochemical Conversion of (111) $BaTiO_3$ Piezoelectric Microplatelets Using $Ba_6Ti_{17}O_{40}$ as the Precursor Published as part of a Crystal Growth and Design virtual special issue on Crystalline Functional Materials in,” *Cryst. Growth Des.*, 19, 111, 1198–1205, 2018.
[111] M. Maček Kržmanc *et al.*, “Tailoring the Shape, Size, Crystal Structure, and Preferential Growth Orientation of $BaTiO_3$ Plates Synthesized through a Topochemical Conversion Process,” *Cryst. Growth Des.*, 17, 6, 3210–3220, 2017.
[112] Y. Saito, H. Takao, and K. Wada, “Synthesis of platelike $CaTiO_3$ particles by a topochemical microcrystal conversion method and fabrication of textured microwave dielectric ceramics,” *Cheram. Inter.* 34, 4, 745–751, 2008.
[113] K. Biradha and R. Santra, “Crystal engineering of topochemical solid-state reactions,” *Chem. Soc. Rev.*, 42, 3, 950–967, 2013.
[114] T. Takeuchi, T. Tani, and T. Satoh, “Microcomposite particles $Sr_3Ti_2O_7$–$SrTiO_3$ with an epitaxial core – shell structure,” *Sol. S. Ion.*108, 67–71, 1998.
[115] Y. Saito and H. Takao, “Synthesis of platelike {100} $SrTiO_3$ particles by topochemical microcrystal conversion and fabrication of grain-oriented ceramics,” *Japanese J. Appl. Physics*, 45, 9B, 7377–7381, 2006.
[116] K. Watari, et al., "Epitaxial growth of anisotropically shaped, single-crystal particles of cubic $SrTiO_3$," *J. Mat. Res.*, 15, 4, 846–849, 2000.
[117] L. Li, A. J. Fijneman, J. A. Kaandorp, J. Aizenberg, and W. L. Noorduin, “Directed nucleation and growth by balancing local supersaturation and substrate/nucleus lattice mismatch,” *Proc. Natl. Acad. Sci. U. S. A.*, 115, 14, 3575–3580, 2018.
[118] M. M. Lencka and R. E. Riman, “Hydrothermal synthesis of perovskite materials: Thermodynamic modeling and experimental verification,” *Ferroelectrics*, 151, 1, 159–164, 1994.
[119] M. M. Lencka and R. E. Riman, “Thermodynamics of the Hydrothermal Synthesis of Calcium Titanate with Reference to other Alkaline-Earth Titanates,” *Chem. Mater.*, 7, 1, 18–25, 1995.

[120] Y. Zhang, L. Zhong, and D. Duan, “Single-step hydrothermal synthesis of strontium titanate nanoparticles from crystalline anatase titanium dioxide,” *Ceram. Int.*, 41, 10, 13516–13524, 2015.
[121] Y. Huang *et al.*, “The application of perovskite materials in solar water splitting,” *J. Semicond.*, 41, 1, 11701-11719, 2020.
[122] European Commission, “2050 long-term strategy.” [Online]. Available: https://climate.ec.europa.eu/eu-action/climate-strategies-targets/2050-long-term-strategy_en (3.12.2022).
[123] Računsko sodišče Republike Slovenije, “REVIZIJSKO POROČILO Udejanjanje e-mobilnosti 2020,” 2020 (3.12.2022).
[124] M. A. Nadeem, M. A. Khan, A. A. Ziani, and H. Idriss, “An overview of the photocatalytic water splitting over suspended particles,” *Catalysts*, 11, 1, 1–25, 2021.
[125] J. Zhu, L. Hu, P. Zhao, L. Y. S. Lee, and K. Y. Wong, “Recent Advances in Electrocatalytic Hydrogen Evolution Using Nanoparticles,” *Chem. Rev.*, 120, 2, 851–918, 2020.
[126] S. Chen, T. Takata, and K. Domen, “Particulate photocatalysts for overall water splitting,” *Nat. Rev. Mater.*, 2, 10, 201750–201766, 2017.
[127] European Commission, “Fossil fuels led in electricity generation in 2021.” [Online]. Available: https://ec.europa.eu/eurostat/web/products-eurostat-news/-/ddn-20220630-1 (4.12.2022).
[128] S. GEN, “Oskrba Slovenije z energijo.” [Online]. Available: https://www.esvet.si/ (5.12.2022).
[129] E. Commission, “Transport emissions.” [Online]. Available: https://climate.ec.europa.eu/eu-action/transport-emissions_en (4.12.2022).
[130] Scania, “Norwegian wholesaler ASKO puts hydrogen-powered fuel cell electric Scania trucks on the road,” 2020. [Online]. Available: https://www.scania.com/group/en/home/newsroom/news/2020/norwegian-wholesaler-asko-puts-hydrogen-powered-fuel-cell-electric-scania-trucks-on-the-road.html (5.12.2022).
[131] Pipistrel Vertical Solution, “Pipistrel Aircrafts.” [Online]. Available: https://www.pipistrel-aircraft.com/sl/ (5.12.2022).
[132] M. Newborough and G. Cooley, “Developments in the global hydrogen market: The spectrum of hydrogen colors,” *Fuel Cells Bull.*, 2020, 11, 16–22, 2020.
[133] International Energy Agency, “The Future of Hydrogen: Seizing today’s opportunities,” *IEA Publ.*, June, 14, 2019 (1.12.2022).
[134] European Commission, “Sustainable and optimal use of biomass for energy in the EU beyond 2020 Final report PricewaterhouseCoopers EU Services EESV’s consortium To EC Directorate General for Energy Directorate C1-Renewables and CCS policy,” 2017 (2.12.2022).
[135] F. Dawood, M. Anda, and G. M. Shafiullah, “Hydrogen production for energy: An overview,” *Int. J. Hydrogen Energy*, 45, 7, 3847–3869, 2020.
[136] T. Takata *et al.*, “Photocatalytic water splitting with a quantum efficiency of almost unity,” *Nature*, 581, 7809, 411–414, 2020.
[137] H. Nishiyama *et al.*, “Photocatalytic solar hydrogen production from water on a 100 m^2 scale,” *Nature*, 598, 7880, 304–307, 2021.
[138] B. McKenzie, “Shaping Tomorrow ’ S Global Hydrogen Market,” Fuell Cells Bulltein, 11, 16-22, 2020.
[139] R. Krishna *et al.*, “Hydrogen Storage for Energy Application,” *Hydrog. Storage*, InTech, Sept. 5, 2012.
[140] C. Wulf *et al.*, “Life Cycle Assessment of hydrogen transport and distribution options,” *J. Clean. Prod.*, 199, 431–443, 2018.
[141] C. Rivkin, R. Burgess, and W. Buttner, “Hydrogen Technologies Safety Guide,” *NREL*, 1, 67, 2015.
[142] The National Hydrogen Association and U.S. Department of Energy, “Hydrogen: Similar but Different,” *Education*, 2, 1875 [Online].
Abailable: https://www1.eere.energy.gov/hydrogenandfuelcells/pdfs/h2_safety_fsheet.pdf (3.2.2023) .
[143] Z. Zhou, Z. Pei, L. Wei, S. Zhao, X. Jian, and Y. Chen, “Electrocatalytic hydrogen evolution under neutral pH conditions: Current understandings, recent advances, and future prospects,” *Energy Environ. Sci.*, 13, 10, 3185–3206, 2020.
[144] S. Ardo *et al.*, “Pathways to electrochemical solar-hydrogen technologies,” *Energy Environ. Sci.*, 11, 10, 2768–2783, 2018.

[145] K. Takanabe, “Photocatalytic Water Splitting: Quantitative Approaches toward Photocatalyst by Design,” *ACS Catal.*, 7, 11, 8006–8022, 2017.
[146] R. Li and C. Li, "Photocatalytic Water Splitting on Semiconductor-Based Photocatalysts", *Advances in Catalysis*, 60, 1-57, 2017.
[147] K. S. Joya, Y. F. Joya, K. Ocakoglu, and R. Van De Krol, “Water-splitting catalysis and solar fuel devices: Artificial leaves on the move,” *Angew. Chemie - Int. Ed.*, 52, 40, 10426–10437, 2013.
[148] S. Cao, L. Piao, and X. Chen, “Emerging Photocatalysts for Hydrogen Evolution,” *Trends Chem.*, 2, 1, 57–70, 2020.
[149] N. Syed, J. Huang, Y. Feng, X. Wang, and L. Cao, “Carbon-Based Nanomaterials via Heterojunction Serving as Photocatalyst,” *Front. Chem.*, 7, 713-720, 2019.
[150] M. Sayed, J. Yu, G. Liu, and M. Jaroniec, “Non-Noble Plasmonic Metal-Based Photocatalysts,” *Chem. Rev.*, 122, 11, 10484–10537, 2022.
[151] J. E. Funk, “Thermochemical hydrogen production: Past and present,” *Int. J. Hydrogen Energy*, 26, 3, 185–190, 2001.
[152] R. Mohanty, S. Mansingh, K. Parida, and K. Parida, “Boosting sluggish photocatalytic hydrogen evolution through piezo-stimulated polarization: a critical review,” *Mater. Horizons*, 9, 5, 1332–1355, 2022.
[153] Q. Tang *et al.*, “Enhanced Piezocatalytic Performance of $BaTiO_3$ Nanosheets with Highly Exposed {001} Facets,” *Adv. Funct. Mater.*, 32, 35, 2–9, 2022.
[154] K. C. Christoforidis and P. Fornasiero, “Photocatalytic Hydrogen Production: A Rift into the Future Energy Supply,” *ChemCatChem*, 9, 9, 1523–1544, 2017.
[155] H. Song, S. Luo, H. Huang, B. Deng, and J. Ye, “Solar-Driven Hydrogen Production: Recent Advances, Challenges, and Future Perspectives,” *ACS Energy Lett.*, 7, 3, 1043–1065, 2022.
[156] I. A. Vasiliadou *et al.*, “Biological and bioelectrochemical systems for hydrogen production and carbon fixation using purple phototrophic bacteria,” *Front. Energy Res.*, 6, 11, 1–12, 2018.
[157] L. C. Biome *et al.*, “Long-Term Sustainability of a,” 314, 10, 479–483, 2006.
[158] “Nanogalvanic Aluminum Powder For Hydrogen Generation,” 59715.
[159] Y. Bilge, C. Guenter, M. C. Petri, and C. Forsberg, “Configuration and Technology Implications of Potential Nuclear Hydrogen System Applications prepared by Nuclear Engineering Division,” *Argonne Natl. Lab.*, 117, 2005.
[160] D. Bürkle and M. Roeb, “DLR scientists achieve solar hydrogen production in a 100-kilowatt pilot plant,” *Dtsch. Zent. für Luft- und Raumfahrt*, 11, 1–3, 2008.
[161] S. Tasleem and M. Tahir, “Current trends in strategies to improve photocatalytic performance of perovskites materials for solar to hydrogen production,” *Renew. Sustain. Energy Rev.*, 132, 10, 110073, 2020.
[162] T. Hisatomi, K. Takanabe, and K. Domen, “Photocatalytic Water-Splitting Reaction from Catalytic and Kinetic Perspectives,” *Catal. Letters*, 145, 1, 95–108, 2015.
[163] P. Zhou et al., “Solar-to-hydrogen efficiency of more than 9 % in photocatalytic water splitting,” *Nature*, 613, 7942, 60-67, 2023.
[164] P. Tang, Y. Tong, H. Chen, F. Cao, and G. Pan, “Microwave-assisted synthesis of nanoparticulate perovskite $LaFeO_3$ as a high active visible-light photocatalyst,” *Curr. Appl. Phys.*, 13, 2, 340–343, 2013.
[165] S. Chen and L. W. Wang, “Thermodynamic oxidation and reduction potentials of photocatalytic semiconductors in aqueous solution,” *Chem. Mater.*, 24, 18, 3659–3666, 2012.
[166] Y. Yang, L. Kang, and H. Li, “Enhancement of photocatalytic hydrogen production of $BiFeO_3$ by Gd^{3+} doping,” *Ceram. Int.*, 45, 6, 8017–8022, 2019.
[167] W. Zhao *et al.*, “Recent advances in photocatalytic hydrogen evolution with high-performance catalysts without precious metals,” *Renew. Sustain. Energy Rev.*, 132, 8, 2019, 110040, 2020.
[168] K. Afroz, N. Bakranov, M. Moniruddin, N. Bakranov, S. Kudaibergenov, and N. Nuraje, “A heterojunction strategy to improve the visible light sensitive water splitting performance of photocatalytic materials,” *J. Mater. Chem. A*, 6, 44, 21696–21718, 2018.
[169] S. Patial, V. Hasija, P. Raizada, P. Singh, A. A. P. Khan Singh, and A. M. Asiri, “Tunable photocatalytic activity of $SrTiO_3$ for water splitting: Strategies and future scenario,” *J. Environ. Chem. Eng.*, 8, 3, 103791, 2020.
[170] P. Li, S. Ouyang, G. Xi, T. Kako, and J. Ye, “The effects of crystal structure and electronic structure on photocatalytic H_2 evolution and CO_2 reduction over two phases of perovskite-structured $NaNbO_3$,” *J. Phys. Chem. C*, 116, 14, 7621–7628, 2012.

[171] J. Kong, T. Yang, Z. Rui, and H. Ji, "Perovskite-based photocatalysts for organic contaminants removal: Current status and future perspectives," *Catal. Today*, 327, February 2018, 47–63, 2019.
[172] U. S. Shenoy, H. Bantawal, and D. K. Bhat, "Band Engineering of $SrTiO_3$: Effect of Synthetic Technique and Site Occupancy of Doped Rhodium," *J. Phys. Chem. C*, 122, 48, 27567–27574, 2018.
[173] P. Zhang, T. Omoya Ochi, M. Fujitsuka, Y. Kobori, T. Majima, and T. Tachikawa, "Photocatalysis Topotactic Epitaxy of $SrTiO_3$ Mesocrystal Superstructures with Anisotropic Construction for Efficient Overall Water Splitting." *Angew. Chem.*, 56, 19, 5299-5303, 2017.
[174] R. Niishiro, S. Tanaka, and A. Kudo, "Hydrothermal-synthesized $SrTiO_3$ photocatalyst codoped with rhodium and antimony with visible-light response for sacrificial H_2 and O_2 evolution and application to overall water splitting," *Appl. Catal. B Environ.*, 150–151, 187–196, 2014.
[175] J. Ling, K. Wang, Z. Wang, H. Huang, and G. Zhang, "Enhanced piezoelectric-induced catalysis of $SrTiO_3$ nanocrystal with well-defined facets under ultrasonic vibration," *Ultrason. Sonochem.*, 61, 10, 104819–104830, 2020.
[176] T. Kimijima, K. Kanie, M. Nakaya, and A. Muramatsu, "Solvothermal Synthesis of Shape-Controlled Perovskite $MTiO_3$ (M = Ba, Sr, and Ca) Particles in H_2O/Polyols Mixed Solutions," 55, 1, 147–153, 2014.
[177] S. Yang *et al.*, "Precisely controlled heterogeneous nucleation sites for TiO_2 crystal growth," *CrystEngComm*, 16, 32, 7502–7506, 2014.
[178] A. Hakki, Y. AlSalka, C. B. Mendive, J. Ubogui, P. C. Dos Santos Claro, and D. Bahnemann, "Hydrogen production by heterogeneous photocatalysis," *Encycl. Interfacial Chem. Surf. Sci. Electrochem.*, 4, 413–419, 2018.
[179] J. J. Velázquez, R. Fernández-González, L. Díaz, E. Pulido Melián, V. D. Rodríguez, and P. Núñez, "Effect of reaction temperature and sacrificial agent on the photocatalytic H_2-production of Pt-TiO_2," *J. Alloys Compd.*, 721, 405–410, 2017.
[180] H. Zhou, J. Guo, P. Li, T. Fan, D. Zhang, and J. Ye, "Leaf-architectured 3D hierarchical artificial photosynthetic system of perovskite titanates towards CO_2 photoreduction into hydrocarbon fuels," *Sci. Rep.*, 3, 1–9, 2013.
[181] R. Van De Krol, Y. Liang, and J. Schoonman, "Solar hydrogen production with nanostructured metal oxides," *J. Mater. Chem.*, 18, 20, 2311–2320, 2008.
[182] K. Sivula and R. Van De Krol, "Semiconducting materials for photoelectrochemical energy conversion," *Nat. Rev. Mater.*, 1, 2, 15010, 2016.
[183] L. Sun, L. Han, J. Huang, X. Luo, and X. Li, "Single-atom catalysts for photocatalytic hydrogen evolution: A review," *Int. J. Hydrogen Energy*, 47, 40, 17583–17599, 2022.
[184] M. Melchionna and P. Fornasiero, "Updates on the Roadmap for Photocatalysis," *ACS Catal.*, 10, 10, 5493–5501, 2020.
[185] S. Bai *et al.*, "Incorporation of Pd into Pt Co-Catalysts toward Enhanced Photocatalytic Water Splitting," *Part. Part. Syst. Charact.*, 33, 8, 506–511, 2016.
[186] C. Kong, Z. Li, and G. Lu, "The dual functional roles of Ru as co-catalyst and stabilizer of dye for photocatalytic hydrogen evolution," *Int. J. Hydrogen Energy*, 40, 17, 5824–5830, 2015.
[187] H. W. Kang, S. N. Lim, D. Song, and S. Bin Park, "Organic-inorganic composite of g-C_3N_4-$SrTiO_3$:Rh photocatalyst for improved H_2 evolution under visible light irradiation," *Int. J. Hydrogen Energy*, 37, 16, 11602–11610, 2012.
[188] Q. Yang *et al.*, "Exploring the mechanisms of metal co-catalysts in photocatalytic reduction reactions: Is Ag a good candidate?," *Appl. Catal. A Gen.*, 518, 213–220, 2016.
[189] X. Li *et al.*, "Single-Atom Pt as Co-Catalyst for Enhanced Photocatalytic H_2 Evolution," *Adv. Mater.*, 28, 12, 2427–2431, 2016.
[190] S. Zhao, D. Su, and A. Orlov, "Enhanced photocatalytic H_2 production by sub-nanometer Au nanoparticles," *Appl. Cat. B*, 126, 153-160, 2012.
[191] T. Takata *et al.*, "Photocatalytic water splitting with a quantum efficiency of almost unity," *Nature*, 581, 7809, 411–414, 2020.
[192] Y. Xu *et al.*, "Review of doping $SrTiO_3$ for photocatalytic applications," *Bull. Mater. Sci.*, 46, 1, 2023.
[193] H. Lyu *et al.*, "An Al-doped $SrTiO_3$ photocatalyst maintaining sunlight-driven overall water splitting activity for over 1000 h of constant illumination," *Chem. Sci.*, 10, 11, 3196–3201, 2019.
[194] Z. Zhao *et al.*, "Electronic structure basis for enhanced overall water splitting photocatalysis with aluminum doped $SrTiO_3$ in natural sunlight," *Energy Environ. Sci.*,

12, 4, 1385–1395, 2019.
[195] Z. Zhao, E. J. Willard, H. Li, Z. Wu, R. H. R. Castro, and F. E. Osterloh, “Aluminum enhances photochemical charge separation in strontium titanate nanocrystal photocatalysts for overall water splitting,” *J. Mater. Chem. A*, 6, 33, 16170–16176, 2018.
[196] T. Xian, H. Yang, L. Di, J. Ma, H. Zhang, and J. Dai, “Photocatalytic reduction synthesis of $SrTiO_3$-graphene nanocomposites and their enhanced photocatalytic activity,” *Nanoscale Res. Lett.*, 9, 1, 1–9, 2014.
[197] M. Abd Elkodous, A. Aatiqah, G. Kawamura, W. K. Tan, and A. Matsuda, “Metallic nanoparticles loaded Al–$SrTiO_3$ supported with $RhCr_2O_3$ and CoOOH cocatalysts for overall water splitting,” *Int. J. Hydrogen Energy*, 47, 85, 36139–36148, 2022.
[198] Y. Qin *et al.*, “La, Al-Codoped $SrTiO_3$ as a Photocatalyst in Overall Water Splitting: Significant Surface Engineering Effects on Defect Engineering,” *ACS Catal.*, 11429–11439, 2021.
[199] J. Cui *et al.*, “Zr-Al co-doped $SrTiO_3$ with suppressed charge recombination for efficient photocatalytic overall water splitting,” *Chem. Commun.*, 57, 81, 10640–10643, 2021.
[200] D. Gao, H. Yu, and Y. Xu, “Direct photoinduced synthesis and high H_2 -evolution performance of Bi-modified TiO_2 photocatalyst in a Bi(III)-EG complex system,” *Appl. Surf. Sci.*, 462, June, 623–632, 2018.
[201] W. Hu, L. Lin, R. Zhang, C. Yang, and J. Yang, “Highly Efficient Photocatalytic Water Splitting over Edge-Modified Phosphorene Nanoribbons,” *J. Am. Chem. Soc.*, 139, 43, 15429–15436, 2017.
[202] Y. Zhao, N. Hoivik, and K. Wang, “Recent advance on engineering titanium dioxide nanotubes for photochemical and photoelectrochemical water splitting,” *Nano Energy*, 30, 728–744, 2016.
[203] W. Zhao, W. Zhao, G. Zhu, T. Lin, F. Xu, and F. Huang, “Black strontium titanate nanocrystals of enhanced solar absorption for photocatalysis,” *CrystEngComm*, 39, 17, 7528–7534, 2015.
[204] J. Li, G. Zhang, S. Han, J. Cao, L. Duan, and T. Zeng, “Enhanced solar absorption and visible-light photocatalytic and photoelectrochemical properties of aluminium-reduced $BaTiO_3$ nanoparticles,” *Chem. Commun.*, 54, 7, 723–726, 2018.
[205] T. Bak, J. Nowotny, M. K. Nowotny, and L. R. Sheppard, “Defect engineering of titanium dioxide,” *J. Aust. Ceram. Soc.*, 44, 2, 63–67, 2008.
[206] S. G. Ullattil, S. B. Narendranath, S. C. Pillai, and P. Periyat, “Black TiO_2 Nanomaterials: A Review of Recent Advances,” *Chem. Eng. J.*, 343, February, 708–736, 2018.
[207] H. Tan *et al.*, “Oxygen vacancy enhanced photocatalytic activity of perovskite $SrTiO_3$,” *ACS Appl. Mater. Interfaces*, 6, 21, 19184–19190, 2014.
[208] X. Zhou *et al.*, “Intrinsically Activated $SrTiO_3$: Photocatalytic H_2 Evolution from Neutral Aqueous Methanol Solution in the Absence of Any Noble Metal Cocatalyst,” *ACS Appl. Mater. Interfaces*, 10, 35, 29532–29542, 2018.
[209] C. Zhen, J. C. Yu, G. J. Liu, and H. M. Cheng, “Selective deposition of redox co-catalyst(s) to improve the photocatalytic activity of single-domain ferroelectric $PbTiO_3$ nanoplates,” *Chem. Commun.*, 50, 72, 10416–10419, 2014.
[210] R. Chen *et al.*, “Charge separation via asymmetric illumination in photocatalytic Cu_2O particles,” *Nat. Energy*, 3, 8, 655–663, 2018.
[211] L. Guan and X. Chen, “Photoexcited Charge Transport and Accumulation in Anatase TiO_2,” *ACS Appl. Energy Mater.*, 1, 8, 4313–4320, 2018.
[212] Y. Si *et al.*, “What is the predominant electron transfer process for Au NRs/TiO_2 nanodumbbell heterostructure under sunlight irradiation?,” *Appl. Catal. B Environ.*, 220, 471–476, 2018.
[213] J. Wang, A. K. Tagantsev, and N. Setter, “Size effect in ferroelectrics: Competition between geometrical and crystalline symmetries,” *Phys. Rev. B - Condens. Matter Mater. Phys.*, 83, 1, 14104-1409, 2011.
[214] L. Wang *et al.*, “Fabrication of $MgTiO_3$ nanofibers by electrospinning and their photocatalytic water splitting activity,” *Int. J. Hydrogen Energy*, 42, 41, 25882–25890, 2017.
[215] Q. Su *et al.*, “Heterojunction Photocatalysts Based on 2D Materials: The Role of Configuration,” *Adv. Sustain. Syst.*, 4, 9, 1–19, 2020.
[216] L. Wang *et al.*, “Monolayer Epitaxial Heterostructures for Selective Visible-Light-Driven Photocatalytic NO Oxidation,” *Adv. Funct. Mater.*, 29, 15, 1–8, 2019.
[217] L. Wang *et al.*, “Boosting NIR-driven photocatalytic water splitting by constructing 2D/3D epitaxial heterostructures,” *J. Mater. Chem. A*, 7, 22, 13629–13634, 2019.
[218] A. Šutka, M. Järvekülg, and K. A. Gross, “Photocatalytic Nanoheterostructures and

Chemically Bonded Junctions Made by Solution-Based Approaches," *Crit. Rev. Solid State Mater. Sci.*, 44, 3, 239–263, 2019.
[219] K. Guo *et al.*, "Fabrication of ZnO/$SrTiO_3$ nanoarrays and its photoelectrochemical performances," *Int. J. Hydrogen Energy*, 39, 25, 13408–13414, 2014.
[220] B. J. Ng, L. K. Putri, X. Y. Kong, Y. W. Teh, P. Pasbakhsh, and S. P. Chai, "Z-Scheme Photocatalytic Systems for Solar Water Splitting," *Advanced Science*, 7. 1903171 (1–42), 2020.
[221] J. Ng, S. Xu, X. Zhang, H. Y. Yang, and D. D. Sun, "Hybridized nanowires and cubes: A novel architecture of a heterojunctioned TiO_2/$SrTiO_3$ thin film for efficient water splitting," *Adv. Funct. Mater.*, 20, 24, 4287–4294, 2010.
[222] N. Subha *et al.*, "Influence of synthesis conditions on the photocatalytic activity of mesoporous Ni doped $SrTiO_3$/TiO_2 heterostructure for H_2 production under solar light irradiation," *Colloids Surfaces A Physicochem. Eng. Asp.*, 522, 193–206, 2017.
[223] M. N. Ha *et al.*, "Morphology-controlled synthesis of $SrTiO_3$/TiO_2 heterostructures and their photocatalytic performance for water splitting," *RSC Adv.*, 6, 25, 21111–21118, 2016.
[224] European Commission, "REPowerEU: A plan to rapidly reduce dependence on Russian fossil fuels and fast forward the green transition." [Online]. Available: https://ec.europa.eu/commission/presscorner/detail/en/IP_22_3131 (13.1.2023).
[225] J. H. Kim *et al.*, "Hetero-type dual photoanodes for unbiased solar water splitting with extended light harvesting," *Nat. Commun.*, 7, 1–9, 2016.
[226] P. M. Voyles, J. L. Grazul, and D. A. Muller, "Imaging individual atoms inside crystals with ADF-STEM," *Ultramicroscopy*, 96, 3–4, 251–273, 2003.
[227] C. G. Ching *et al.*, "Effects of the nitric acid concentrations on the etching process, structural and optical properties of porous zinc oxide thin films," *Sains Malaysiana*, 42, 9, 1327–1332, 2013.
[228] K. F. Nurhaziqah *et al.*, "Effect of HNO_3 concentration on etch rate and structure of Si wafer etched in the mixture of HF and HNO_3 solutions," *ASM Sci. J.*, 11, Special Issue 1, 68–74, 2018.
[229] V. Leca, G. Rijnders, G. Koster, D. H. A. Blank, and H. Rogalla, "Wet etching methods for perovskite substrates," *Mater. Res. Soc. Symp. - Proc.*, 587, January, 3.6.1-3.6.4, 2000.
[230] T. Zhang, H. Huang, and R. Chen, "Wet chemical etching process of BST thin films for pyroelectric infrared detectors," *Ferroelectrics*, 410, 1, 137–144, 2011.
[231] R. Asiaie, W. D. Zhu, S. A. Akbar, and P. K. Dutta, "Characterization of submicron particles of tetragonal $BaTiO_3$," *Chem. Mater.*, 8, 1, 226–234, 1996.
[232] H.-I. Hsiang and F.-S. Yen, "Dielectric Properties and Ferroelectric Domain of $BaTiO_3$ Powders," *Jpn. J. Appl. Phys.*, 32, 1, 5029–5035, 1993.
[233] M. MačEk Kržmanc *et al.*, "$SrTiO_3$/$Bi_4Ti_3O_{12}$Nanoheterostructural Platelets Synthesized by Topotactic Epitaxy as Effective Noble-Metal-Free Photocatalysts for pH-Neutral Hydrogen Evolution," *ACS Appl. Mater. Interfaces*, 13, 1, 370–381, 2021.
[234] A. Čontala, N. Daneu, S. Gupta, M. Spreitzer, A. Meden, and M. Maček Kržmanc, "Hydrothermal topotactic epitaxy of $SrTiO_3$ on $Bi_4Ti_3O_{12}$ nanoplatelets: understanding the interplay of lattice mismatch and supersaturation," *Nanoscale Adv.*, 5, 3005–3017, 2023.
[235] Y. Saito and H. Takao, "Synthesis of polycrystalline platelike $KNbO_3$ particles by the topochemical micro-crystal conversion method and fabrication of grain-oriented $(K_{0.5}Na_{0.5})NbO_3$ ceramics," *J. Eur. Ceram. Soc.*, 27, 13-15, 4085-4092, 2007.
[236] K. C. Huango, T. C. Huango, and W. F. Hsieh, "Morphology-controlled synthesis of barium titanate nanostructures," *Inorg. Chem.*, 48, 19, 9180–9184, 2009.
[237] K. Watari, B. Brahmaroutu, G. L. Messing, S. Trolier-McKinstry, and S. C. Cheng, "Epitaxial growth of anisotropically shaped, single-crystal particles of cubic $SrTiO_3$," *J. Mater. Res.*, 15, 4, 846–849, 2000.
[238] R. E. Riman, "Thermodynamic Modeling of Hydrothermal Synthesis of," *Chem. Mater.*, 5, 8, 61–70, 1993.
[239] K. G. Knauss, M. J. Dibley, W. L. Bourcier, and H. F. Shaw, "Ti (IV) hydrolysis constants derived from rutile solubility measurements made from 100 to 300 C," *Geofluids*, 10, 20-40, 2001.
[240] E. Bartonickova, J. Cihlar, and K. Castkova, "Microwave-assisted synthesis of bismuth oxide," *Process. Appl. Ceram.*, 1, 1–2, 29–33, 2007.
[241] V. Kalyani *et al.*, "Hydrothermal Synthesis of $SrTiO_3$: Role of Interfaces," 2015.
[242] N. A. Lomanova, V. L. Ugolkov, and V. V. Gusarov, "Thermal behavior of layered perovskite-like compounds in the $Bi_4Ti_3O_{12}$-$BiFeO_3$ system," *Glas. Phys. Chem.*, 33, 6, 608–612, 2007.

[243] D. de Ligny and P. Richet, “High-temperature heat capacity and thermal expansion of and perovskites,” *Phys. Rev. B - Condens. Matter Mater. Phys.*, 53, 6, 3013–3022, 1996.
[244] E. Popova *et al.*, “Mechanism of the lattice relaxation in thin epitaxial films of iron oxides: Generalization from the case of ilmenite-hematite solid solution,” *Surf. Sci.*, 605, 11–12, 1043–1047, 2011.
[245] J. Narayan and B. C. Larson, “Domain epitaxy: A unified paradigm for thin film growth,” *J. Appl. Phys.*, 93, 1, 278–285, 2003.
[246] J. W. Matthews, “Defects Associated With the Accommodation of Misfit Between Crystals.,” *J Vac Sci Technol*, 12, 1, 126–133, 1974.
[247] R. C. Snyder and M. F. Doherty, “Faceted Crystal Shape Evolution During Dissolution or Growth,” *AlChE J.,* 53, 5, 1337-1348, 2007.
[248] S. Adireddy, C. Lin, B. Cao, W. Zhou, and G. Caruntu, “Solution-based growth of monodisperse cube-like $BaTiO_3$ colloidal nanocrystals,” *Chem. Mater.*, 22, 6, 1946–1948, 2010.
[249] M. Acosta *et al.*, “$BaTiO_3$-based piezoelectrics: Fundamentals, current status, and perspectives,” *Appl. Phys. Rev.*, 4, 4, 41305 2017.
[250] T. Gao *et al.*, “Highly oriented $BaTiO_3$ film self-assembled using an interfacial strategy and its application as a flexible piezoelectric generator for wind energy harvesting,” *J. Mater. Chem. a*, 3, 18, 9965–9971, 2015.
[251] B. Yuan, J. Wu, N. Qin, E. Lin, and D. Bao, “Enhanced Piezocatalytic Performance of $(Ba,Sr)TiO_3$ Nanowires to Degrade Organic Pollutants,” *ACS Appl. Nano Mater.*, 1, 9, 5119–5127, 2018.
[252] J. Wu, N. Qin, and D. Bao, “Effective enhancement of piezocatalytic activity of $BaTiO_3$ nanowires under ultrasonic vibration,” *Nano Energy*, 45, November 2017, 44–51, 2018.
[253] S. K. Ray, J. Cho, and J. Hur, “A critical review on strategies for improving the efficiency of $BaTiO_3$-based photocatalysts for wastewater treatment,” *J. Environ. Manage.*, 290, December 2020, p. 112679, 2021.
[254] A. Sood *et al.*, “A Comprehensive Review on Barium Titanate Nanoparticles as a Persuasive Piezoelectric Material for Biomedical Applications: Prospects and Challenges,” *Small*, 19, 12, 2023.
[255] A. A. A. Torimtubun, A. C. Augusty, E. Maulana, and L. Ernawati, “Affordable and sustainable new generation of solar cells: Calcium titanate ($CaTiO_3$) - Based perovskite solar cells,” *E3S Web Conf.*, 67, 1–6, 2018.
[256] M. Passi and B. Pal, “A review on $CaTiO_3$ photocatalyst: Activity enhancement methods and photocatalytic applications,” *Powder Technol.*, 388, 274–304, 2021.
[257] G. Gralik, A. E. Thomsen, C. A. Moraes, F. Raupp-Pereira, and D. Hotza, “Processing and characterization of $CaTiO_3$ perovskite ceramics,” *Processing and characterization of ceramics*, 8, 2, 53–57, 2014.
[258] L. S. Cavalcante *et al.*, “Synthesis, structural refinement and optical behavior of $CaTiO_3$ powders: A comparative study of processing in different furnaces,” *Chem. Eng.* 143, 1-3, 299–307, 2008.
[259] M. L. Moreira *et al.*, “Structural and optical properties of $CaTiO_3$ perovskite-based materials obtained by microwave-assisted hydrothermal synthesis: An experimental and theoretical insight,” *Acta Materialia*, 57, 5174–5185, 2009.
[260] T. Kimijima, K. Kanie, M. Nakaya, and A. Muramatsu, “Hydrothermal Synthesis of Size- and Shape-Controlled $CaTiO_3$ Fine Particles and their Photocatalytic Activity,” *Cryst. Eng. Comm.* 16, 25, 5591–5597, 2014.
[261] C. Han, J. Liu, W. Yang, Q. Wu, and H. Yang, “Photocatalytic activity of $CaTiO_3$ synthesized by solid state, sol–gel and hydrothermal methods,” *J. Sol-Gel Sci. Technol.*, 81, 806–813, 2017.
[262] Y. Hang, Y. Si, Q. Zhou, H. Yin, A. Wang, and A. Cao, “Morphology-controlled synthesis of calcium titanate particles and adsorption kinetics, isotherms, and thermodynamics of Cd(II), Pb(II), and Cu(II) cations,” *J. Hazard. Mater.*, 380, June 2018, 120789, 2019.
[263] T. Křenek, T. Kovářík, J. Pola, T. Stich, and D. Docheva, “Nano and micro-forms of calcium titanate: Synthesis, properties and application,” *Open Ceram.*, 8, 12, 100177, 2021.
[264] D. Wang, Z. Guo, Y. Chen, J. Hao, and W. Liu, “In situ hydrothermal synthesis of nanolamellate $CaTiO_3$ with controllable structures and wettability,” *Inorg. Chem.*, 46, 19, 7707–7709, 2007.
[265] R. Wang, S. Ni, G. Liu, and X. Xu, “Hollow $CaTiO_3$ cubes modified by La/Cr co-doping for efficient photocatalytic hydrogen production,” *Appl. Catal. B Environ.*, 225, 139–147, 2018.

[266] W. Dong, Q. Bao, X. Gu, and G. Zhao, “Controlled synthesis of flower-like $CaTiO_3$ and effects of morphology on its photocatalytic activities,” *J. Ceram. Soc. Japan*, 123, 1440, 643–648, 2015.
[267] Y. Yan, H. Yang, X. Zhao, H. Zhang, and J. Jiang, “A Hydrothermal Route to the Synthesis of $CaTiO_3$ Nanocuboids Using P25 as the Titanium Source,” *J. Electron. Mater.*, 47, 5, 3045–3050, 2018.
[268] J. Zhuang, Q. Tian, S. Lin, W. Yang, L. Chen, and P. Liu, “Precursor morphology-controlled formation of perovskites $CaTiO_3$ and their photo-activity for As(III) removal,” *Appl. Catal. B Environ.*, 156–157, 108–115, 2014.
[269] Q. Kuang and S. Yang, “Template synthesis of single-crystal-like porous $SrTiO_3$ nanocube assemblies and their enhanced photocatalytic hydrogen evolution,” *ACS Appl. Mater. Interfaces*, 5, 9, 3683–3690, 2013.
[270] Newport, “Medium Power Xenon Research Light Sources,” 2023. [Online]. Available: https://www.newport.com/f/medium-power-xenon-light-sources.
[271] Q. Kuang and S. Yang, “Template synthesis of single-crystal-like porous $SrTiO_3$ nanocube assemblies and their enhanced photocatalytic hydrogen evolution,” *ACS Appl. Mater. Interfaces*, 5, 9, 3683–3690, 2013.
[272] T. Puangpetch, T. Sreethawong, S. Yoshikawa, and S. Chavadej, “Hydrogen production from photocatalytic water splitting over mesoporous-assembled $SrTiO_3$ nanocrystal-based photocatalysts,” *J. Mol. Catal. A Chem.*, 312, 1–2, 97–106, 2009.
[273] B. S. Huang and M. Y. Wey, “Properties and H_2 production ability of Pt photodeposited on the anatase phase transition of nitrogen-doped titanium dioxide,” *Int. J. Hydrogen Energy*, 36, 16, 9479–9486, 2011.
[274] Z. L. Wu *et al.*, “A Semi-Conductive Copper-Organic Framework with Two Types of Photocatalytic Activity,” *Angew. Chemie - Int. Ed.*, 55, 16, 4938–4942, 2016.
[275] G. Zhang, Z. A. Lan, L. Lin, S. Lin, and X. Wang, “Overall water splitting by Pt/g-C_3N_4 photocatalysts without using sacrificial agents,” *Chem. Sci.*, 7, 5, 3062–3066, 2016.
[276] Q. Wang, T. Hisatomi, S. S. K. Ma, Y. Li, and K. Domen, “Core/shell structured La- and Rh-Codoped $SrTiO_3$ as a hydrogen evolution photocatalyst in Z-scheme overall water splitting under visible light irradiation,” *Chem. Mater.*, 26, 14, 4144–4150, 2014.
[277] P. Makuła, M. Pacia, and W. Macyk, “How To Correctly Determine the Band Gap Energy of Modified Semiconductor Photocatalysts Based on UV-Vis Spectra,” *J. Phys. Chem. Lett.*, 9, 23, 6814–6817, 2018.
[278] M. Milosevic and S. L. Berets, “A review of FT-IR diffuse reclection sampling considerations" 4928, 2002, 2007.
[279] S. J. Miklavcic, “Revised Kubelka – Munk theory II Unified framework for homogeneous and inhomogeneous optical media" *J. Opt. Soc*. 21, 10, 1942-1952, 2004.
[280] A. B. Murphy, “Band-gap determination from diffuse reflectance measurements of semiconductor films, and application to photoelectrochemical,” *Sol. Energ. and Sol. Cells,* 91, 14, 1326–1337, 2007.
[281] A. Escobedo-Morales, I. I. Ruiz-Lopez, M. del Ruiz-Peralta, et al., “Automated method for the determination of the band gap energy of pure and mixed powder samples using di ff use reflectance spectroscopy,” *Heliyon*, 5, 4, 1–19, 2019.
[282] S. Landi, I. R. Segundo, E. Freitas, M. Vasilevskiy, J. Carneiro, and C. J. Tavares, “Use and misuse of the Kubelka-Munk function to obtain the band gap energy from diffuse reflectance measurements,” *Solid State Commun.*, 341, July 2021, 1–7, 2022.
[283] X. P. Lin, F. Q. Huang, W. D. Wang, and K. L. Zhang, “A novel photocatalyst $BiSbO_4$ for egradation of methylene blue,” *Appl. Catal. A Gen.*, 307, 2, 257–262, 2006.
[284] M. Mousavi, A. Habibi-Yangjeh, and M. Abitorabi, “Fabrication of novel magnetically separable nanocomposites using graphitic carbon nitride, silver phosphate and silver chloride and their applications in photocatalytic removal of different pollutants using visible-light irradiation,” *J. Colloid Interface Sci.*, 480, 218–231, 2016
[285] T. Cao *et al.*, “$Bi_4Ti_3O_{12}$ nanosheets/TiO_2 submicron fibers heterostructures: In situ fabrication and high visible light photocatalytic activity,” *J. Mater. Chem.*, 21, 19, 6922–6927, 2011.
[286] R. S. Mulliken, “A new electroaffinity scale; Together with data on valence states and on valence ionization potentials and electron affinities,” *J. Chem. Phys.*, 2, 11, 782–793, 1934.
[287] R. S. Mulliken, “Electronic structures of molecules XI. Electroaffinity, molecular orbitals

and dipole moments," *J. Chem. Phys.*, 3, 9, 573–585, 1935.

[288] J. M. Bolts and M. S. Wrighton, "Correlation of photocurrent-voltage curves with flat-band potential for stable photoelectrodes for the photoelectrolysis of water," *J. Phys. Chem.*, 80, 24, 2641–2645, 1976

[289] P. Zhang, T. Ochi, M. Fujitsuka, Y. Kobori, T. Majima, and T. Tachikawa, "Topotactic Epitaxy of $SrTiO_3$ Mesocrystal Superstructures with Anisotropic Construction for Efficient Overall Water Splitting," *Angew. Chemie - Int. Ed.*, 56, 19, 5299–5303, 2017.

[290] X. Zhao, H. Yang, S. Li, Z. Cui, and C. Zhang, "Synthesis and theoretical study of large-sized $Bi_4Ti_3O_{12}$ square nanosheets with high photocatalytic activity," *Mater. Res. Bull.*, 107, May, 180–188, 2018.

[291] A. Hankin, F. E. Bedoya-Lora, J. C. Alexander, A. Regoutz, and G. H. Kelsall, "Flat band potential determination: Avoiding the pitfalls," *J. Mater. Chem. A*, 7, 45, 26162–26176, 2019.

[292] F. Cardon and W. P. Gomes, "On the determination of the flat-band potential of a semiconductor in contact with a metal or an electrolyte from the Mott-Schottky plot," *J. Phys. D. Appl. Phys.*, 11, 4, 1978.

[293] N. Denisov, J. E. Yoo, and P. Schmuki, "Effect of different hole scavengers on the photoelectrochemical properties and photocatalytic hydrogen evolution performance of pristine and Pt-decorated TiO_2 nanotubes," *Electrochim. Acta*, 319, 61–71, 2019.

[294] W. Yu and T. Peng, "Enhanced photocatalytic activity of g-C_3N_4 for selective CO_2 reduction to CH_3OH via facile coupling of ZnO: a direct Z-scheme mechanism," *J Mater Chem A*, 3, 39, 19936–19947, 2015.

[295] F. Dong, Q. Li, Y. Sun, and W. K. Ho, "Noble metal-like behavior of plasmonic Bi particles as a cocatalyst deposited on $(BiO)_2CO_3$ microspheres for efficient visible light photocatalysis," *ACS Catal.*, vol. 4, no. 12, pp. 4341–4350, 2014.

[296] X. Xu *et al.*, "Bi spheres SPR-coupled Cu_2O/Bi_2MoO_6 with hollow spheres forming Z-scheme $Cu_2O/Bi/Bi_2MoO_6$ heterostructure for simultaneous photocatalytic decontamination of sulfadiazine and Ni(II)," *J. Hazard. Mater.*, vol. 381, no. August 2019, p. 120953, 2020.

[297] S. Weng, B. Chen, L. Xie, Z. Zheng, and P. Liu, "Facile in situ synthesis of a Bi/BiOCl nanocomposite with high photocatalytic activity," *J. Mater. Chem. A*, vol. 1, no. 9, pp. 3068–3075, 2013.

[298] Y. Yu *et al.*, "A Bi/BiOCl heterojunction photocatalyst with enhanced electron-hole separation and excellent visible light photodegrading activity," *J. Mater. Chem. A*, vol. 2, no. 6, pp. 1677–1681, 2014.

[299] Wang Z., et. al. "Investigation of Optical and Photocatalytic Properties of Bismuth Nanospheres Prepared by a Facile Thermolysis Method," *J. Phys. Chem. C,* 118, 2, 1155–1160, 2014.

[300] T. H. Chiang *et al.*, "Efficient Photocatalytic Water Splitting Using Al-Doped $SrTiO_3$ Coloaded with Molybdenum Oxide and Rhodium-Chromium Oxide," *ACS Catal.*, 8, 4, 2782–2788, 2018.

[301] Z. Zhao *et al.*, "Environmental Science Electronic structure basis for enhanced overall water splitting photocatalysis with aluminum doped $SrTiO_3$ in natural sunlight," *Energ. Environ. Sci.* 12, 1385–1395, 2019.

Bibliography

Publications Related to the Thesis

Original Scientific Articles

A. Čontala, N. Daneu, S. Gupta, M. Spreitzer, A. Meden and M. Maček Kržmanc, "Hydrothermal Topotactic Epitaxy of $SrTiO_3$ on $Bi_4Ti_3O_{12}$ Nanoplatelets: Understanding the Interplay of Lattice Mismatch and Supersaturation," *Nanoscale Advances*, vol. 5, no. 11, pp. 3005-3017, 2023.

M. Maček, N. Daneu, A. Čontala, S. Santra, K. M. Kamal, B. Likozar and M. Spreitzer, "$SrTiO_3$/$Bi_4Ti_3O_{12}$ nanoheterostructural platelets synthesized by topotactic epitaxy as effective noble-metal-free photocatalysts for pH-neutral hydrogen evolution," *ACS applied materials & interfaces*, vol. 13, no. 1, pp. 370-381, 2021.

A. Čontala, M. Maček and D. Suvorov, "Plate-like $Bi_4Ti_3O_{12}$ particles and their topochemical conversion to $SrTiO_3$ under hydrothermal conditions," *Acta chimica slovenica*, vol. 65, no. 3, pp. 630-637, 2018.

Published Scientific Conference Contribution Abstract

M. Maček Kržmanc, A. Čontala, S. Gupta, N. Daneu and M. Spreitzer, „$SrTiO_3$ based two dimensional nanoplatelets for low-cost solar hydrogen generation" in *Materials today conference*, 2-5 August, 2023, Singapore Expo, Singapore.

A. Čontala, N. Daneu, A. Meden, M. Spreitzer and M. Maček, "Steering the hydrothermal topotactic epitaxy of $SrTiO_3$ on $Bi_4Ti_3O_{12}$ platelets by supersaturation, " in *Book of abstracts: 14th Jožef Stefan International Postgraduate School Students' Conference*, 1st - 3rd June, 2022, Kamnik, Slovenia. Ljubljana: Jožef Stefan International Postgraduate School, pp. 8, 2022.

A. Čontala, N. Daneu, M. Spreitzer and M. Maček, "Topochemical conversion for the formation of functional heterostructural perovskite titanates from $Bi_4Ti_3O_{12}$ platelets," in *Book of abstracts: 28th Annual Meeting of the Slovenian Chemical Society*, 21.-23. september 2022, Portorož, Slovenija. Ljubljana: Slovensko kemijsko društvo, pp. 100, 2022.

A. Čontala, N. Daneu, K. M. Kamal, B. Likozar, M. Spreitzer and M. Maček, "Hydrogen evolution with $SrTiO_3$/$Bi_4Ti_3O_{12}$ nanoheterostructural platelets as nobel-metal free photocatalyst" in *Proceedings: Throughout knowledge towards a green new world: 13th Jožef Stefan International Postgraduate School Students' Conference and 15th Young Researchers' Day of Chemistry, material science, biochemistry and environment, (CMBE day),* 27th-28th May 2021, online. Ljubljana: Jožef Stefan International Postgraduate School: Jožef Stefan Institute, pp. 57, 2021.

A. Čontala, M. Spretzer and M. Maček, "Mechanism of topochemical conversion of $Bi_4Ti_3O_{12}$ plates to $SrTiO_3$ plates under hydrothermal conditions" in *Book of abstracts: Science of the future how to stay up-to-date with your research!* 11th Jožef Stefan International Postgraduate School Students' Conference and 13th Young Researchers' Day, 15th and 16th May 2019, Planica, Slovenia. Ljubljana: Jožef Stefan International Postgraduate School: Jožef Stefan Institute, pp. 75, 2019.

A. Čontala, N. Daneu, M. Spreitzer and M. Maček "Topochemical conversion of $Bi_4Ti_3O_{12}$ nanoplatelets to $MTiO_3$ (M = Sr, Ca, Ba) nanoparticles under hydrothermal conditions,", in *Program and book of abstracts. 27th International Conference on Materials and Technology*, 16-18 October 2019, Portorož, Slovenia. Ljubljana: Inštitut za kovinske materiale in tehnologije, pp. 38, 2019.

A. Čontala, N. Daneu, M. Spreitzer and M. Maček, "Mechanism of topochemical conversion of $Bi_4Ti_3O_{12}$ in $SrTiO_3$ nanoplates under hydrothermal conditions," in *Programme and the book of abstracts: Yucomat*, Belgrade: Materials Research Society of Serbia, pp. 65, 2019.

A. Čontala, M. Maček and D. Suvorov, "Topochemical conversion of $Bi_4Ti_3O_{12}$ to $SrTiO_3$ under hydrothermal conditions," in *Programme and book of abstracts: 25th International Conference on Materials and Technology*, 16-19 October 2017, Portorož, Slovenia. Ljubljana: Inštitut za kovinske materiale in tehnologije, pp. 49, 2017.

A. Čontala, M. Maček and D. Suvorov, "Synthesis of $SrTiO_3$ particles: Tailoring the shape, size and crystal growth orientation," in Proceedings: 9th Jožef Stefan International Postgraduate School Students' Conference and 11th Young researchers' Day, 19.-20. 4. 2017, Ljubljana, Slovenija. Ljubljana: Jožef Stefan International Postgraduate School, Jožef Stefan Institute, pp. 48, 2017.

Published Scientific Conference Contribution Abstract (Invited Lecture)

M. Maček, A. Čontala, N. Daneu and M. Spreitzer, "$SrTiO_3/Bi_4Ti_3O_{12}$ nanoplatelets as effective photocatalysis for hydrogen evolution," in *Book of abstracts: JSI meeting on the synthesis, characterization and catalysts applications*, 25. 5. 2023 Ljubljana, Slovenia. Ljubljana: Department for nanostructured materials - K7, Jožef Stefan Institute, pp. 21, 2023.

N. Daneu, A. Čontala, M. Spreitzer and M. Maček, "Formation mechanism of $SrTiO_3/Bi_4Ti_3O_{12}$ nanoheterostructural platelets revealed by atomic-resolution STEM," in *Knjiga povzetkov*: *4. slovensko posvetovanje mikroskopistov:* 12.-13. maj, Ankaran. Ljubljana: Slovensko društvo za mikroskopijo, pp. 17, 2022.

Unpublished Invited Conference Lecture

D. Suvorov, M. Maček, A. Čontala and H. Uršič Nemevšek, "Topochemical conversion under hydrothermal conditions as a route for the preparation of anisotropic perovskite particles". Presentation at the Technical meeting and exhibition MS&T17, Materials Science & Technology, October 8-12, 2017, Pittsburgh, Pennsylvania, USA.

Award

The greenest research Award for the contribution: "Hydrogen evolution with $SrTiO_3/Bi_4Ti_3O_{12}$ nanoheterostructural platelets as nobel-metal free photocatalyst" at *Throughout knowledge towards a green new world: 13th Jožef Stefan International Postgraduate School Students' Conference and 15th Young Researchers' Day of Chemistry, material science, biochemistry and environment, (CMBE day),* 27th-28th May 2021, online.

Other – Secondary Authorship (Editor)

N. Kuzmić (ed.), A. Čontala (ed.) et al., Book of abstracts. 15th Jožef Stefan International Postgraduate School Students' Conference, 31st May - 2nd June, 2023, Kamnik, Slovenia Ljubljana: Jožef Stefan Institute: Jožef Stefan International Postgraduate School, 2023.

R. Novak (ed.), A. Čontala (ed.) et al., Book of abstracts: 14th Jožef Stefan International Postgraduate School Students' Conference, 1st - 3rd June, 2022, Kamnik, Slovenia. Jožef Stefan International Postgraduate School, 2022.

Biography

B. Sc. Chemistry
2011-2014
Faculty of Chemistry and Chemical Engineering, University of Maribor, Slovenia

M. Sc. Chemistry
2014-2016
Faculty of Chemistry and Chemical Engineering, University of Maribor, Slovenia

Ph.D. Nanosciences and Nanotechnologies
2016-2023
International Postgraduate School Jožef Stefan, Jožef Stefan Institute, Ljubljana, Slovenia